

Institut für Geowissenschaften, Universität Potsdam

**Heterogeneities in the D'' layer beneath the southwestern Pacific  
inferred from anomalous P- and S-waves.**

Dissertation

zur Erlangung des akademischen Grades

Doktor der Naturwissenschaften

(Dr. rer. nat.)

in der Wissenschaftsdiziplin Geophysik

eingereicht an der

Mathematisch-Naturwissenschaftlichen Fakultät

der Universität Potsdam

von

Tadashi Kito

geboren am 17.12.1970 in Okazaki in Japan

Potsdam, im April 2003

### **Abstract**

The P- and S-wave velocity structure of the D'' layer beneath the southwestern Pacific was investigated by using short-period data from 12 deep events in the Tonga-Fiji region recorded by the J-Array and the Hi-net in Japan. A migration method and reflected wave beamforming (RWB) were used in order to extract weak signals originating from small-scale heterogeneities in the lowermost mantle. In order to acquire high resolution, a double array method (DAM) which integrates source array beamforming with receiver array beamforming was applied to the data. A phase-weighted stacking technique, which reduces incoherent noise by employing complex trace analysis, was also applied to the data, amplifying the weak coherent signals from the lowermost mantle. This combination greatly enhances small phases common to the source and receiver beams. The results of the RWB method indicate that seismic energy is reflected at discontinuities near 2520 km and 2650 km, which have a negative P-wave velocity contrast of 1% at the most. In addition, there is a positive seismic discontinuity at a depth of 2800 km. In the case of the S-wave, reflected energy is produced almost at the same depth (2550 km depth). The different depth (50 km) between the P-wave velocity discontinuity at the depth of 2800 and a further S-wave velocity discontinuity at the depth of 2850 km may indicate that the S-wave velocity reduction in the lowermost mantle is about 2-3 times stronger than that of P wave. A look at a 2D cross section, constructed with the RWB method, suggests that the observed discontinuities can be characterized as intermittent lateral heterogeneities whose lateral extent is a few hundred km, and that the CMB might have undulations on a scale of less than 10 km in amplitude. The migration shows only weak evidence for the existence of scattering objects. Heterogeneous regions in the migration belong to the detected seismic discontinuities. These anomalous structures may represent a part of hot plume generated beneath the southwestern Pacific in the lowermost mantle.

### **Abstract (German)**

Die P- und S-Wellen-Geschwindigkeitsstruktur der D'' Schicht unter dem südwestlichen Pazifik wurde mittels kurzperiodischer Daten von 12 Tiefbeben in der Tonga-Fiji-Region untersucht, die vom J-Array und Hi-net-Array in Japan registriert wurden. Es wurde für Punktstreuer und ebene Schichten migriert, um schwache Signale zu extrahieren, die an relativ kleinräumigen Heterogenitäten des unteren Mantels entstehen. Um eine höhere Auflösung zu erzielen, wurde die Double Array-Methode (DAM) verwendet, die Empfängerarray und Quellarray gleichzeitig nutzt. Hierbei ist auch das Phase-Weighted Stack-Verfahren angewendet worden, um inkohärentes Rauschen zu reduzieren und somit schwache kohärente Signale aus dem unteren Mantel aufzulösen. Das Ergebnis der Ebenen-Schichten-Methode (RWB) zeigt, dass sich in der D''-Schicht negative Geschwindigkeitsdiskontinuitäten mit P-Wellen Geschwindigkeitskontrasten von höchstens  $-1\%$  in den Tiefen von 2520 km und 2650 km befinden. Zusätzlich befindet sich eine positive Geschwindigkeitsdiskontinuitäten in der Tiefe von 2800 km. Bei den S Wellen treten Geschwindigkeitsdiskontinuitäten in einer Tiefe von etwa 2550 km und 2850 km auf. Die scheinbare Verschiebung (50 km) der S-Wellen-Geschwindigkeitsdiskontinuität in der Tiefe von 2850 km deutet darauf hin, daß die S-Wellen-Geschwindigkeitsreduktion im unteren Mantel 2-3 mal stärker ist als die P- Wellen-Geschwindigkeitsreduktion.

Ein zweidimensionaler Querschnitt, der mittels der RWB Methode und der Aufspaltung des Gesamtempfängerarrays in Subarrays gewonnen wurde, deutet darauf hin, dass die beobachteten Diskontinuitäten als intermittierende laterale Heterogenitäten mit einer Wellenlänge von einigen hundert km charakterisiert werden können. Die Kern-Mantel-Grenze (KMG) weist möglicherweise Undulationen mit einer Amplitude von 10 km auf. Die Migration weist nur schwache Hinweise für räumliche Streukörper auf. Die in der Migration abgebildeten heterogenen Regionen korrespondieren mit den mittels der RWB Methode gefundenen seismischen Diskontinuitäten. Bei den gefundenen Heterogenitäten könnte es sich um einen Teil eines aufsteigenden heißen Stroms unter dem südwestlichen Pazifik handeln.

## Contents

<b>1. Introduction.....</b>	<b>6</b>
1.1 General View of the Earth's Structure.....	6
1.2 Role of the Earth's Heat.....	6
1.3 Seismic Structure of the Earth's Interior.....	7
1.4 Origin of the D' Layer.....	10
1.5 Ultra Low Velocity Zone.....	11
1.6 D'' Anisotropy.....	12
1.7 Lateral Velocity Variation of the Lowermost Mantle and D'' Discontinuity.....	12
<b>2. Geological setting of the Tonga-Fiji Region and the Japanese Arc.....</b>	<b>16</b>
2.1 Tonga-Fiji Region.....	16
2.2 The Japanese Islands Arcs.....	16
2.3 Source and receiver regions.....	17
<b>3. Data.....</b>	<b>19</b>
3.1 J-Array.....	19
3.2 Hi-net.....	19
3.3 Deep Focus Events in the Tonga-Fiji Region.....	20
<b>4. Observations.....</b>	<b>23</b>
4.1 Characteristics of PcP (ScS) and PdP (SdS) Phases.....	23
4.2 Fresnel Zone and Resolution.....	27
4.3 Depth phases pP and sP.....	27
<b>5. Theory of Array Methods.....</b>	<b>28</b>
5.1 Introduction.....	28
5.2 Double Beam Forming.....	28
5.3 Reflected Wave Beamforming (RWB).....	30
5.4 Migration.....	33
5.5 Subarrays.....	34
5.6 Bootstrap Method.....	36
<b>6. Coherence Measurements.....</b>	<b>36</b>
6.1 Introduction.....	36

6.2 Linear Stack.....	38
6.3 Beam Power.....	39
6.4 Semblance.....	39
6.5 Phase Weighted Semblance.....	40
<b>7. Data Preprocessing.....</b>	<b>41</b>
7.1 Rotation Process for S-wave Data.....	41
7.2 Common Preprocessing for P and S-waves.....	41
7.3 Source and Receiver Corrections.....	48
<b>8. Synthetic Tests.....</b>	<b>51</b>
8.1 Calculations of Synthetic Seismograms.....	51
8.2 Analysis of Synthetic Seismograms.....	52
<b>9. Results.....</b>	<b>67</b>
9.1 Results using the RWB method.....	67
9.2 Results from Bootstrap Analysis.....	75
9.3 Results from the RWB method (using subarrays).....	77
9.4 Results from the Migration.....	90
9.5 Comparison of Observational Data and Synthetic Data.....	95
9.6 Comparison between the P- and S-Wave Velocity Discontinuities.....	96
9.7 Comparison between different frequency bands.....	96
9.8 Inferred 1-D P-Wave Velocity Model beneath the Southwestern Pacific.....	98
<b>10. Discussion.....</b>	<b>100</b>
10.1 Anomalous PcP and ScS Travel Times.....	100
10.2 Influence of the Slab beneath the Tonga-Fiji Region.....	103
10.3 Variation of the Travel-Time Difference between PcP and P.....	104
10.4 Anomalies of PcP/P and ScS/S Amplitude Ratios.....	105
10.5 Mislocation of Events and other Problems.....	107
<b>11. Conclusions.....</b>	<b>108</b>
<b>Acknowledgements.....</b>	<b>110</b>
<b>References.....</b>	<b>111</b>
<b>Appendix.....</b>	<b>122</b>

## **1. Introduction**

### **1.1 General View of the Earth's Structure**

The Earth consists of several global layers, including inner core, outer core, mantle and crust after separation of the iron-alloy core and silicate-oxide mantle early in the history of the Earth. Seismology has played an important role in the investigation of the interior structure of the Earth. Propagation of seismic waves through the interior of the Earth is the only direct signal that can supply information on elastic properties and the dynamic structure of the solid Earth. Since the beginning of the 20<sup>th</sup> century, seismological studies revealed that the Earth's structure is radially symmetric with several discontinuities and/or transitions that separate regions of different elastic properties. Ever since Mohorovicic (1909) determined the thickness of the crust, many seismologists have contributed to our knowledge of the P- and S-velocity structure inside the Earth's layers. For instance, Gutenberg (1914) presented an accurate determination of the depth of the Core Mantle Boundary (CMB) and discovered the existence of inhomogeneous structures in the lowermost mantle. Lehmann (1936) presented the first evidence for the existence of the Earth's inner core. She observed small signals called PKiKP from the Inner Core Boundary (ICB) in the shadow zone and attributed these phases to a seismic discontinuity inside the core where P-wave velocity increases dramatically. Although evidence for the solidity of the inner core is derived from observations of free oscillations of the Earth, there are still few observations of PKJKP that propagate in the inner core as an S-wave, which would be direct evidence for the solidity of the inner core. One of the reasons for the difficulty in observing PKJKP is that the expected amplitude of PKJKP phase could be below typical noise levels (Doombos, 1974). After the gross symmetric seismic structure of the Earth had been determined, body wave and surface wave travel time tomography analyses began to be used to resolve the long and intermediate scale structures of the Earth's crust and mantle, which determines the three dimensional structure (Aki et al., 1976, Woodhouse and Dziewonski, 1984, Dziewonski, 1984, Nataf et al., 1986, Tanimoto, 1987, 1988). To determine the finer structure of the Earth, the study of reflected, scattered or converted body waves becomes important and reveals that the Earth contains more complicated heterogeneous structures than previously assumed.

### **1.2 Role of the Earth's Heat**

Mantle convection plays an important role in heat transfer (Tozer, 1972), since convection is more effective than conduction in heat transfer of the solid Earth. Continental drift is just the top boundary manifestation of global-scale convection throughout the 3000-km thick mantle, driven by the presence of heat within the Earth's deep interior that can not be transported by conduction alone (Holmes, 1931, 1933, 1945). There are two major sources of the Earth's heat, one of which is the cooling of the Earth since its early history when its internal temperature was much higher as

compared to the present. The other source of heat is the decay of long-lived radioactive isotopes such as  $^{238}\text{U}$ ,  $^{235}\text{U}$ ,  $^{232}\text{Th}$  and  $^{40}\text{K}$  (Rybach, 1976). Lateral or vertical heterogeneities throughout the Earth's interior are the result of mantle convection, which is in turn caused by heat dissipation, since mantle convection accompanies the movement of mantle material. One could say that the lateral heterogeneities or seismic discontinuities in the various depth ranges are signs of the dynamics of the Earth, such as mantle convection (Montagner, 1994).

### 1.3 Seismic Structure of the Earth's Deep Interior

In many aspects of the Earth's dynamical processes, such as fundamental constraints on mantle convection or the rheological properties of the mantle, our understanding of global geophysical processes has benefited from advances in the study of the Earth's magnetic and gravity fields, laboratory experiments on mantle minerals under high temperature and pressure conditions, as well as computer simulations of convection. Among these, seismological studies have provided us with the most stringent constraints on the Earth's deep structure, because they provide us with a present-day snapshot of the mantle convection.

As seismological observations have accumulated, major mantle discontinuities have been found by using short-period body waves which reflect and/or convert to P or S-waves at seismic velocity discontinuities (Jeffreys, 1939, Niazi and Anderson, 1965, Lay and Helmberger, 1983, Lay, 1989). The mantle contains two global depth intervals which are characterized by anomalous seismic properties, which are the D' layer at the base of the mantle and the transition zone between upper and lower mantle at a depth between 410 km and 660 km. (Niazi and Anderson, 1965, Lay and Helmberger, 1983, Lay, 1989). The upper mantle transition zone is characterized by at least two worldwide discontinuities at a depth of about 410 km and 660 km and an increased velocity gradient between both discontinuities. The D' layer has a thickness of about 200 km to 400 km and acts as a thermal boundary layer above the core-mantle boundary (CMB) at a depth of about 2890 km (Jones, 1977). The density contrast across the CMB is about  $4.3 \times 10^3 \text{ kg/m}^3$ , which is even larger than the contrast between surface rocks and the atmosphere (about  $2\text{-}3 \times 10^3 \text{ kg/m}^3$ ). The velocity contrast reaches 58.4 % for P waves (based on the IASP91 model), which is the largest seismic discontinuity in the Earth.

The D'' layer was first defined by Bullen (1949) and it is now established that the D'' layer is heterogeneous. For instance, small-scale heterogeneities are assumed to explain observations of high frequency, scattered body waves which travel through the core or the codas of *Pdiff* (e.g. Doornbos and Vlaar, 1973, Bataille et al., 1990, Loper and Lay, 1995, Bataille and Lund, 1996) and long-scale length heterogeneities are visible in tomographic studies (e.g. Dziewonski, 1984, Wysession et al., 1994).

The CMB and the Earth's surface are the two largest discontinuities in the Earth and the D'' region

and lithosphere are in contact with these two discontinuities as their boundary layers, respectively. In many ways, the geophysical characteristics of the D'' region are similar to those of the lithosphere. Wyssession (1996) called the D'' structures "continents of the core" because of the analogy between the continents at the Earth's surface and the continent-sized heterogeneities and small-scale features of the D'' layer.

It is important to extract small seismic signals from the Earth's deep interior to determine the seismic structure of the Earth. In order to suppress noise to identify very small amplitude signals, many seismic analysis techniques have been developed. For instance, non-linear stacking techniques such as the n-th root process were developed by Muirhead (1968) and Kanasewich et al. (1973). The advantage of non-linear stacking is its superior suppression of unexpected noise, while the severe distortion of the original waveforms proves to be a disadvantage. The n-th root stack has been successfully applied in detecting weak non-prominent phases in the Earth's deep interior. Using the n-th root stack, Richards and Wicks (1990) found s670P conversions. Kawakatsu and Niu (1994) detected s920P conversions in the Tonga-Fiji subduction zone, which indicates the existence of a 920-km seismic discontinuity and provides us with important information about the mantle convection.

The first discovery of S-wave triplication in the distance range from 70° to 95° by Lay and Helmberger (1983) suggests that the top of the D'' layer is a first-order discontinuity with a regional velocity jump of 2 to 3 % at a depth of about 2620 km. This study indicates that the D'' layer may be a material boundary layer whose depth can vary by about 40 km. For P waves, the earliest suggestions of a first order discontinuity at the top of the D'' layer were proposed by Wright et al. (1980, 1985). The discovery of these studies conducted in the early 1980s, namely a deep-mantle S-wave reflector several hundred kilometers above the CMB, led to the method of analyzing reflections and refractions to map the lateral extent of localized stratification, its depth and material contrasts.

The existence of precursors to core phases of PKP and PKKP, travel time anomalies of short-period PcP, ScS, SKS and PKIKP, or long-period P-diffracted and S-diffracted waves, and the discovery of P- and S-wave triplication has furthered a general understanding of heterogeneities near the CMB (e.g. Young and Lay, 1990, Weber, 1993, Garnero and Helmberger, 1993, Ritsema et al., 1997, Thomas et al., 1999, Niu and Wen, 2001). It has been recognized that the lowermost mantle contains even more heterogeneities than previously assumed. Using tomographic methods, Fukao et al. (1993) found a 1 % anomaly in P wave velocity on a global scale at the depth range of 2700-2900 km. This 1 % perturbation is too large to explain the D'' layer as just a thermal discontinuity. Because the distribution of high-velocity anomalous regions in the mantle transition zone is relatively similar to that of high-velocity anomalous regions in the lowermost mantle, they suggest that high-velocity anomalies in the D'' layer can be related to subducted oceanic slabs, which



were deposited at the bottom of the upper mantle (at the 660-km discontinuity) and dropped into the D'' layer.

Haddon and Cleary (1974) found precursors of PKP waves and suggested that one possible structure which could produce such precursors is a volumetric heterogeneity within the D'' layer. However, such precursors can also be explained by a 300-m amplitude undulation of the CMB (Bataille et al., 1990). Cleary and Haddon (1972) interpreted the observed short-period precursors to PKIKP as waves scattered from small-scale heterogeneities near the CMB. This suggests that both volumetric anomalies in the D' layer and small-scale undulations of the CMB can explain their observations. Bataille and Flatte (1988) examined global PKP precursors, but could not distinguish between CMB topography and three-dimensional inhomogeneities in the D' layer. Their studies revealed the detailed structure of small-scale heterogeneities based on precise determination of scattered core waves. These waves are short-period waves, which are precursors to PKIKP, PKKP, and PKPPKP. Recent work on the PKP precursors by Niu and Wen (2001) indicated that the onset times of the PKP precursors could be explained by the existence of seismic scatterers in the lowermost 100 km of the mantle west of Mexico, within an area of 200-300 km. On one hand, Thomas et al. (1999) suggested that the PKP precursors possibly originate from scattering in partial melt at the base of the mantle, because they have detected scatterers in regions where ultralow-velocity zones (ULVZ) have been discovered recently (e.g., Garnero et al., 1993, Mori and Helmberger, 1995, Garnero and Helmberger, 1995, 1996, Garnero et al., 1998, Revenaugh and Meyer, 1997, Vidale and Hedlin, 1998). On the other hand, Hedlin et al. (1997) suggest that the scattering volume that can generate the PKP precursors exists not only in the D'' layer but is spread throughout the Earth's mantle. Their results are consistent with models of small-scale compositional heterogeneity in the mantle (Davis, 1984, Davis, 1990, Gurnis, 1986). The analysis of the scattered waves has been based on the single-point scattering theory using the Born approximation (e.g., Doornbos, 1978, Aki, and Richards, 1980). The heterogeneities have been quantitatively estimated by using either global network data (e.g. WWSSN and GDSN) or through array observation (e.g. NORSAR). However, it is still difficult to determine whether the primary scattering structure is caused by volumetric heterogeneities near the CMB or by undulation of the CMB topography.

Furumoto (1992) estimated the topography of the CMB by observing steep-angle scattered S-waves, which do not propagate along the great circle path, using stations with a dominant period of 5 s managed by the Japan Meteorological Agency (JMA). He used a migration method to calculate semblance values and the migration method should be a powerful tool for detecting the small scale of heterogeneities near the CMB. Various migration methods have been applied to investigate the fine structure of the lowermost mantle in many areas (e.g. Lay and Young, 1996, Bilek and Lay, 1998, Freybourger et al., 2001).

#### 1.4 Origin of the D'' Layer

The origin of the heterogeneous structure in the lowermost mantle is one of the most important issues for the Earth's dynamic behavior, such as mantle convection, the generation of hot plumes and the behavior of subducted slabs. It is generally accepted that the lowermost mantle contains large and local scaled lateral heterogeneities. There are many explanations for the structural heterogeneities at the base of the mantle. Recent tomographic studies on the lowermost mantle (e.g. Inoue et al., 1990, Fukao, 1993, M. Wysession, 1996, R.D. van der Hilst et al., 1997, Boschi et al., 1999, Valenzuela et al., 2000, Karason and R.D. van der Hilst, 2001) suggest that there are some regions in the lowermost mantle that can be characterized as anomalously high-velocity zones. Tkalcic et al. (2002) used PKP (AB-DF), PKP (BC-DF) and PcP-P travel time data to determine the P velocity structure in the deep mantle and they discovered similar velocity perturbation patterns as those gained from tomographic studies. For instance, the lower mantle structure beneath northern Siberia shows up as distinct seismic high-velocity anomaly in the tomographic studies (e.g. Inoue et al., 1990, Fukao, 1993, M. Wysession, 1996, R.D. van der Hilst et al., 1997, Boschi et al., 1999, Valenzuela et al., 2000, Karason and R.D. van der Hilst, 2001). Investigations of the lower mantle beneath northern Siberia (e.g. Weber, 1993, Thomas, Ch., and M. Weber, 1997, Scherbaum. et al., 1997, Freybourger, et al., 1999, 2001) show distinct P- and S-wave discontinuities or scattering objects which may imply the presence of old subducted material. Arrival-time tomography also indicates that slabs may penetrate into the lower mantle and descend down to the CMB in some regions of the globe (Creager and Jordan, 1986, van der Hilst et al., 1997). Kendall and Shearer (1994) mapped the thickness distribution of D'' using SdS phases, which indicates that the areas where SdS phases were detected are consistent with the high-velocity anomalous area in the tomogram obtained by Su et al. (1994). Furthermore, the thickness of the D'' layer detected by using SdS phases is several times that of the oceanic plates. If the high-velocity anomalies in the D'' layer are related to fragments of subducted slabs, this might imply that enormous megaliths exist in the lowermost mantle.

Another possible cause for the D'' layer is a chemical reaction between iron alloys in the core and silicates in the lowermost mantle. One possible chemical process in the D'' layer is the chemical reaction of (Mg, Fe) SiO<sub>3</sub> Perovskite with liquid iron to the MgSiO<sub>3</sub>, SiO<sub>2</sub>, and FeO and FeSi Metal. In addition to the chemical heterogeneous structure, a phase transformation of SiO<sub>2</sub> to a high-pressure phase (Kingma et al., 1995) could cause seismic velocity anisotropy and a world-wide discontinuity in the D'' region.

It has generally been accepted that D'' contains a thermal boundary layer at its base which transmits about 10 to 15 % of the Earth's heat flow (Davies, 1980). Kendall and Shearer (1994) proposed a relationship between the distribution of heterogeneities and the flow in the lowermost

mantle. Jeanloz and Richter (1979) and Jeanloz and Morris (1986) suggested that the D' layer is a thermal boundary layer which is formed by heat flow from the outer core. Convection simulations show that a thermal boundary layer should exist in the lowermost mantle (Jarvis and Peltier, 1984). Sidorin et al. (1999) tested a phase change model for the origin of the D' seismic discontinuity by comparing the results of convection modeling with seismic observations. They found that one of the best fits is obtained for phase transitions characterized by a Clapeyron slope of  $-6 \text{ MpaK}^{-1}$  and an elevation above the CMB of  $-150 \text{ km}$  under adiabatic temperature. Though there are a lot of studies on the origin of the D' layer, this issue is still rather controversial and therefore one might suppose that the D' layer is a complex structure combining many factors mentioned above.

### **1.5 Ultra Low Velocity Zone**

During the past several years, many observations using core-related phases such as ScP, PKP, SKS or SPdKS led to the discovery of drastic local velocity reduction just above the CMB. These recently discovered low-velocity layers at the base of the mantle yield P- and S-wave velocity reductions exceeding 10 %, which corresponds to a thickness of 5-10 km for these layers (e.g., Garnero et al., 1993, Mori and Helmberger, 1995, Garnero and Helmberger, 1995, 1996, Garnero et al., 1998, Revenaugh and Meyer, 1997, Vidale and Hedlin, 1998). The velocity variations of such low-velocity zones are much greater than those suggested by travel-time tomography, and this structure is therefore referred to as an ultra-low-velocity zone (ULVZ) (e.g., Garnero et al., 1993, Mori and Helmberger, 1995, Garnero and Helmberger, 1995, 1996, Garnero et al., 1998, Revenaugh and Meyer, 1997, Vidale and Hedlin, 1998). Extensive regions of such ULVZs are found beneath the central Pacific Ocean, Alaska, Iceland and Africa. However, other areas have been examined and do not show evidence of this structure, suggesting either that it is not present or that it is less than a few km thick. In the latter case, it may be seismically invisible to current analysis methods. In areas such as the central Pacific, the ULVZ shows significant lateral variations in thickness (Garnero and Helmberger, 1996). ULVZs at the CMB are probably the most anomalous structures in the mantle with S velocity reduced by up to 30 % and P-wave velocity up to 10 % (Garnero and Helmberger, 1996). Thomas et al. (1998) observed a reflected phase from a low-velocity lamella in D' which is located at 282 km above the CMB with a thickness of 8 km beneath Western Siberia.

Partial melt in the D' layer reduces strongly the S-wave velocity, which is considered the main cause for ULVZs. However, a partially molten layer is not sole cause for ULVZs. There is evidence for a possible ULVZ which reduces only the P wave velocity under the Gulf of Alaska (Castle and van der Hilst, 2000). This might indicate that the ULVZ could be interpreted as being a chemical origin as well.

There is an intriguing correlation between the lateral variation of seismic wave velocity in the lowermost mantle and the existence of ULVZs. Castle et al. (2000) indicated that the low-velocity

anomalies in the lowermost mantle discovered through tomographic studies could be connected to ULVZs, because the ULVZs were more often found in low-velocity zones than in high-velocity zones in the lowermost mantle.

### **1.6 D'' Anisotropy**

Seismic anisotropy causes a birefringence that splits the S-waves into orthogonal polarizations that travel with different velocities owing to organized mineralogical or petrographic fabrics. Evidence of shear-wave anisotropy in the lowermost mantle offers additional constraints on the nature of the region. Despite initial observations of time separations between radially and transversely polarized core-reflected shear waves (ScS) (Mitchell and Helmberger, 1973, Lay and Helmberger, 1983), anisotropy was not considered as an explanation for the D'' layer until the late 1980s. In an effort to explain the earlier observation, Cormier (1986) modeled the waveforms in a transversely isotropic D'' layer. Kendall and Silver (1996) indicated that a 'graveyard' for subducted lithosphere could produce seismic anisotropy in the high-velocity anomalous region in the lowermost mantle due to the velocity contrast between the lithospheric mantle and material that formerly constituted the oceanic crust. They obtained positive values (up to 5 s) of the difference between the travel times of radial ( $S^{SV}$ ) and transverse ( $S^{SH}$ ) components of S or ScS waves. The same observation was obtained for other regions of D'' beneath Alaska (Lay and Young, 1991, Matzel et al., 1996, Garnero and Lay, 1997) and the northeastern Pacific (e.g., Vinnik et al., 1995, Ritsema et al., 1998). On the other hand, smaller values of travel-time difference, ranging from -2 to +2 s, are observed for the D'' layer beneath the central Pacific, where the shear wave velocity is relatively low (Pulliam and Sen, 1998, Ritsema et al., 1998, Russel et al., 1998). Vinnik et al. (1989, 1995) have reported D'' anisotropy beneath the Pacific based on observations of anomalously high-amplitude SVdiff arrivals at epicentral distances beyond 106 degrees. Vinnik et al. (1995) also note that SVdiff is delayed by roughly a quarter period and that it is higher in frequency content than the SHdiff arrival. In contrast, Pulliam and Sen (1998) have observed that S/ScS on the radial component arrives earlier than S/ScS on the transverse component, using Fiji events recorded on stations in south-central USA. Little evidence of S/ScS splitting was observed in the data from Fiji events recorded in Canada which also map the central Pacific. Fiji events recorded in South America suggest that D'' beneath the southern Pacific is also isotropic (Kendall and Silver, 1998). In separate studies, Vinnik et al. (1998) and Russell et al. (1998) show evidence for a localized region with a high degree of anisotropy, which they attribute to processes associated with the entrainment of material towards the mid-Pacific hot plume. In summary, these observations suggest that the anisotropy in the D'' region beneath the Pacific varies in style and magnitude over relatively short distances.

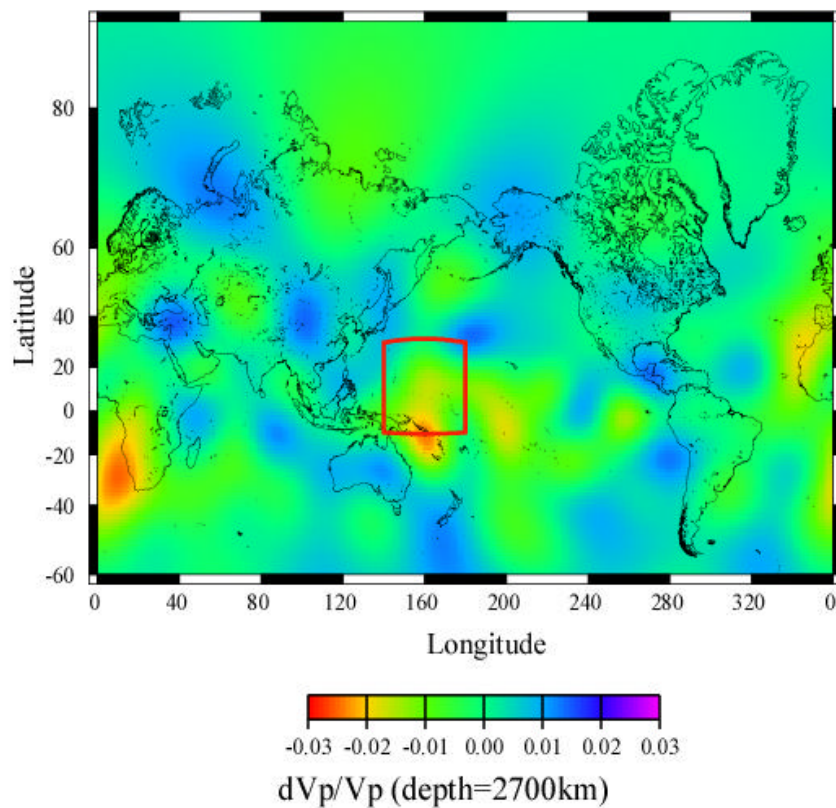
### **1.7 Lateral Velocity Variation of the Lowermost Mantle and D'' Discontinuity**

According to recent tomographic work of the lowermost mantle (e.g. Inoue et al., 1990, Fukao, 1993, M. Wyssession, 1996, R.D. van der Hilst et al., 1997, Boschi et al., 1999, Valenzuela et al., 2000, Karason and R.D. van der Hilst, 2001), there are a few global-scale lateral velocity patterns in the lower mantle. Figure 1.1 shows a P wave velocity tomogram by Boschi and Dziewonski (1999) and Figure 1.2 shows S-wave velocity perturbations obtained by different recent studies. Some of the most distinct features are two large low-velocity anomalous regions beneath the western Pacific and Africa, and one high-velocity region surrounding the Pacific Ocean. This can be recognized both in P wave perturbation and in S-wave perturbation. This global pattern of seismic velocity anomalies is consistent with the gravity distribution (Hager et al., 1985). Both P- and S-waves beneath the southwestern Pacific region and Africa propagate a few percent (P- 1%, S- 2%) slower than in other areas. This implies that the lower mantle beneath the southwestern Pacific and Africa can be characterized as a distinguished lower P- and S-velocity zone, which might be attributed to hot plume generation. Romanowicz (1997, 1998) indicates the existence of a degree 2 pattern in Q (Quality factor) in the lowermost mantle with high attenuation centered in the Pacific and under Africa, surrounded by a ring of low attenuation. This would suggest a thermal origin of the longest wavelength lateral heterogeneity observed in the D'' layer and would confirm the common interpretation of the large-scale low velocities in the Pacific and under Africa in terms of upwelling hot plumes. As far as low velocity regions in the lower mantle are concerned, Ritsema et al. (1999) found evidence for a tilted low-velocity zone extending from the CMB region beneath the southeastern Atlantic Ocean into the upper mantle beneath eastern Africa. Yamada and Nakanishi (1996, 1998) suggest that there are short-wavelength lateral variations of a P velocity positive reflector in the depth range of 270 km – 170 km above the CMB beneath the southwestern Pacific, which is same area as covered in this study. Shibusaki et al. (1995) also found indications that there may be velocity discontinuities in same region, but with a velocity jump of +1-2% between 2600 and 2700 km. Studies using long-period S-waves for the central Pacific were carried out by Garnero et al. (1993). They suggest a + 3% S-wave velocity discontinuity at 2700 km depth. Russell et al. (2001) presented evidence for the coexistence of velocity discontinuities in both S- and P-wave velocity, whose increase are 1.7% in S velocity and 0.75% in P velocity, 230 km above the CMB beneath the central Pacific. Ritsema et al. (1997) constructed a velocity model for the central-eastern Pacific region (M1), which has a strong negative gradient with 0.5% reduction in shear-wave velocity relative to the preliminary reference Earth model (PREM, Dziewonski and Anderson, 1981) at 2700 km depth and 3% reduction at 2891 km depth and slight velocity reductions from 2000 to 2700 km depth with 0-0.5% lower velocities than PREM.

Analysis of reflected shear wave data reveals that ScS travel times are 3-5 s slower for PREM in the D'' region beneath the central Pacific. This may indicate that the gradient in structure reflects

inflow and ascent of material feeding a plume (Russell et al., 1999). All these seismological studies suggest that the lowermost mantle beneath the southwestern Pacific is a typical region with hot mantle streams and corresponding seismic anomalous structures.

## P wave velocity perturbation in the lowermost mantle



(BDP98, Boschi and Dziewonski, 1999)

**Figure 1.1** P-wave velocity perturbation at a depth of 2700 km. The perturbation data were taken from Boschi and Dziewonski (1999). This velocity perturbation was calculated with respect to the PREM model (Dziewonski and Anderson, 1981). Red zones indicate fast P wave velocity anomalies and blue zones indicate low P wave velocity anomalies. The area marked by a red line is the study area, where a distinguished low velocity anomaly is visible.

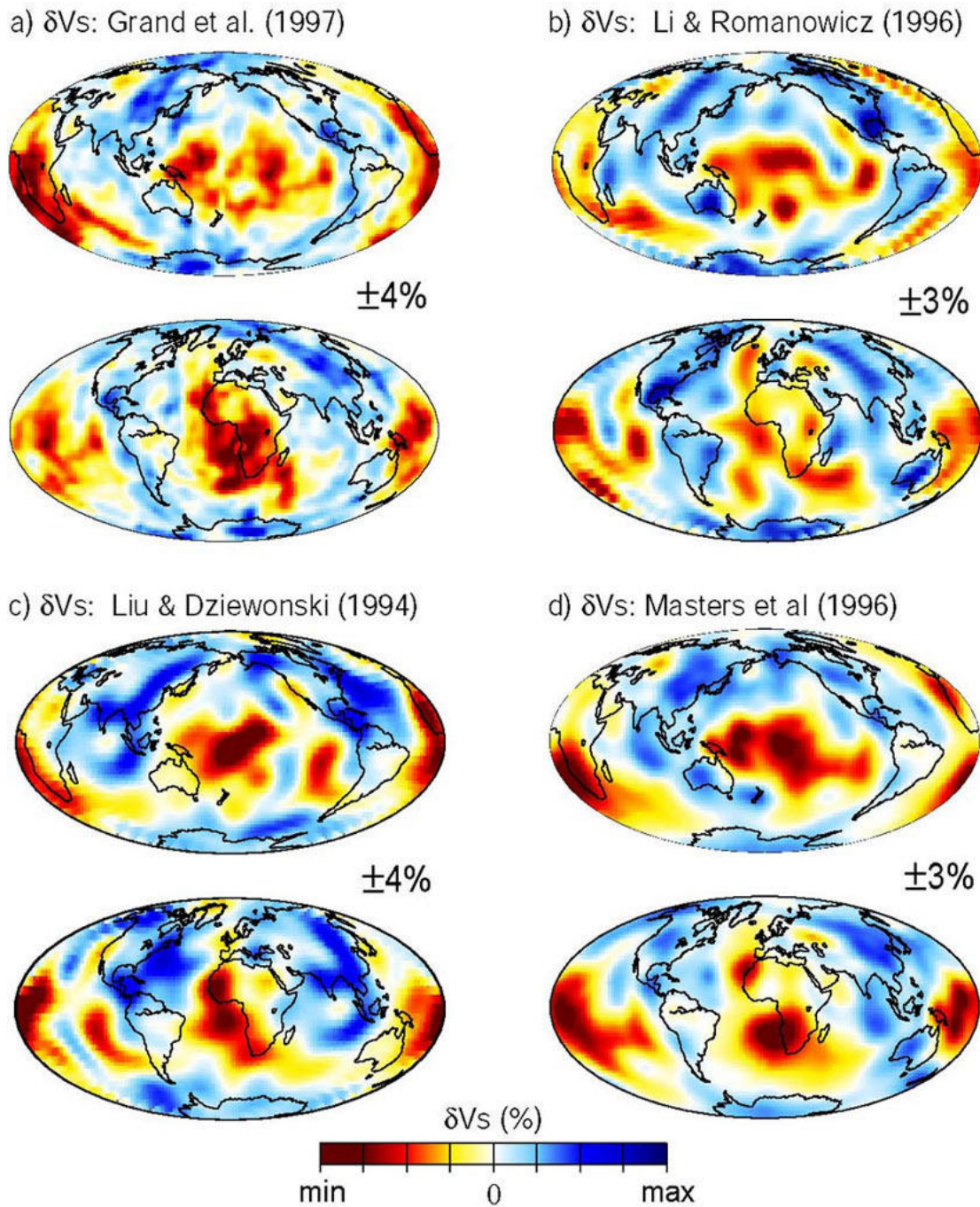


**Figure 1.2** S-wave velocity perturbation from various tomograms in the lowermost mantle. Two panels for each model are displayed (S-waves): one centered on the central Pacific, the other on the Atlantic Ocean. The red colors indicate below-average velocity, which may indicate warmer regions. Blue colors indicate higher velocities, which might indicate colder regions. [The tomograms were taken from *Garnero (2000)*]. In all tomograms, a distinguished low-velocity zone can be seen in the southwestern Pacific region (the study area), where a hot plume may be generated.

## **2. Geological setting of the Tonga-Fiji Region and the Japanese Arc**

The sources of this study are located in the Tonga-Fiji region and the receivers of this study are located in the Japanese Islands. These two regions belong to the circum-Pacific subduction system. The Pacific Ocean came into existence by the continental break-up of Gondwanaland at 600 – 700 Ma and increasingly grew in size until 450 Ma (Hoffman, (1991), Dalziel, 1992). Since then, the subduction has continued up to the present along most margins of the Pacific Ocean.

### **2.1 Tonga-Fiji Region**

The Tonga-Fiji region forms a part of the circum-Pacific subduction system where the slab penetrates into the uppermost lower mantle. Specifically, trenches exist parallel to the island arcs, which are bow shaped and convex toward the trenches and have a marginal sea on the other side. There are many active volcanoes on the islands. Seismicity is very high, many deep earthquakes occur, and where one plate is thrust over the other, the shear causes great earthquakes at shallow depths. Below this region, earthquakes are systematically distributed within the subducting plate and form an inclined Wadati-Benioff seismic zone which may extend for several hundred kilometers into the mantle. Terrestrial heat flow is low on the trench side of the island arc and high on the back-arc basin side.

Zhou et al. (1990), Zhao et al. (1997) and van der Hilst (1995) found indications in the P-velocity models which suggest that the subducted slab is dipping from the Tonga Trench and then deflected horizontally near the 660-km discontinuity. The long, horizontally deflected slab imaged by the P-wave tomography is consistent with the horizontal spread of a fast anomaly in the transition region in the long-wavelength S-velocity models by Su et al. (1994) and Li et al. (1996). Subduction of the oceanic plate has continued up to the present for most regions around the Pacific (Fukao, 1994). Niu and Kawakatsu (1995) derived the depth variation of the 660-km discontinuity beneath Tonga by using S-P converted waves, and Kawakatsu and Niu (1994) have reported that a mid-mantle seismic discontinuity exists at a depth of about 920 km beneath Tonga. This might indicate that the structure beneath the Tonga-Fiji region is controlled by subducted slabs and the discontinuity represents the bottom of the subducted slabs' garnet layer.

### **2.2 The Japanese Islands Arcs**

The Japanese Islands region is located above a typical subduction zone of the circum-Pacific region and can be recognized by the existence of the Wadati-Benioff seismic zones. These zones were recognized as an expression of the Pacific plate subducting beneath the Eurasian plate.

Many tomographic studies have probed the seismic structure beneath Japan (e.g. van der Hilst et al. (1991), Fukao et al. (1992, 1994), van der Hilst (1993)). According to these studies, the deflected



slab beneath Japan is clearly seen in P-velocity models as a fast velocity anomaly. Nakajima et al. (2001) estimated the three-dimensional velocity structure of P, S, and P / S velocity ratio, and their results suggested that partial melting under northeastern Japan spread out from the uppermost mantle along the volcanic front up to the midcrust directly beneath active volcanoes. Moho depth in the central part of northeastern Japan varies within 10 km (Nakajima et al., 2002). They suggest that the Moho depth is approximately 34 km beneath the central part of northeastern Japan, while the Moho depth is about 30 km beneath the coastline of the Japan Sea and 27-29 km beneath the coastline of the Pacific Ocean. Many of the above-mentioned studies on the structure under the Japanese Islands portray the crustal and upper mantle structure beneath Japan as rather complex.

### 2.3 Source and receiver regions

As mentioned above, both sources and receivers are located in rather complex structural regions. A cross section along the great circle path that connects the source region and the receiver region is shown in Figure 2.1. The whole geometry for the source region in the Fiji Islands, the receiver region in the Japanese Islands and the study area is shown in Figure 2.2. In both Figures a low velocity zone can be recognized around the PcP (reflected P wave from the CMB) bounce points.

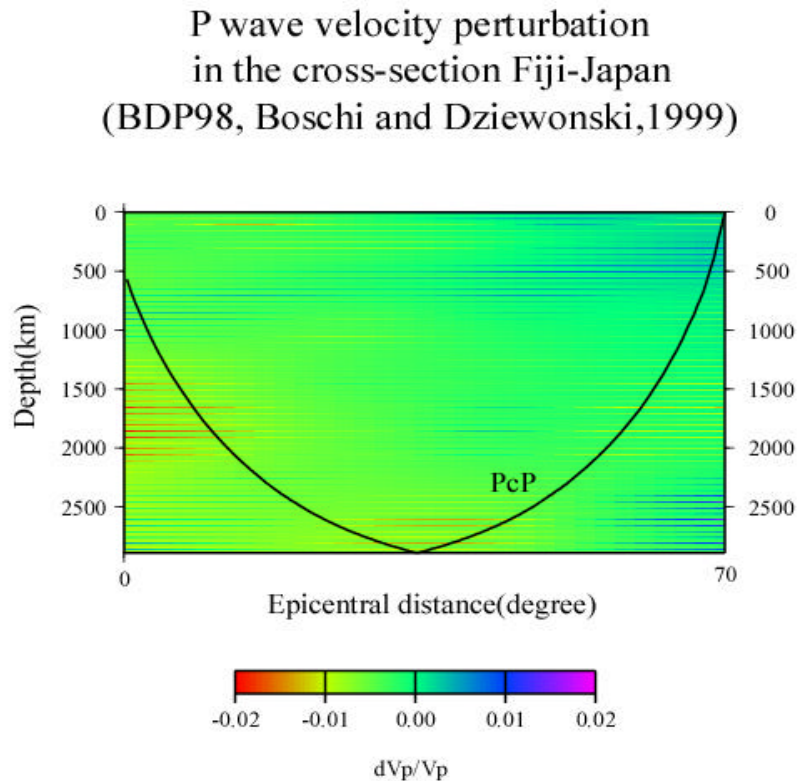


**Figure 2.1** A typical ray path of PcP (500 km source depth and 70 degrees epicentral distance) is plotted in the vertical cross-section between the Tonga-Fiji region and Japan, where P-wave velocity perturbation by Boschi and Dziewonski (1999) is shown in the background. The ray path was calculated based on the IASP91 model. A distinguished low-velocity zone can be recognized in the lowermost mantle near the PcP reflection points.

## Receiver-Source Geometry

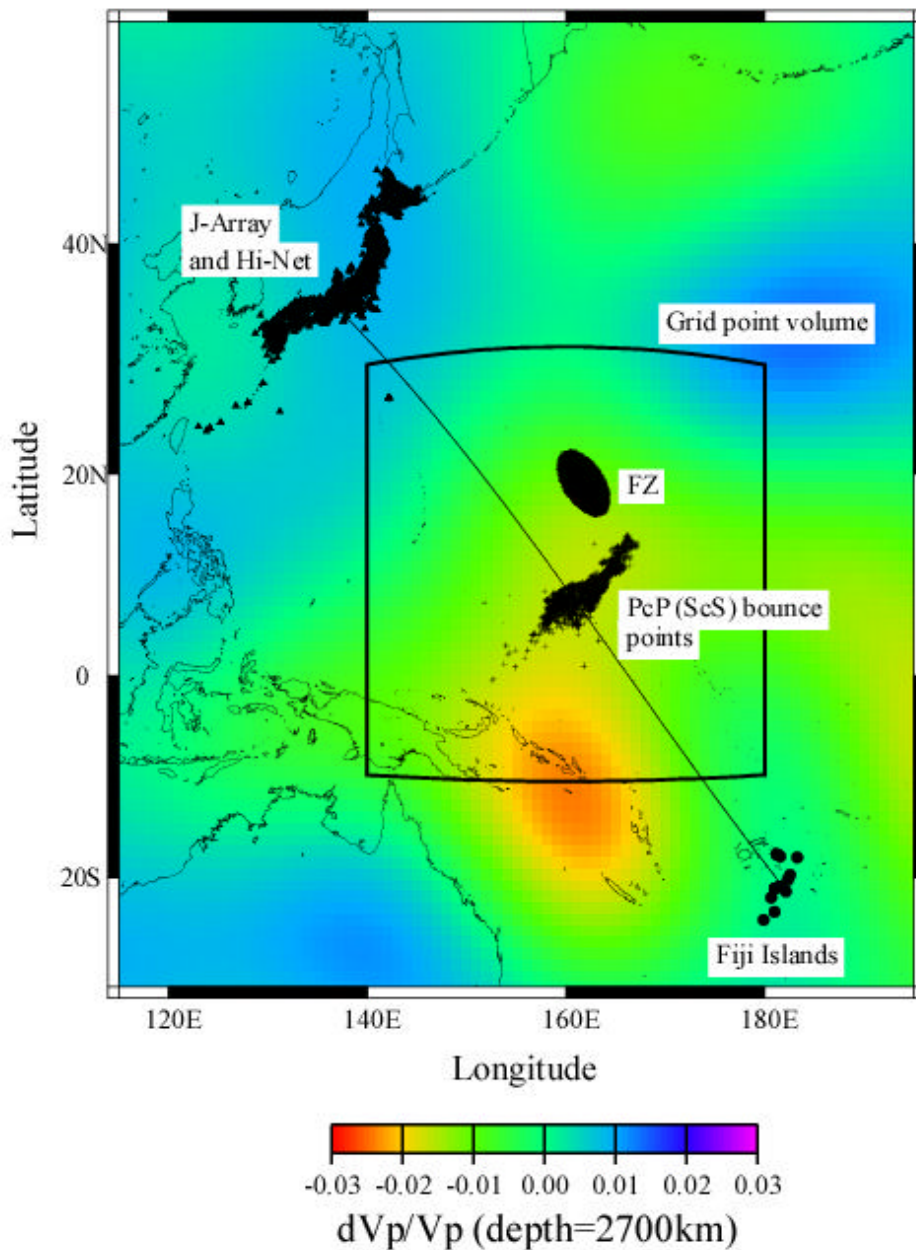


**Figure 2.2** Geometry of the sources (circles), stations (triangles) and the area containing the three-dimensional grid points used for the migration. Also shown are the theoretical bounce points of PcP and ScS (crosses) and the great circle path (solid line) between the center of gravity of sources in the Tonga-Fiji region and that of the stations of the J-Array and the Hi-net in Japan. The ellipse marked by FZ indicates the Fresnel zone at the CMB for a P wave whose dominant period is 2 s. P wave velocity perturbation by Boschi and Dziewonski (1999) is indicated in the background. The study area is located at the edge of the distinct low-velocity zone in the lowermost mantle.

### **3. Data**

#### **3.1 J-Array**

When Japanese government launched a project for earthquake prediction in 1964, microseismic networks were set up in different regions of Japan, which formed the basic network for the J-Array. The term "J-Array" stands for "Japanese large-aperture seismic array" and "J" represents the shape of the Japan Islands. In 1990, the J-Array was founded as a part of the "Central Core of the Earth" project and can be described as a giant telescope aimed at the Earth's interior. This project was designed to distinguish signals of teleseismic earthquakes from background noise by amplifying the signals through array methods. When the J-Array project started, it consisted of several seismic networks operated by universities and national institutions for earthquake prediction. The J-Array has been maintained by eight universities (Hokkaido University, Hirosaki University, Tohoku University, University of Tokyo, Nagoya University, Kyoto University, Kochi University, and Kyushu University) and two institutions (Japan Meteorological Agency and National Research Institute for Earth Science and Disaster Prevention). In December 1992, the Okinawa Weather Bureau of the JMA (Japan Meteorological Agency) was included in the network, turning the J-Array into a large-aperture short-period seismic array whose dimensions measure 3000 km in length along the Japanese Islands and 300 – 500 km in width (J-Array Group, 1993).

Since May 1991, the J-Array has continuously recorded digital waveform data at a sampling rate of 20 Hz. The number of seismic stations was 161 at the time of the project launch in May 1991 and grew to 218 by December 1992. The seismic stations include more than 200 vertical component stations, most of which have seismometers with the natural frequency of 1Hz, but there are few horizontal component stations in the J-Array. The distribution of the J-Array stations is shown in Figure 3.1. One of the advantages of using a large seismic array for detecting later phases is that thanks to the array's size spanning 3000 km and the large station number, the effects of the heterogeneities beneath the individual stations cancel out. This is very beneficial since the crust and upper mantle structures beneath Japan are rather inhomogeneous as discussed in section 2.2.

The J-Array was an attempt to form a single Japan-wide array by collecting and combining the data collected within each network. The trigger method, which starts recording data after the seismometer senses an earthquake, is apt to miss weak signals originating from the Earth's deep interior, such as those which arrive at stations more than 20-30 minutes after the P-onset time. In order to detect weak later phases, it is necessary to record seismic data continuously. The goal of the J-Array project was to view the detailed structure of Earth's deep interior.

#### **3.2 Hi-net**

The other large seismic array used in this study is Hi-net (High Sensitivity Seismograph Network)

installed by the National Research Institute for Earth Science and Disaster Prevention (NIED). The original purpose of Hi-net was to determine the location of micro-earthquakes that occur in the inland of Japan. Since micro-earthquakes in the inland of Japan often occur in a depth range less than 15-20 km, it was necessary to install highly sensitive seismometers at the bottom of observational wells in the region where the level of artificial noise is quite low. The basic policy was to deploy seismic stations with an interval of 20 km and to give priority to filling the observational blank spaces throughout the Japanese Islands. Since September 2000, the data have been available for various seismological studies. The Hi-net is also very suitable for searching weak phases originating from Earth's deep interior due to its high sensitivity and dense station distribution. There are more than 500 stations along the Japan Islands equipped with a three-component seismometer with 1 Hz eigenfrequency. The distribution of Hi-net stations is shown in Figure 3.1. In comparison with the distribution of the J-Array stations, the distribution of Hi-net stations is relatively uniform.

Distribution of J-Array and Hi-Net stations

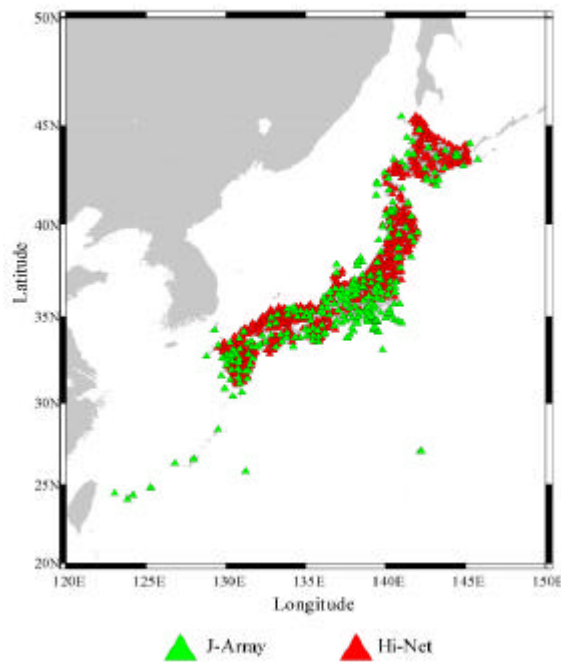


**Figure 3.1** This map shows the station distribution used in this study. The J-Array stations are indicated by green triangles and Hi-net stations are represented by red triangles. The J-Array consists of more than 200 stations with vertical seismometers, and the Hi-net consists of more than 500 stations with three component seismometers with an eigenfrequency of 1 Hz.

### 3.3 Deep Focus Events in the Tonga-Fiji Region

12 deep-focus events in the Tonga-Fiji region used in this study were recorded by the J-Array and the Hi-net in Japan. Events with magnitudes greater than 5.5 (mb) were selected to get clear P-wave

and S-wave arrivals and events with a depth exceeding 350 km were selected to avoid contamination by depth phases such as pP and sP (reflected or converted phases from the Earth's surface). Depth phases have relatively large amplitude and usually include longer periods in comparison with direct P-waves due to attenuation in the upper mantle above the hypocenters. The hypocenters are distributed between 367 km and 655 km. The distribution of the events used in this study is shown in Figure 3.3.

Source mechanisms of these events are shown in Figure 3.2. If a nodal plane happens to lie between P (S) and PcP (ScS), the polarity of either P (S) or PcP (ScS) would be reversed, which can be a serious problem for the Double Array stacking process. Since the polarity of PcP could vary among the events, the summation process for PcP or later phases could not work effectively. Fortunately, there is no event for which the nodal plane lies between P (S) and PcP (ScS) and P (S) and PcP (ScS) have the same polarity (see Figure 3.2). The total number of selected data from both arrays is 2017 P-wave traces and 863 S-wave traces. The source parameters of all events are shown in Table 1 in Appendix 6.

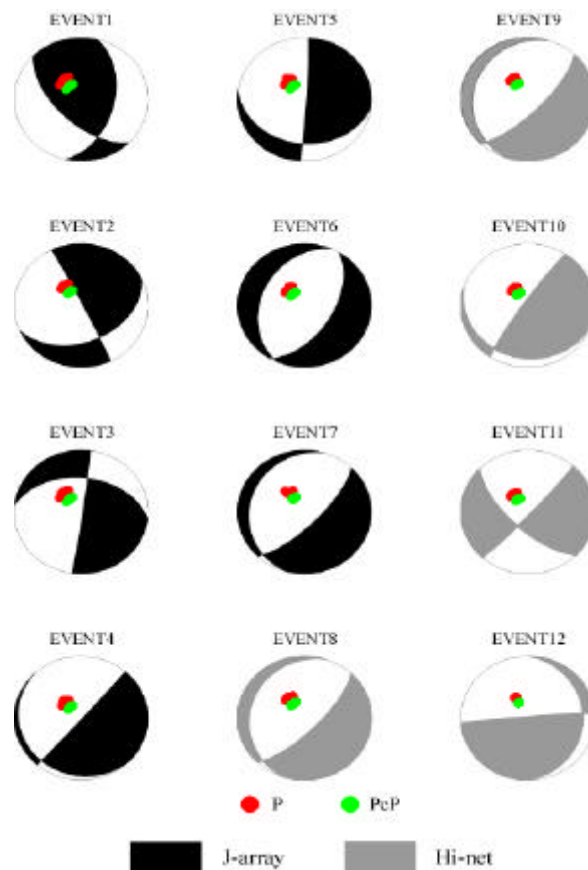
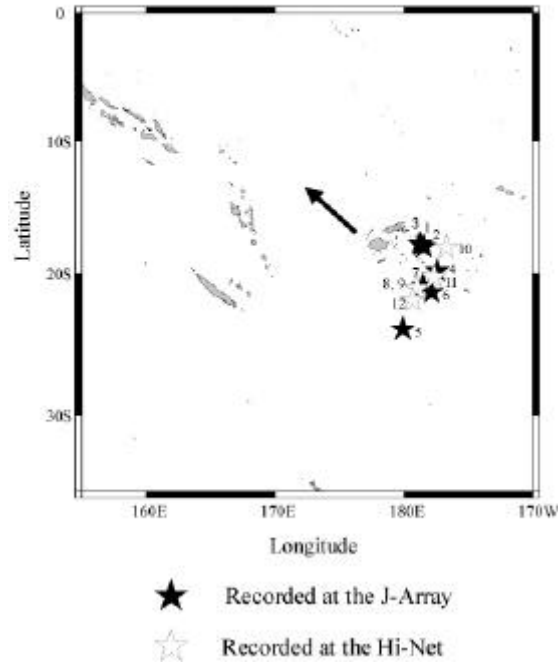


**Figure 3.2** This figure shows beach balls representing the source mechanisms of each event in Fiji-Tonga region. The ray angles of each P and PcP phase are plotted by red circles and light green circles, respectively. Note that the nodal planes do not lie between P and PcP for all events, which means that P and PcP phases have the same polarity.

Distribution of Events used in this study  
(Fiji Islands)



Distribution of Events in the vertical cross section

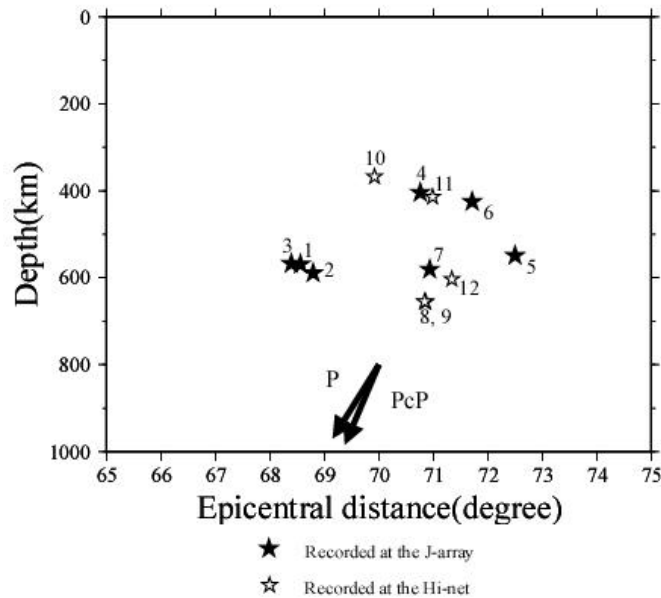


**Figure 3.3** Distribution of the events used in this study. Parameters are taken from Engdahl (1998) for J-Array data and Harvard CMT solution catalogue for Hi-net data. All 12 events are deep focus earthquakes (>350 km) and their magnitudes are greater than 5.5 mb. The upper diagram shows the horizontal event distribution indicated by stars and the lower map shows the event distribution in the vertical cross section indicated by stars. In the lower map, the take-off angles for P and PcP are indicated by the arrows.

## 4. Observations

### 4.1 Characteristics of PcP (ScS) and PdP (SdS) Phases

In teleseismic seismograms, PcP phases (the reflected P-wave from the CMB) can be observed about 15 to 25 s after the direct P onset time in the epicentral distance range of about 70 degrees. These relative travel times also vary with respect to event depth. Though amplitude varies with epicentral distances, PcP phases have relatively large amplitude among the later phases such as PcP, PKP and PKiKP, and can contain useful information about the CMB and the lowermost mantle.

Typical ray paths of P and PcP waves are shown in Figure 4.1.

In the case of S-waves, ScS phases (the reflected S-wave from the CMB) can also be observed about 30 to 40 s after the direct S onset time at the same epicentral distance. Since S-waves cannot propagate through the outer core, the reflection coefficient of SH waves is 1.0 for all incident angles (Figure 4.3). Therefore, ScS amplitude is usually larger than that of PcP phase. SKS phases, which penetrate the CMB, propagate in the outer core as P-waves and incident into the mantle again, appear just before the ScS phases. If there is no anisotropic structure in the medium, SKS phases can be recognized only on the radial component. Example seismograms for P and PcP phases (J-Array data) and S and ScS (Hi-net data) are shown in Figure 4.2.

Detection of the D' discontinuity involves observations of PdP and SdS phases, the waves reflected at a discontinuity in the D' layer. PdP (SdS) phases show up between P (S) and PcP (ScS) phases both in travel time and in slowness (see Figure 4.1 and 4.2). Depending on the epicentral distance, these phases correspond to different wavefield interactions with the D' discontinuity. If the D' layer is a high velocity zone, the following is true: At distances less than 70 degrees, PdP and SdS are simple reflections off the discontinuity. This is called pre-critical reflection. At greater distances, PdP and SdS involve two separate phases, reflection off the D' discontinuity and refraction just below the discontinuity, respectively. Before the crossover distance of about 80 degrees (for an earthquake with a depth of 600 km), the two different phases arrive between P (S) and PcP (ScS). For most distances less than the cross-over point, these two phases arrive too close in time to be distinguished from each other and therefore appear as a single arrival. At greater epicentral distances, these phases become increasingly separated. Most studies on the D' reflection phases use observations of the composite PdP (SdS) phases at the epicentral distance between 65 degrees and 80 degrees. If the D' layer is a low velocity zone, the way of refraction begins to change; namely, the refracted wave becomes steeper than the incident wave.

In this study, the composite PdP and SdS phases were analyzed in the epicentral distance range between approximately 60.8 and 75.0 degrees. Therefore, the station-event geometry in this study is suitable for searching for the PdP (SdS) phase. One of the differences between PdP and PcP is that a change in the waveform occurs for PdP due to phase shifts at an epicentral distance of more than

about 70 degrees at a positive velocity discontinuity, while P and PcP waveforms do not change at the same distance.

It is important to consider how PdP and PcP reflection coefficients are changing in proportion to an increase of the epicentral distance. The reflection coefficients of PdP and PcP (ScS and SdS) are shown in Figure 4.3. In the epicentral distance range of 70.0 degrees, for instance, the incidence angle at the CMB or at the depth of the D' layer reaches approximately 73 degrees, where the reflection coefficient of PdP (in this case the reflected wave from a discontinuity with  $-1\%$  velocity contrast) starts to increase, while that of PcP is decreasing. In the epicentral distance range used in this study (from about 60 to about 75 degrees) the polarity of PcP and PdP is constant; however, the polarity of the PdP phase is reversed in comparison with that of PcP if the PdP reflects at a negative discontinuity.

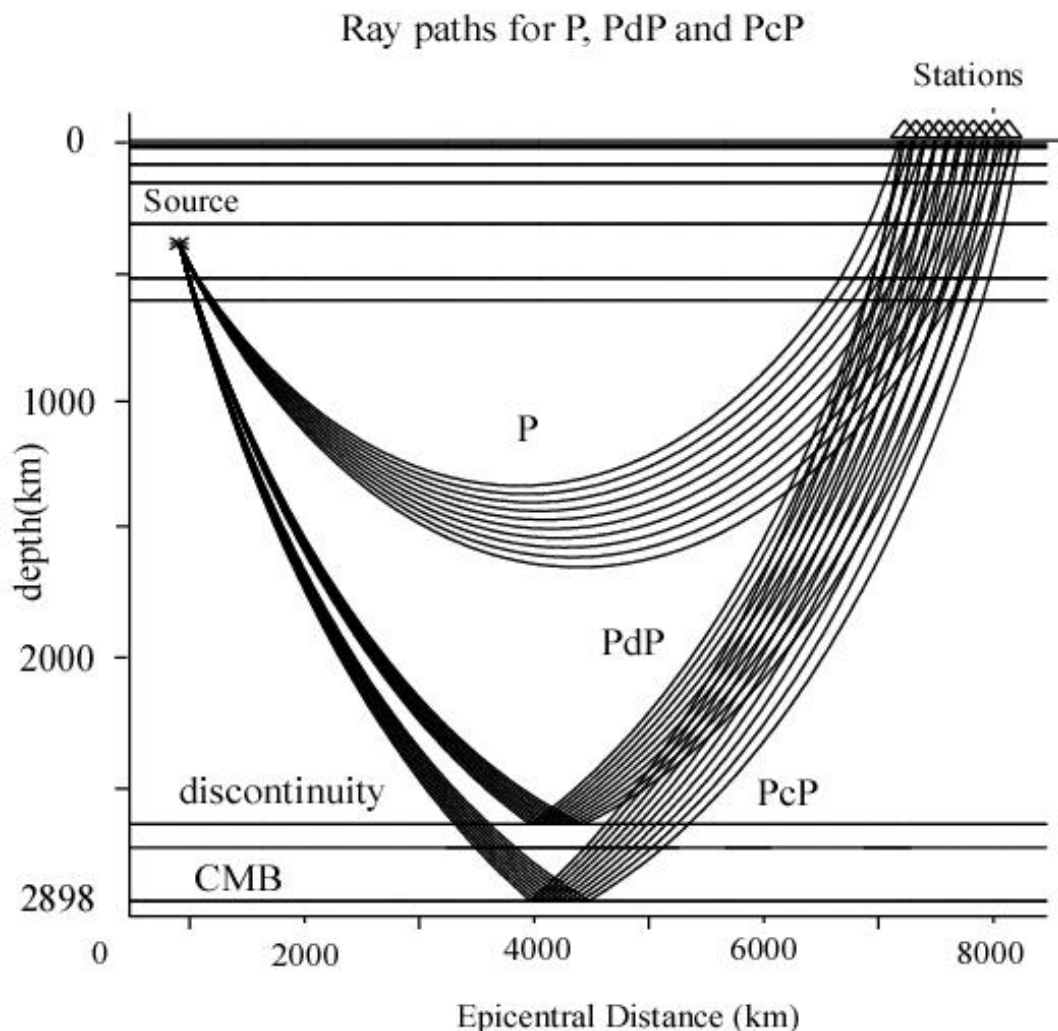


**Figure 4.1** Ray paths for P (direct wave), PdP (reflected wave at a discontinuity in the lowermost mantle) and PcP (reflected wave at the CMB). The source depth is 500 km and ray paths were calculated based on the IASP91 model by the Xgbm program (Davis and Hensen, 1993).



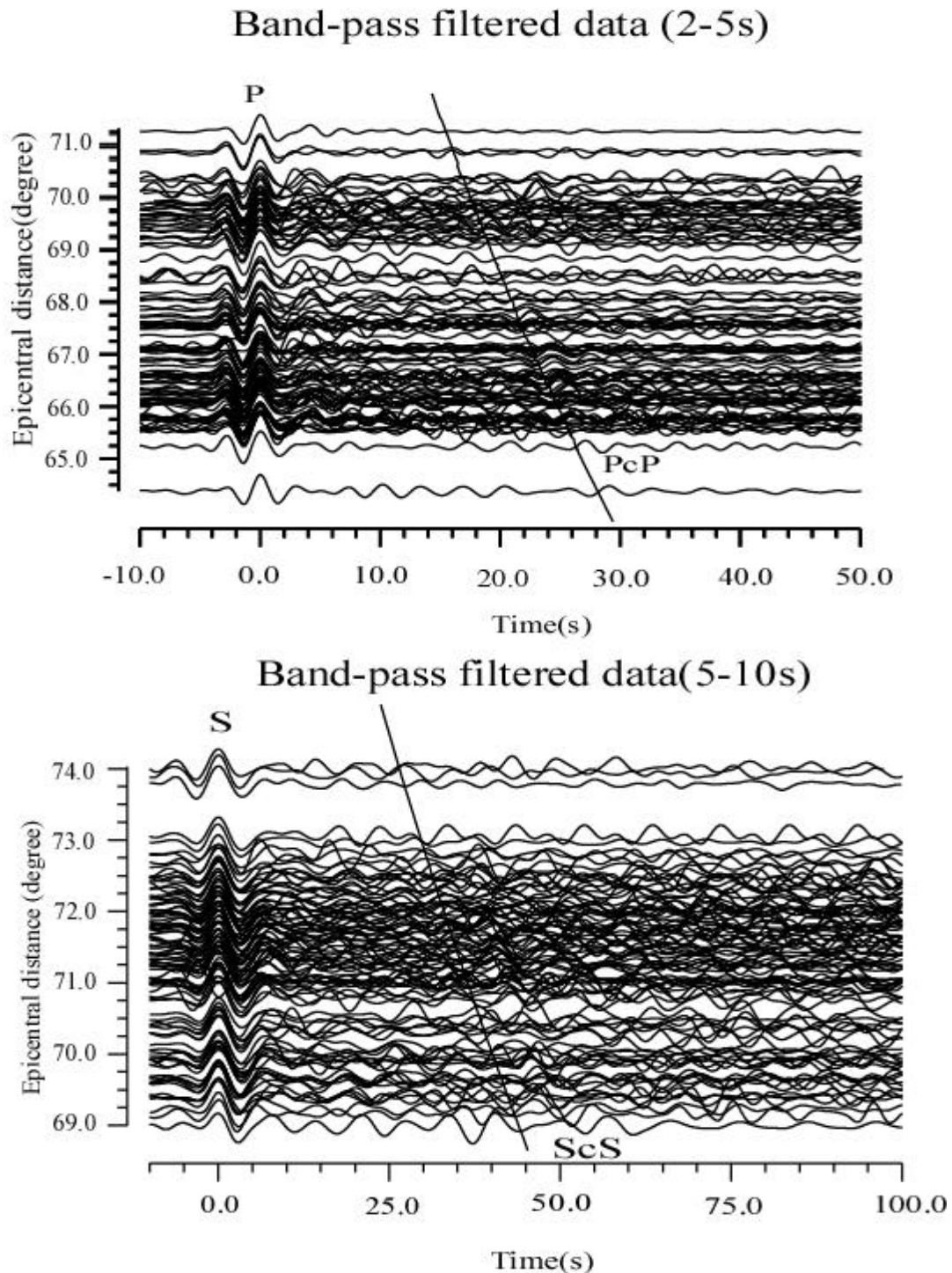


**Figure 4.2** Examples of observed seismograms. The upper P-wave seismograms are taken from the J-Array (Event 1) and the lower S-wave seismograms are taken from Hi-net stations (Event 8, for the source parameters see Table 1 in Appendix 6). A Butterworth band-pass filter (2-5s for P-wave and 5-10s for S-wave) was applied to the seismograms for both P- and S-wave data. PcP and ScS phases can be recognized near the theoretical travel time curves of PcP and ScS, though the amplitude of PcP and ScS are much smaller than those of the direct P- and S-waves.

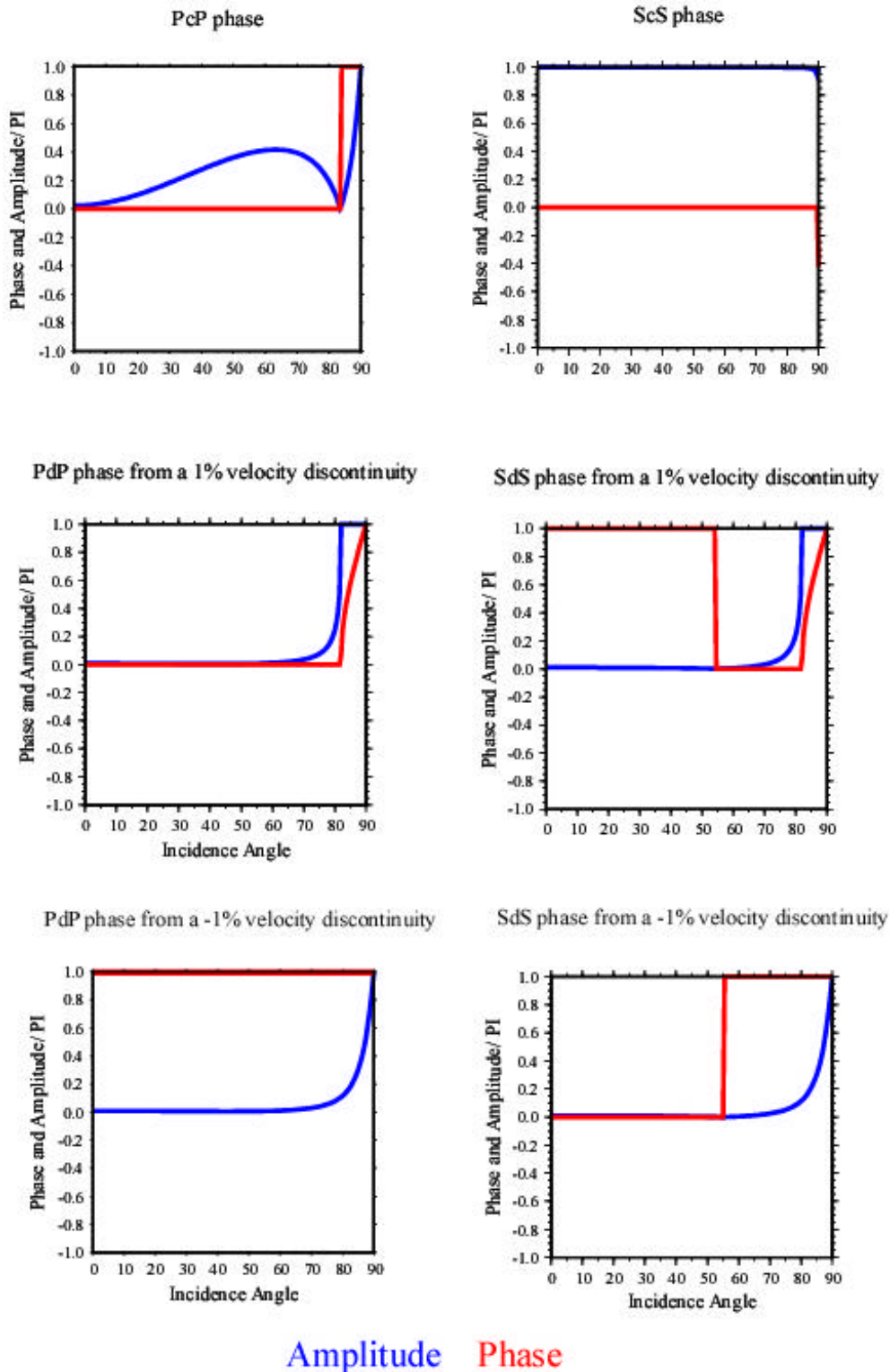


**Figure 4.3** Reflection coefficients versus ray angle for a down going P-wave and SH wave incident on the CMB and on discontinuities with 1% and -1% velocity contrasts at a depth of 2650 km. The magnitude of the reflection coefficient (amplitude) and the change in the phase angle are plotted by the blue and red solid lines, respectively. To produce these graphic diagrams the program REFTRA .F written by M. Weber was used.

## **4.2 Fresnel Zone and Resolution**

The ray theory is valid only in the high frequency limit, which results in a limit for the lateral dimensions or vertical irregularities of the reflectors that can be detected with waves of a certain wavelength. As a rule of thumb, vertical dimensions are only detectable if they are greater than a quarter of the signal wavelength. When evaluating horizontal dimensions of reflectors, the Fresnel zone (Hilterman, 1982) has to be taken into account. In a certain area of a reflector, where travel time differences of reflected waves are within half of the dominant period of the signal, the energy from this area interferes constructively. This area is defined as the first Fresnel zone (Sheriff, 1984) and the lateral resolution therefore depends on the size of the Fresnel zone. The long axis of the Fresnel zone lies along the direction of wave propagation, i.e., it is aligned with the great circle path between source and receiver. This long axis measures approximately 360 km and the shorter axis is approximately 190 km at the CMB in the case of a P-wave whose dominant period is 2 s at the epicentral distance of 70 degrees. In the source-receiver geometry of this study, the azimuth is around 135 degrees, in which case the Fresnel zone would be enlarged in the direction of NW-SE. The shape of the Fresnel zone for 2s dominant period P-wave can be seen in Figure 2.4.

## **4.3 Depth Phases pP and sP**

In the teleseismic seismogram, the depth phases (reflected or converted waves at the Earth's surface) have relatively large amplitude in comparison with the later phases like PcP and PdP. The pP phase is relatively complex in comparison with the direct P-wave owing to multiple phases from the sedimentary layers and structures in back-arc basins which contribute additional energy to the pP coda (e.g. Engdahl and Kind, 1986, Wiens, 1987). After the arrival of the pP phase, sP phases appear in the seismogram. Most depth phases in the observed data contain lower frequencies than that of the direct P-wave signal because the short period signals lose energy when they propagate through the relatively heterogeneous upper mantle and reflect at the surface where attenuation is very strong. In the case of deep focus earthquakes, which occur in the area deeper than the lithosphere, the depth phases propagate in the heterogeneous region of the upper mantle two times. This is one of the main causes for the lower frequencies of the depth phases. If the depth phases such as pP and its coda are used for the analysis, the detectable region in the lowermost mantle is increased (Weber, 1993). The depth phases in the data observed from deep-focused events in the Tonga-Fiji region, however, have waveforms which are too complicated to identify the phases coming from the lowermost mantle. Therefore, the depth phases were not analyzed in this study.

## **5. Theory of Array Methods**

### **5.1 Introduction**

To identify anomalous phases originating in the lowermost mantle, I applied two methods. Since seismic wave propagation in heterogeneous media is normally very complicated, anomalous phases can involve various wave types such as reflected waves, scattered waves, diffracted waves and converted waves. This study focuses on two different types of waves. These are reflected waves (reflection at a plane discontinuity) and scattered waves (isotropic point scattering). If a large-aperture seismic array is employed for stacking process, slant stack, which uses only slowness information, is not enough to resolve phases originating from the lowermost mantle, because the plane wave approximation is not valid due to the curvature of the Earth's surface. It is therefore necessary to calculate theoretical travel times for the reflected waves or scattered waves in a global Earth model by using a ray-tracing program. In this study the IASP91 Earth model (Kennett and Engdahl, 1991) was used as a reference velocity model. The IASP91 model is one of the recently developed refined models based on the ISC catalog for 1964-1988 with a better fit to the observed travel time data (Kennett and Engdahl, 1991). When the theoretical travel time is calculated, the effect of the elliptical shape of the Earth leads to travel time variations ranging from 0.0 s to 0.5 s. Variation of the altitude of the stations from about 0 m to about 3000 m above sea level also influences the travel time of the direct P (S) wave and PcP (ScS) waves, with corresponding travel time differences reaching a maximum of 0.5 s. The incidence angles of P and PcP on the receiver side are very similar to each other, however, such that both P and PcP are influenced by the altitude differences in almost the same way. Therefore, the effects of the altitude variation of the stations on the travel time differences between P (S) and PcP (ScS) cancel out and can be neglected in the analysis.

### **5.2 Double Array Beamforming**

Although receiver array techniques are widely used for detection of both local and global structure in the Earth's interior, it is not very common to employ source arrays and teleseismic data to investigate the lowermost mantle. Due to the reciprocity theorem for Green's functions, clusters of sources can be used as a source array (Spudich and Bostwick, 1987). The signals from an array of sources can be interpreted as if they originated at the station and were recorded in the source region.

A Double Array Method has been set up analogous to the Double Beam Method (DBM) (Krüger et al., 1993, 1995, 1996). The general scheme of the DBM is shown in Figure 5.1. If the size of both arrays (receiver array and source array) is small (less than 300 km x 300 km), standard array processing techniques based on plane wave approximations (such as vespagram or frequency-wavenumber analysis) are adequate. It is possible to detect azimuthal deviations for short-period reflected phases, which can have a large effect on the estimation of the depth of

discontinuities in the lowermost mantle. In the case of the large array used in this study, whose size exceeds 300 km x 300 km, it is necessary to calculate the travel times including the effect of the Earth's curvature.

If the aperture of both arrays is large, it can happen that the crustal and upper mantle structure is very different within the aperture of one array such that in turn, their effect on travel time cannot be neglected. If the DAM is applied to a large array, it is necessary to estimate the effect of lateral heterogeneities in the upper mantle and crust beneath both arrays.

To construct double beams, both the source and receiver configuration are integrated. First of all, the theoretical travel times of the scattered waves or reflected waves are calculated based on the standard Earth Model (IASP91 in this study) for a certain combination of station and source (see chapters 5.3 *Reflected Wave Beamforming* and 5.4 *Migration* for details). Subsequently, for each station of the receiver array the traces are shifted with respect to the theoretical travel time and summed up in the usual way to form a source array beam for a specific phase (Krüger et al., 1996). In the second step, the theoretical travel time is calculated for each station in the receiver array, and the source array beams are shifted with respect to the theoretical travel time and summed up to form a double beam. Compared with a single receiver array, the enhancement factor of the DAM using a source array of the same aperture as the receiver array is larger by a factor proportional to  $\sqrt{K}$ , where  $K$  is the number of sources. It is one of the most advantageous aspects of the DAM that the effect of heterogeneous structure beneath the source array region can be reduced by using many sources, in which case only common phases between source array and receiver array, such as lower mantle phases, are enhanced.

In order to form source array beams, the waveforms of the different sources must have the same shape and the source parameters, such as origin times, coordinates and depths of the sources, must be well known. One of the technical problems in the source array beamforming derives from inaccurate origin-time information, causing serious travel time miscalculations. These uncertainties are often of the order of 1 s for teleseismically located events (Krüger et al., 1996). The origin times should therefore be avoided in the processing of the DAM.

In order to use a source array for the extraction of weak signals from the lowermost mantle, the travel-time errors caused by many factors mentioned above must be minimized as much as possible. One quarter of the signal's dominant period can be considered as a safe boundary for an acceptable error, which means that the shifting times of the traces should be accurate to within 0.5 s for short-period (dominant period of 2 s) arrivals. Errors in the source depth or deviations of the medium velocities from the global model below the source array are additional sources of travel-time errors. This problem is important when natural earthquake clusters are used as a source array. Using relative travel times between P and later phases such as PdP or SdS will help to reduce these travel time errors. Tests on the effects of source mislocation regarding travel times will be discussed in the

chapter 10.5.

The source parameters have been taken from Engdahl et al. (1998) for the J-Array data set, because their hypocenter determination was significantly improved by using the arrival times of PkiKP, PKP $df$ , in addition to regional and teleseismic P and S phases, as well as the teleseismic depth phases such as pP, pwP, and sP in the relocation procedure. For the relatively new events of the Hi-net data set, Engdahl's source parameters are not published yet, so the source parameters for Hi-net data set have been taken from the Harvard CMT solution catalogue.

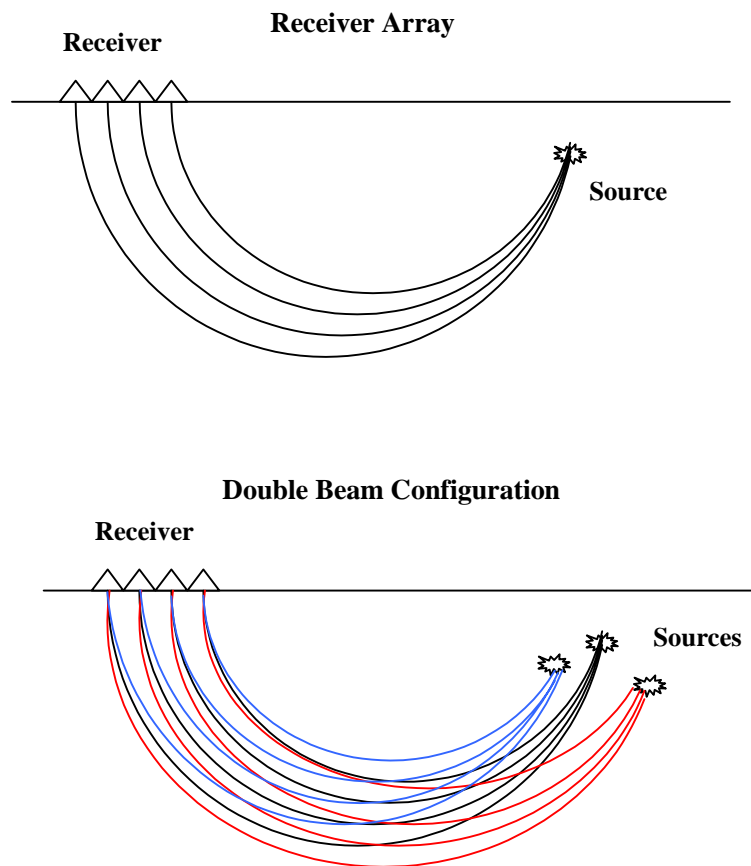


**Figure 5.1** This schematic diagram shows a scheme for the Double Beam Method (DBM) (Krüger et al., 1996). The upper diagram represents a conventional receiver array configuration and the lower diagram represents Double Beam configuration. By the simultaneous stacking of many events the resolution is increased significantly.

### 5.3 Reflected Wave Beamforming (RWB)

In the reflected wave beamforming method (hereafter RWB), it is assumed that all reflected waves propagate along the great circle paths and that the seismic structure of the lowermost mantle is laterally homogeneous in the local area of the bounce points of PdP (reflected waves from discontinuities). A schematic diagram for the RWB is shown in the upper panel of Figure 5.2. Potential plane discontinuities were defined in the lowermost mantle at vertical intervals of 5 km in

the depth range from 3000 km (about 110 km below the CMB) to 2300 km. The program (LAUFZE) by J. Schweitzer was used for calculating the theoretical travel times. For each discontinuity, theoretical travel time tables were calculated based on the IASP91 model (Kennett and Engdahl, 1991). Then the theoretical travel times for the corresponding epicentral distance of each source-station combination were calculated by an interpolative procedure. For the depth range beyond the CMB (2889 km depth) in the outer core, the velocity structure of the lowermost mantle (2740 km - 2889 km) in the IASP91 Earth model was extrapolated and extended. The reason of this extension is that the depth of the CMB is not always consistent with the theoretical one (2889 km in the IASP91) and can vary up to 20 – 30 km in the resulting image due to undulation of the CMB or anomalous velocity structure somewhere within the mantle. Another advantage of introducing this expanded artificial lower mantle in the depth range of 2889 km to 3000 km is that a vertical (depth) resolution of the CMB in both directions can be estimated as a reference for the D'' seismic discontinuity. A stacked seismogram  $DB(t, g)$  calculated with the RWB can be expressed as,

$$DB(t, g) = \frac{1}{M} \sum_{i=1}^M S_i(t - (T^{obs.(P)}_i + T^{theo.(PdP-P)}_i)),$$

where  $M$  is the number of traces,  $S_i$  is the  $i$ -th trace,  $T^{obs.}_i$  is travel time of maximum amplitude peak for direct P-wave,  $T^{theo.(pdp-p)}_i$  is the theoretical travel time difference between P and PdP. With this method, the area of PcP or PdP reflection points can be sampled for each depth. Based on the theoretical travel time differences between direct P-waves and waves reflected at the plane discontinuities in the lower mantle, the energy of the reflected waves from the plane discontinuities was calculated by using stacking techniques. The amount of the reflected energy can be estimated by this method and the resulting values may indicate where anomalous structures, such as a discontinuity in the lowermost mantle, might exist. This method is similar to the method used by Yamada and Nakanishi (1996, 1998).

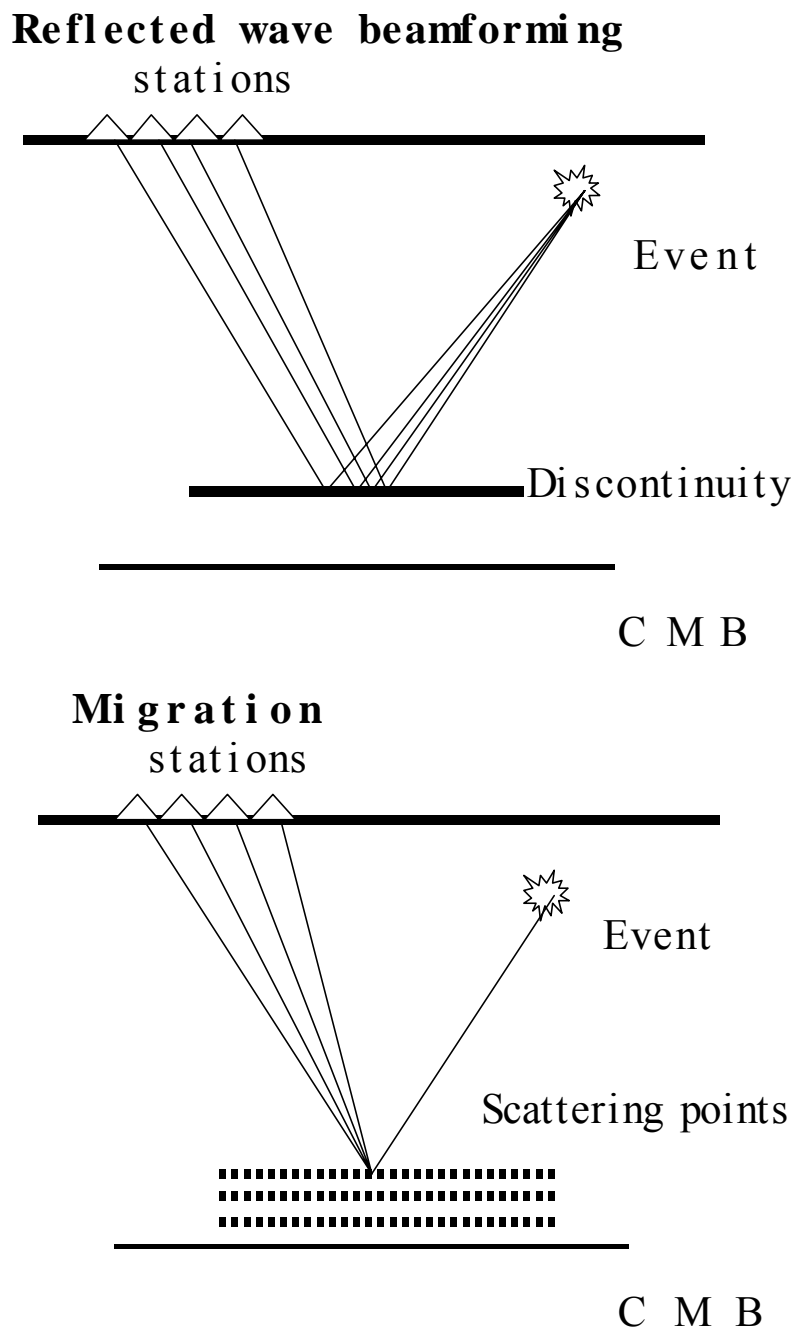


**Figure 5.2** The upper sketch shows a scheme for the Reflected Beam Method (RBM) and the lower one shows one for the Migration Method. In the RBM all rays obey the Snell's law, however most rays do not obey Snell's law in the Migration Method.



## 5.4 Migration

Many different migration techniques have been widely used for detecting small-scale heterogeneities in Earth's interior. For instance, Revenaugh (1995) applied the Kirchhoff migration method to short-period seismic data in order to investigate the upper 200 to 300 km of the mantle beneath southern California. Castle and Creager (1999) used a waveform migration technique and Nth root stacking (Muirhead, 1968) to image scatterers in the lowermost mantle at depths of 1000 km.

In this study, a full waveform migration similar to Freybourger et al. (2001) was applied to the data from the deep-focused events in the Tonga-Fiji region. A schematic diagram for migration method is shown in the lower panel of Figure 5.2. First, a grid point was set on the CMB (2889 km depth) at the center of the study area, which is located in the middle between the sources and receivers. Starting from this, a grid was set up with an interval spacing of 20 km in both N-S direction and W-E direction. The total number of grid points in this area was 1681. Subsequently, the same grids were added in the depth range from 2950 km to 2500 km with a vertical interval of 50 km, thus defining a volume of potential point-like scatterers in the lower mantle. The theoretical travel time between the source and a grid point  $T_{so}(j)$  and the theoretical travel time between a grid point and a station  $T_{st}(k)$  were first calculated based on the IASP91 model. The travel time  $ScatT(j, k)$  of the scattered waves that propagate from the source to a specific grid point, are scattered there and finally arrive at J-Array or Hi-net stations, can be expressed in terms of the following equation:

$$ScatT(j, k) = T_{so}(j) + T_{st}(k), \quad (5.1)$$

where  $so(j)$  is a set of J sources and  $st(k)$  is a set of K receivers. In order to calculate the theoretical travel time differences between the direct P-waves and scattered waves, the theoretical travel time of the direct P-waves was subtracted from the travel time of scattered waves.

$$T_{(scat-p)} = ScatT(j, k) - T_p(j,k), \quad (5.2)$$

where  $T_{(scat-p)}$  is the theoretical travel time differences between the direct P-waves and scattered waves and  $T_p(j,k)$  is the theoretical travel time of the direct P-waves.

The grid sampling is chosen with respect to the dominant period of the signals so that the travel-time difference between the wave scattered at two neighboring grid points is smaller than the dominant period of the signals. Since the dominant period of the filtered data range from 1-10 s, a 20 km lateral interval spacing of the grid points is chosen, whose corresponding travel-time difference varies approximately from 0.1 s to 2.0 s in the whole scattering volume.

For the depth slices deeper than the CMB (2889 km depth) actually occupied by the outer core, the velocity structure of the lowermost mantle (2740 km - 2889 km) in the IASP91 Earth model was extrapolated to a depth range from the CMB to 2950 km using the same procedure as employed for the RWB. After calculating the theoretical travel time of the scattered waves, scattering energy from each grid point can be estimated by stacking all traces, after shifting them with respect to the theoretical travel time for each grid point, assuming isotropic point scattering.

Theoretically, it would be possible to produce a scattered wave by volumetric anomalies whose sizes are larger than  $\lambda/4$  ( $\lambda$  is the wavelength). The dominant period is about 2.5s for band-pass filtered data (2-5s) and about 8s for band-pass filtered data (5-10s), so the size of detectable scattering volume should be larger than about 7 km and about 30 km, respectively. However, the amplitude of the scattered waves is so small that the observation of such scattered waves at the surface of the Earth is actually not possible.

If the waves are incident on a large object compared with the wavelength, the incident waves would be scattered on the surface of the object. In general, total scattering or reflection takes place at the boundary between two transparent media when a ray in a medium of higher index of refraction approaches the other medium at an angle of incidence greater than the critical angle. In such a case, the scattering waves in the lowermost mantle can be observed at the Earth's surface with the migration method. One of the advantages of the migration is that three-dimensional structure such as dipping plane or plane having a large amount of curvature could be detected. This migration method used in this study is closely related to 'double beam migration' used by Scherbaum et al. (1997), Kaneshima and Helffrich (1998) or Freybourger (2001).

## 5.5 Subarrays

The lateral extension of both receiver arrays J-Array and Hi-net is quite large and it is therefore not suitable to use all array stations for the detection of more regional and local structures in the lowermost mantle. If all array stations are used for the analysis, the structural image of the lower mantle is smoothed in the area of the bounce points, which is suitable for detecting structures of larger scale. Due to the large number of traces, it is possible to divide the whole array into several smaller arrays called 'subarrays' in order to acquire a higher lateral resolution. The whole array was divided into 19 subarrays, each with a lateral extension of 5 degrees in latitude and longitude (see Figure 5.3). The projection of one subarray aperture at the CMB reaches 300 x 300 km and the lateral extent of the whole array corresponds to 770 km length at the CMB. These subarrays allow to more clearly delineate lateral variation of the smaller-scale structure (~100 km) in the D'' layer and undulation of the CMB. Since the density of the J-Array or Hi-net stations is not uniform, the number of stations included in a subarray differs, resulting in resolution differences between the subarrays. On the whole, there is a higher concentration of stations in the middle region of the whole

array as compared with the northern and southern part of the array. Since the receiver array is shaped like an arc in NE-SW direction, the shape of the area sampled by the different subarrays is also arc-like, yielding, in effect, a cross section in the D" layer.

The physical meaning of "values" in the RWB with subarrays and migration are different from each other. While a grid point in the migration represents point scattering energy from the grid, a value in the RWB contains all energy of the reflected wave at a certain depth in a subarray. Since the reflected points extend in a certain area determined by the distribution of the receivers and sources, the value in the RWB with subarray is sensitive to regional plane anomalous structure. Another aspect of the differences between the migration and the RWB using subarrays is that all rays obey the Snell's law in the RWB, while almost no rays can be traced by Snell's law in the migration. If anomalous structures have a plane surface, the RWB is suitable for detection of anomalous phases from this kind of anomalies. If anomalous structure contains a scattering volume, the migration is more suitable.

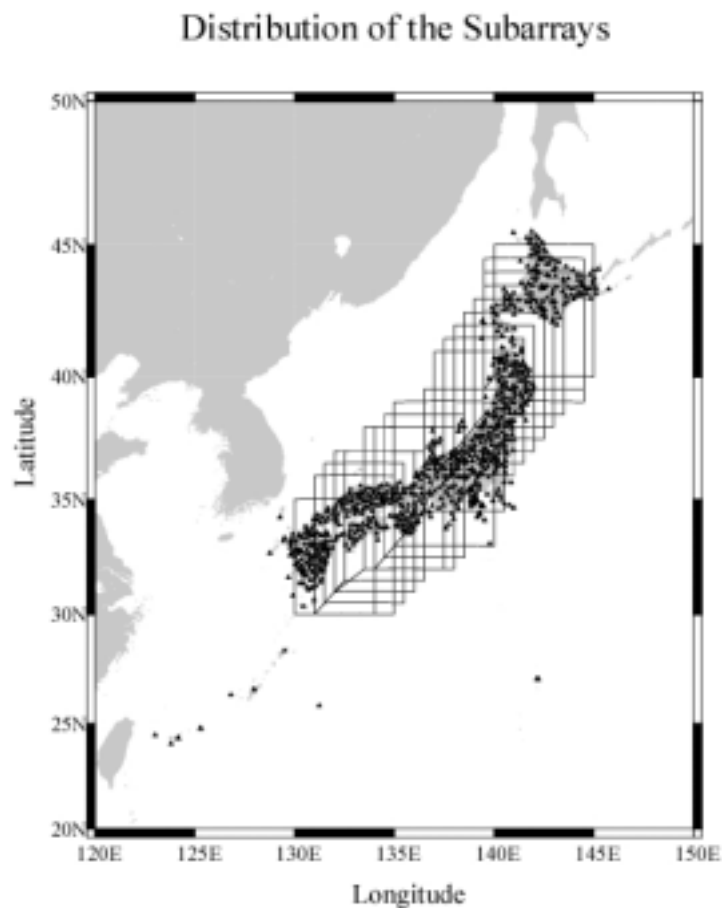


**Figure 5.3** The distribution of the subarrays used in this study is shown. The aperture of each subarray is about 5 by 5 degrees and the Japanese Islands are covered by 19 subarrays.

## 5.6 Bootstrap Method

In order to estimate the confidence of the results obtained with the RWB method, a bootstrap algorithm was applied to the observed data (Efron and Tibshirani, 1986). The bootstrap method is generally performed by the following steps: The original data set can be written as

$$X = (x_1, x_2, x_3, \dots, x_n), \quad (5.2)$$

where  $x_i$  is the original data value and  $X$  is the original data set. In the next step, a new data set called bootstrap sample is produced. The bootstrap sample is defined as a random sample of size  $N$ , which is the number of the original data. The bootstrap sample can be expressed as

$$X^b = (x_1^b, x_2^b, x_3^b, \dots, x_n^b), \quad (b=1, 2, 3, \dots, B) \quad (5.3)$$

where  $x_i^b$  represents bootstrap data points,  $X^b$  is the bootstrap sample (data set) and  $B$  is the number of the bootstrap sample. Afterwards, a statistic probability is calculated by using each bootstrap sample, which can be expressed as

$$\theta(b) = \mathbf{S}(X^b) \quad b=1, 2, 3, \dots, B, \quad (5.4)$$

where  $\mathbf{S}$  is an operator obtained through statistic probability from the data set (here a group of the traces). Subsequently, the confidence of the statistic probability ( $=\theta$ ) is estimated for the original data set. This algorithm was applied to the RWB method to estimate the stability of the results.

For this purpose, data sets (bootstrap samples) were devised by selecting stations from the original data set at random, permitting repetition. The number of stations in the bootstrap sample must correspond to the number in the original data set. The number of the bootstrap sample is 300 in this study. Calculations using the RWB were carried out for each bootstrap sample, and then the mean values and standard deviations were calculated. The result of the bootstrap analysis will be described in the *Results* chapter.

## 6. Coherence Measurement

### 6.1 Introduction

There are several coherency measures well suited for enhancing weak seismic signals. In order to detect small amplitude phases, it is necessary to reduce unexpected noise and amplify coherent phases without distorting the original information about the fine structure. One of the important aspects is how to extract coherent phases from relatively noisy data. To do so, several different coherency measures were applied to the data and to synthetic seismograms.

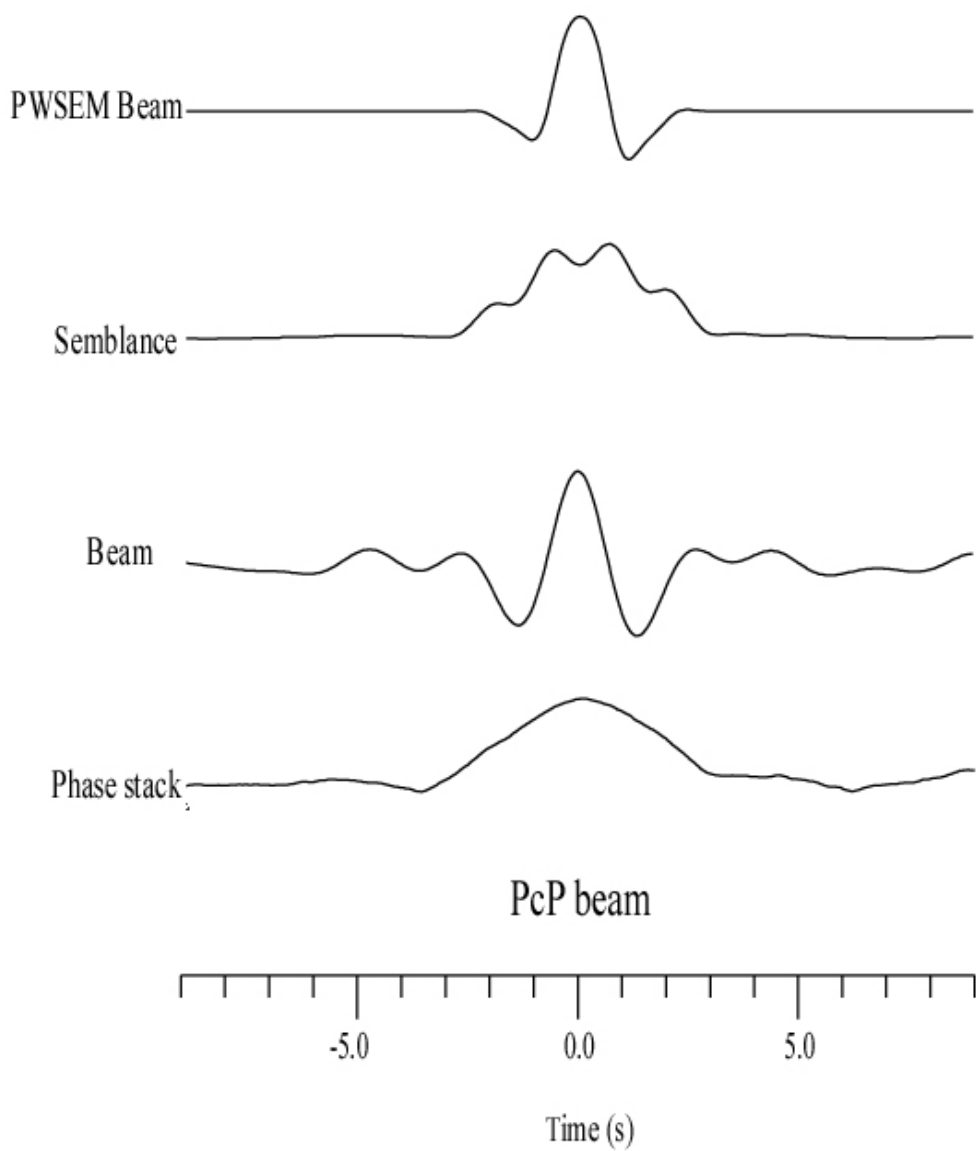


**Figure 6.1** Four different coherency measures are shown using a PcP beam (using Event 2). The first trace (the lowermost one) is the Phase stack  $c(t)$ , the second one is a normal amplitude beam, the third one is the semblance  $s(t)$  and the fourth one is 'Phase Weighted Semblance Beam' (PWSEM Beam) used in this study. PWSEM Beam can be obtained by multiplication of the three coherency measures (Phase stack, semblance and beam).

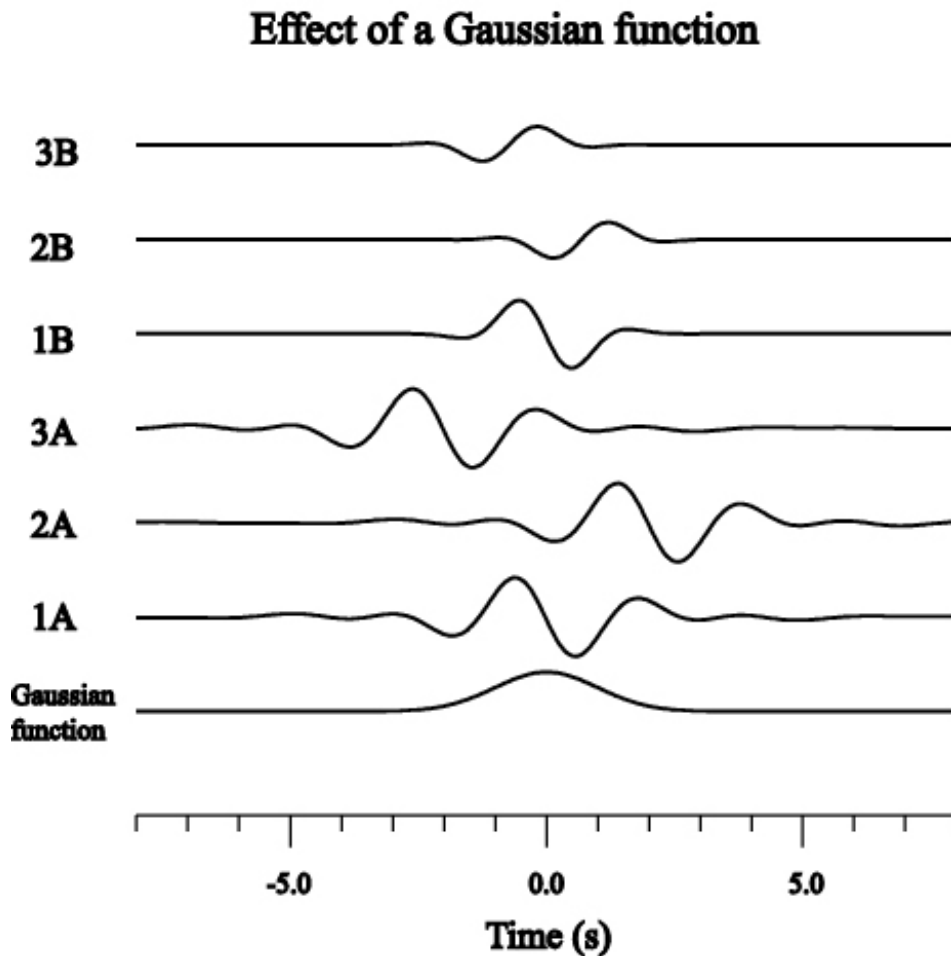


**Figure 6.2** These synthetic seismograms show how an application of a Gaussian function to the corresponding time window reduces wave energy which does not arrive at the expected travel time. The lowermost trace is a Gaussian function with 4s length. The trace 1A arrives at the theoretical travel time (0 s in this case) and the traces 2A and 3A arrive with time difference of 2s and -2s relative to the correct travel time, respectively. The trace 1B, 2B and 3B were constructed by multiplication by the Gaussian function to the traces 1A, 2A and 3A. This shows that the energy of 2A and 3A was reduced, while the energy of 1A remains.

### 6.2 Linear Stack

The most classical array method is the linear stack in which the seismograms are simply summed up. In the linear stack, however, it is difficult to distinguish phases whose amplitude is relatively large but not consistent through all the traces from coherent small phases, because the linear stack is easily influenced by the dominant amplitude of incoherent signals. An example of a linear stack using a PcP phase is the trace labeled 'Beam' in Figure 6.1.

### 6.3 Beam Power

The beam power (BP) can be obtained by squaring each data value in a specific time window producing the sum as the following equation:

$$Beam(t) = \frac{\sum_{i=1}^M f_{ij}^2(t - \tau)}{M}, \quad (6.1)$$

where M is the number of stations used for the analysis,  $f_{ij}(t - \tau)$  is the waveform of source j at the i-th station and  $\tau$  is shift time with respect to corresponding grid point or depth.

The beam power is sensitive to energy of waveform rather than its coherency. In the analysis, the beam power values are taken from the maximum beam power in each time window. This actually corresponds to the energy of the waveform at a certain time and always assumes positive values.

### 6.4 Semblance

Another classical coherency measure is the semblance (Taner and Koehler, 1969) which is defined by the following equation:

$$S(t) = \frac{\sum_{j=s(i)}^{e(i)} \left( \sum_{i=1}^M f_{ij}(t - \tau) \right)^2}{M \sum_{j=s(i)}^{e(i)} \sum_{i=1}^M f_{ij}^2(t - \tau)}, \quad (6.2)$$

where M is the number of stations used for the analysis,  $f_{ij}(t - \tau)$  is the waveform of source j at the i-th station and  $\tau$  is shift time with respect to corresponding grid point or depth.

S(i) is the first data sample in the time window and e(i) is the last one in the time window estimated from the duration of the PcP beam (the stacked waveform with respect to PcP phases). S(i) corresponds to the theoretical travel time of the scattered or reflected waves. The semblance is the power in the beam divided by M times the total power in the traces  $f_{ij}$ . The semblance function varies in the range  $0 < S < 1$ . A semblance value of 1 means that the waveforms are perfectly coherent and a semblance value of close to 0 means that the waveforms are very incoherent, both of which rarely happens in reality. A semblance value of 0 can only occur in the case of  $M \rightarrow \infty$ . The semblance value is not completely independent of the amplitude information of the waveform, and we must take into consideration that the semblance includes not only coherency information but also

amplitude information. An example of semblance using a PcP phase is the trace labeled ‘Semblance’ in Figure 6.1.

### 6.5 Phase-Weighted Semblance

In order to isolate the reflected and scattered waves in a better way, the Phase-Weighted Stack technique (Schimmel and Paulssen, 1997) was applied to the data set. The Phase Stack  $c(t)$  is defined by the following two equations (6.3) and (6.4), where  $Z(t)$  is a complex trace,  $S(t)$  is the original trace,  $H(t)$  is the Hilbert transformation of the original trace,  $A(t)$  is the envelope of the original trace,  $M$  is the number of stations and  $\theta(t)$  is called the instantaneous phase (Bracewell, 1965).

$$Z(t) = s(t) + iH(s(t)) = A(t) \exp\{i\Theta(t)\} \quad (6.3)$$

$$c(t) = \frac{1}{M} \left| \sum_{j=1}^M \exp(i\Theta_j(t)) \right| \quad (6.4)$$

The Phase Stack  $c(t)$  carries no amplitude information and can be considered as an amplitude-independent measure of wave field coherency. As mentioned before, the semblance  $S$  (defined in the equation) is a slightly amplitude-dependent measure of coherency. If the wave field shows perfectly similar signals with differing amplitude, the semblance value will be decreased (see Eq. 6.2). This means that the semblance is in some sense a stricter coherency measure than the Phase Stack. These two different coherency measures were multiplied and this function was defined as "Phase Weighted Semblance" (PWSEM) (Kito and Krüger, 2001) :

$$PWSEM(t) = S(t) \cdot c(t) = \frac{\sum_{j=s(i)}^{e(i)} \left( \sum_{i=1}^M f_{ij}(t-\tau) \right)^2}{M \sum_{j=s(i)}^{e(i)} \sum_{i=1}^M f_{ij}^2(t-\tau)} \cdot \frac{1}{M} \left| \sum_{j=1}^M \exp(i\Theta_j(t)) \right| \quad (6.5)$$

Additionally, the Phase-Weighted Semblance was multiplied by the beam power corresponding to each grid point or each discontinuity respectively in order to be able to amplify the difference between weak signals and noise.

A Gaussian function was used to weight the PWSEMBP (Phase-Weighted Semblance beam power) in the time window used for the calculation of the PWSEMBP in order to reduce the energy in the time window which does not arrive at the correct theoretical travel time. The advantage of the application of the Gaussian function can be seen in Figure 6.2. A typical dominant period in the



deconvolved data, 4 s, was chosen as the time window length. An example for a PWSEM beam using a PcP phase is the trace labeled ‘PWSEM Beam’ in Figure 6.1. Using this new function, the resolution of RWB or migration was considerably improved.

## 7. Data Preprocessing

In this chapter the data processing for P- and S-waves will be described in detail. Except for the rotation process and different band-pass filters, the same data processing was applied to both P and S waveform data. Therefore, first the rotation process for the S-waves will be described, followed by an explanation of the common data preprocessing.

### 7.1 Rotation Process for S-wave Data

The S-wave data (N-S and E-W components) were rotated to get transverse and radial components, and the transverse component was used for the analysis. In the transverse component, S and ScS waves are clearer as compared to those on the radial component. SKS phases appear between S and ScS phases for the distance range used here, but in theory they carry no energy on the transverse component if there is no seismic anisotropy in the media along the ray path of SKS phases. This is an advantage of using the transverse component because SKS phases can disturb weak signals from the lowermost mantle. As compared with the P-wave data set, S-wave data are relatively noisy and have a low signal-to-noise ratio. It is not possible to observe the direct S-wave clearly before data filtering (see also Figure 7.4). After the rotation process, only traces with good signal-to-noise ratio were chosen.

### 7.2 Common Preprocessing for P- and S-Waves

Under rather general assumptions, the spectrum of the teleseismic P-wave signal of each station  $W_i(\omega)$  can be modeled as the product of different spectral factors:

$$W_i(\omega) = S(\omega) * B(\omega) * R_i(\omega) * I_i(\omega), \quad (7.1)$$

where  $S(\omega)$  represents the source time function,  $B(\omega)$  is the attenuation spectrum of the mantle,  $R_i(\omega)$  is the response of the crust and the uppermost mantle just beneath stations,  $I_i(\omega)$  is the instrumental response of a station,  $i$  is the station index and  $\omega$  is the angular frequency. The attenuation factor of the mantle  $B(\omega)$  along the ray path from the source to the upper mantle beneath the array is almost identical across the whole array. This is because geometrical spreading and attenuation in the mantle are not drastically changing in the epicentral distance range of teleseismic events. Therefore, this factor can be regarded as constant throughout the J-Array and the Hi-net. The source time function  $S(\omega)$  can also be considered to be a constant quantity, even for the large

aperture J-Array and Hi-net, because the range of take-off angles of rays at the source is small (see Figure 3.3 and Figure 4.1). Therefore, the amplitude variation due to the radiation pattern and the directivity of rupture propagation can be neglected, unless ray directions are very close to the P-wave nodal plane.  $R_i(\omega)$  is normally different for each station and is influenced by local structure beneath the stations. The recording systems including the seismometer of the J-Array and Hi-net are not fully calibrated, so some uncertainties regarding instrumental responses persist.

In a first processing step, all direct P-waves (S-waves) were manually picked with respect to the maximum peak of P signals, and mean values of each trace were removed from all traces in order to compensate for different absolute values in the seismograms. There were some traces in the J-Array whose polarities are reversed, but after the traces were multiplied by  $-1$ , those traces were also suitable for the analysis. An instrumental deconvolution was applied to the data to amplify longer-period energy. Subsequently, a 2-5 s acausal band-pass filter (for P-wave) and a 5-10 s acausal band-pass filter (for S-wave) were applied to remove high- and low-frequency noise. After these procedures, all traces were aligned with respect to the theoretical travel time of direct P-waves (S-waves) in order to remove the travel time residual caused by heterogeneities in the upper mantle and crust beneath both source and receiver arrays. At this point, a summation was applied to all traces with respect to the P onset time (S onset time) in order to create a ‘P beam’ (‘S beam’), which is the common portion of waveforms across the array and contains the source time function, the mantle response, and the averaged response of the receiver structure. The spectrum of the P beam can be expressed as:

$$W(\omega)^{\text{beam}} = (1/N) * \sum_{i=1}^N W_i(\omega) = S(\omega) * B(\omega) * R(\omega)^{\text{beam}} * F(\omega)^{\text{beam}} \quad (7.2)$$

where  $N$  is the number of stations used for stacking, and  $R(\omega)^{\text{beam}}$  and  $F(\omega)^{\text{beam}}$  represent the average responses of the crust and uppermost mantle structure beneath the array and the average instrumental responses including the band-pass filter, respectively. Next, all the traces were deconvolved with the P beams of each corresponding event in order to remove the complexity of source time functions and the mantle response. The deconvolved waveforms  $DW(\omega)$  can now be expressed by the following equation in the frequency domain:

$$DW_i(\omega) = W_i(\omega) / W(\omega)^{\text{beam}} = R_i(\omega) / R(\omega)^{\text{beam}}, \quad (7.3)$$

which indicates that the deconvolved traces consist of relative differences in responses of the near-receiver structure and the instrument since the source time function  $S(\omega)$  and the attenuation factor of the mantle  $B(\omega)$  were cancelled by the deconvolution.

As the spectral holes of  $W(\omega)^{\text{beam}}$  in the denominator might cause artificial peaks in the deconvolved traces, it is necessary to apply the water-level method (Clayton et al., 1976) to stabilize the deconvolution process. By using the water-level method,  $DW_i(\omega)$  can now be defined as:

$$DW_i(\omega) = \{W_i(\omega) * W(\omega)^{-\text{beam}} / \Phi(\omega)\} * G(\omega), \quad (7.4)$$

where

$$\Phi(\omega) = \max\{|W(\omega)^{\text{beam}}|^2, c \max |W(\omega)^{\text{beam}}|^2\} \quad (7.5)$$

and

$$G(\omega) = \exp(-\omega^2/4a^2), \quad (7.6)$$

where  $W(\omega)^{-\text{beam}}$  denotes the complex conjugate of  $W(\omega)^{\text{beam}}$  and  $c$  is the water-level parameter which determines the minimum allowable spectral amplitude of the denominator. The water-level parameter ranges from 0 to 1.0. If the water level  $c$  is a large value,  $DW_i(\omega)$  becomes stable, but detailed features in observed waveforms that would contain important information on anomalous structures in the Earth's deep interior disappear in  $DW_i(\omega)$ . In this study,  $10^{-6}$  was taken as a water-level parameter  $c$ . The low-pass Gaussian filter  $G(\omega)$  is used to exclude high-frequency noise and to control the frequency range. After the deconvolution, a 2-5 s acausal band-pass filter (for P-wave) and a 5-10 s acausal band-pass filter (for S-wave) were applied to remove high- and low-frequency noise generated by the deconvolution processes.

Normalization has been applied in order to suppress the amplification of the amplitude of signals due to the crustal structure and site effects beneath the stations. All traces were normalized by the maximum amplitude of the P-waves. As the result of these procedures, the waveforms became very simple, so that the stacking was effective for the whole data set. Example seismograms are shown in Figure 7.2. and 7.3 for P-waves and in Figure 7.4 for S-waves. Although it is not possible to see directly in each trace how later phases like PcP were simplified by the deconvolution, it can be assumed that the PcP wavelet in each trace probably became simpler as well, because the PcP beams after deconvolution show simple waveforms which are very similar to each other (see Figure 7.1).

Since large aperture seismic arrays are used, the shift time  $\tau$  can be quite large. Therefore it can happen that the direct P-waves (S-waves) appear in the time window which is used to extract the weak signals coming from lowermost mantle. Since the direct P-waves (S-waves) have much larger amplitude than the later phases, the P-waves (S-waves) can disturb the weak signals originating from the lowermost mantle. In addition to the direct P-waves (S-waves), P coda (S coda) can also disturb

the later phases. Therefore, the P-wave (S-wave) was removed by subtracting the P beam (stacked P-wave of the deconvolved traces after alignment on the P-wave onset) of each event from each trace, respectively. P coda (S coda) should also be removed by the subtraction process more or less, because P coda (S coda) has almost the same slowness as that of the direct P-wave (S-wave).

In spite of the subtraction of the direct P-wave (S-wave) and a substantial part of the P coda (S coda), some P coda (S coda) remains in the traces from which the P beam was subtracted. This P coda may not be coherent throughout all the stations, but may be generated by more regional crustal structures just beneath the stations. In order to reduce this remainder of the P coda (S coda), a taper with the first half of a Gaussian function was applied to the time window between the P-wave onset time and 10 s after the P-wave, and the time window between the S-wave onset time and 20 s after the S-wave. In the time window between 20 s and 40 s after the P-wave, which is where signals from the lowermost mantle appear, relatively large amplitude coda is conspicuous in some traces although only traces with good signal-to-noise ratio have been selected. Since this can also disturb the extraction of small signals from the lowermost mantle, the traces whose coda's amplitude maximum exceed 50 % of the direct P-wave (S-wave) amplitude in the time window of 35 - 40 s after the direct P-wave or in the time window of 70 - 80 s after the direct S-wave, have been removed from the analysis.

Furthermore, it must also be taken into consideration whether or not the P-waveforms and PcP waveforms have the same polarities. If the polarity of PcP is reversed with respect to P due to the focal mechanism, the polarity of the scattered wave can also very likely be reversed for a subset of the seismogram. This, in turn, poses a serious problem to the Double Array Migration method. In these data sets, all PcP beams show the same polarities as that of the P beams (see Figure 3.2).

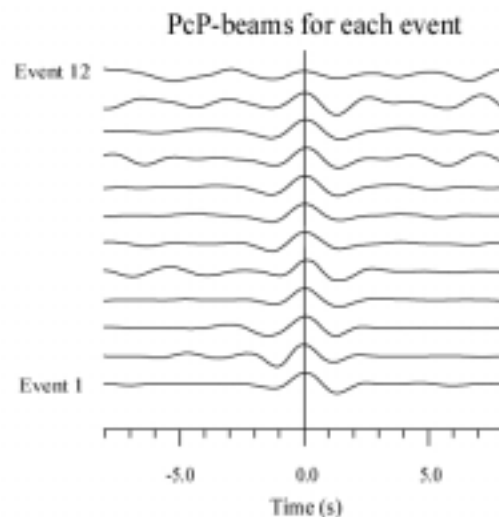


**Figure 7.1** PcP beams for each event after the deconvolution. All traces are aligned with respect to the peak of PcP. Note that the PcP waveforms are very similar to each other.

## Examples of seismograms (Event1 J-Array)

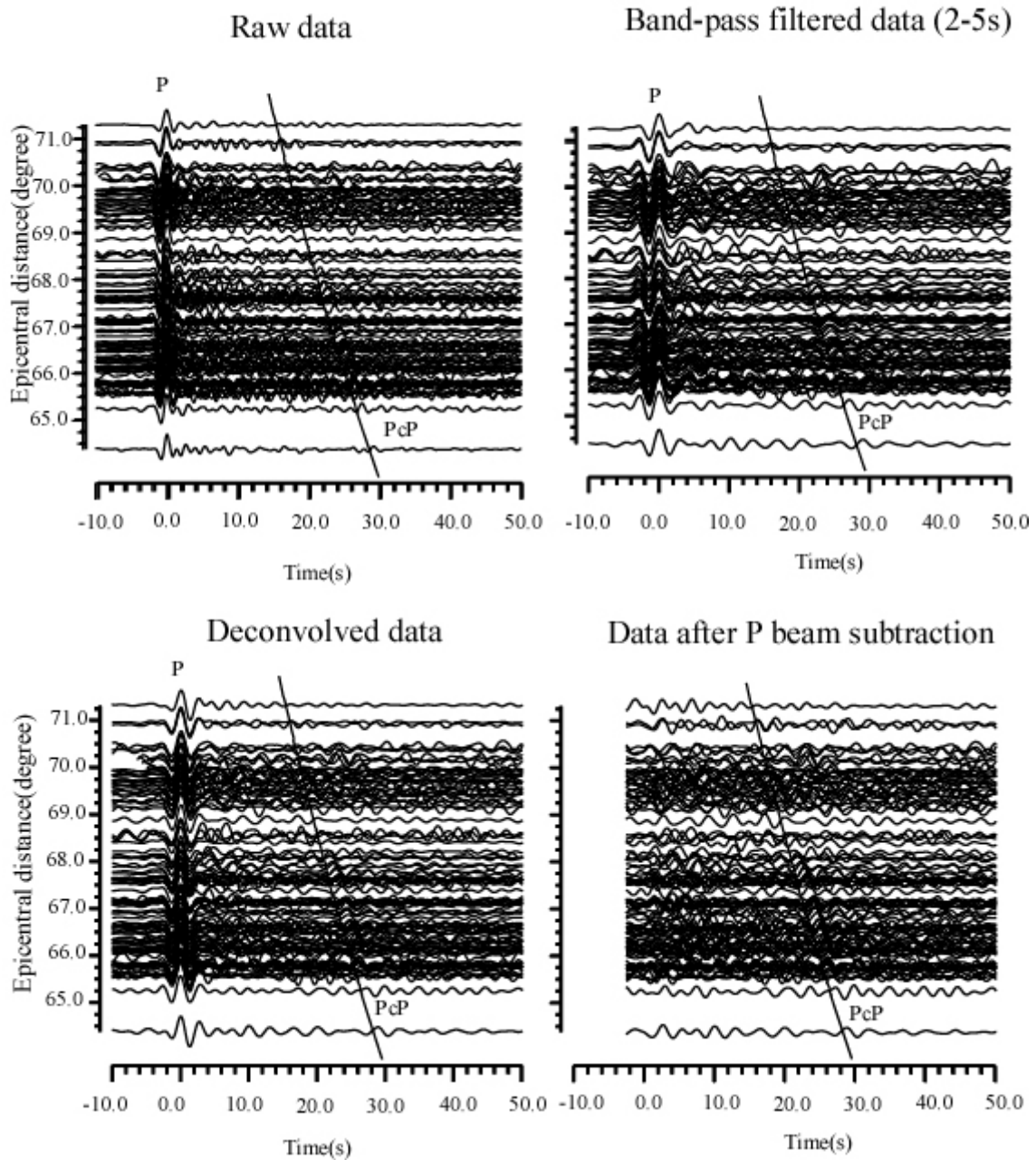


**Figure 7.2** P-wave example records of an event from the J-Array (Event 1) sorted by increasing epicentral distances aligned on the P-wave onsets. The upper left seismogram indicates the raw data, the upper right one is the data deconvolved by the instrument response of the seismometers and is then band-pass filtered in a 2-5s band (Butterworth filter of order 3). The lower left panel shows the traces deconvolved by the source time function. All traces are aligned on the P-wave peak and each trace is normalized for itself. About 20s after the P arrivals weak PcP onsets can be seen. The solid lines indicate the theoretical travel time of PcP calculated for the IASP91 model. Note that the arrival times of the PcP phases vary along the epicentral distance with respect to IASP91.

## Examples of seismograms (Event 10 Hi-net)

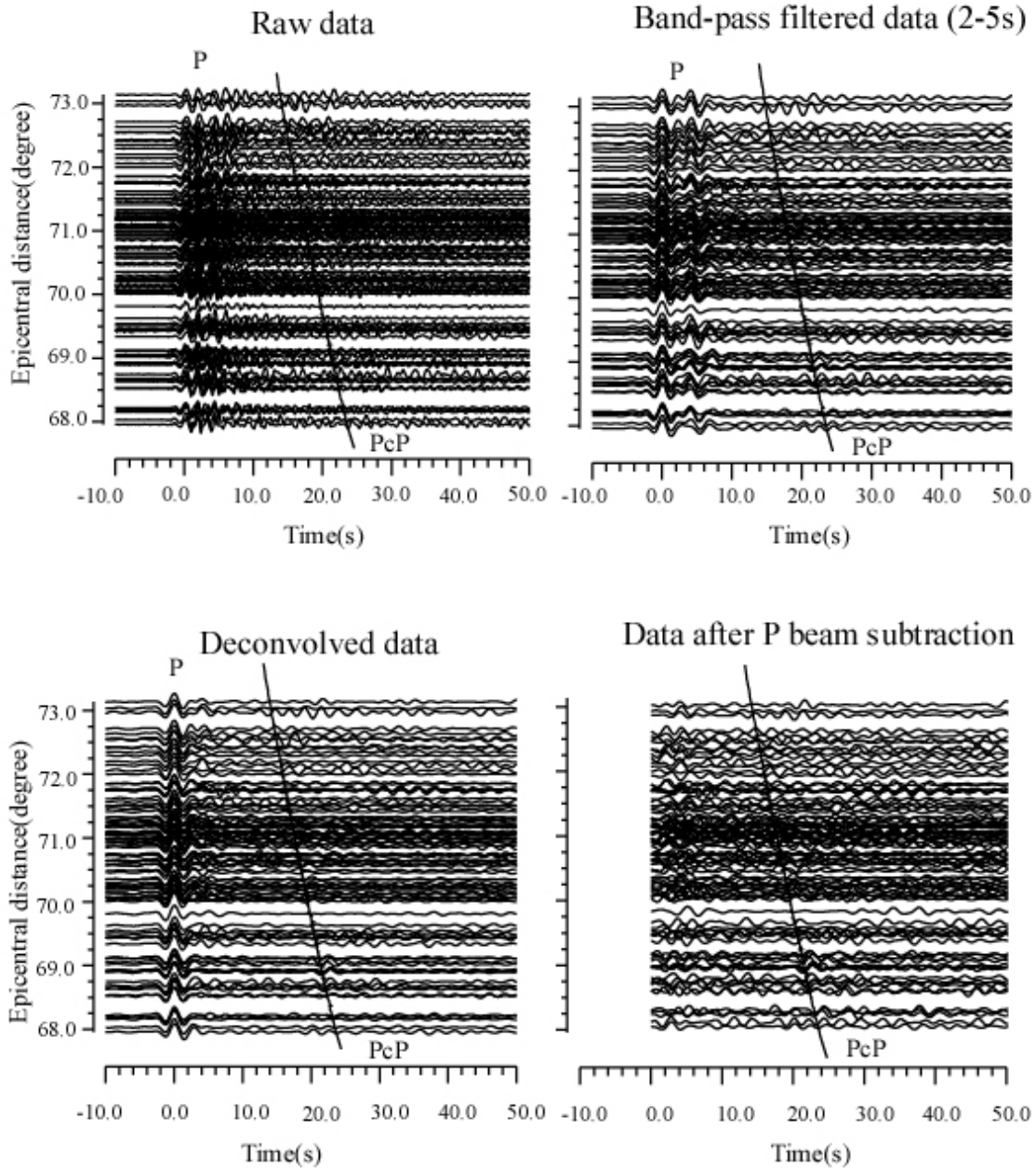


**Figure 7.3** P-wave example records of an event from the Hi-net data (Event 10) sorted by the epicentral distance. The seismograms are aligned with respect to the P-waves. The solid lines indicate the theoretical travel time of PcP phases. The source time function in this event is relative long and rather complicated. It can be clearly seen that the complicated P waveforms are simplified by the deconvolution procedure.

### Examples of seismograms (Event 8 Hi-net)

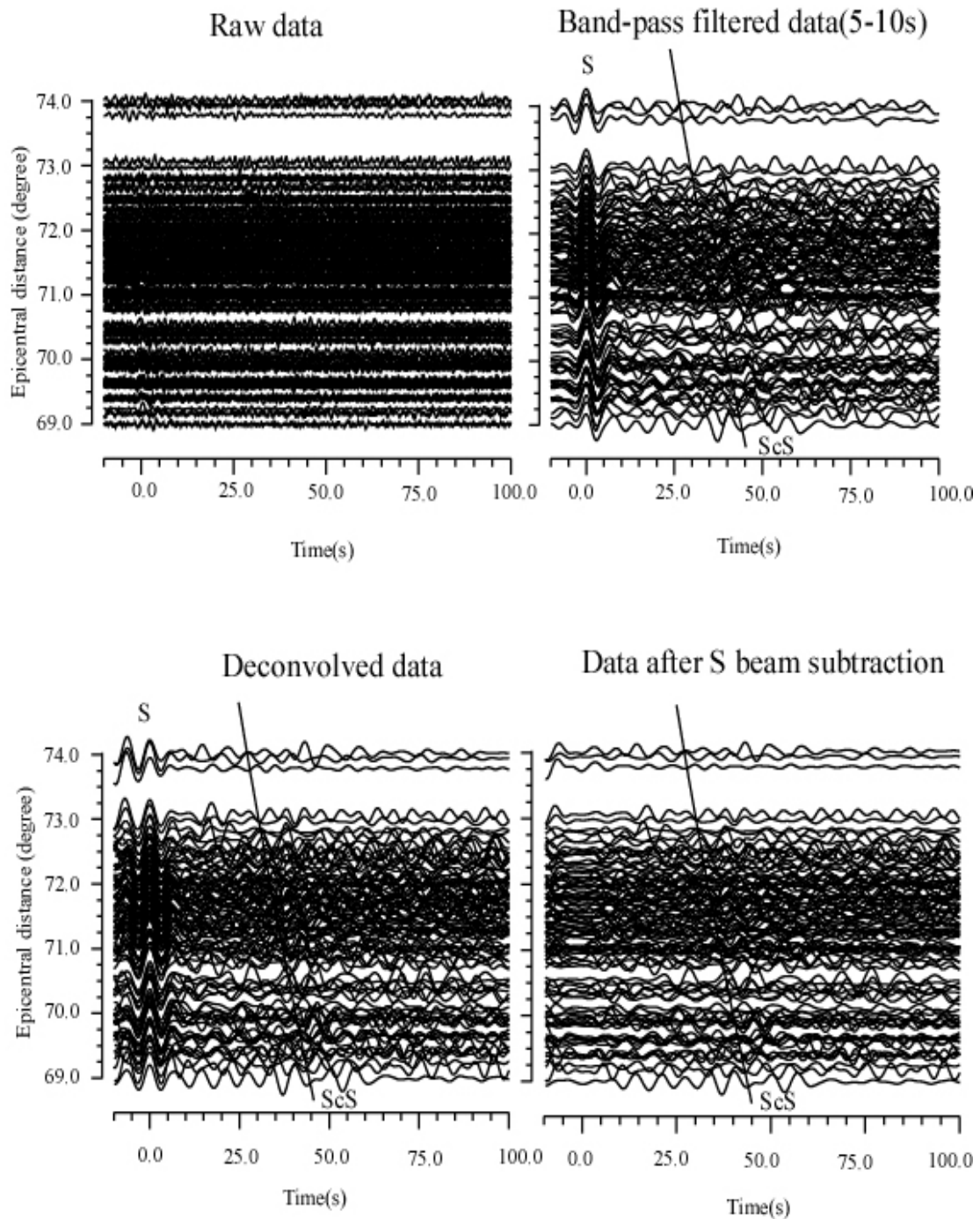


**Figure 7.4** Example records of an event from the Hi-net (Event 8) sorted by increasing epicentral distances for S-waves (transverse component). The solid lines indicate the theoretical travel times of ScS. The data are processed in the same way of P-waves except for the rotation process in order to get the transverse and radial component. A 5s-10s band-pass filter was applied. ScS phases are visible after the S arrival.

### 7.3 Source and Receiver Corrections

Though the travel time residuals due to the heterogeneities both beneath the source side and receiver side were corrected by an alignment procedure of direct P-waves, it is still difficult to isolate the effect of heterogeneities beneath the receiver side from that of the source side. In order to know the travel time residuals of source side and receiver side separately, the relative travel time residuals for each subarray and for each event were estimated. First, PcP-P travel times relative to the theoretical one were measured for each subarray and each event. The fluctuation of the relative travel time residuals with respect to subarrays can be considered a receiver-side effect. The fluctuation of the PcP beam for each event can be regarded as a source-side effect. Thomas and Weber (1997) estimated travel time residuals in a similar way. They calculated the average value of the relative travel time residuals  $AVE\Delta T_{rec}$  (one event at all stations) and the average values of all events for one station  $AVE\Delta T_{sou}$ . What makes the method used in this study different from their method is that subarrays were used instead of single stations. In general, an observed travel time of P-wave  $T_P$  is written by the following equation:

$$T_P = T_{P(theo)} + \Delta T_{P(sou)} + \Delta T_{P(res)} + \Delta T_{P(mantle)},$$

where  $T_{P(theo)}$  is theoretical travel time for P-wave,  $\Delta T_{P(sou)}$  is travel time residual for P-wave in the source region,  $\Delta T_{P(res)}$  is travel time residual for P-wave in the receiver region and  $\Delta T_{P(mantle)}$  is travel time residual for P-wave caused by the mantle structure. In the same way as P-wave, an observed travel time of PcP wave is written by the following equation:

$$T_{PcP} = T_{PcP(theo)} + \Delta T_{PcP(sou)} + \Delta T_{PcP(res)} + \Delta T_{PcP(mantle)},$$

where  $T_{PcP(theo)}$  is theoretical travel time for PcP wave,  $\Delta T_{PcP(sou)}$  is travel time residual for PcP wave in the source region,  $\Delta T_{PcP(res)}$  is travel time residual for PcP wave in the receiver region and  $\Delta T_{PcP(mantle)}$  is travel time residual for PcP wave caused by the mantle structure. Therefore, the travel time difference between observed PcP wave and P ( $T_{PcP} - T_P$ ) is written by the following equation:

$$\begin{aligned} T_{PcP} - T_P &= \{T_{PcP(theo)} + \Delta T_{PcP(sou)} + \Delta T_{PcP(res)} + \Delta T_{PcP(mantle)}\} - \{T_{P(theo)} + \Delta T_{P(sou)} + \Delta T_{P(res)} + \\ &\quad \Delta T_{P(mantle)}\} \\ &= \{T_{PcP(theo)} - T_{P(theo)}\} + \{\Delta T_{PcP(sou)} - \Delta T_{P(sou)}\} + \{\Delta T_{PcP(res)} - \Delta T_{P(res)}\} + \{\Delta T_{PcP(mantle)} - \\ &\quad \Delta T_{P(mantle)}\} \end{aligned}$$



The second term corresponds to travel time residuals of PcP – P in the source region (source correction) and the third term corresponds to travel time residuals of PcP – P in the receiver region (receiver correction). These travel time residuals should be estimated respectively. The average travel time residuals of all subarrays for each event were calculated by the following equation:

$$RES_{avesource}(i) = \frac{\sum_{j=1}^{MS} RES_{obs}(j, i)}{MS}, \quad (7.7)$$

where  $RES_{obs}(j,i)$  is observed travel time residual of each event for each subarray,  $RES_{avesource}(i)$  is average travel time residual of all subarrays for each event and MS is the number of subarrays (19). These average values,  $RES_{avesource}(i)$ , contain all effects along the P and PcP wave ray paths and the effect of the source mislocation (mantle and source region). In order to remove the source related effects these average values were subtracted from the observed residuals (see Eq. 7.8). Subsequently, average residuals of all events for each subarray were calculated to extract the common fluctuation of all events with respect to a specific subarray by the following equation:

$$RES_{sub}(j) = \frac{\sum_{i=1}^M \{RES_{obs}(j, i) - RES_{avesource}(i)\}}{M}, \quad (7.8)$$

where  $RES_{sub}(j)$  is average travel time residual in each subarray using all events with the source effect correction and M is the number of events.  $RES_{sub}(i)$  can be regarded as travel time residuals almost only influenced by the lateral heterogeneous structure beneath the receivers without containing the effect of the sources and their surrounding areas (receiver correction). These travel time residuals were added to the theoretical travel time to correct for the different influences of the structure beneath the receiver region. The same procedure was applied for S-wave. In Figure 7.5 the  $RES_{sub}(j)$  for PcP-P and ScS-S travel time residuals are shown. On the left hand side of Figure 7.5, corresponding to the northern part of the whole array, the relative travel-time residuals increase, indicating that the structure in the crust and upper mantle beneath the northern part of Japan is different from that of the southern part of Japan. These relative travel time residuals for P-wave and S-wave range from  $-0.48$  s to  $0.24$  s and from  $-1.67$  to  $0.68$ , respectively. S-wave residuals vary more drastically than those of P-waves. However, the tendency of the curve for both P- and S-wave is roughly similar.

In addition to the travel time correction of the upper mantle and the crust in the receiver region, it is necessary to correct travel time residuals caused by heterogeneous structure in the vicinity of the

source region. This correction (source correction) is expressed as the following equation:

$$RES_{source}(j) = RES_{aversource}(i) - \frac{\sum_{i=1}^M RES_{aversource}(i)}{M}, \quad (7.9)$$

where  $RES_{source}(j)$  is the source correction for each event. In principle, the second term in the equation 7.9 corresponds to the effect of the mantle structure, especially the effect of the lowermost mantle. In other words, the source correction is equal to the travel time fluctuations of PcP beams after the general time delays caused by the lower mantle are subtracted from the PcP beam delay times in each event with respect to IASP91. The  $RES_{source}(j)$  (travel time fluctuation of PcP beams) were added to the theoretical travel time as a source correction. In Table 7.1 the  $RES_{source}(j)$  for P and S are shown. The effect of the application of these two travel time corrections will be seen by comparing results in Figure 9.6a-c in the chapter 9.3 of *Results from RWB (using Subarrays)* and results in Figure 1Aa-c in Appendix 5.

Event	Source residuals (P-wave)	Source residuals (S-wave)
1	0.24	No data
2	0.18	No data
3	0.40	No data
4	-0.02	No data
5	0.30	No data
6	-0.14	No data
7	0.03	No data
8	-0.19	0.70
9	-0.19	No data
10	0.38	-2.38
11	-0.54	1.7
12	Not visible	No data

**Table 7.1** The fluctuations of the travel time residuals for PcP-P and ScS-S in each event, which were applied as a source correction.

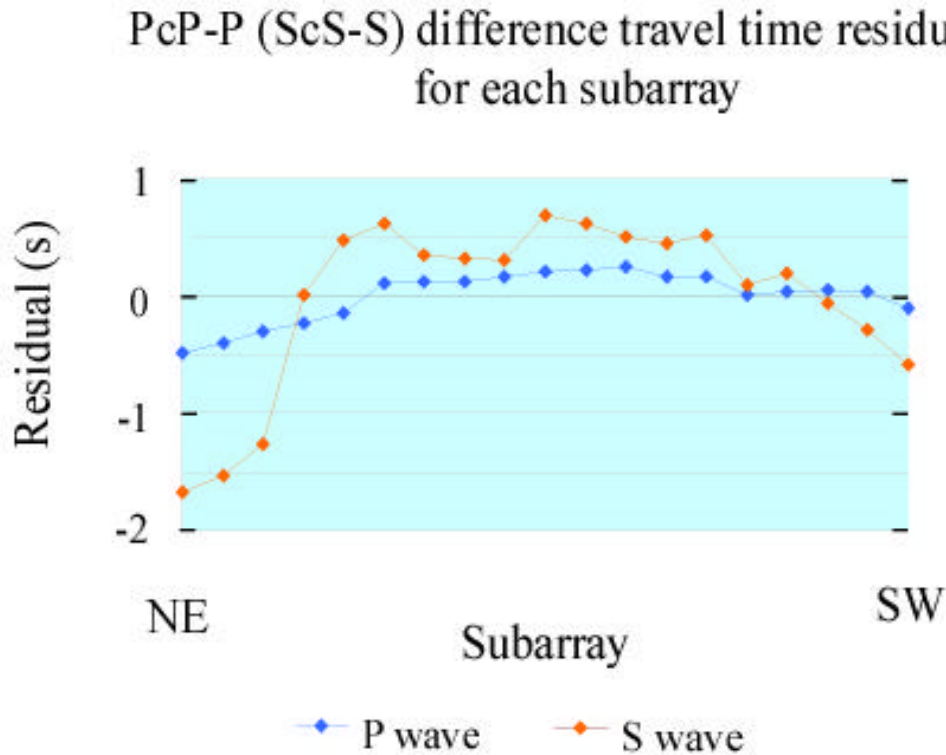


**Figure 7.5**  $RES_{sub(j)}$  are plotted as average PcP-P and ScS-S travel time residuals (see Eq. 7.8). The vertical axis indicates the relative travel-time residuals between the theoretical and observed value. PcP-P residuals are indicated by blue line with diamonds and ScS-S residuals are indicated by orange line with diamonds. These travel time residuals for each subarray were applied to the observed data as an upper mantle and crust in the receiver region (receiver correction).

## 8. Synthetic Tests

Synthetic seismograms were calculated in order to confirm the method applied to the observed data and in order to apply a quantitative constraint to the observed anomalous structures. Synthetic seismograms were calculated using the program REFGREEN, which is a modification of REFSEIS.F written by J. Ungerer (1990). The calculation is based on the reflectivity method (Müller, 1985) and the IASP91 Earth model was taken as a reference velocity model.

### 8.1 Calculation of Synthetic Seismograms

First, Green's functions for each trace were calculated and then combined to displacement seismograms. The source mechanism was taken from the CMT solution (Harvard CMT Catalogue). Due to the limitation of computation time, the sampling rate of the synthetic seismograms is 10 Hz

while that of the observed seismograms is 20 Hz. The deviating sampling rate, however, has no effect on the analysis. 2 s was chosen as the duration of the source time function. Since the observed seismograms were velocity data, the synthetic seismograms were differentiated to obtain velocity seismograms.

The distribution of the stations used in the synthetic calculations is the same as that of the observed seismograms. Since only information of the epicentral distances between sources and receivers is used for the synthetic seismograms, the effect of the Earth's ellipse was not taken into account. After the synthetic seismograms were calculated for all 12 events, noise was added to the synthetic seismograms in order to better match the synthetic seismograms to the observed ones. The noise was obtained from the seismogram portion before the P-waves (S-waves) in the observed data. The seismic data before the P-waves are assumed to contain white noise filtered by the instrumental response of the seismometers. The amplitude of the added noise is approximately 5 % of that of P-waves (S-waves). The attenuation model (Q-model) and density model were taken from PREM (Dziewonski and Anderson, 1981). Examples of synthetic seismograms are shown in Figure 8.1 for P-waves and Figure 8.2 for S-waves. Noticeable features are that the waveforms are simpler than those of observed seismograms and that the amplitude of the PcP and ScS phases is relatively larger than those of observed seismograms. These are very likely due to the relatively simple model in IASP91 in comparison with the complexities at the CMB region and crustal structures in the real Earth.

## 8.2 Analysis of the Synthetic Seismograms

After the synthetic seismograms were calculated, the same processing steps used to process the real data were also applied to the synthetic seismograms. Since the synthetic traces are broadband seismograms, the instrument deconvolution was not applied. The rest of the processing for the synthetic seismograms is the same. See chapter 7 (*Data preprocessing*) for a detailed description. After the same processing was applied, the waveforms of the synthetic seismograms became similar (see Figure 8.3).

In order to test the method described in the chapters 5 and 6, the RWB and the migration were applied to the calculated synthetic seismograms. The results are shown in Figure 8.4a, Figure 8.4b and Figure 8.4c for P-waves and in Figure 8.5a, Figure 8.5b and Figure 8.5c for S-waves. The red zones at the depth of the CMB (2889 km) indicate the PcP energy and the PWSEMBP has the best resolution among the three different coherency measurements. The reason for the relatively low resolution in PWSEM is due to the relatively simple waveforms of the synthetic seismograms, because the PWSEM is sensitive only to similarity of the waveforms. On the other hand, PcP energy is imaged in the standard beam with quite high resolution, because the beam is very sensitive to the amplitude of the waveforms. The slight change of the width of the red zones from left to right, which

corresponds to vertical resolution, is due to the number of traces in each subarray. The more the number of traces increases, the more the width of the PcP energy zones becomes narrow. In the case of S-wave, the aliasing effect of ScS is stronger than that of PcP. The results of the migration method are seen in Figure 8.7a, Figure 8.7b and Figure 8.7c. PcP energy is focused at the depth of 2889 km, but its aliasing effect is visible in every depth range. This aliasing effect of PcP must be distinguished from reflected waves or scattered waves in the D' layer.

A -1% velocity discontinuity was introduced at the depth of 2650 km in order to see how the synthetic velocity discontinuity is imaged by the RWB and the migration. Figure 8.5a, Figure 8.5b and Figure 8.5c show the results in the RWB, and Figure 8.8a, Figure 8.8b and Figure 8.8c show the results for the migration. In both methods the energy of the reflected waves from the synthetic velocity discontinuity are clearly visible almost at the same level.

In order to examine the lateral resolution in the RWB method, synthetic seismograms with a discontinuity with 1% negative P-wave velocity contrast at the depth of 2650 km were calculated. This synthetic discontinuity produces reflected waves that reach only the stations west of Long. 137° West, while for the other stations a model (IASP91) without a discontinuity was used. The same process as was used for the observed data was applied to this synthetic data set. The result indicates that the transition zone between the area with discontinuous structure and the area with standard velocity model (IASP91) is visible in the subarray 12, 13 and 14 in Figure 1A in Appendix 1, since the P-wave velocity in the zone between the introduced discontinuity at the depth of 2650 km and the CMB (2889 km depth) is reduced by 1%, it is reasonable that the depth of the CMB in the eastern part of the area is depressed by about 20 km. The resolution in the middle area is higher than in the remaining area due to the higher station density.

In Figure 8.7a-c the results of synthetic test in the migration method are presented. Figure 8.8a-c show the results using the synthetic seismograms for the IASP91 model which contains a -1% velocity discontinuity at the depth of 2650 km. A comparison of both results suggests that the introduced velocity discontinuity shows up in the center of the 'PcP aliasing ring' at the corresponding depth.

## Examples of synthetic seismograms

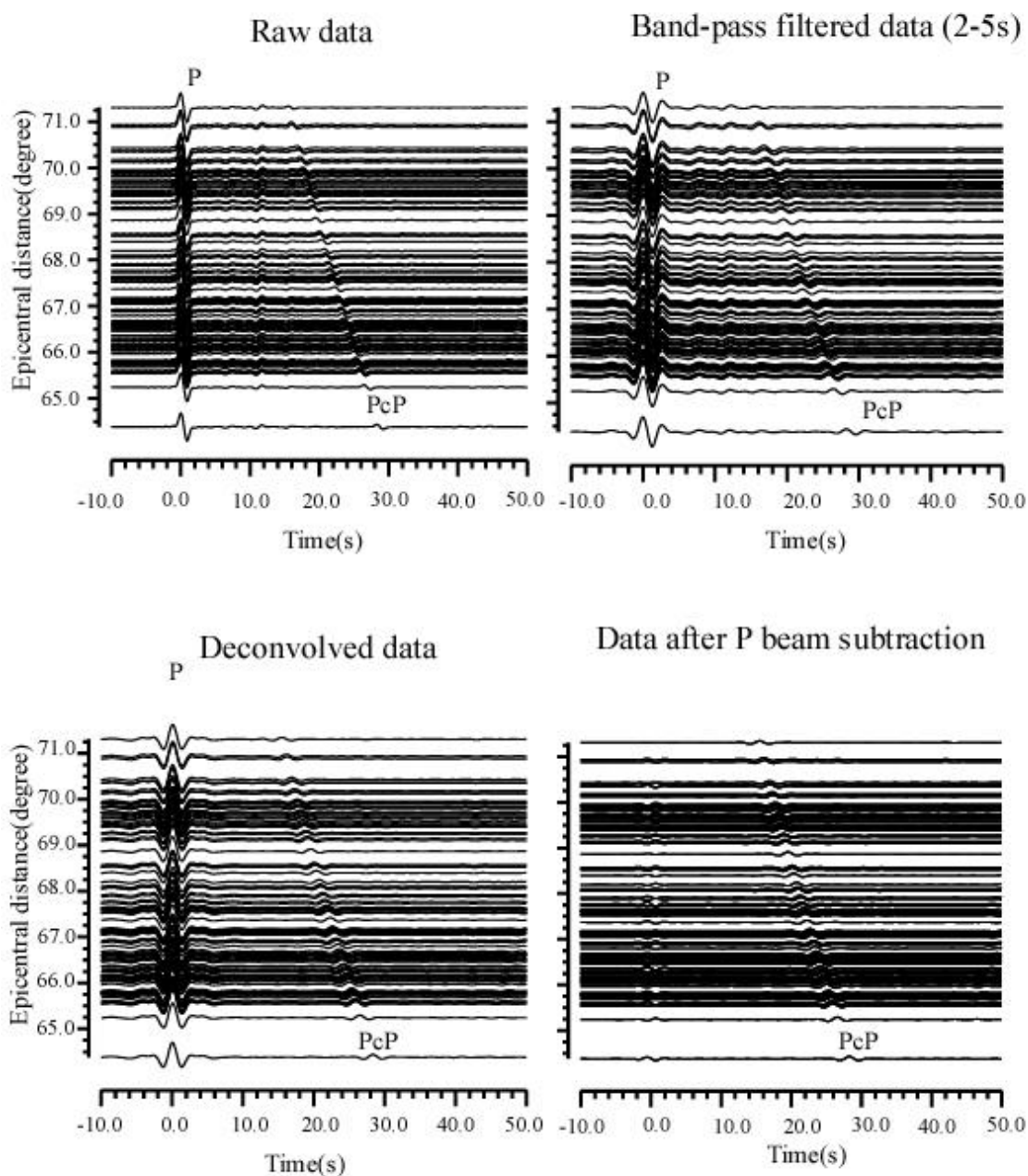


**Figure 8.1.** Examples of synthetic seismograms. The procedure applied to the synthetic seismograms is the same as that for the observed seismograms except for the instrumental deconvolution which was not applied, because the synthetic data are broadband data sets. In comparison with the observed data P and PcP waveforms are relatively simple and PcP phases are clearer than the observed ones. The source depth is 569.3 km and source parameters such as strike, dip and slip (14,49,138) were taken from the Harvard CMT solution catalogue (Event1 J-Array, see Table 1).

## Examples of synthetic seismograms

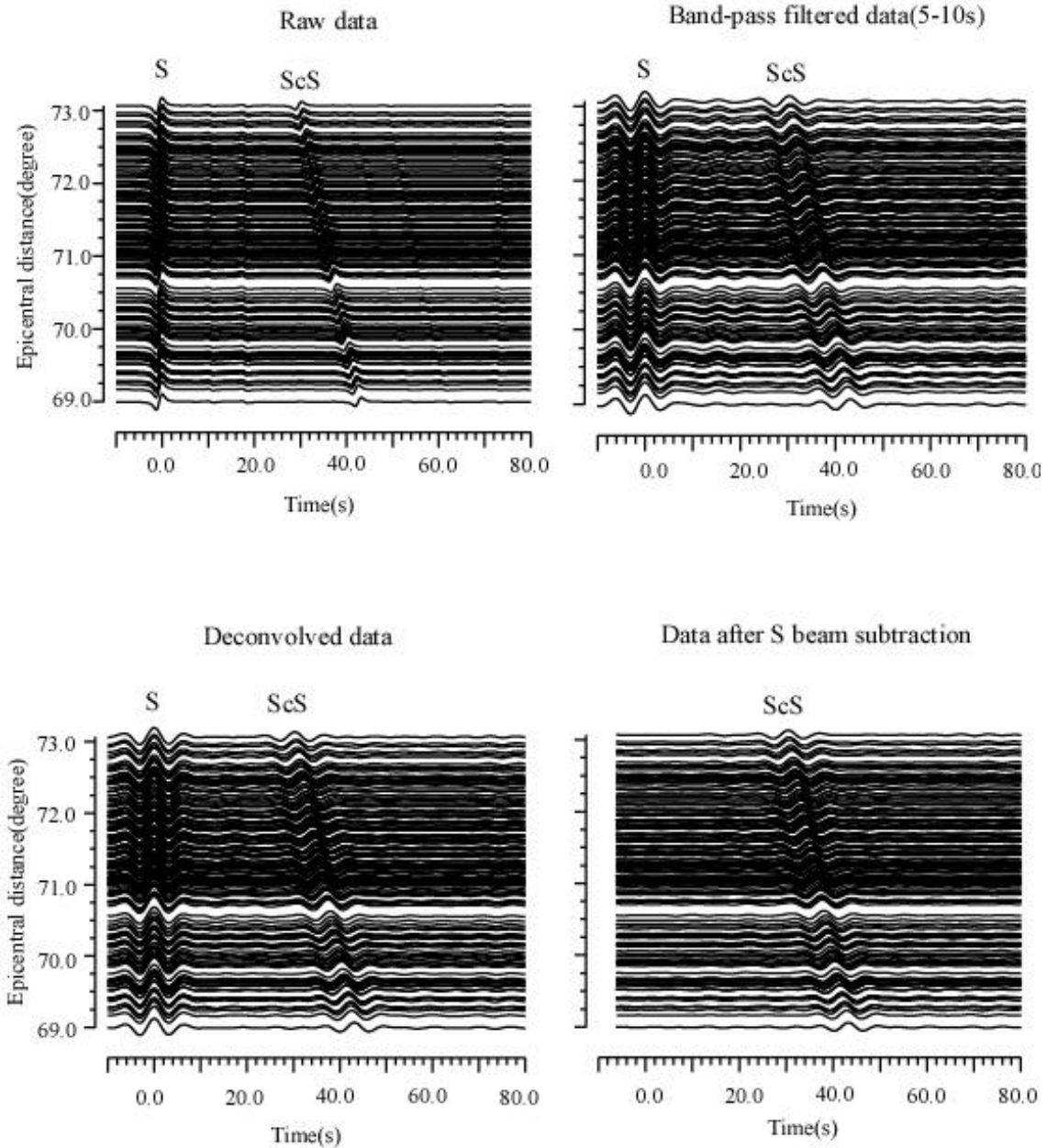


**Figure 8.2.** Synthetic seismograms for S-wave in the transverse component. Theoretically, there is no SKS phase on the transverse component, if there is no anisotropic structure along the ray path. The amplitude of ScS is rather high, because the reflection coefficient of the SH phase at the CMB is nearly 1. The source depth is 655.7 km.

### PcP and ScS beams in a subarray (sub. 10)

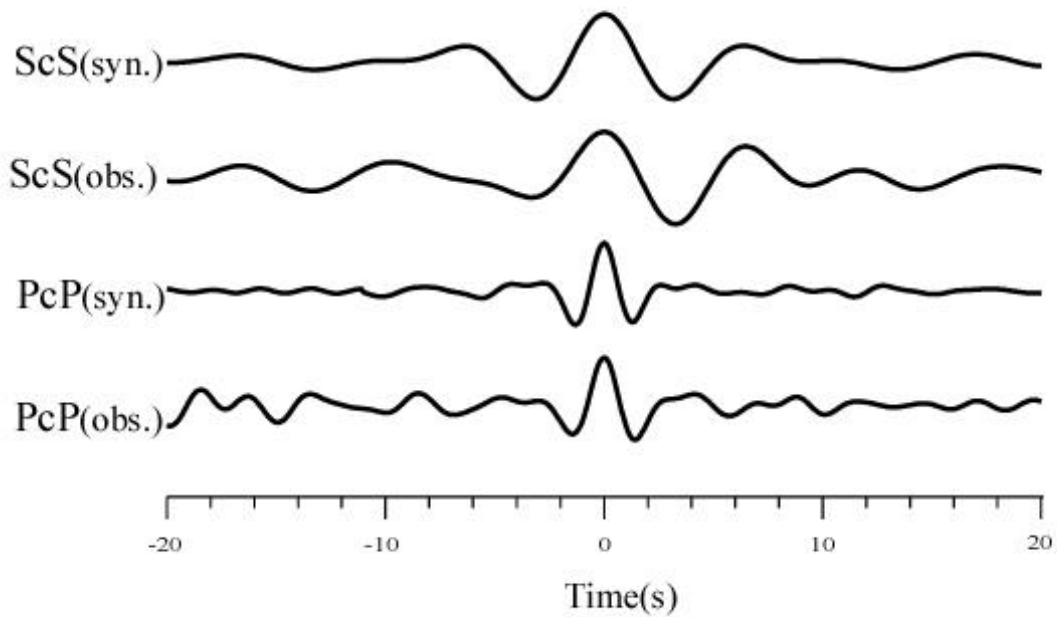


**Figure 8.3** PcP (2-5s) and ScS (5-10s) beams for observed seismograms and for synthetic seismograms in a subarray. Noise from the observed data was added to the synthetic data. All waveforms are aligned at the time of 0.0. Note that the waveforms of PcP and ScS are very similar, if the observed data and synthetics are compared.



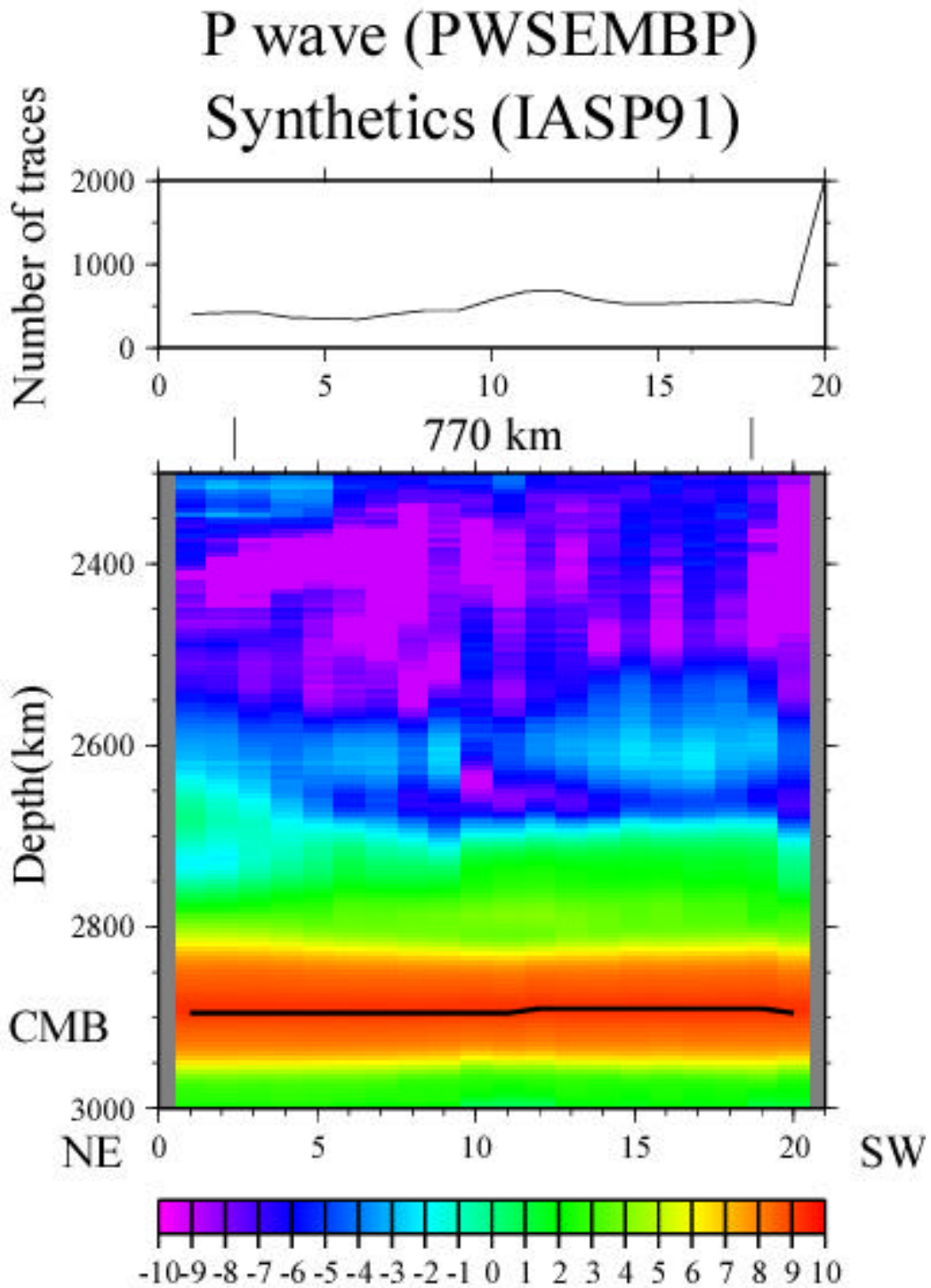


**Figure 8.4a** The coherency measure, PWSEMBP is shown in the vertical cross section in the RWB method using synthetic seismograms. The horizontal axis indicates the subarrays and the vertical axis indicates the depth. The left side of the panel corresponds to the northeastern part of the study area and the right side of the panel corresponds to the southwestern part of the study area. The horizontal scale of the mapped area is about 770 km at the CMB. In the upper diagram in each figure the number of the traces which were used to calculate the coherency measures in each subarray are shown. The coherency measure is plotted in a logarithmic scale.

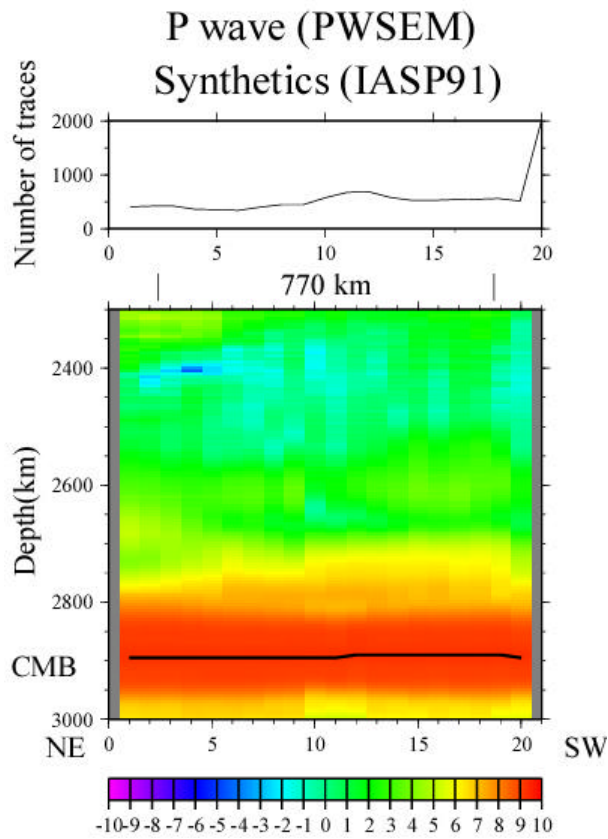


**Figure 8.4b** same as the Figure 8.4a, but for PWSEM.

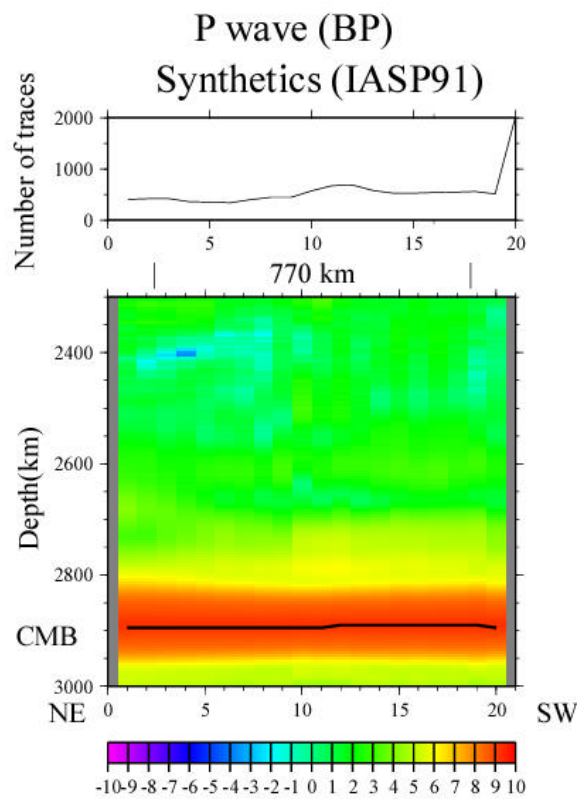


**Figure 8.4c** same as the Figure 8.4a, but for BP.

# P wave (PWSEMBP) Synthetics

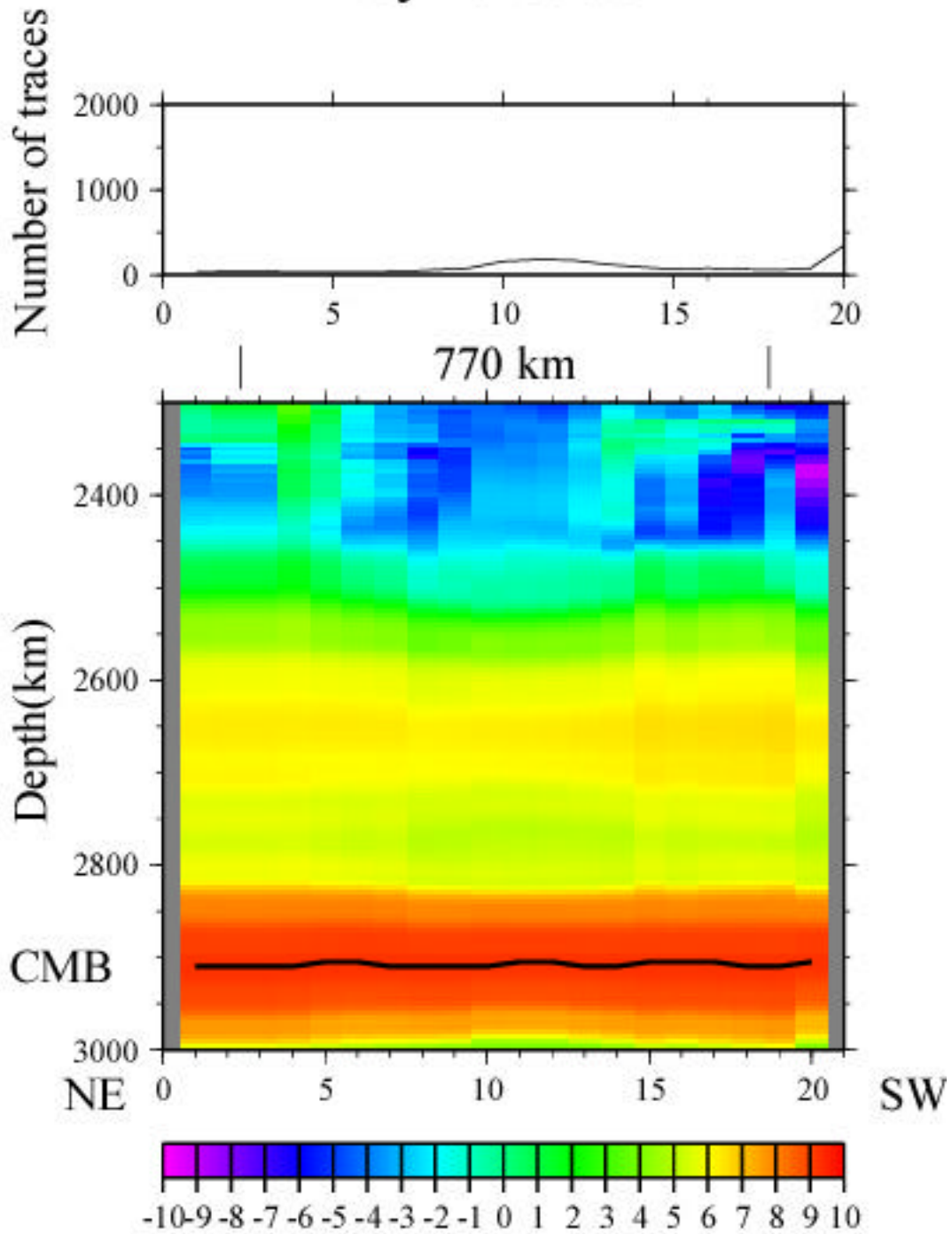


**Figure 8.5a** PWSEMBP for P-wave synthetic data with a  $-1\%$  velocity discontinuity at the depth of 2650 km.

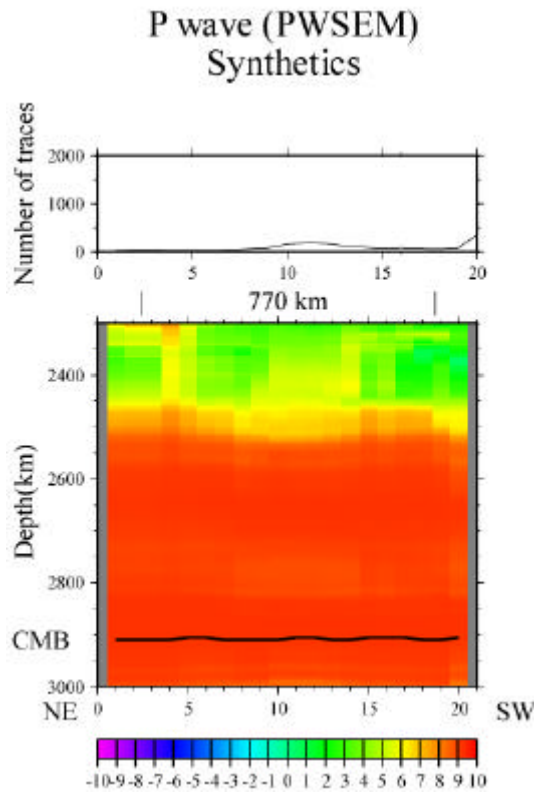


**Figure 8.5b** same as the Figure 8.1A.a, but for PWSEM.

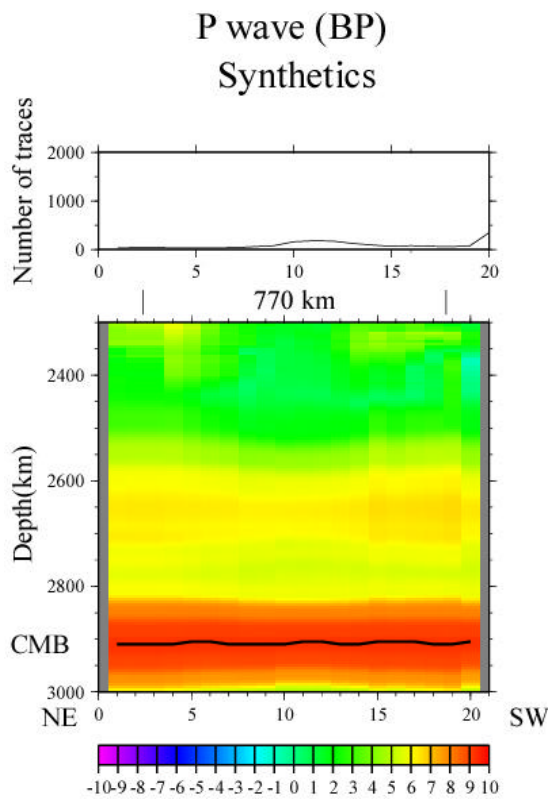


**Figure 8.5c** same as the Figure 8.1A.a, but for BP

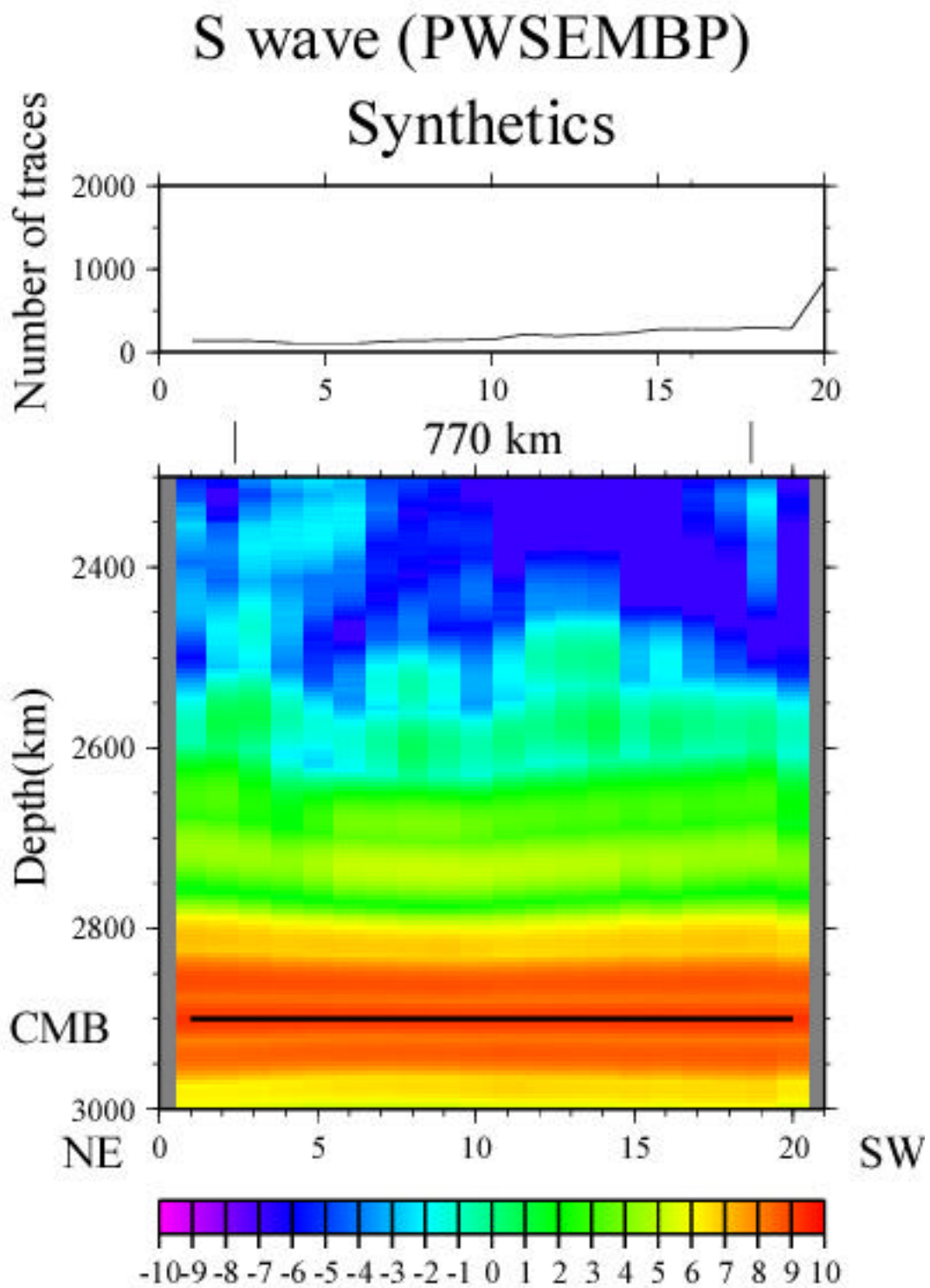


**Figure 8.6a** same as the Figure 8.4a, but for S-wave.

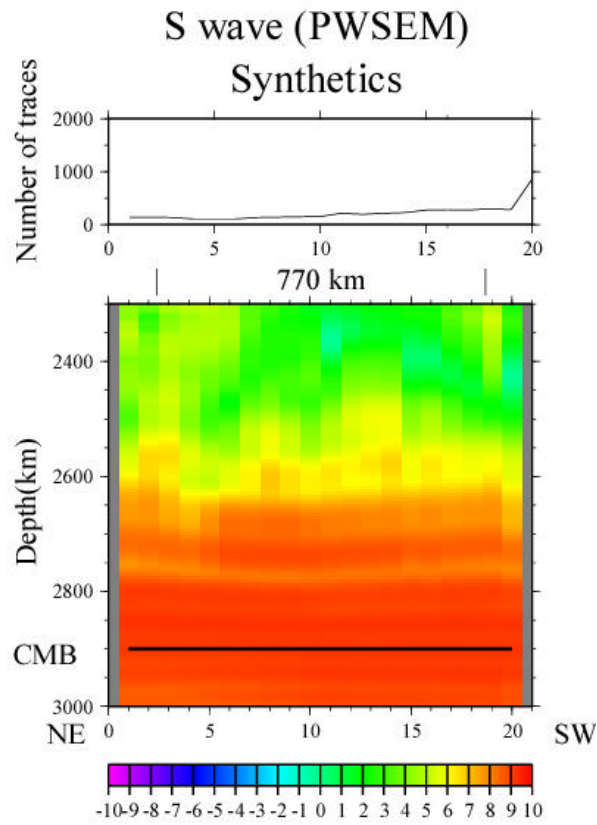


**Figure 8.6b** same as the Figure 8.4b, but for S-wave

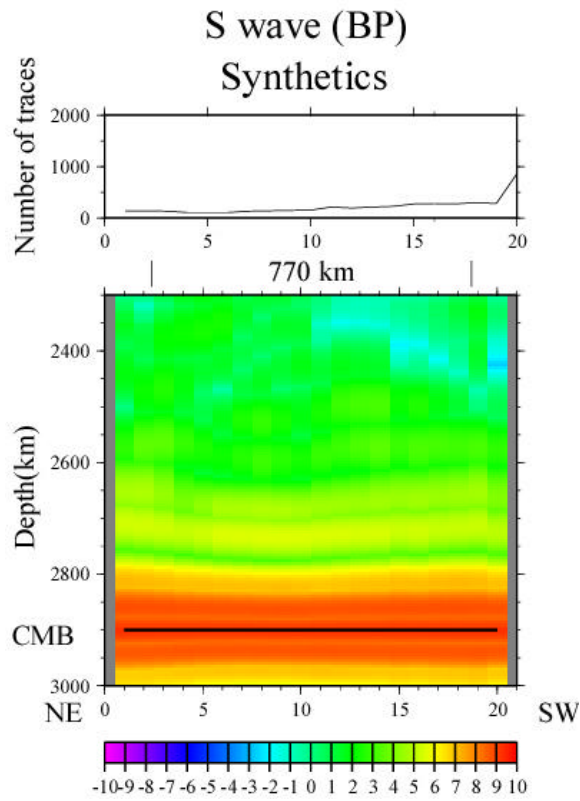


**Figure 8.6c** same as the Figure 8.4c, but for S-wave.

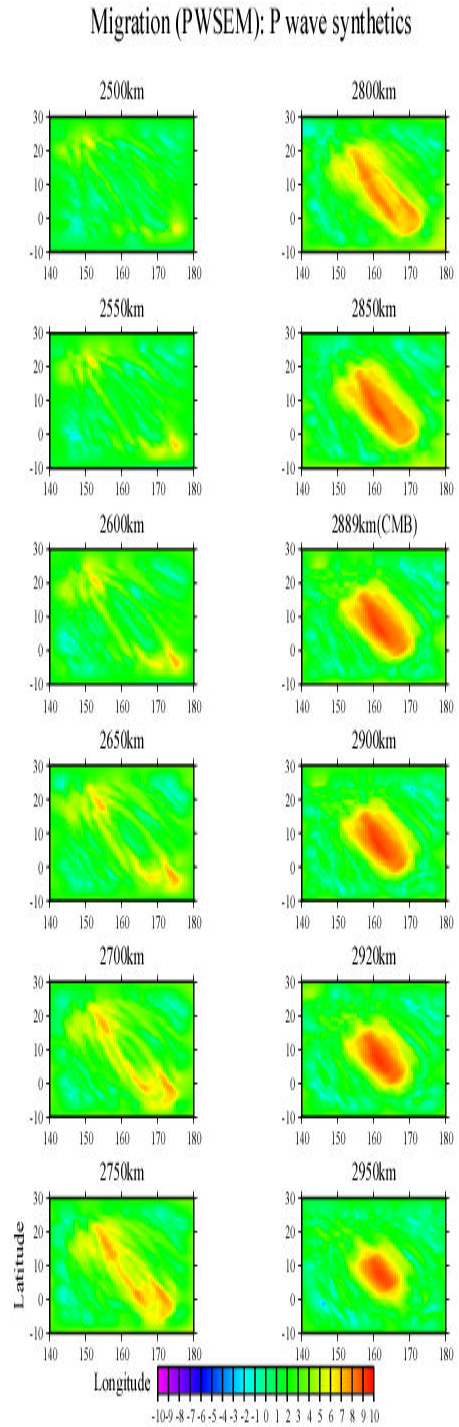
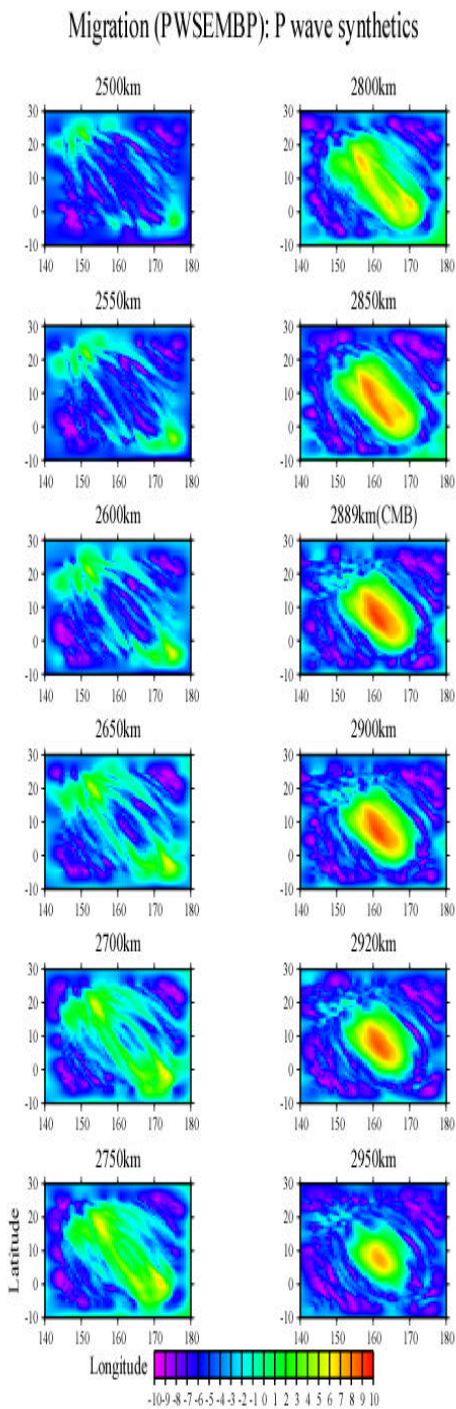


**Figure 8.7a**

**Figure 8.7b**

**Figure 8.7a-c** Double Array Migration indicated by various coherency measures (PWSEMBP, PWSEM and BP) by a logarithmic scale with synthetic seismograms to which real noise was added. The 2017 synthetic seismograms correspond to exact same paths as the observed data.

### Migration (BP): P wave synthetics

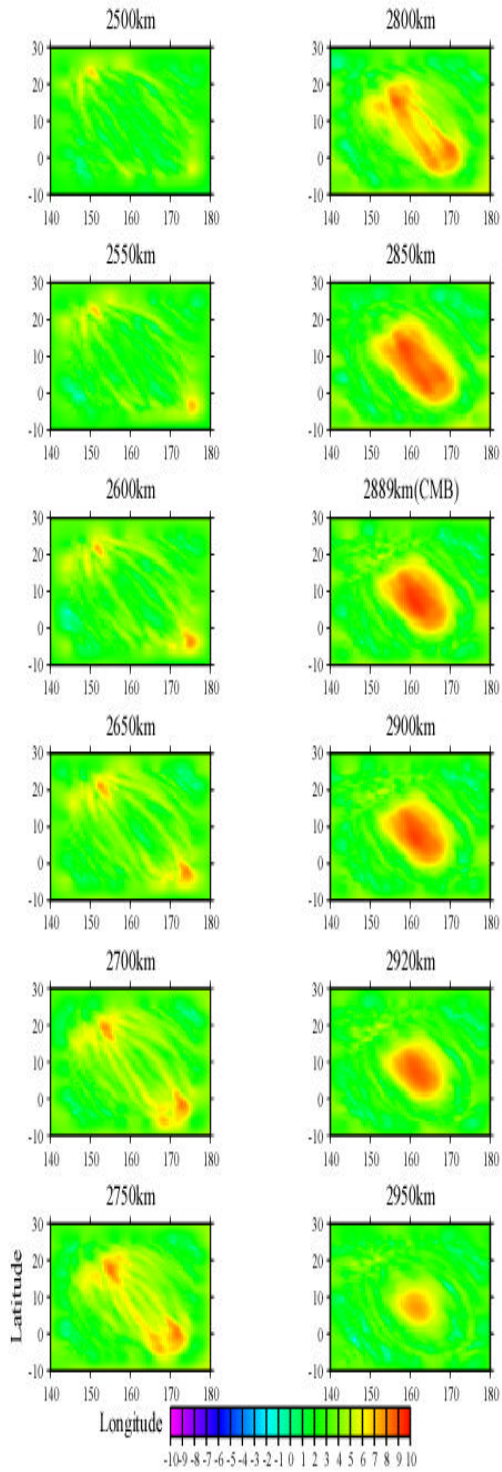


**Figure 8.7c**



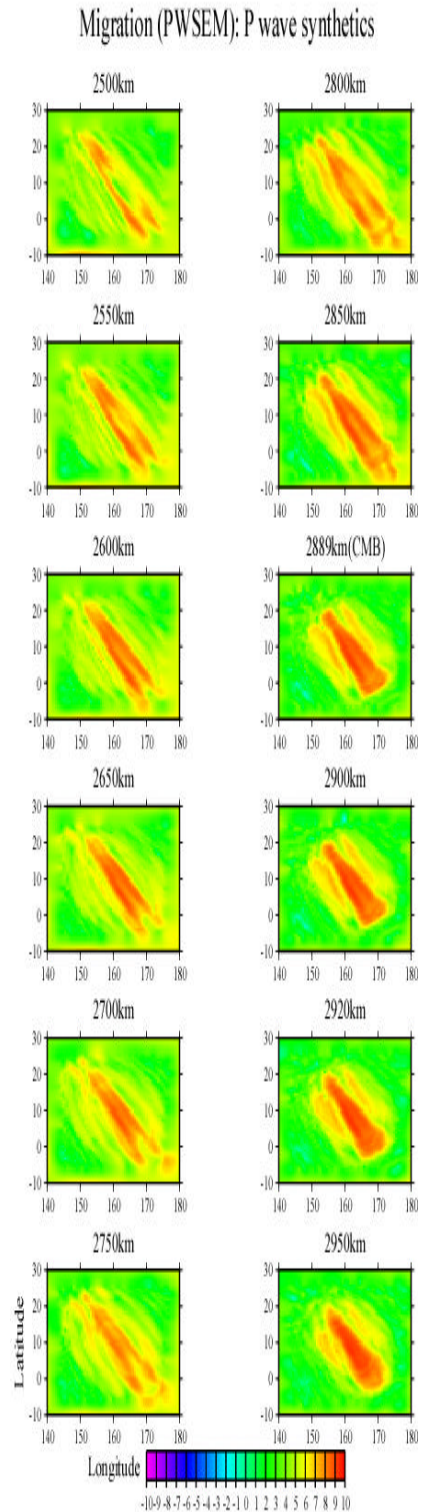
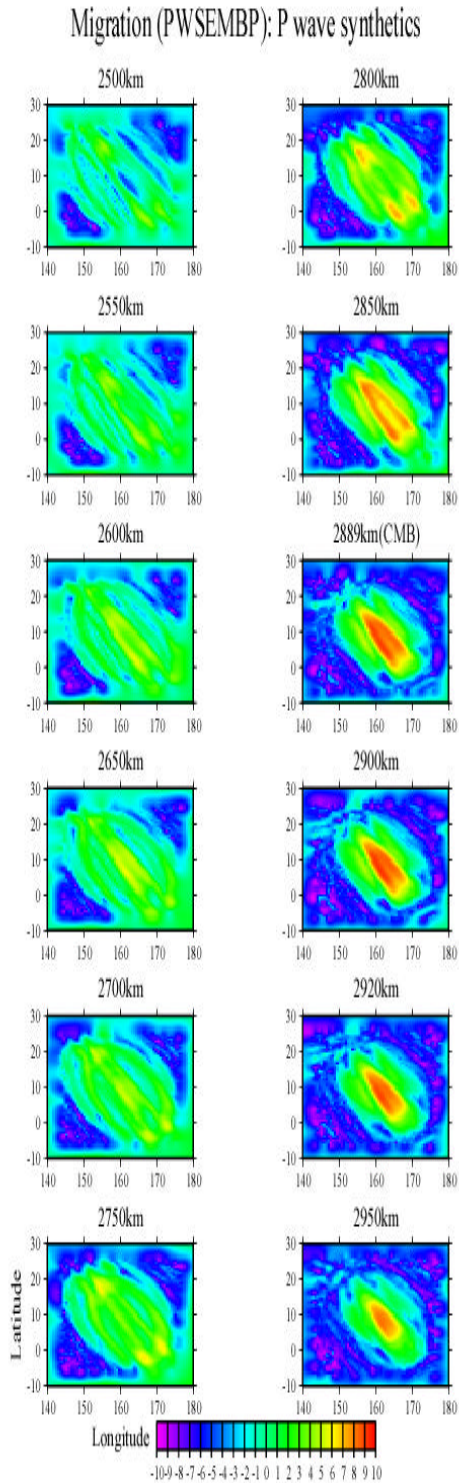


**Figure 8.8a**

**Figure 8.8b**

**Figure 8.8a-c** Double Array Migration indicated by PWSEMBP values (logarithmic scale) with synthetic seismograms which involved a discontinuity of  $-1\%$  velocity contrast at a depth of 2650km with three events.

### Migration (BP): P wave synthetic

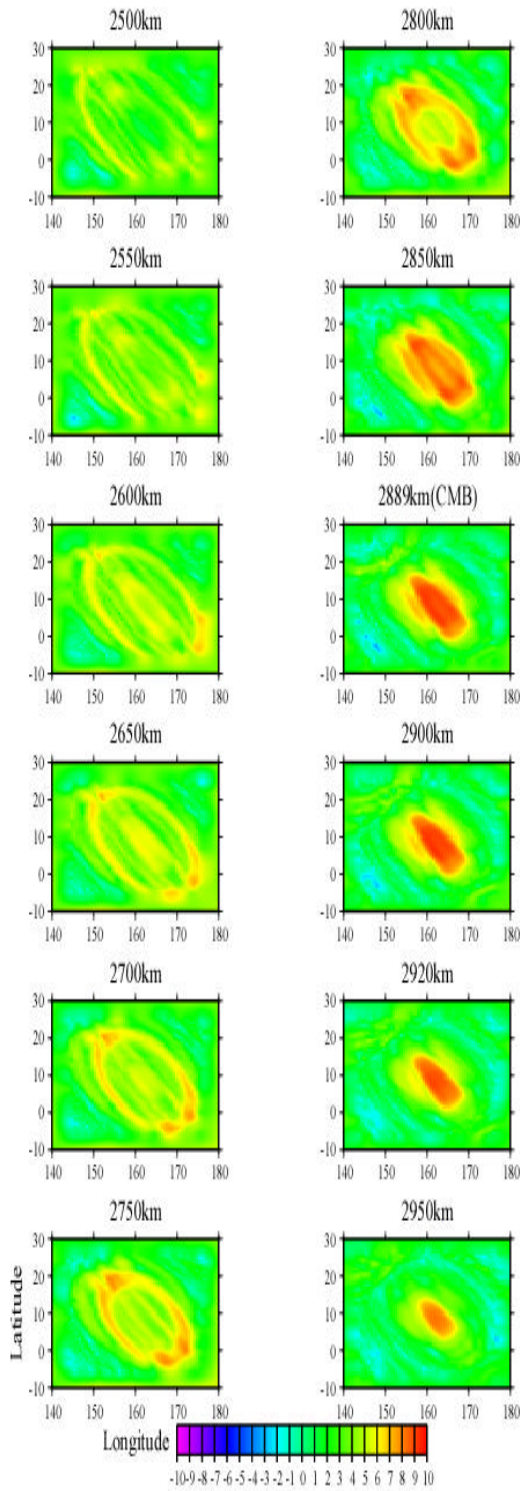


Figure 8.8c

## 9. Results

### 9.1 Results using the RWB method

As the synthetic tests show (Figure 8.4a-c and 8.5a-c), the three different kind of coherency measures, PWSEMBP, PWSEM and BP contain different information on the characteristics of the weak phases from the D'' layer. PWSEM can indicate where anomalous structures exist independent of its velocity or density contrast. BP can mainly represent the intensity (or Energy) of the phases from anomalous structures. PWSEMBP is a combination of these two different aspects. These quantities will be the basic information on the character of anomalous structures, which were acquired by the three different coherency measures.

In the RWB method using the whole array (J-Array and Hi-net), anomalous regions can be detected in the depth ranges from 2510 km to 2530 km (hereafter PdP1) and from 2620 km to 2650 km (hereafter PdP2), and at 2800 km depth (hereafter PdP3) in the frequency band of 2-5s (Figure 9.1a). In order to resolve smaller scale heterogeneities and larger scale heterogeneities, data in the frequency band of 1-2s and 5-10s were also analyzed. In these frequency bands, the anomalous peaks can be visible, but the depths of the anomalous regions are slightly different. In Figure 9.1b there are 4 peaks except for PcP Phases, but it is not clear that all peaks are reflected waves from velocity discontinuities in the D'' layer. The third one may be an aliasing or just noise in the frequency band of 1-2s because this peak is not recognizable in the other frequency bands and in the S-wave. In the frequency band of 5-10s, only one peak is recognizable at a depth of 2550 km. Due to a lower resolution in this frequency band, the two discontinuities are not isolated.

The increase in the Phase-Weighted Semblance Beam Powers (PWSEMBP) value at about 2400 km depth can originate from P-coda energy (crustal reverberations) which has not been reduced by the P subtraction process and taper. The PdP/PcP amplitude ratio corresponding to the maximum peak of the PdP reaches 0.12. In any frequency band, it can be recognized that the apparent depth of the CMB is slightly shifted. Figure 9.5 shows that PcP phases are delayed with respect to the IASP91 model, which is the cause of the general depression of the CMB. Figure 9.3 shows stacked waveforms for the anomalous region. The polarity of PdP1 and PdP2 is clearly reversed relative to PcP, which is strong evidence that these PdP phases are produced at negative discontinuities in the lowermost mantle. It is impossible for a positive velocity jump to produce a reversed polarity for the reflected phase (Weber, 1994). Shibutani et al. (1995) suggest that the discontinuities beneath the southwestern Pacific have a positive velocity contrast. However, if the results of the recent tomographic studies are taken into account, it is reasonable that the discontinuities in the low velocity anomalous zone have a negative velocity contrast beneath the southwestern Pacific region where distinguished lower velocity anomalies exist.

The travel time delay of the PcP phases are probably due to the lower mantle anomalous structure, but the original depth of PdP phases, which are less influenced by the low velocity zone, should be determined more accurately. One question is why there are three discontinuities in the same area. As Yamada and Nakanishi (1998) have pointed out, there are considerable short-wavelength lateral heterogeneities in this area. As regards the two discontinuities at a depth of 2520 km and 2650 km, one of the possible reasons could be that the height of D'' is suddenly changing from about 2520 km to about 2650 km in the sampling area (PcP reflection points), which could produce two reflected waves at different depths.

PWSEMBP peaks can be found in the case of the S-wave (SdS phases). Figure 9.2 shows the SdS phases in the depth between ca. 2540 km and ca. 2600 km. Due to a lower resolution and larger effect of the low-velocity zone in the case of the S-wave in comparison with the P-wave, the discontinuities are not clearly distinguishable, and the observed discontinuities at a depth of about 2850 km are deeper by about 50 km in comparison with the observed P-wave discontinuities (PdP3).

The amplitude of PdP1 and PdP2 is approximately 10 % of the PcP amplitude and the amplitude of PdP3 is approximately 15 %. According to a theoretical calculation of the reflection coefficients for seismic velocity discontinuities in the D' layer and the CMB at the epicentral distance of 70 degrees, an approximately -0.5% velocity contrast is enough to produce the observed amplitude of the PdP1 and PdP2 phases. The amplitude of PdP3 is significantly larger than those of PdP1 and PdP2. Because the discontinuity at 2800 km depth has positive velocity jump (see Figure 9.3), the reflection coefficient is larger than that of a negative discontinuity with the same velocity jump. Therefore, the velocity contrast of the discontinuity at the depth of 2800 km is almost same as those of PdP1 and PdP2.

In the case of S-wave, the amplitude of SdS is approximately 20 % of the ScS amplitude. This requires an about -2% S-wave velocity jump in the D' layer. This velocity jump value is relative small compared to the seismic discontinuities with a few % velocity contrasts found in other areas. This might indicate that the low velocity discontinuities at the top of the D'' layer or in the D'' layer beneath the southwestern Pacific contain a relatively gradual transitional velocity structure rather than a sharp velocity jump on the top of the D' layer, while the wavelength in the lower mantle limits the width of the discontinuities to being not much larger than  $\lambda/4$ , approximately 8 km at the dominant frequency of 2.5 s for P-waves (Richards, 1972).

Kito and Krüger (2001) showed that seismic energy is reflected at two negative discontinuities near 2550 and 2650 km by using only J-Array data covering the same sample region in the D' layer. When the Hi-net data set was added to the previous J-Array data, the depths of the discontinuities have stayed at almost the same positions in comparison with the result of Kito and Krüger (2001). However, the amplitude ratio between the two PdP phases has changed slightly (see Figure 9.1a-9.1c and Figure 5 in Kito and Krüger (2001)). A possible explanation for the slight different shape of the

PWSEMBP curve between the results of Kito and Krüger (2001) and those of this study might be three-dimensional effects somewhere in the mantle or crust due to slightly different station distribution of both arrays. Another possible reason could be a systematic difference of source parameters between Engdahl et al. (1998) used for J-Array events and Harvard CMT solution catalog used for Hi-net events. The source parameters from Engdahl et al. (1998) do not exist at this moment because only relatively new events were available from Hi-net (see also Table 1 in Appendix 6 for all event parameters). The necessary accuracy of the source parameters will be discussed in the chapter 10.5 (*Mislocation of events and other problems*).

## PWSEMBP (2-5s)

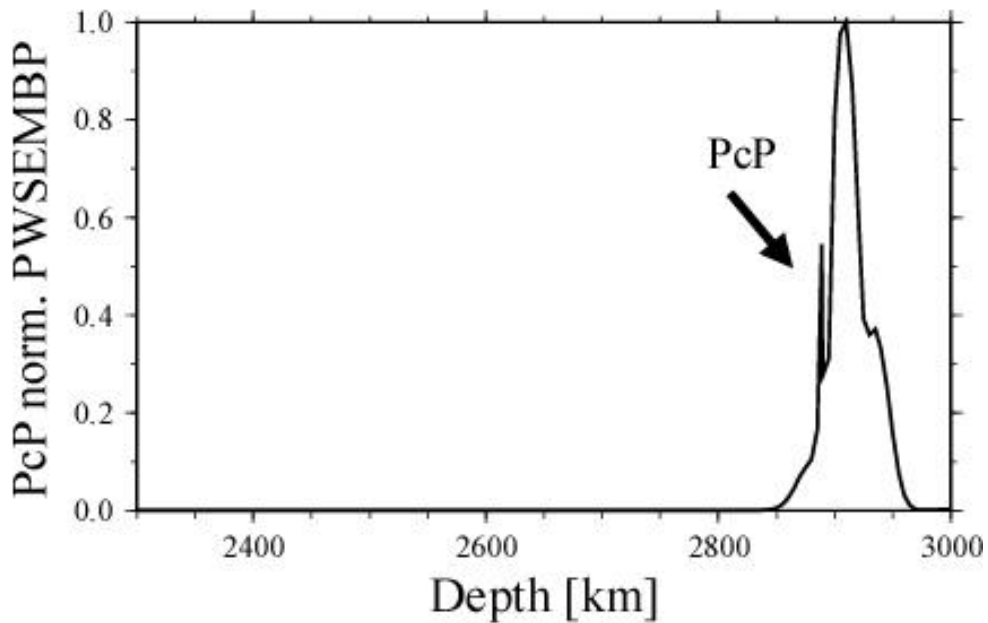
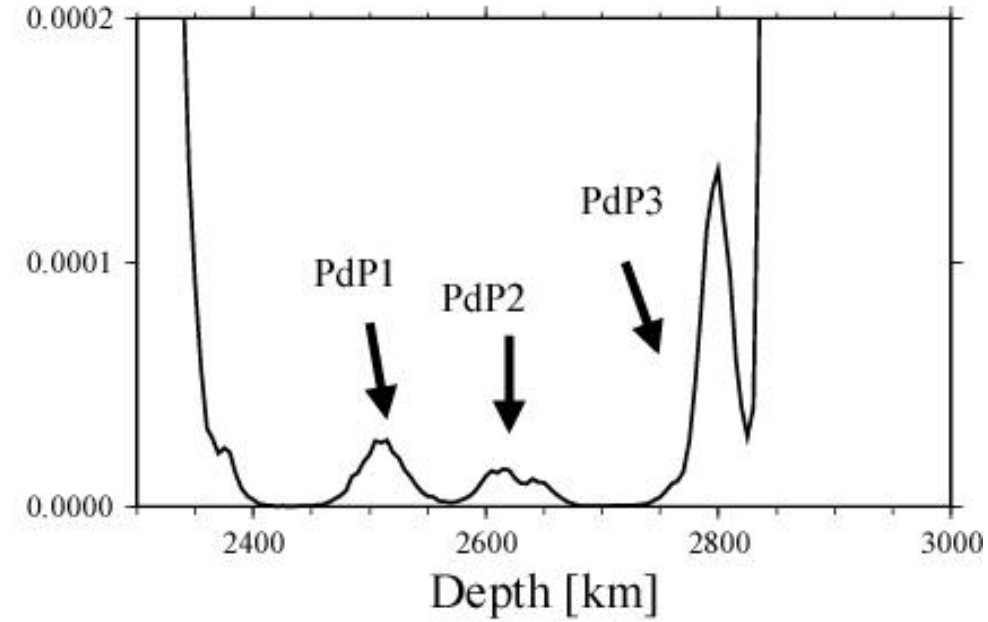


**Figure 9.1a** PWSEMBP for each depth. The graph in the lower diagram is normalized by PcP energy and the upper diagram shows the magnification of the lower graph. PcP and PdP phases are clearly seen. The PdP phases correspond to the energy from about 2520 km depth (PdP1), about 2650 km depth (PdP2) and about 2800 km depth (PdP3), respectively.

### PWSEMBP (1-2s)

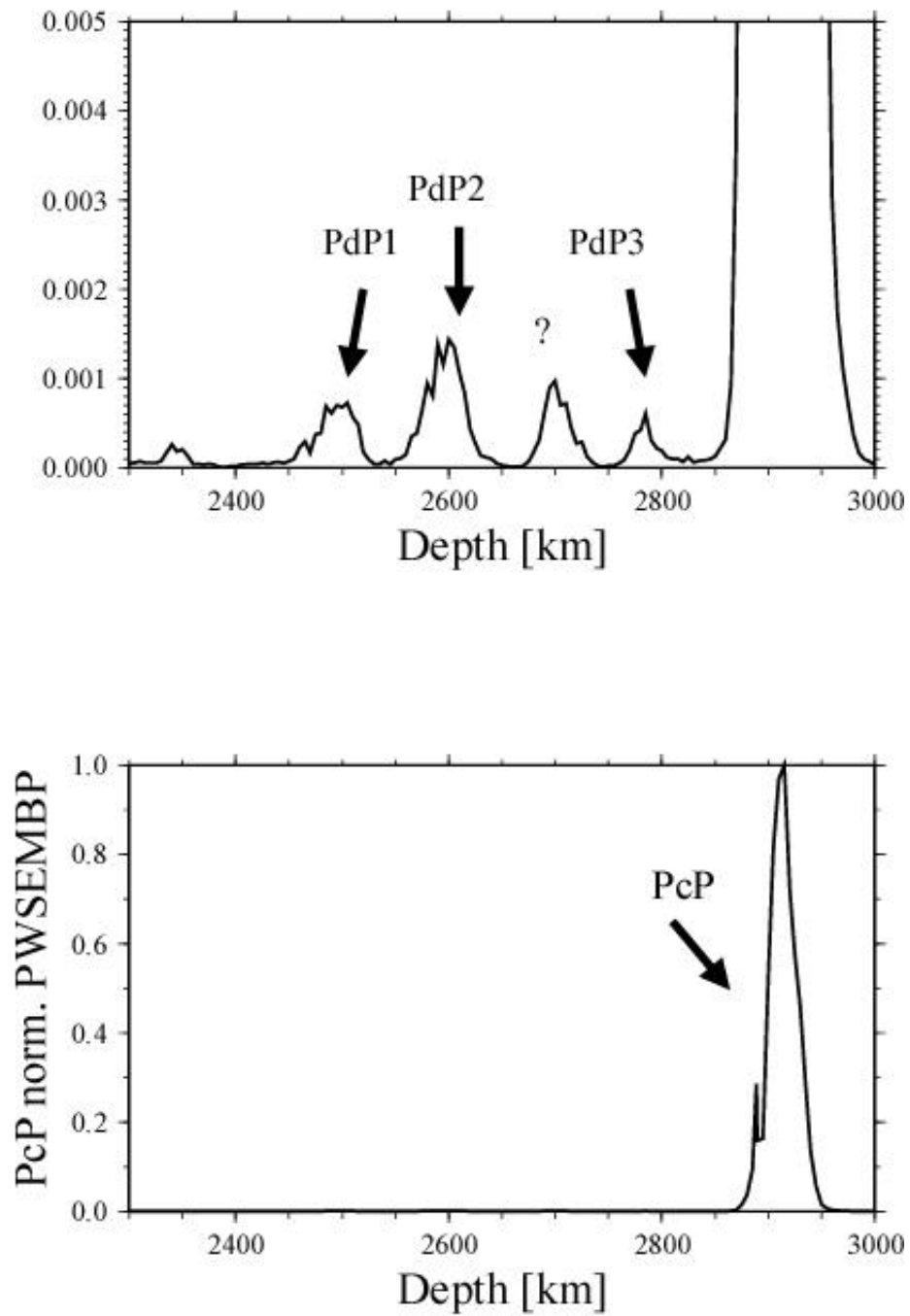


**Figure 9.1b** same as Figure 9.1a, but for the frequency band of 1-2s.

### PWSEMBP (5-10s)

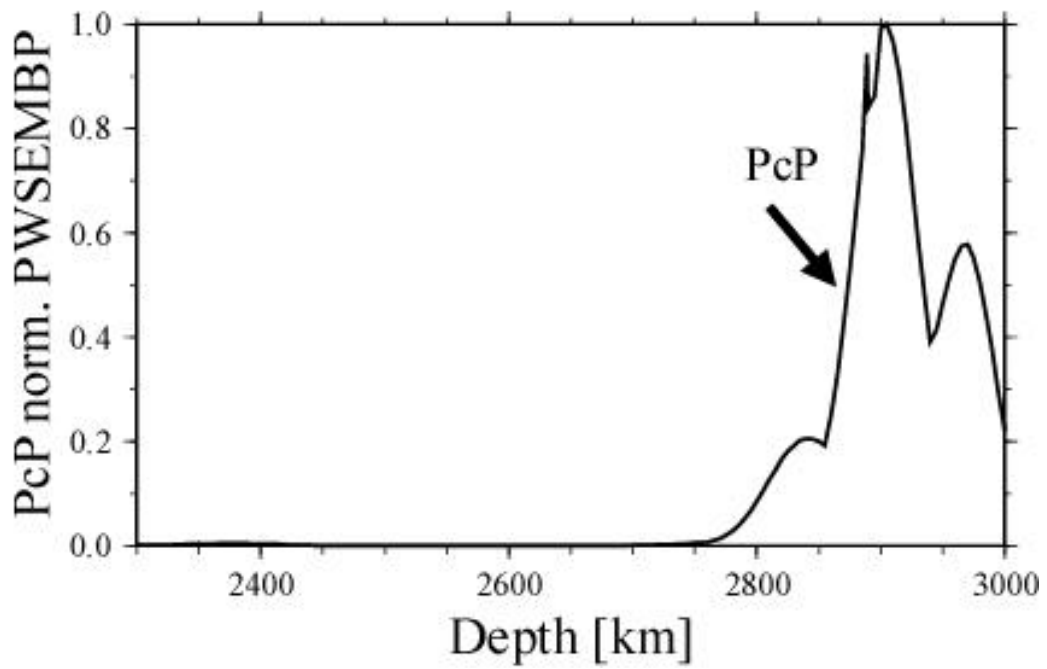
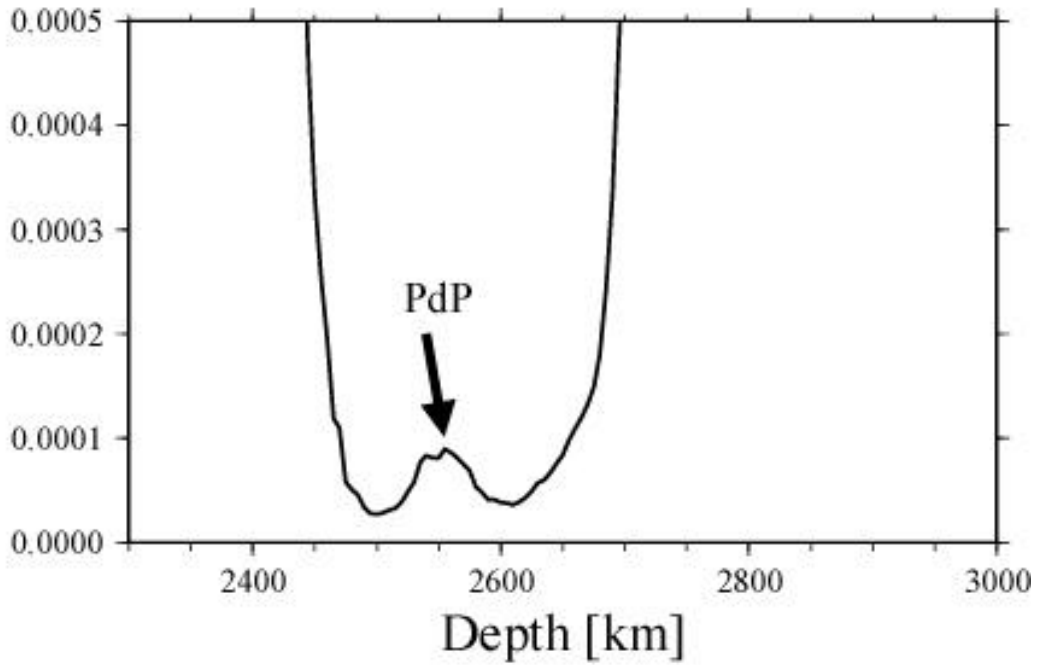


**Figure 9.1c** same as Figure 9.1a, but for the frequency band of 5-10s.



## PWSEMBP (S wave)

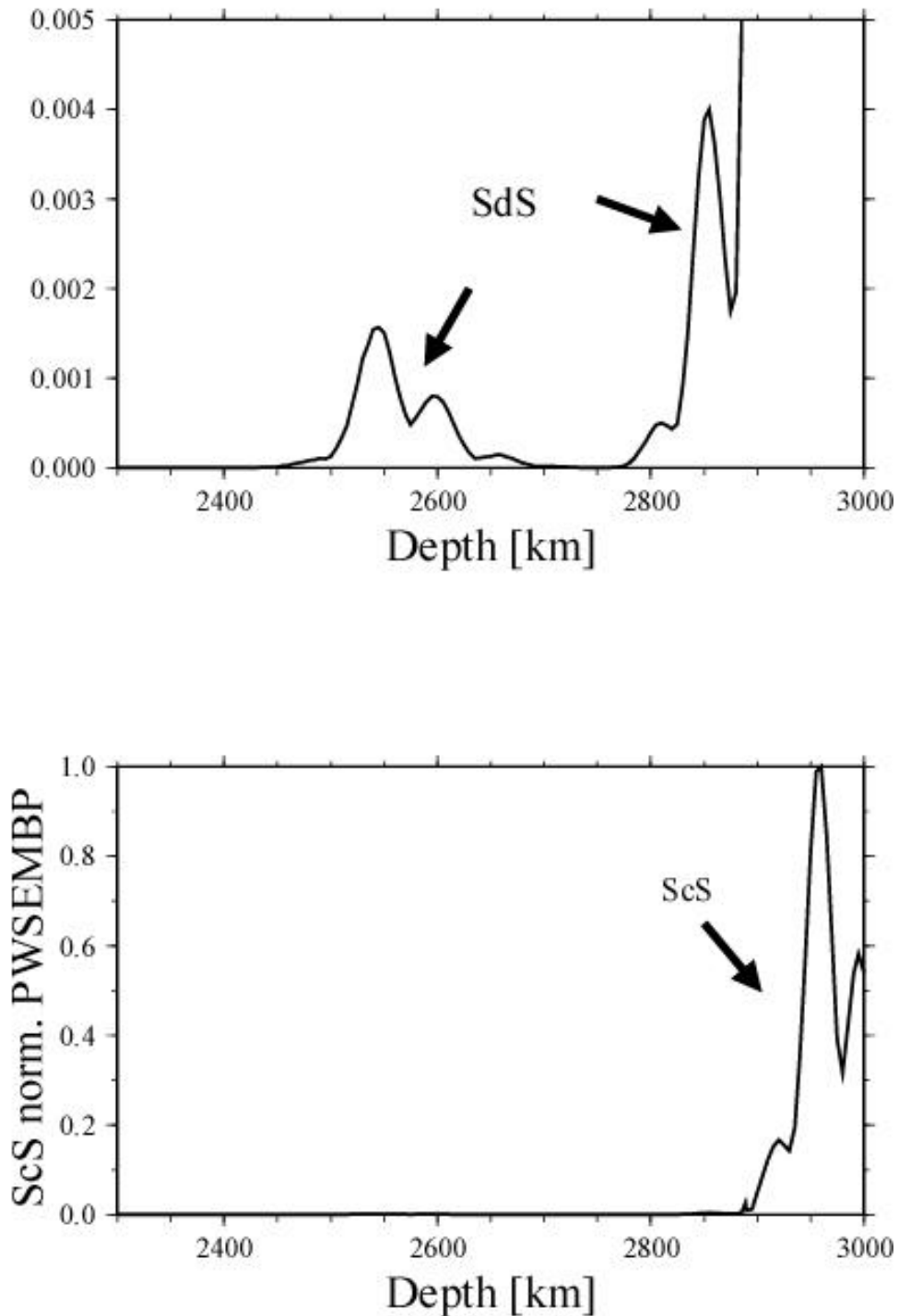


**Figure 9.2** S-wave PWSEMBP from each synthetic discontinuity with Hi-net data by the RWB. The values are normalized by the maximum energy of ScS. The resolution of the S-wave data is lower than that of short period (1-2s or 2-5s) P-wave data. Note that the depths of the discontinuities are almost same as those of P-wave.

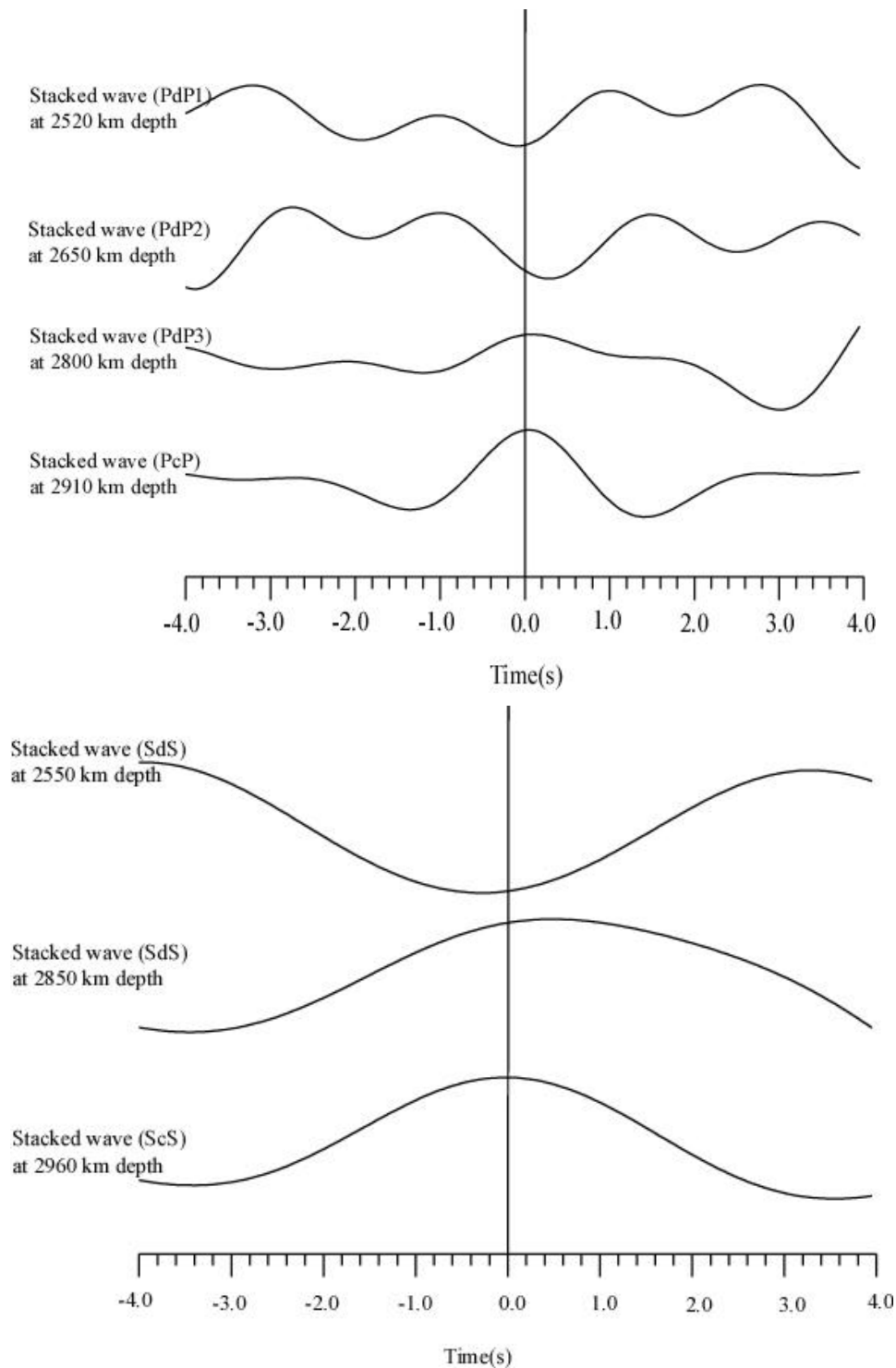


**Figure 9.3** Stacked waveforms at depths of 2520 km (PdP1), 2650km(PdP2), 2800km (PdP3) and 2910km (PcP) are shown in the upper panel and stacked waveforms at depths of 2550km, 2850km (SdS) and 2960km(ScS) are shown in the lower panel. Note that the polarity of the PdP1 and PdP2 phases (negative) is reversed with respect to those of PdP3 and PcP. The polarity of SdS phase at 2550 km is also reversed with respect to those of SdS at 2850 km depth and ScS.

## 9.2 Results from Bootstrap Analysis

Figure 9.4 shows the results of the bootstrap analysis for the observed data. In this case the number of bootstrap samples, which are equivalent to the groups of traces, is 300. The solid lines indicate the mean values for all bootstrap samples for each depth. Standard deviations at each depth are indicated by error bars. Though the lower boundaries of the standard deviation are close to 0, the shape of the original PWSEMBP value curve fits the results of the bootstrap samples, indicating that the original PWSEMBP curve was not produced by noise by chance, but represents the energy of the PdP phases with a reliable value. It is notable that the three peaks corresponding to the PdP1, PdP2 and PdP3 carry over into the result of the bootstrap analysis, which suggests that the PdP phases are not signals generated by random noise.

### Bootstrap Test (PWSEMBP)

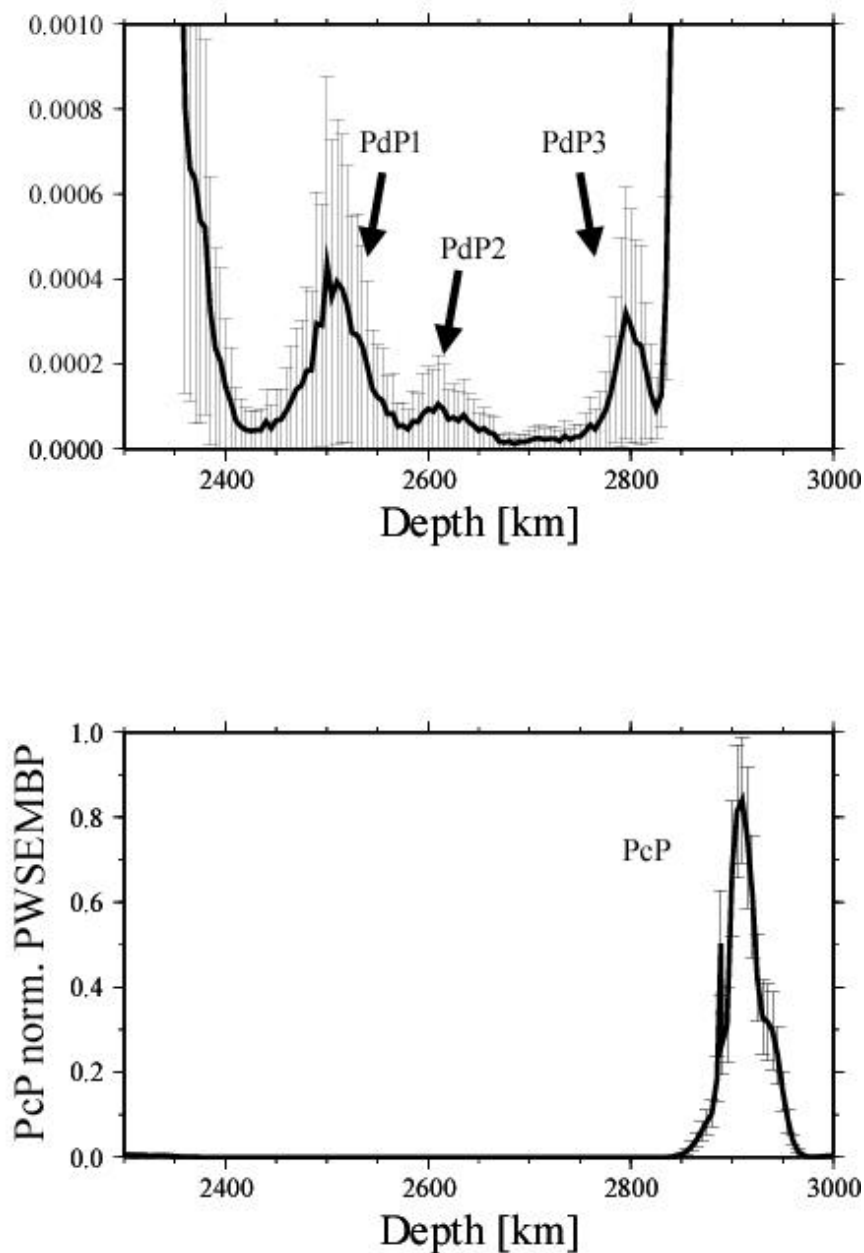


**Figure 9.4** Test of the confidence of the PWSEMBP result by the bootstrap method. The solid line is mean values in each bootstrap samples (for each depth) and standard errors are shown by the error bars. The upper diagram is a magnification of the lower diagram. Although the data in each bootstrap samples were normalized by PcP, the peak of the mean values does not reach 1.0, because the PcP peak (the depth of the CMB) is not always at the same position in each bootstrap sample.

### 9.3 Results from the RWB method (using subarrays)

In order to resolve lateral variations of the heterogeneous structure, the PWSEMBP in each subarray is visualized in a logarithmic color scale. In addition, PWSEM and BP are shown in the same way.

The upper graph indicates the number of the traces in each subarray that were used to calculate the PWSEMBP, PWSEM and BP in Figure 9.6a-c (for P-waves) and Figure 9.8a-c (for S-waves). Owing to the inhomogeneity of the station distribution of J-Array and Hi-net, the number of the traces in each subarray varies, which can slightly influence the resolution of each subarray. Since there is a high station density in the middle part of the whole array, the stack traces used in the subarrays from 9 to 14 are also relatively high in number, and the resolutions are higher than those for the remaining subarrays. Another effect of the variation of the number of the traces in each subarray is the change of the noise level which determines the background level in each subarray. However, this effect is very small with respect to the lateral variation of PWSEMBP or the other coherency measures. The more crucial factor contributing to the change of the background level is the difference among the three measurements. Since PWSEMBP is a multiplication of PWSEM and BP and these two measurements are always smaller than 1, the PWSEMBP takes smaller values than those of PWSEM and BP.

There are a few noticeable patches in the upper right and left part of the panels (e.g. Figure 9.6a and 9.8a). These patches are probably due to P coda (S coda) which has been not removed by the subtraction of the P and S beams and has not been reduced by the taper as well. In the middle part of the panels, the P and S coda are not visible because the codas in these regions have been averaged out by more traces. Another reason for the absence of the P and S coda is the below-average epicentral distances in the middle part of the subarrays, which increases the travel-time difference between P and PdP. Therefore, P coda is not likely to disturb the signals from the lowermost mantle in the middle part of the subarrays. Although it is not so easy to recognize a continuous plane discontinuity in Figure 9.6a-c and 9.8a-c, there seem to be two arched discontinuities at the depth of about 2520 km and about 2650 km. These are better visible in the BP (Figure 9.6c and 9.8c). These intermittent discontinuities are clearly independent of the P-coda energy. Some anomalous regions can be clearly recognized at a depth of around 2650 km in the middle part of the panel. The lateral extent of the anomalous region is about 300 - 500 km in the NE-SW direction. In the northeastern region, energy of the reflected waves seems to be focused at the depth of about 2600 km and then the anomalous region extends to the direction of the southwestern region branching out into two anomalous areas. Since the anomalous regions are rendered in a two-dimensional representation, the three-dimensional shape of the structural anomalies is not revealed. It is, however, obvious that the discontinuities are not one-dimensional simple plane discontinuities but more complicated

intermittent discontinuities, although the discontinuity at the depth of 2650 km seems to be relatively continuous. The polarities of the reflected waves from the discontinuities are shown in Figure 9.10a-c. These beams are obtained by stacking with respect to each depth where the corresponding PWSEMBP take maximum values around 2650 km and around 2800 km depth in each subarray. While the first 4 subarrays show a positive polarity, the beams in the other subarrays show negative ones. The depth where the polarity is reversed is just the depth where the corresponding PWSEMBP maximum values change suddenly. The anomalous regions where more seismic energy is reflected or scattered are independent of the number of traces used in each subarray. It is not possible to attribute these patches to a result of the below-average number of traces in the northern part of the array, which can cause a lower resolution, because such an effect can not be recognized in the synthetic data except for the CMB region area and the shallow depth range where coda has some influence (see Figure 8.4a-8.4c for P-wave and Figure 8.6a-8.6c for S-wave).

The relatively continuous anomalous region at about 2800 km depth can not be seen everywhere at the depth of about 2800 km. There are no such patches in the synthetic data, in which the PcP waveforms are very similar to those of PcP waveforms in the observed data (see Figure 8.3, Figure 8.4a-c and Figure 9.6a-c). This means that energy of sidelobes or an aliasing effect of PcP in the observed data is unlikely to contribute to the '2800 km depth anomalies'.

One of the plausible causes for these anomalies might be structure such as an ultralow velocity zone (ULVZ). Many seismological studies (Garnero et al., 1993, Mori and Helmberger, 1995, Garnero and Helmberger, 1995, 1996, Garnero et al., 1998, Revenaugh and Meyer, 1997, Vidale and Hedlin, 1998, Helmberger et al., 2000) suggest that there are ULVZs beneath the central Pacific which is located in the eastern part of this study area. Although it might be possible to consider these anomalous structures to be a part of ULVZ which are widely existent in the central Pacific region, there are a few features about this anomaly not corresponding to those of 'normal ULVZ'. One of the different features of the here-obtained anomaly is that the polarity of the reflected wave from this anomaly is same as that of PcP which has positive polarity (see Figure 9.3, 9.10a-c). This may indicate that this anomaly has a positive velocity jump and is not a 'ULVZ'. One thing to take into consideration is the fact that a reflected wave with positive polarity might be produced by a negative velocity jump, if the increase of the density is high enough to produce positive polarity (for instance the CMB). This seems to be unlikely to happen in the D'' layer from quantitative considerations. A synthetic test shows that a pure density increase only can not produce the same amplitude of the reflected waves without introducing any velocity contrast. For example, even a 20 % positive jump in density can produce only 1% energy of reflected wave. According to the recent studies on ULVZ, the velocity reduction is up to 30 % in the S-wave and up to 10 % in the P-wave. If these anomalous structures have such velocity jumps up to 10 %, the observed PdP amplitude from this anomaly is too small. If one takes these features of this anomaly into consideration, this anomaly may be of a

chemical origin such as a chemical mixture between perovskite in the lowermost mantle and liquid iron in the outer core rather than partial melt. From a geodynamical viewpoint, it would be possible to consider this anomaly to be a segment of root of the super hot plume beneath the southwestern Pacific where hot plume is rising.

In the PWSEMBP, the reflected energy from the CMB is clearly seen at a depth of around 2900 km. One of the factors which shift the average depth of the CMB in this study area is the low velocity zone in the lowermost mantle. Another possible factor could be high velocity zones in the middle mantle that only affect P-waves. Such structures would advance the arrival time of the P-waves, leading to increased travel time differences between P and PcP. However, according to tomographic studies (e.g. Inoue et al., 1990, Fukao, 1993, M. Wysession, 1996, R.D. van der Hilst et al., 1997, Boschi et al., 1999, Valenzuela et al., 2000, Karason and R.D. van der Hilst, 2001) there is no evidence for a high-velocity zone in the mid mantle beneath the southwestern Pacific. Therefore, the low-velocity zone in the lowermost mantle is very likely the cause of the general apparent depression of the CMB.

It is recognizable that the depth of the CMB varies within  $\pm 10$  km; however, this undulation of the CMB can also be due to heterogeneities in the upper mantle beneath Japan, where the effects on the travel time of P and PcP are somewhat different. Another possible cause for the apparent undulation of the CMB is perturbation of velocity in the D'' layer. Figure 9.5 shows the PcP (ScS) beams for each subarray. The travel time residuals with respect to IASP91 fluctuate from subarray to subarray, which also corresponds to apparent depth of the CMB. Figure 9.7 shows the PcP travel time delay with respect to IASP91 and PcP/P amplitude ratios which are also plotted in Figure 9.6a, 9.6b and 9.6c. The correlation of these two parameters is rather good. This could be also explained by undulation of the CMB. If there is an undulation of the CMB whose wavelength is exceeding about 100 km, focusing and defocusing can happen, which can change the PcP amplitude (Kampfmann and Müller, 1989). If the PcP travel time delay represents the undulation of the CMB, the fluctuation of the PcP/P amplitude ratios and the variation of the PcP travel time delay can have a common cause.

As regards the S-wave, the results are slightly different from those of the P-wave. One of the noteworthy features is that a general depression of the CMB is observed except for the northwestern part of the study area. The reason for that the depth of the CMB beneath the northwestern part of the study area is different from the CMB depth in the other area can be due to S-wave perturbations in the upper mantle beneath Japan. On the whole, the results of S-waves are of lower quality due to the relatively small number of traces, long-period data and low signal to noise ratio in comparison with the P-waves data. It is, however, noticeable that there seem to be anomalous regions at the depth of around 2600 km in the middle part of the panels (see Figure 9.8a, 9.8b and 9.8c). The polarity of the reflected phases from the anomalous regions at the depth of about 2550 km is negative, while the

polarity of anomalous phases reflected at a depth of about 2850 km is positive. This is consistent with the polarity of the P-wave reflected waves at the corresponding depths. There is a 50 km difference between the 2800 km discontinuity of P-wave and that of S-wave. This suggests that the velocity reduction between the top of the D'' layer and the 2800 km discontinuity is stronger in the case of S-wave. The results of the RWB using subarrays are also shown in modified plots in Appendix 2.

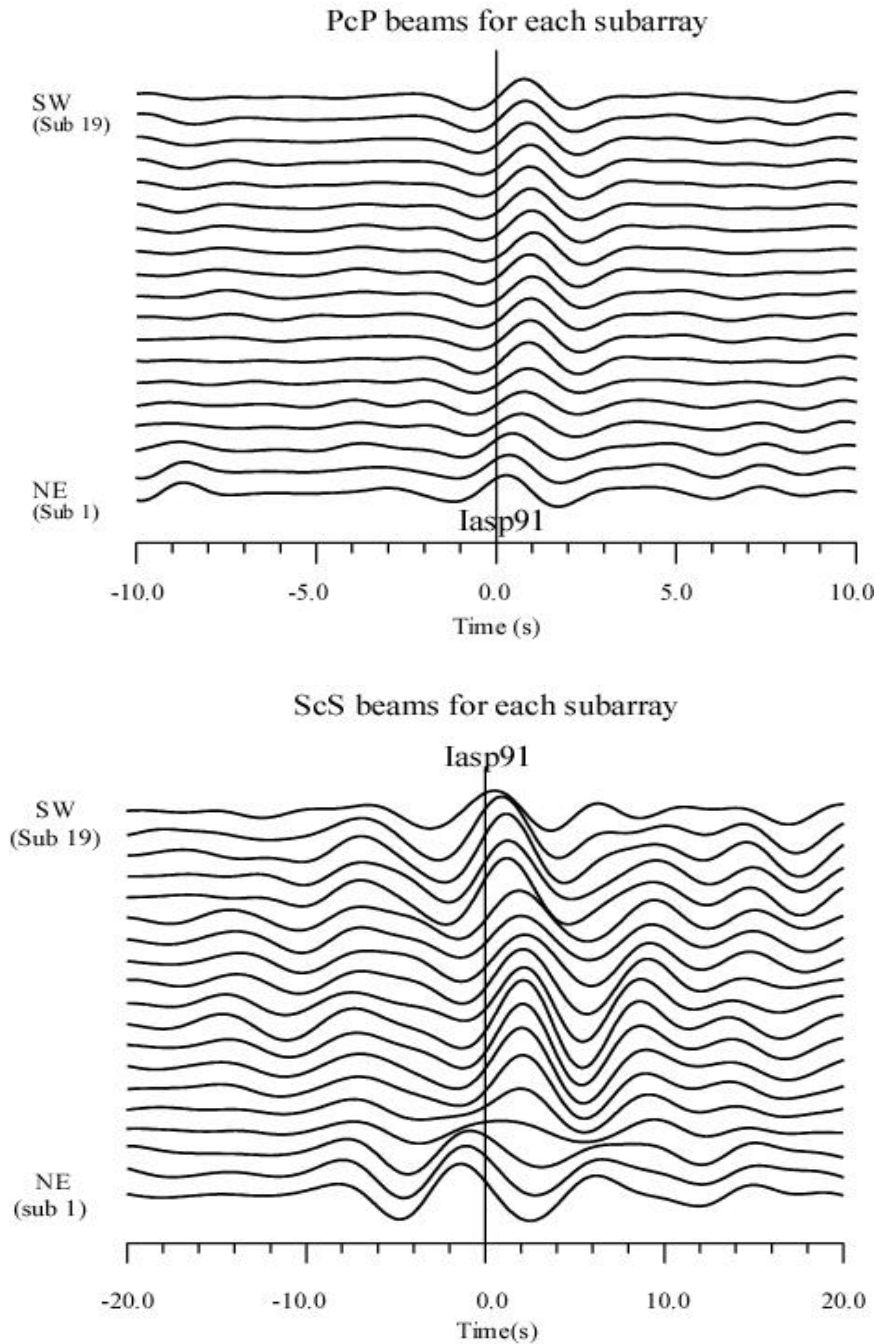


**Figure 9.5** PcP and ScS beams for each subarray using all events. Note that the delays of the PcP and ScS onset time fluctuate from subarray to subarray.



## P wave (PWSEMBP, 2-5s)

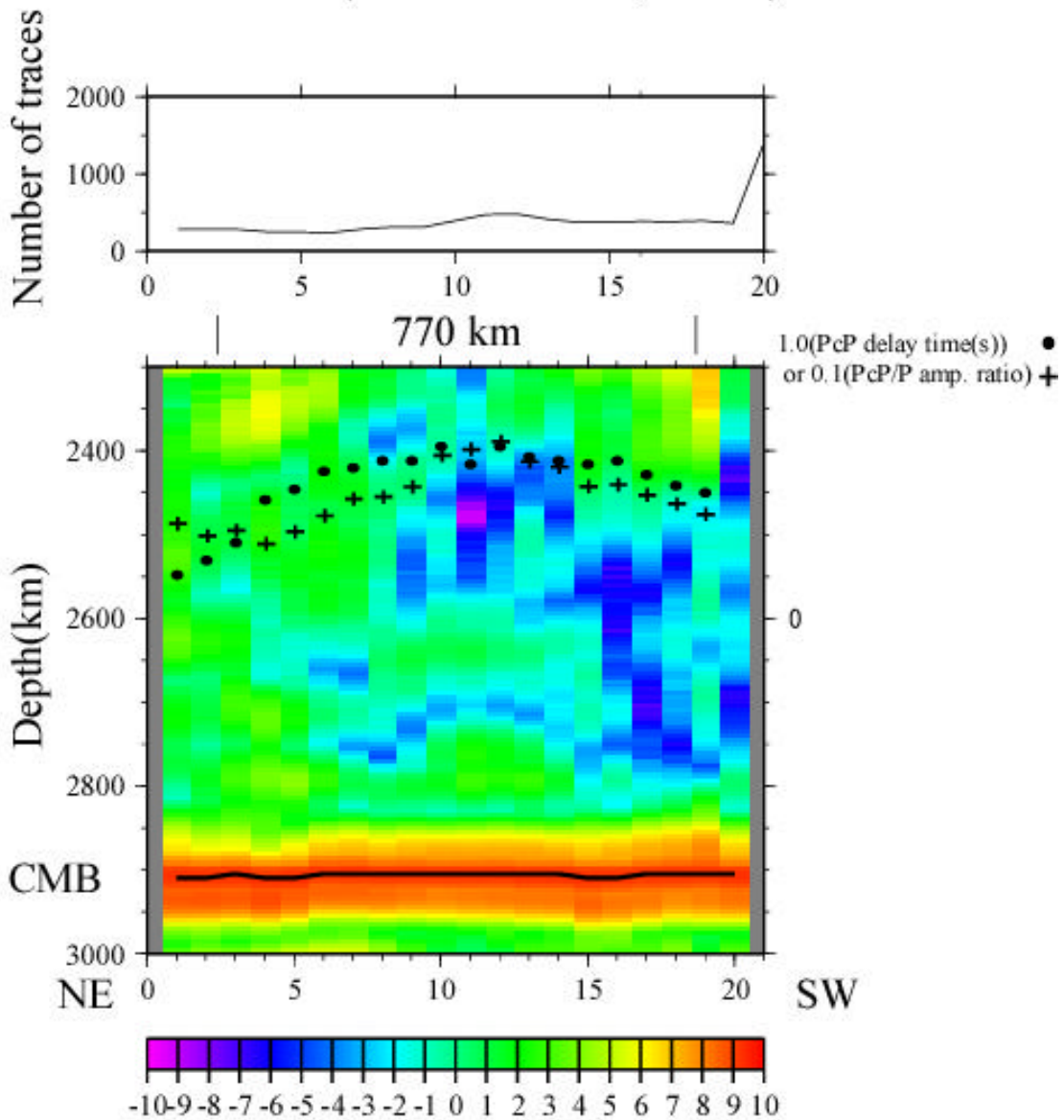


**Figure 9.6a**

**Figure 9.6a-c.** Various coherency measures, PWSEMBP (figure 9.6a), PWSEM (figure 9.6b) and BP (figure 9.6c) values are shown in the vertical cross section in the RWB method. The horizontal axis indicates the subarrays and the vertical axis indicates the depth. The left side of the panel corresponds to northeastern part of the study area and the right side of the panel corresponds to southwestern part of the study area. The horizontal scale of the mapped area is about 770 km at the CMB. In the upper diagram the number of the traces which were used to calculate the coherency measures are shown in each subarray. The solid line around the CMB indicates the maximum peak for each subarray, which is usually considered to indicate the CMB depth. The coherency measures are plotted in a logarithmic scale. In the upper part of the panel, PcP travel time delays with respect to IASP91 and PcP/P amplitude ratios are plotted by solid circle and cross, respectively. These two parameters correlate quite well.

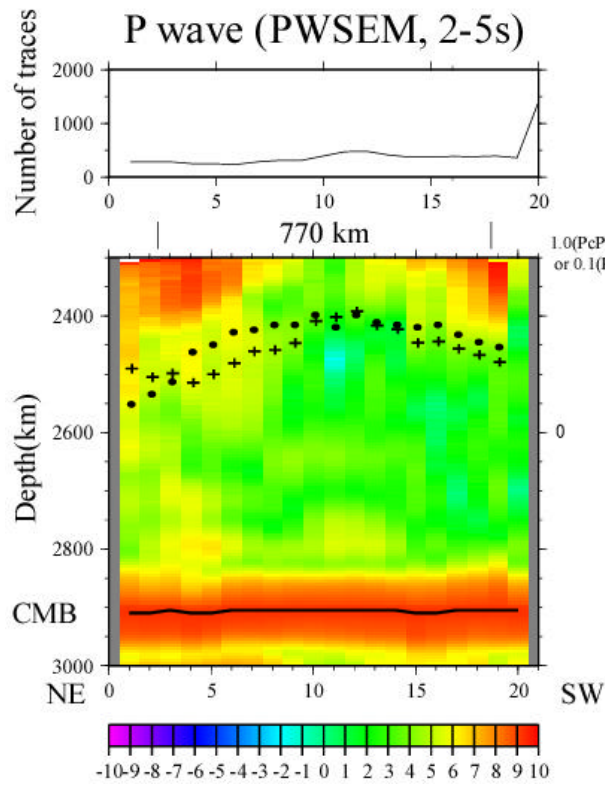


Figure 9.6b

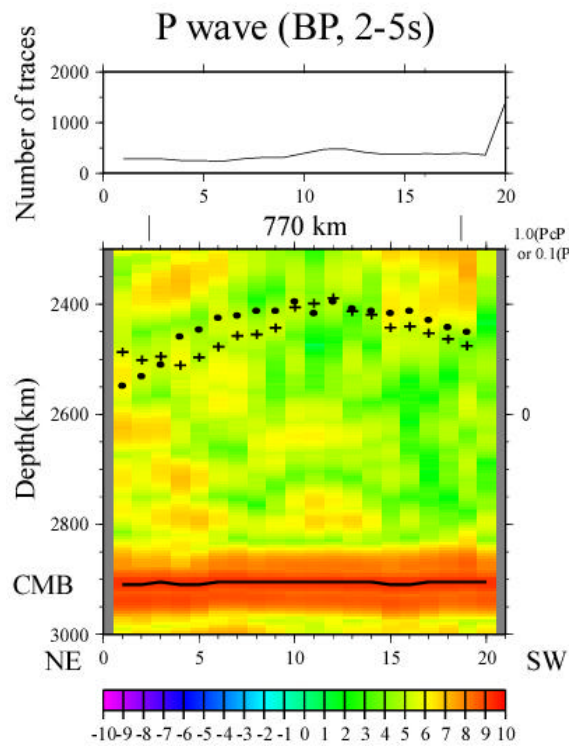
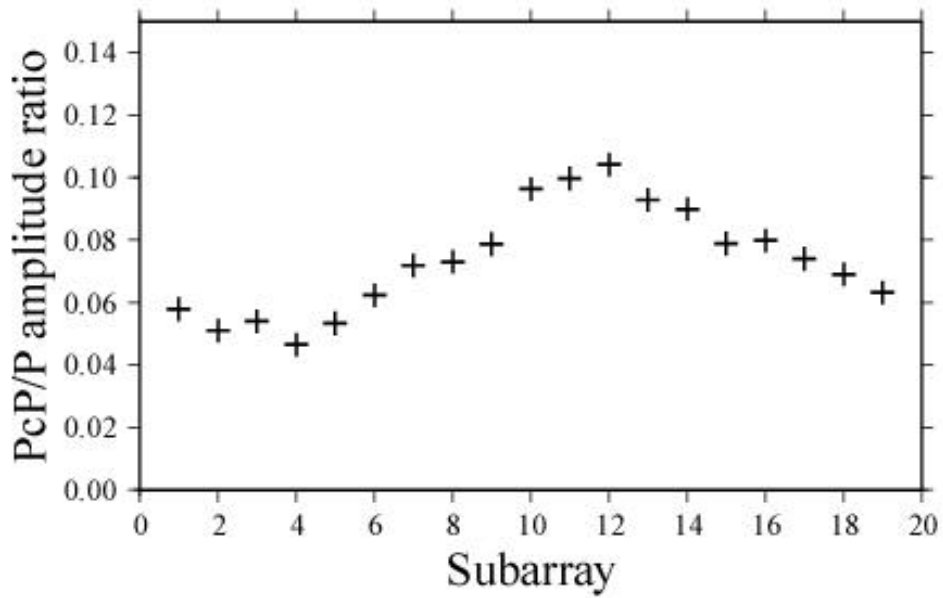
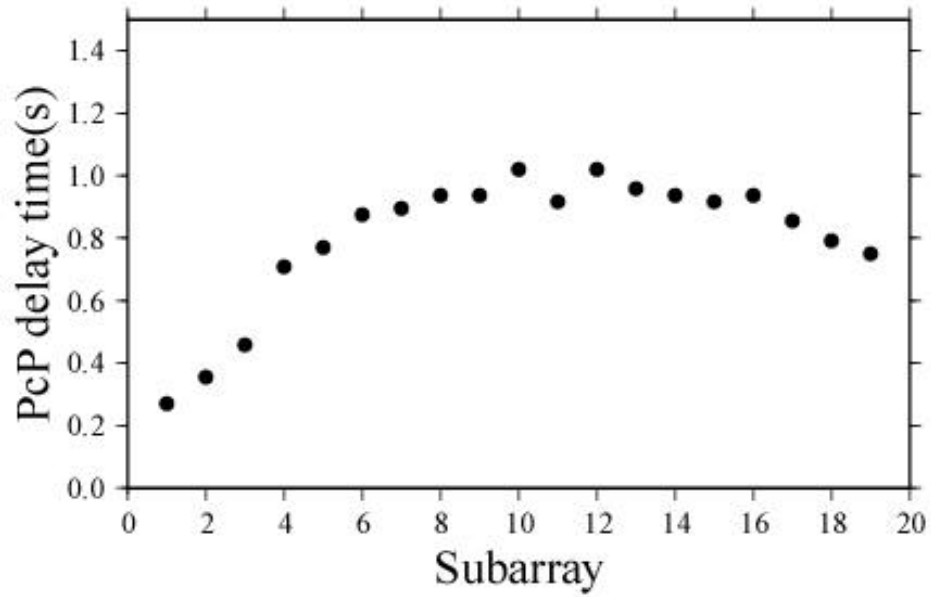


Figure 9.6c



**Figure 9.7** The travel time delay of PcP with respect to IASP91 for each subarray and PcP/P amplitude ratios for each subarray, which are plotted in Figure 9.6a, 9.6b and 9.6c. The arrival time delay of PcP correlates with the PcP/P amplitude ratios.

# S wave (PWSEMBP)

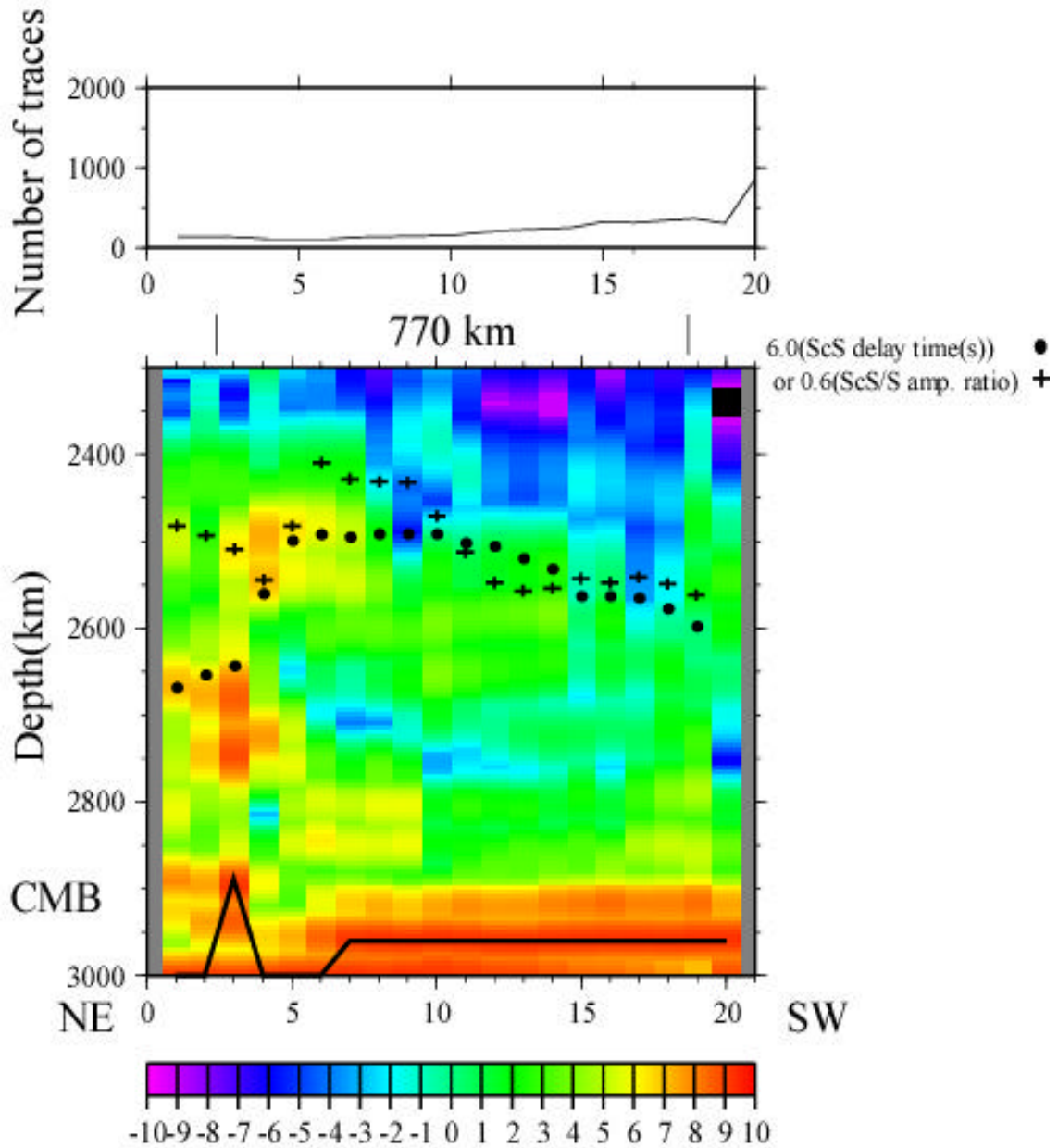
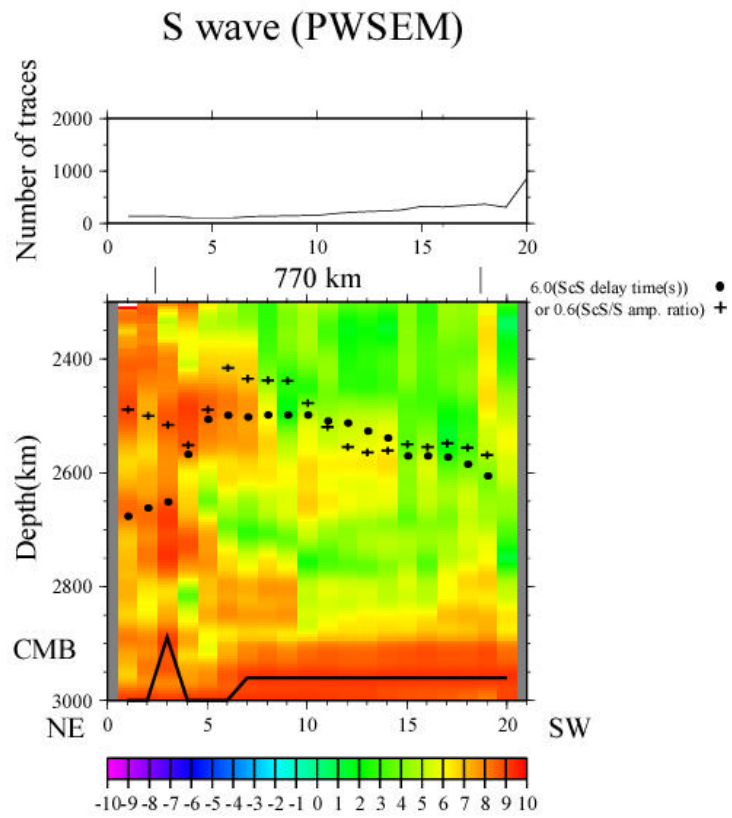
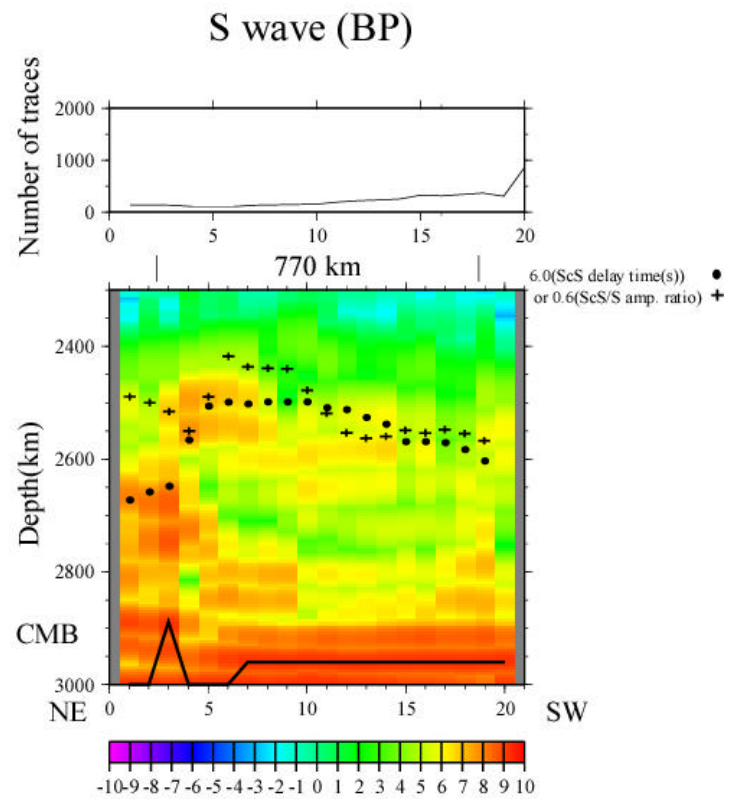


Figure 9.8a

Figure 9.8a-c, same as Figure 9.6, but for S-wave.



**Figure 9.8b**



**Figure 9.8c**

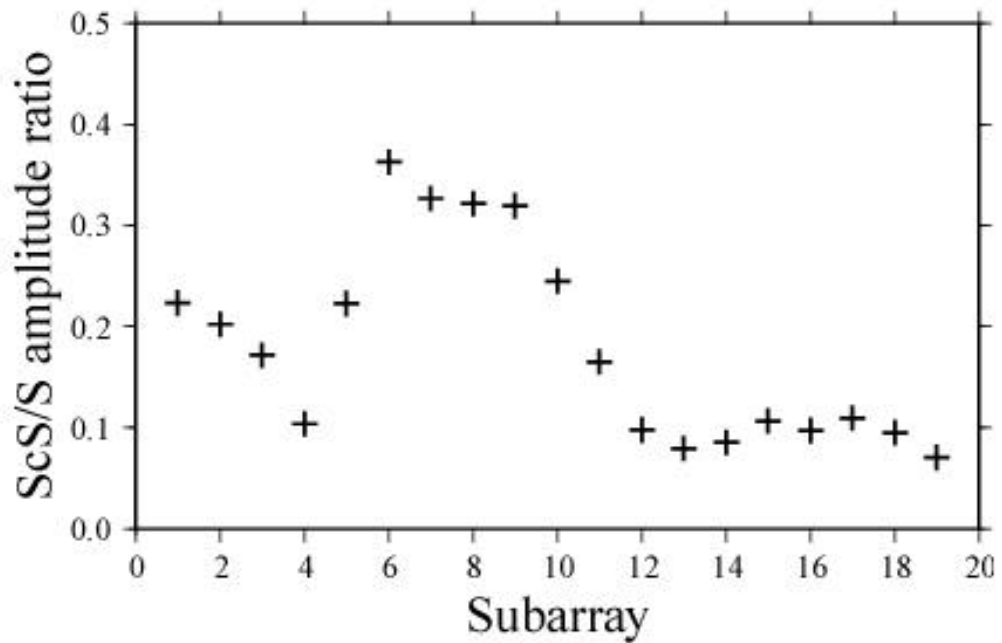
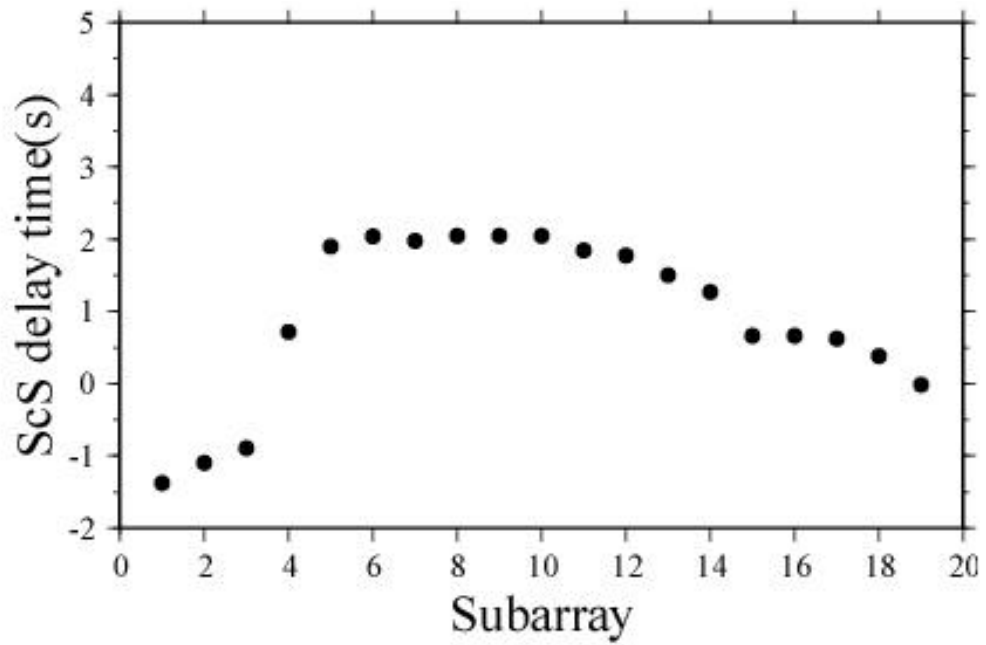


**Figure 9.9** The travel time delay of ScS with respect to IASP91 for each subarray and ScS/S amplitude ratios for each subarray, which are plotted in Figure 9.8a, 9.8b and 9.8c. The arrival time delay of ScS roughly correlates with the ScS/S amplitude ratios.

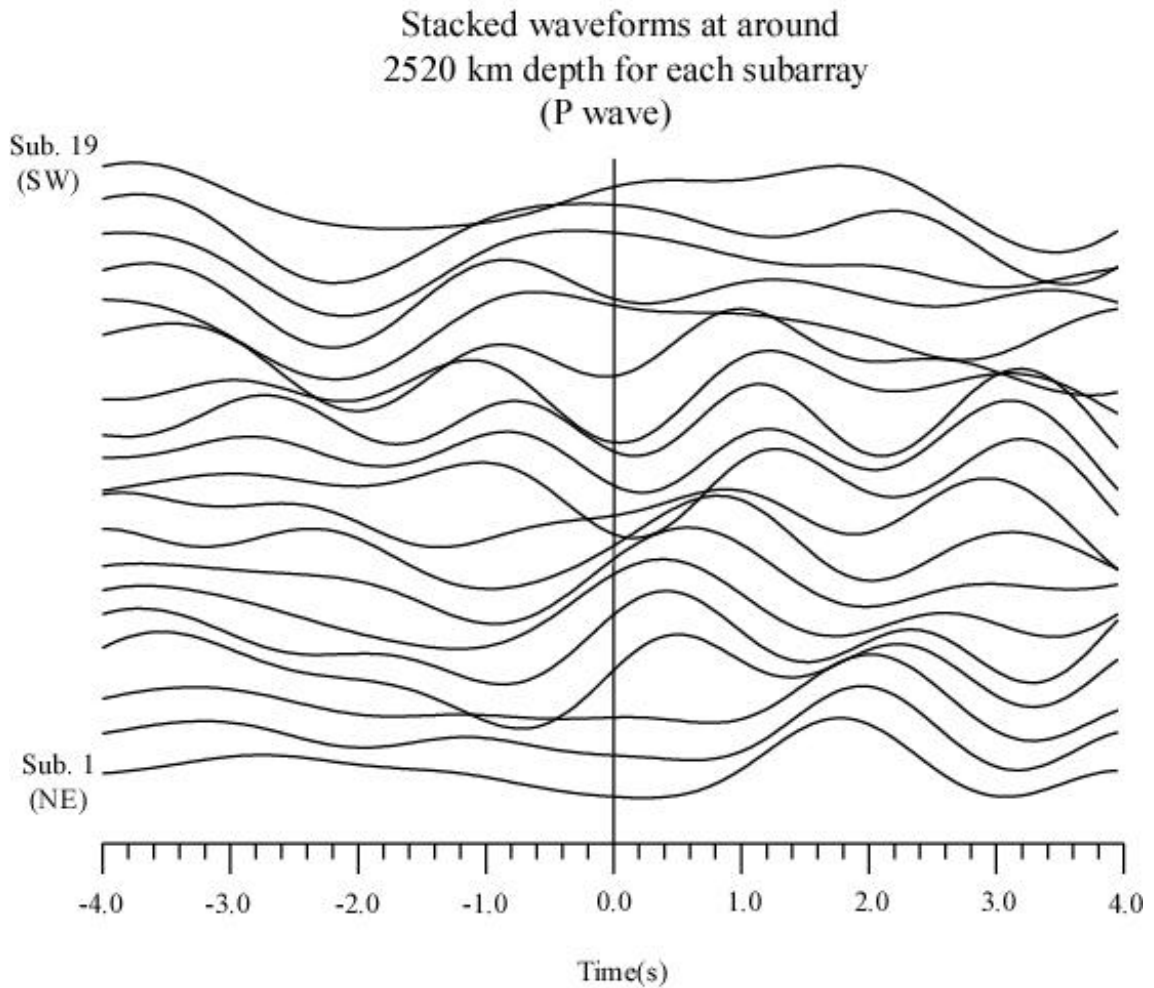


**Figure 9.10a**

**Figure 9.10a-c** Beams for each subarray at 2520 km, 2650 km and 2800 km depths for P-wave in the frequency band of 2-5s. Time = 0.0 is the theoretical travel time for the reflected wave at the corresponding depths.

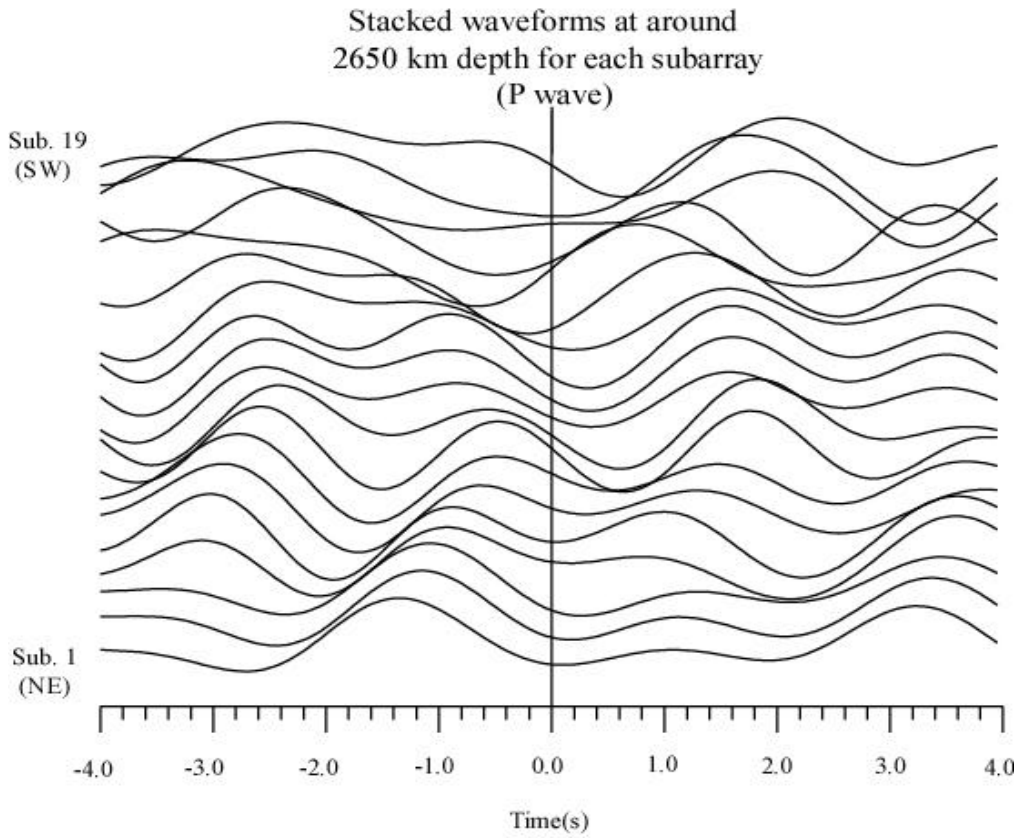


**Figure 9.10b**

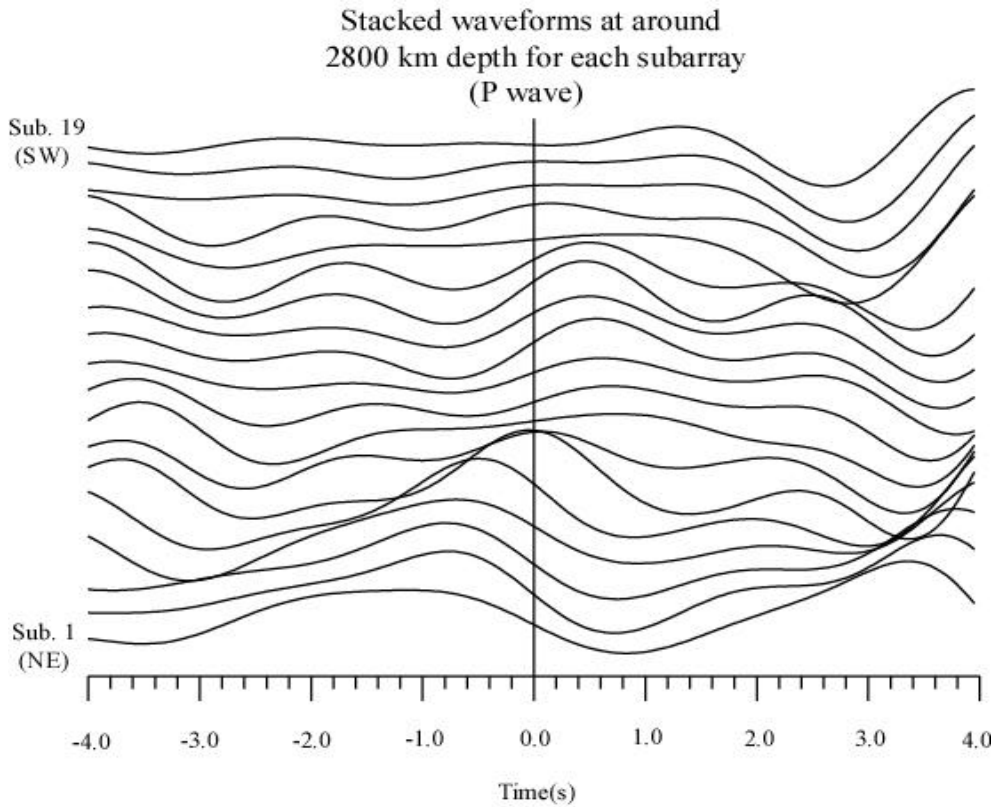


**Figure 9.10c**



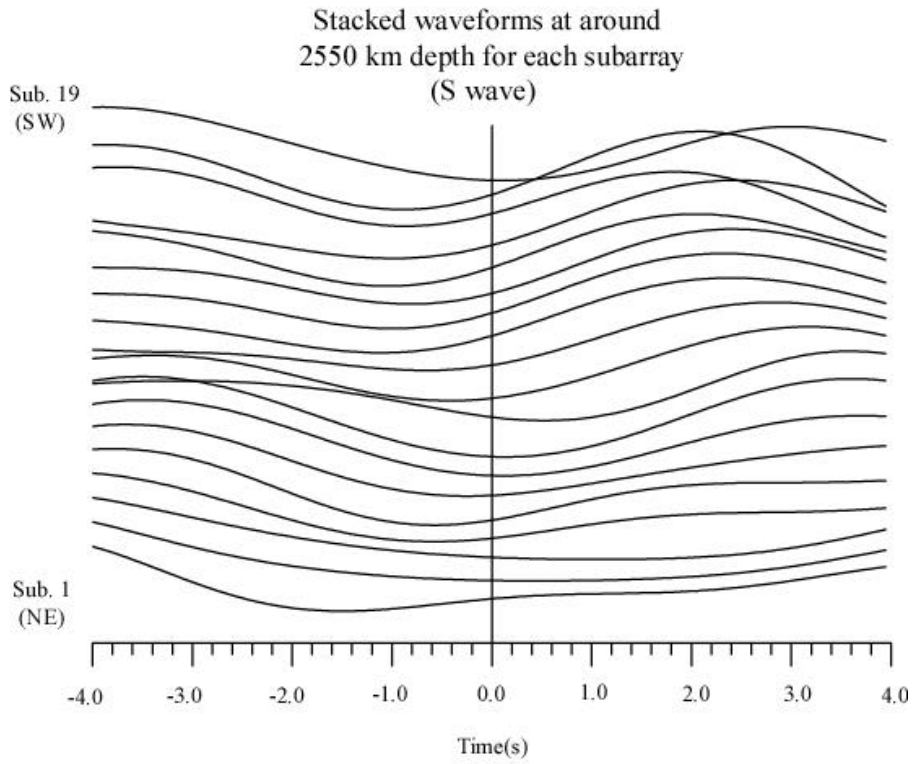


**Figure 9.11a**

**Figure 9.11a-b**

Beams for each subarray at 2550 km and 2850 km depths for S-wave in the frequency band of 5-10s. Time = 0.0 is the theoretical travel time for the reflected wave at the corresponding depths.

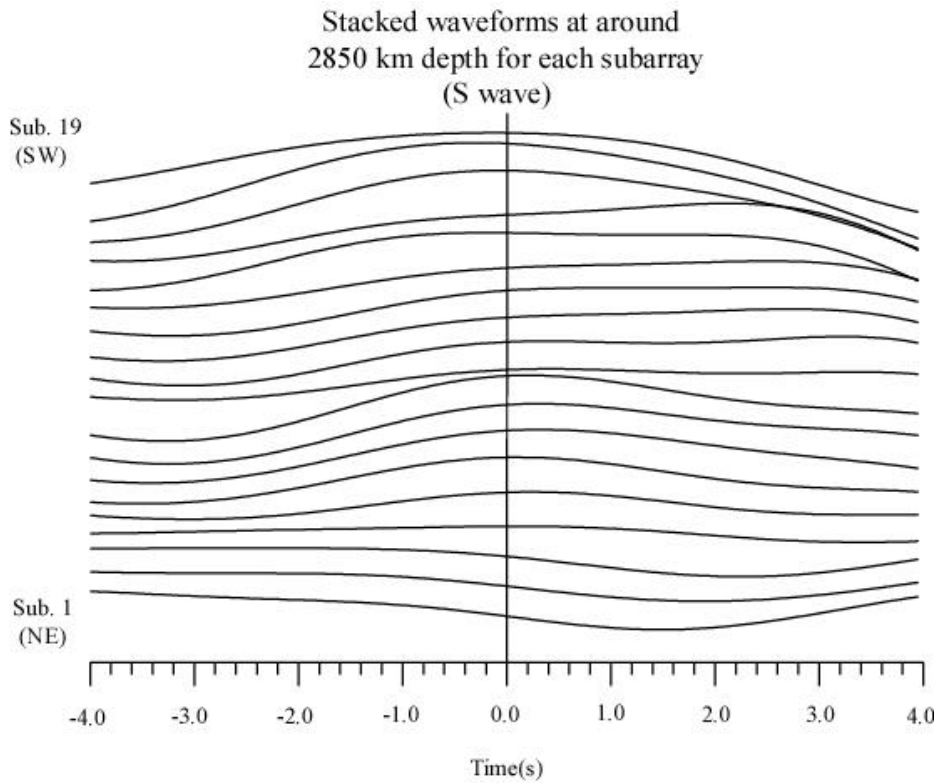


**Figure 9.11b**

#### **9.4 Results from the Migration**

At first sight, the migration method seems to yield no clear findings of scattering objects in Figure 9.12a, 9.12b and 9.12c (for P-wave) and Figure 9.13a, 9.13b and 9.13c (for S-wave). However, there might be some candidates for scattering objects in the depth range of about 2550 km and about 2650 km within the PcP aliasing ring. These candidates for scattering objects are relatively well visible in the BP image (Figure 9.12c). As synthetic data show, there is little energy within the PcP aliasing ring, although there is relatively high noise outside of the PcP aliasing ring. Therefore it would be possible to regard the weak energy patches within the PcP aliasing ring in the observed data as scattering objects or reflectors. However, for the rest of the region, it is difficult to assert which patches are indeed scattering objects, because they are not clearly distinguishable from the aliasing effect of PcP.

Since the energy of scattered waves is estimated under the assumption that the scattering objects act as isotropic point scatterer, the migration method is not optimal in imaging two or three-dimensional plain structures. It is hard to imagine that small volumes (less than several km) can produce point scattering observable at the Earth's surface. A more realistic scenario is that the P-waves are scattered at a surface of scattering volumes which might exhibit undulation. One possible reason for the rather small energy of scattered waves could be that the stacking in the migration method may not be a suitable representation of the actual structure of the D'' layer in this region. The two negative discontinuities detected by the RWB method may correspond to the anomalous region as scattering objects at the corresponding depth in the migration. Though scattered waves were produced by the discontinuities, it would be hard to detect the scattered waves, if they are not scattered forward. Since all stations are used in the migration, the scattered waves are not amplified efficiently, if the scattering is not isotropic.

The theoretical travel times of the scattered waves are never completely correct for PcP phases because the scattered waves do not satisfy the Snell's law. Nevertheless, PcP phases are clearly seen at the CMB just due to their large amplitude. The PcP focusing depth (at the depth of the CMB) exceeds the theoretical depth of 2889 km (IASP91) by 10 km - 15 km because of the low-velocity zone in the lowermost mantle. However, the location of the candidates of scattering volumes should be determined correctly by IASP91 since they are much less affected by the low velocity zone, if at all.

In the case of S-wave, it is not so easy to confirm anomalous regions corresponding to any scattering objects or discontinuities because of relatively low signal to noise ratio.

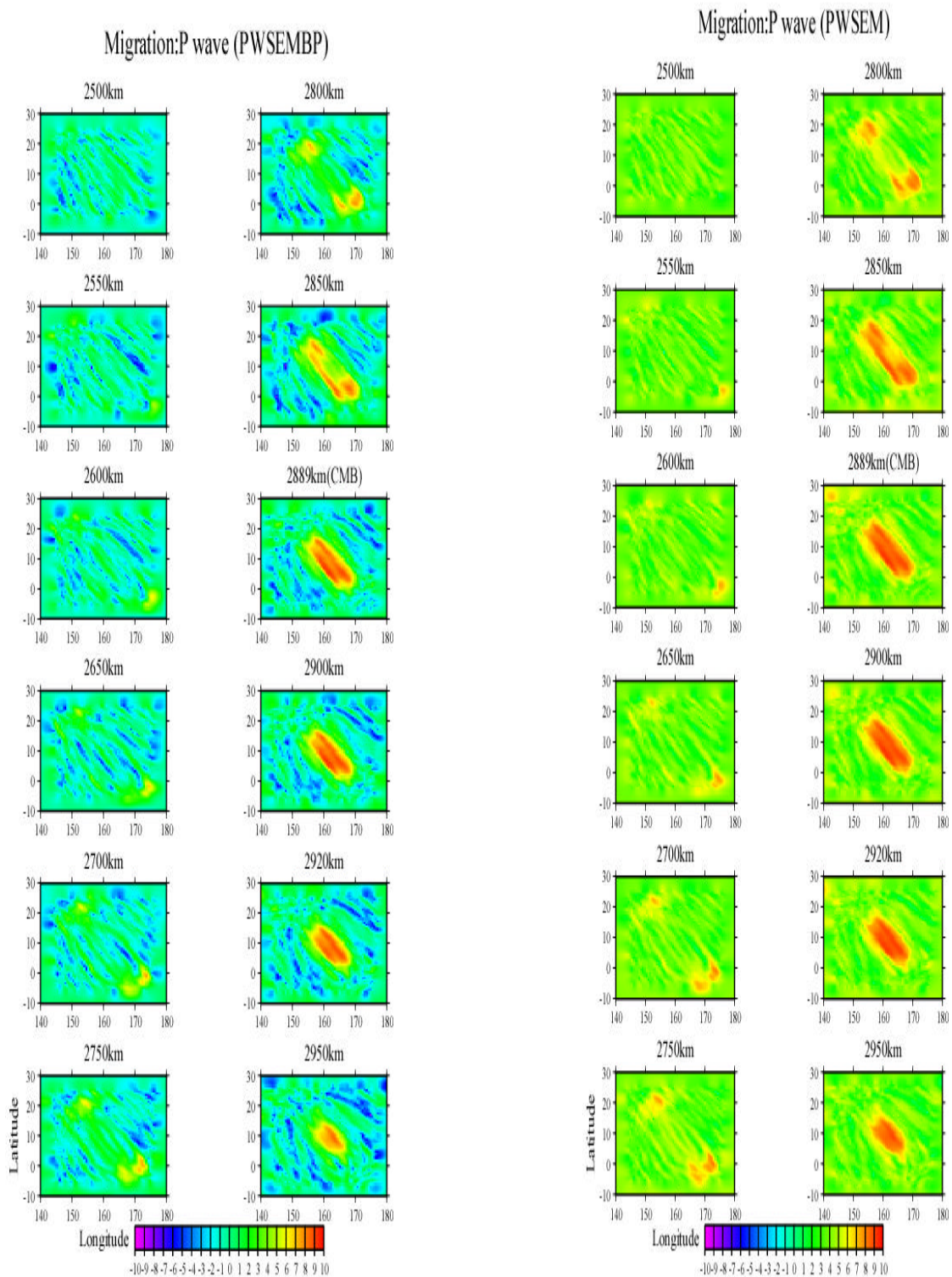


**Figure 9.12a**

**Figure 9.12b**

**Figure 9.12a-c** Double Array Migration indicated by PWSEMBP (logarithmic scale) (Figure 9.12a), PWSEM (Figure 9.12b) and BP (Figure 9.12c) for Pwaves. Each panel shows a horizontal cross section for each depth in the depth range from 2500 km to 2950 km. The strong energy of PcP is recognizable and there might be some candidates for scattering objects for P-wave in the center of panel (within the “PcP aliasing ring”) in the depth of about 2650 km, though these are very weak signals.

### Migration:P wave (BP)

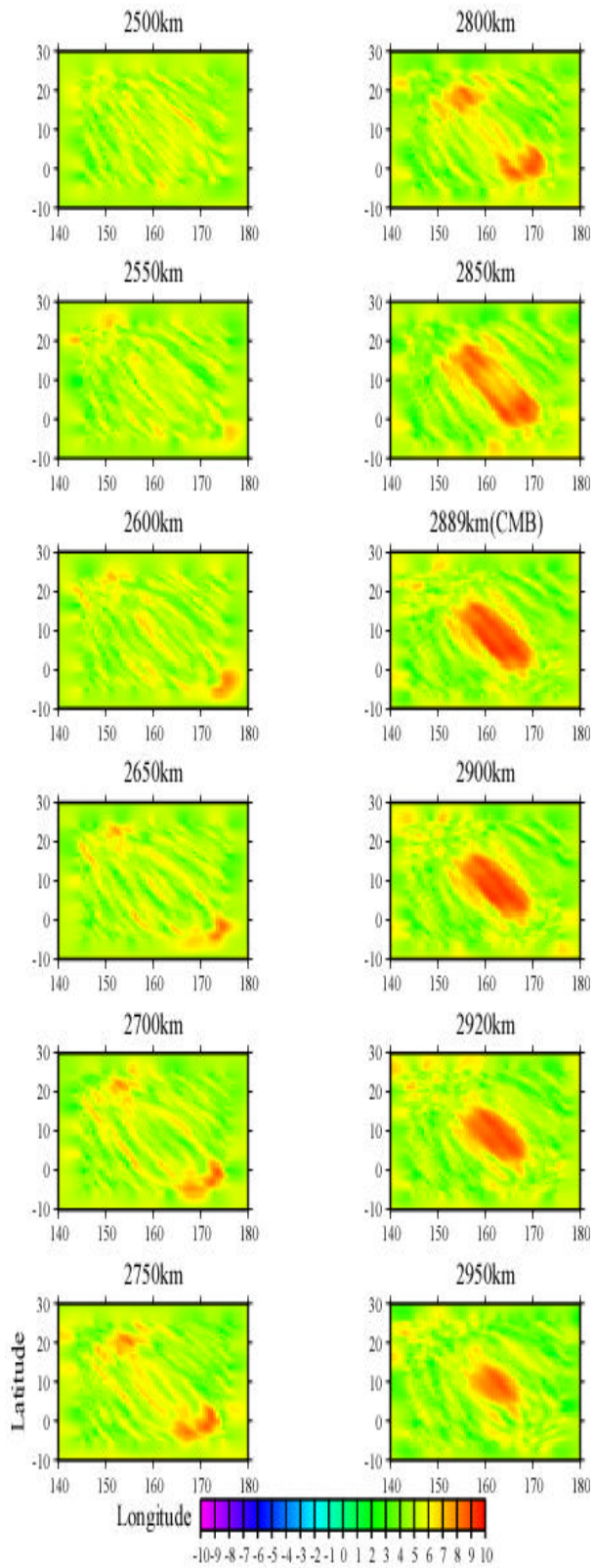


**Figure 9.12c**

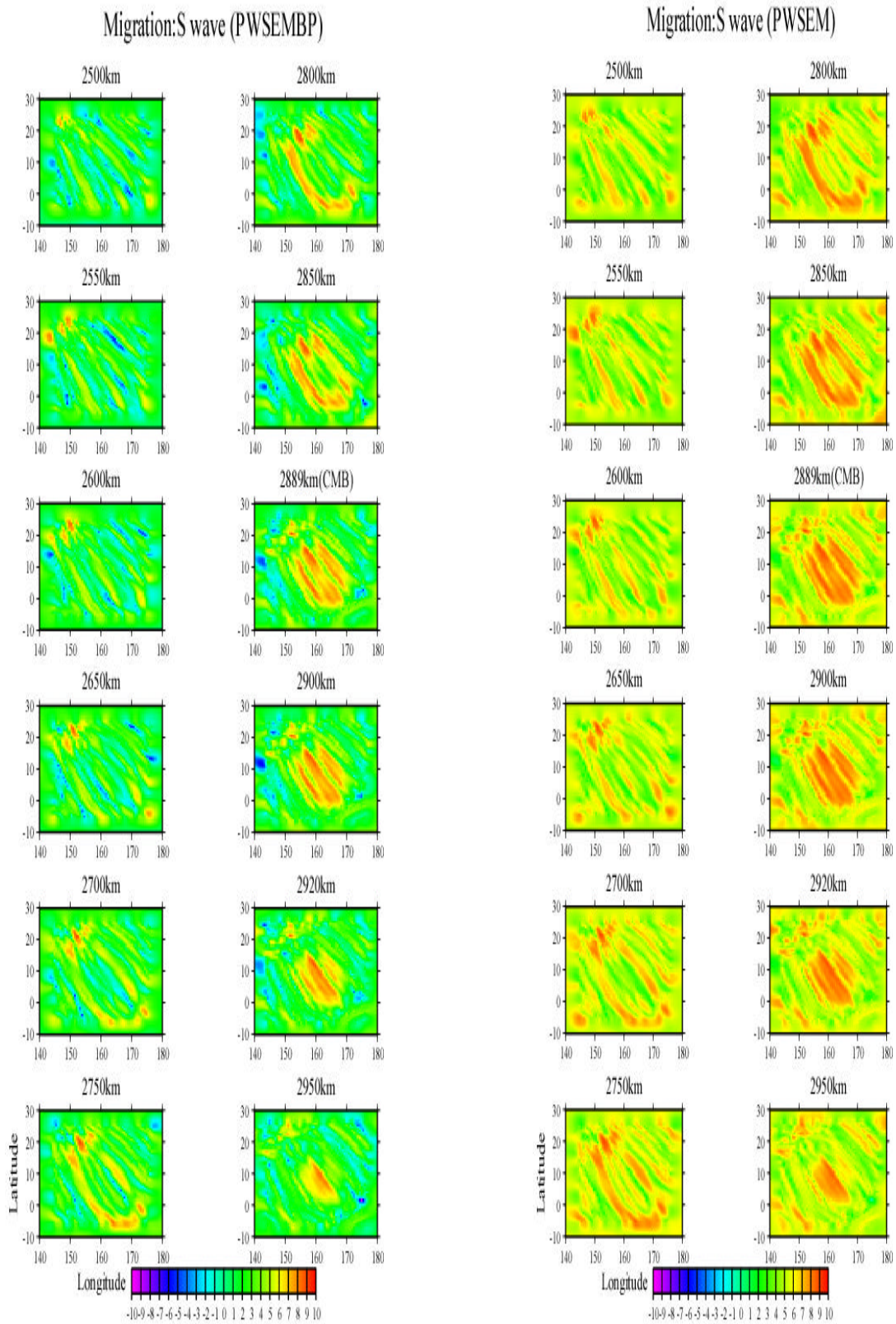


**Figure 9.13a**

**Figure 9.13a-c** same as Figure 9.12a-c, but for S-wave.

### Migration:S wave (BP)

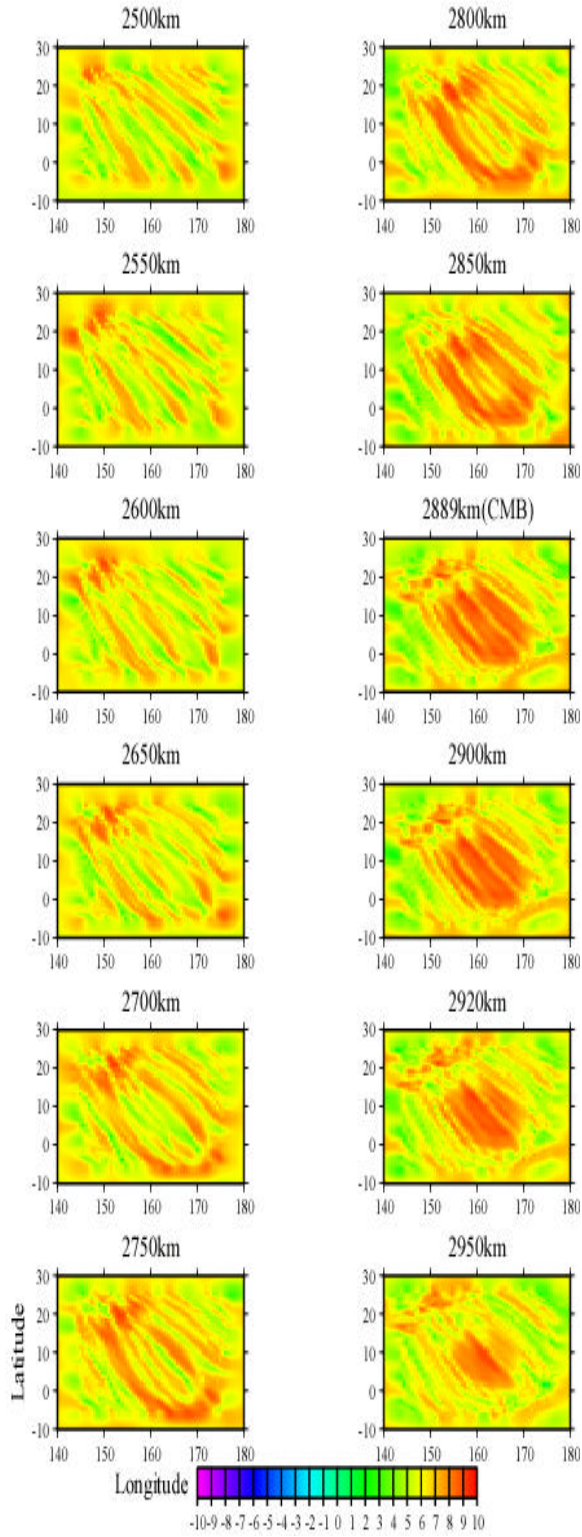


Figure 9.13c

## 9.5 Comparison of Observational Data and Synthetic Data

In order to estimate the velocity perturbation in the low velocity zone with respect to the average speed, it was assumed that the top of the low-velocity zone is at 2520 km where the first PdP phase was detected. If a perturbation of the P-wave velocity of -1 % is used in the low velocity zone with respect to the IASP91 model, the travel time residual of PcP is +1.32 s (epicentral distance is 70.1 deg.). This indicates that the P-wave velocity perturbation in the lowermost mantle beneath the southwestern pacific region is less than -1 % with respect to the IASP91 model, because the observed PcP travel-time residuals range from 0.10 s to 1.18 s. A synthetic test with reflectivity seismograms (Müller, 1985) shows that the amplitude of a PdP phase with a -1 % velocity contrast at the depth of 2520 km is up to 10 % of PcP. Since the value of 10 % was determined using the normal stacking process, it is much higher than that of PWSEMBP. The PdP amplitude in the observed data is also 10 % at the maximum, which is consistent with the synthetic data.

Figure 1A.a and 1A.b in Appendix. 3 show the results of the RWB with synthetic data for each subarray. In each subarray, the PWSEMBP was normalized by the maximum vales of PcP. In comparison with the observed data, the shapes of the PWSEMBP curve in the synthetic data are much simpler, because the P waveforms and P coda in the synthetic data are simpler than those in the observed data. This is due to the relatively simple crustal structure used in the IASP91 Earth model. Another possible effect may be that noise in the portion before the direct P-wave, which was added to the synthetic, is different from the noise in the time window between P and PcP. The amplitude ratio of PcP and PdP is almost constant throughout all subarrays in the synthetic data. Naturally enough, the maximum peaks of the curve indicate the correct depth of the CMB (at the depth of 2889 km in the IASP91 Earth model) based on the IASP91 Earth model (without discontinuities), while the PcP peaks were shifted to the right (deeper) direction in the model where synthetic velocity anomalies or discontinuities (negative one in the case of this study) were introduced. At the depth of 2650 km, where a synthetic discontinuity with a negative velocity jump of 1 % was introduced, small peaks can be seen in all subarrays. The pulse corresponding to the PcP energy extends from about 2840 km to about 2940 km, which can be regarded as the depth resolution for any discontinuous heterogeneity in this method. On the other hand, the discontinuities discovered here in the observed data can not be seen in all subarrays, meaning the discontinuities are visible in some subarrays while they are invisible in others. This indicates that the discontinuities may be rather intermittent in the lowermost mantle beneath the southwestern Pacific.

Figure 8.8a-c in the chapter 8 (*Synthetic Test*) show the result of the migration using the synthetic seismograms with 1 % negative discontinuity at the depth of 2650 km. It is clearly recognizable that the reflected phases from the introduced plane discontinuity are imaged around the depth of 2650 km. On the other hand, there is only weak evidence for such distinguished blob in the observed data in the migration method. If the detected anomalous phases are reflected at a plane discontinuity, the

velocity contrasts of the discontinuities should be smaller than 1 %.

### **9.6 Comparison between the P- and S-Wave Velocity Discontinuities**

The depth ranges where the seismic velocity discontinuities were found are almost same in P- and S-waves. For the P-wave, the discontinuities lie at depth ranges from 2510 to 2530 km and from 2600 to 2650 km, and at about 2800 km. In the case of S-wave, the two discontinuities at the depth of 2520km and 2650 km are not isolated well due to a lower resolution. While the discontinuities at the depth of 2520 km and 2650 km are almost at the same position for in P- and S-waves, the discontinuity at the depth of 2800 km seems deeper (about 2850 km depth) for S-waves. This may indicate that the velocity reduction between the CMB and the first discontinuity (at the depth of 2520 km) is stronger for S-waves. If tomograms for P- and S-waves are compared, S-wave velocity reduction is about 2-3 times stronger than that of P-wave in the lowermost mantle beneath the southwestern Pacific (e.g. Garnero and Helmberger, 1993, Li and Romanowicz, 1996, M. Wyession, 1996, van der Hilst et al., 1997, Boschi et al., 1999, Valenzuela et al., 2000, Karason and van der Hilst, 2001). The P- and S-wave velocity structures detected in this study are consistent with the results of tomographic studies. Though the P- and S-wave velocity structure are consistent with each other, there are differences between them such as slightly different depth of the P- and S-wave velocity discontinuities. One possible reason is that the different frequencies for observed PdP and SdS phases are focused differently by the seismic discontinuity topography. It could happen that the low velocity zone in the D'' layer influences the P-wave velocity discontinuities and S-wave velocity discontinuities differently.

### **9.7 Comparison between different frequency bands**

For P-wave data, three different frequency bands (1-2s, 2-5s, 5-10s) were used to investigate a possible frequency dependency of the images of the discontinuities or the scattering volumes. The results from the RWB in the frequency band of 1-2s and 5-10s are shown in Appendix 4. In general, longer-period data have high coherency and low resolution and shorter-period data possess low coherency and high resolution. The short-period data band (1-2s) is noisier than the other frequency bands (2-5s and 5-10s). The CMB has been imaged relative sharp with the short-period data, but the image is relative noisy on the northeastern part (on the left hand side). One of the remarkable features is that the depth of the CMB jumps by 50km suddenly, but this can not be real structure. Vespagrams of the short-period data show that the travel time and the slowness of the PcP waves do not correspond to the theoretical ones. This derives from the low coherency of the short-period data and its low signal to noise ratios. The sudden CMB jump results from the low quality of the short-period data, especially in the area of subarray 1-5. The reason for the indistinct discontinuities might also be a gradient structure. Since the discontinuities are clearly seen in the middle frequency



band (2-5s), a several km thick gradient zone might be preferable for the discontinuities. The discontinuities in the D'' layer are delineated best in the middle frequency band (2-5s). In the long-period data (5-10s), the resolution is not enough to distinguish the discontinuities.

The observed depth of the CMB is also dependent on the dominant period of the wave. The CMB depth in the frequency band of 5-10s is 2905 km, 2910 km in the frequency band of 2-5s, and 2915 km in the frequency band of 1-2s, respectively (see Figure 9.1a-c). The corresponding delay times with respect to the theoretical ones are approximately 0.45s, 0.6s and 0.8s, respectively. This indicates that the P-wave propagates slower or that the PcP wave propagates faster in the lower frequency band. One possible reason can be the effect of the attenuation. In general, it is known that body wave velocity changes as a function of attenuation (Liu et al., 1976, Kanamori and Anderson, 1977). The velocity of a seismic wave, whose dominant period is T changes with respect to the velocity at the reference period  $T_0$ . This is expressed in the following equation:

$$\frac{V(T)}{V(T_0)} = 1 - \frac{1}{pQ} \ln \frac{T}{T_0},$$

where Q is the attenuation factor. This velocity change derives from the anelasticity of the Earth's material (Liu et al., 1976). The intrinsic attenuation defined by the quality factor Q can delay the maximum peak of the wavelet, while the onset time is not affected by the intrinsic attenuation. The lowest Q values (highest attenuation) occur in the upper mantle in the Earth (Dziewonski and Anderson, 1981). When P and PcP waves propagate in the upper mantle, both phases are affected by the attenuation in the upper mantle a little bit differently, because the PcP waves propagate steeper than the P-waves. This causes the maximum peak of the P-wave to be delayed more than the PcP wave. In other words, the attenuation effect can cause a pulse width broadening which is dependent on the frequency. In order to estimate the effect of the attenuation in the upper mantle to the relative travel time between PcP and P in the different frequency bands, the theoretical travel time including the effect of the attenuation factor (Q model from the PREM, (Dziewonski and Anderson, 1981)) was calculated at the dominant periods of 1s and 5s. The difference of the relative travel times between PcP and P at the dominant period of 1s and 5s is 0.07 s at the epicentral distance of 70 degrees. On the other hand, 0.35 s are required to shift the CMB by 10 km. The 0.35 s travel time difference in the different frequency band can not be explained only by the attenuation effect in the upper mantle.

One of the explanations might be that the local sharpness of the CMB can change the apparent depth of the CMB. If there were a transition zone at or just above the CMB, the apparent depth of the CMB would shift upwards for the longer-period seismic waves, while the apparent depth of the CMB for the shorter-period seismic waves would stay at the same depth.

### **9.8 Inferred 1-D P-wave Velocity Model beneath the Southwestern Pacific**

One-dimensional P-wave velocity model would be the following model, although any one-dimensional would not fit real three-dimensional structures (see Figure 9.14). At the depth of 2520 km there is a negative velocity discontinuity with less than about 0.5 % velocity jump. There is a negative velocity discontinuity at the depth of 2650 km, where sharpness is about 5 km at most and velocity contrast is less than 0.5 %, because the discontinuity can also be detected in the short-period frequency band (1-2s) (see Figure 9.1a). In the area between 2650 km depth and 2800 km depth the velocity perturbation relative to the IASP91 model is about -1%. At 2800 km depth there is a positive velocity discontinuity with velocity contrast of about 0.5%. This model can explain the PcP travel time delay of approximately 1.0 s (at a epicentral distance of 70 degrees) and the depth of the P-wave velocity discontinuity in the lowermost mantle. The general depression of the observed CMB depth can also be explained by the PcP travel time delay due the lower velocity zone. In the case of S-wave, ScS travel time delay calculated for this model is approximately 1.5s (at a epicentral distance of 70 degrees). This is smaller than observed ScS travel time residuals (max. 6.88 s), which indicates that the S-wave velocity reduction is stronger than that of P-wave in the lowermost mantle beneath the southwestern Pacific.

## Inferred 1-D P-wave velocity model

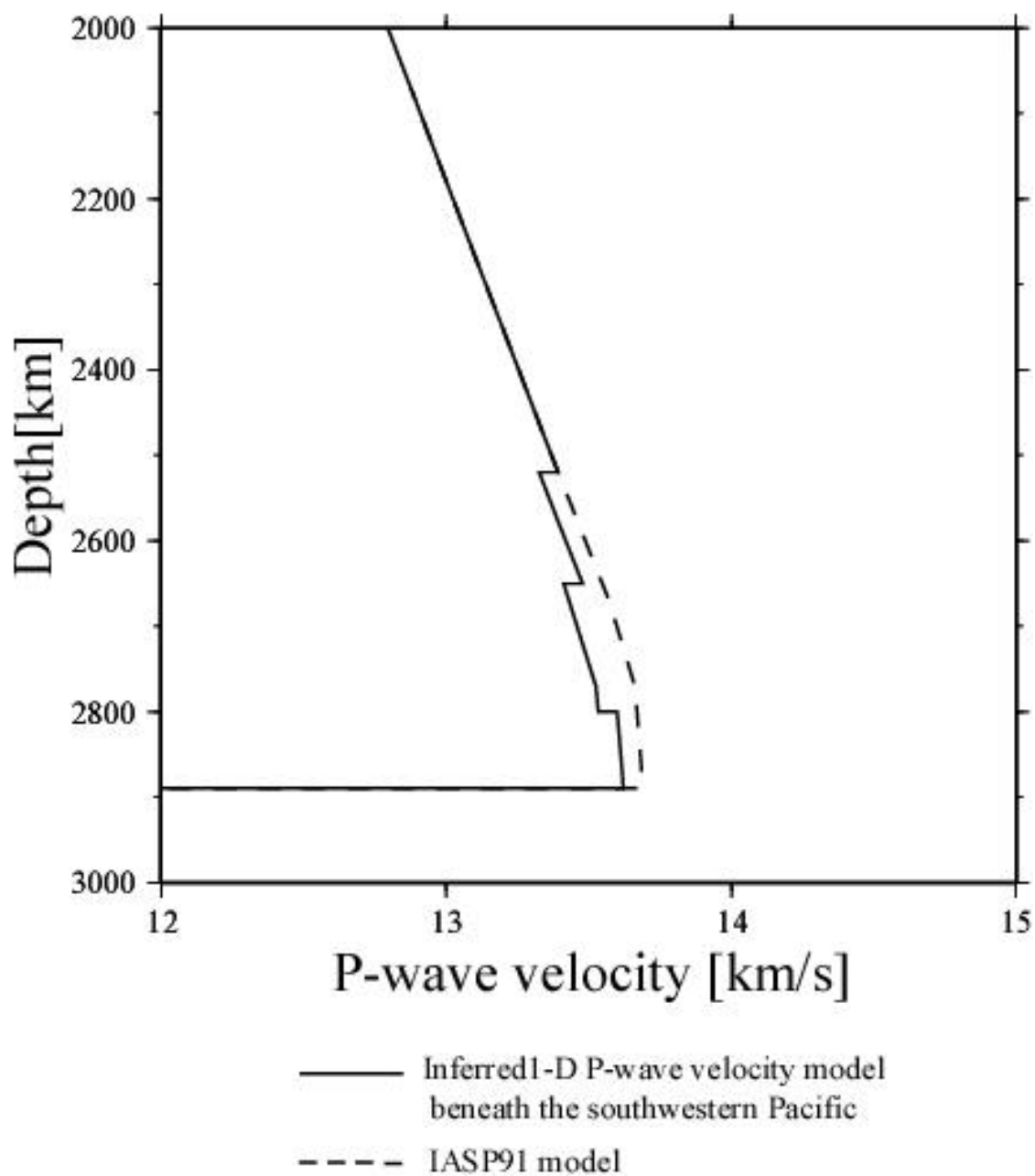


**Figure 9.14** Inferred 1-D P-wave velocity model in the lowermost mantle beneath the southwestern Pacific. The solid line indicates the possible model and the dotted line indicates the P-wave velocity model in the IASP91 model.

## 10. Discussion

### 10.1 Anomalous PcP and ScS Travel Times

Although the travel time residuals of the direct P-waves—which are generated by the heterogeneous structure in the crust and uppermost mantle beneath the receiver array and source array—have been corrected with respect to the theoretical one through the alignment procedure of the direct P-wave, it is plainly recognizable that the arrival times of the PcP beams and ScS beams are slower when compared to the theoretical ones. Figure 10.1 shows PcP and ScS beams for each event. In the case of event 12, the PcP beam is not clearly visible due to the relatively small number of traces used in forming the PcP beam. One can notice that the peaks of the PcP and ScS beams are slightly delayed as compared to the IASP91 model. The time delay of PcP ranges from 0.10 s to 1.18 s (see Table 10.1). In the case of the S-wave, there are also noticeable travel-time delays relative to IASP91 varying from 2.8 s to 6.8 s. These delays of ScS - S are larger than those of PcP - P, which results in a general shift of the CMB inferred from ScS to 2960 km, while the CMB depth inferred from PcP is 2910 km.

One possible reason for the general travel-time delays of PcP and ScS might be a large-scale (more than 1000-km wavelength) undulation of the CMB. However, it is implausible that the CMB itself plays a vital role in the travel time delays of PcP and ScS due to the following reason: Morelli and Dziewonski (1987) investigated the undulation of the CMB with an inversion method using the travel time of PcP and PKP with respect to PREM (Dziewonski and Anderson, 1981). According to their results, the amplitude of unevenness of the CMB varies within 5 km, and the CMB beneath the Indian Ocean, the North Pacific and the North Atlantic is shallower, while the CMB beneath Africa, Eastern Asia, New Zealand and the western coast of South America is deeper. Beneath the Southwestern Pacific (the study area), the CMB shows up at about average depth. Therefore, it is hard to attribute these general travel time delays of PcP and ScS to the undulation of the CMB. The most plausible scenario is that these time delays of the PcP beams and ScS beams are due to the low velocity zone (e.g. M. Wyssession, 1996, R.D. van der Hilst et al., 1997, Boschi et al., 1999) in the lowermost mantle beneath the southwestern Pacific, because the ray paths of P and PcP (or S and ScS) are different from each other in the lower mantle but are very similar in the upper mantle and crust. Therefore, only PcP (or ScS) is influenced by this anomalous structure of the lowermost mantle. Since the travel-time residuals of P and PcP (or S and ScS) fluctuate slightly differently throughout the subarrays (see Figure 7.5 for P and S-waves and Figure 9.5 for PcP and ScS waves), it is not easy to isolate the effect of the anomalous structure in the lower mantle from the effect of the anomalous structure in the upper mantle and crust. The fluctuations of the travel time differences between P and PcP (or S and ScS) used in this study contain various factors which can affect the travel time of P and PcP everywhere in the mantle and crust, respectively.

Though these travel-time anomalies of PcP (or ScS) yield an incorrect CMB depth, the travel-time anomalies were not corrected because PdP (or SdS) phases are less influenced by this low velocity zone if PdP (or SdS) is a reflected wave from the top of the low velocity zone.

Figure 9.5 in chapter 9 shows the PcP and ScS beams for each subarray using all events. As was the case with the PcP and ScS beam for each event using all stations, the travel time delays of PcP and ScS show up as well. The fluctuation range is almost the same as in the case of PcP and ScS beam for each event. While the PcP beams align with a slight curve in an arc, there are two relatively drastic jumps in the case of ScS beams, one between subarray 3 and subarray 5, the other between subarray 14 and subarray 15, although the pattern of the fluctuation is more or less similar. This indicates that there might be a structure which has a much greater effect on the S-wave than the P-wave such as partial melting in the lowermost mantle beneath the southwestern Pacific.

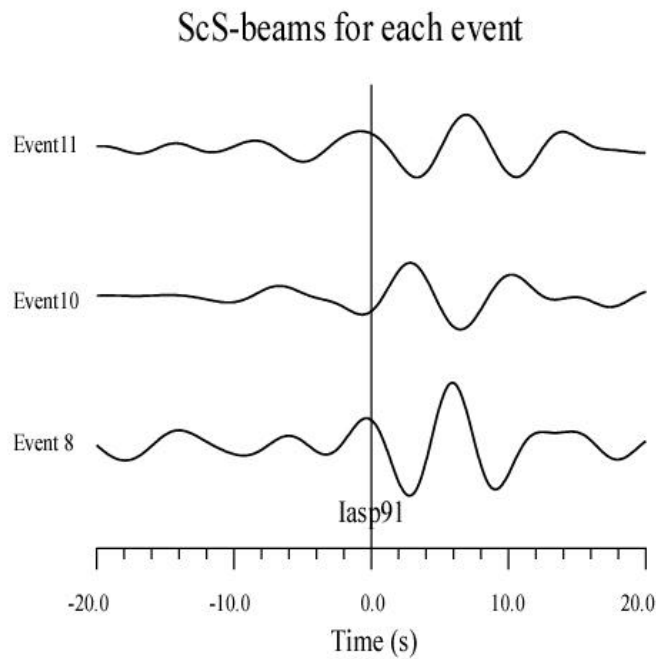
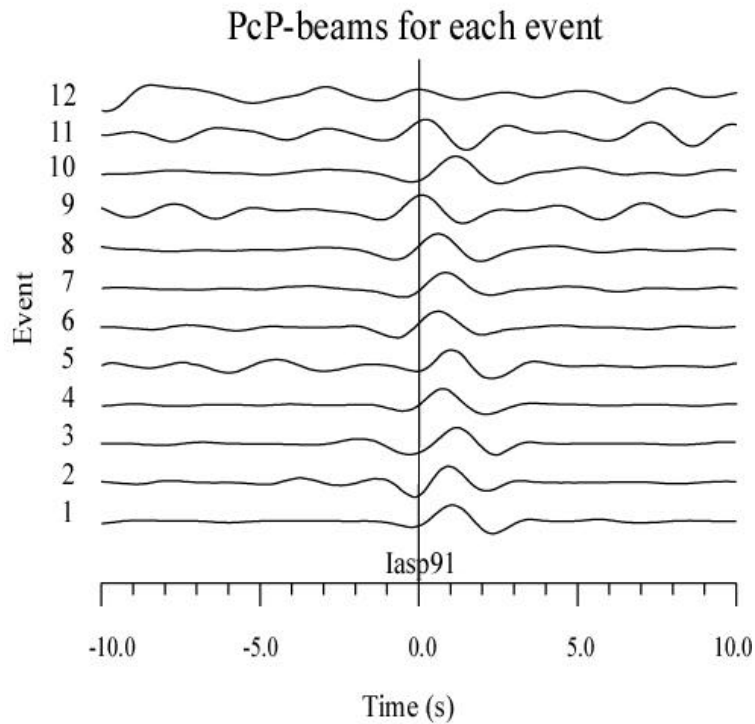


**Figure 10.1** PcP and ScS-beams for each event. Note that the onset times of the PcP-beams and ScS-beams are delayed with respect to the theoretical ones (IASP91) due to the low velocity zone in the lowermost mantle. Naturally, this effect is stronger for the S-waves than for the P-waves. The small amplitude of the PcP phases in Event 12 is due to the small number of traces (see Table 1 in Appendix 6.).

Event Nr.	Delay of PcP-P travel times with respect to IASP91 (s)	Delay of ScS-S travel times with respect to IASP91 (s)
1	1.02	No data
2	0.96	No data
3	1.18	No data
4	0.76	No data
5	1.08	No data
6	0.64	No data
7	0.81	No data
8	0.59	5.88
9	0.10	No data
10	1.16	2.80
11	0.24	6.88
12	Not visible	No data

**Table 10.1** the travel time delay of PcP and ScS with respect to IASP91 for each event.

## 10.2 Influence of the Slab beneath the Tonga-Fiji Region

The travel time and the waveform of the P(S) and PcP (ScS) phases can be influenced by the subducting slabs (Cormier 1985, Weber 1990), inside of which velocity is normally higher than in the surrounding area. Since the Tonga-Fiji region is a typical subduction zone as mentioned above, a synthetic model of a slab with a velocity perturbation of +10 % was defined underneath the Tonga-Fiji region in order to estimate the influence on the travel time differences between PcP and PdP. This velocity perturbation of +10 % is high with respect to what is expected in the real Earth (e.g. Fukao et al. 2001). It was assumed that the slab is subducting to a depth of about 600 km. IASP91 was used as a reference model and a low-velocity zone with a -1 % velocity perturbation in the depth range between 2889 km and 2650 km was introduced. An event with a depth of 404 km (the shallowest event in this study), which would be most influenced by the heterogeneities around the source region, was selected and was used for calculating travel times and synthetic seismograms. For the 2D modeling, the program Xgbm by Davis and Hensen (1993) has been used. This program enabled us to create and manipulate intricate, laterally heterogeneous, two-dimensional (2-D) velocity models of the Earth's interior and then to compute synthetic seismograms for these models using the Gaussian beam method. According to the resulting synthetic seismograms, the differential travel times between PcP and PdP used in this study are 8.17 s with the slab and 8.06 s without the

slab at the epicentral distance of 70 degrees, although absolute travel times of P, PcP and PdP vary by up to 3s. Even in the case of such an extreme condition with +10 % velocity perturbation in the slab, the influence of the travel time differences on the results of the stacking is almost negligible. Reflected waves and S-to-P conversion at the borders of the subduction could distort the waveform of the later phases such as PdP and PcP phases. In order to produce reflected waves and S-to-P conversion, however, it is necessary that the thickness of the boundary which forms slab has to be narrower than about 50 % of the dominant wavelength of the phases (Weber and Davis, 1990). Such a sharp contrast of the slab's boundary is not likely to extend over a depth range from 350 to 650 km, where the sources are located. Therefore this effect is also negligible in this study.

### 10.3 Variation of the Travel-Time Difference between PcP and P

Although the arrival times of the P-waves were aligned with respect to the IASP91 model, the travel-time difference between PcP and P varies among the subarrays due to the 3-D regional heterogeneities under both the Japanese archipelago and Fiji archipelago. Figure 10.2 shows the P-wave travel time residuals for each station for event 1. Though the absolute travel times can be influenced by all effects on the path between the source and the stations, fluctuation of the residuals among the stations is likely due to the crustal structure just beneath the stations.

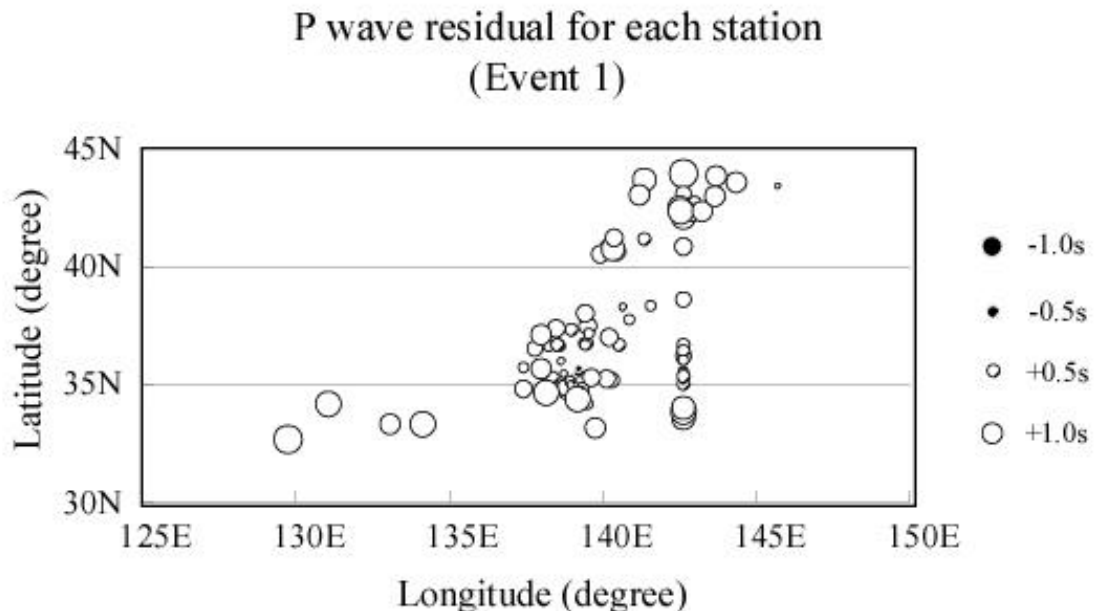


**Figure 10.2** P-wave residuals with respect to IASP91 for each station. The size of the circles indicates the residuals. On the whole, the travel time of the direct P-waves are slower than the theoretical one.

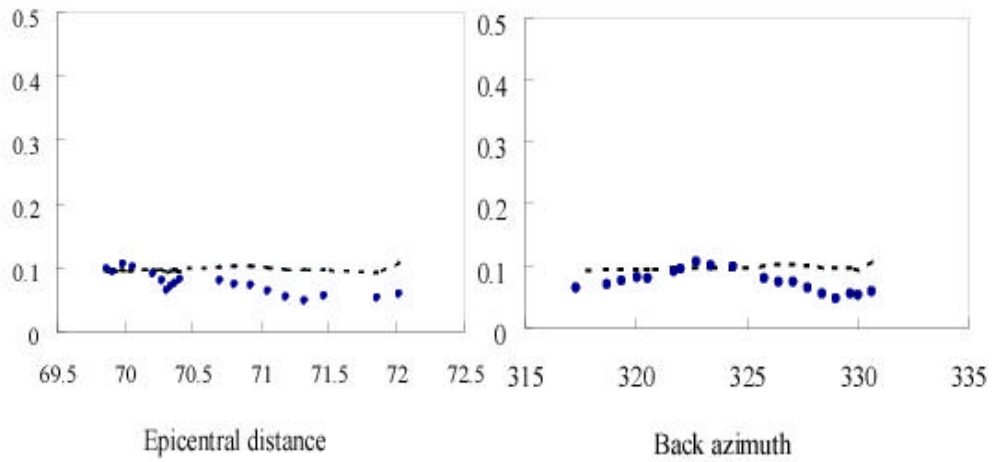


#### **10.4 Anomalies of PcP/P and ScS/S Amplitude Ratio**

Figure 10.3 shows the PcP/P amplitude ratio for each subarray. In comparison with the theoretical PcP/P amplitude ratios (IASP91), the observed ones have smaller amplitude overall. It seems that all PcP/P amplitude ratios can be divided into four groups which are independent of epicentral distances. One possible explanation of the relative small amplitude ratio of PcP/P with respect to the theoretical one may be strong attenuation in the lowermost mantle. Schlittenhardt (1986) investigated PcP/P ratios at large distances, 70- 84 degrees, and found generally low values, compared with predictions by standard earth model PREM and models having modified velocity-depth gradients in the D'' layer. His suggestion is that the PcP amplitude reduction is due to regional reduction of the quality factor of P-waves in D'', with values as low as 100.

For a large-aperture array, amplitude anomalies are affected by changes in geometrical spreading and inelastic attenuation through the mantle between a source and an array. The aperture of the J-Array is about 5-6 degrees in the epicentral distance for events in the Tonga-Fiji region, which leads to about 5-7 % change in amplitude due to geometrical spreading (based on the IASP91 Earth model). Since the J-Array and Hi-net are long, narrow arrays, the aperture changes significantly with the arrival direction. Kampfmann and Müller (1989) investigated the effect of topography of the CMB on the amplitude of PcP by applying the 3D Kirchhoff theory. According to their synthetic analysis, if sinusoidal topographies on the CMB have a wavelength exceeding 100 km, pronounced amplitude variations occur with respect to the amplitude curve for a spherical CMB, because of focusing by valleys and defocusing by hills on the CMB. If sinusoidal topographies on the CMB have a wavelength less than 50 km, the amplitude curve is smooth with lower values with respect to the amplitude curve for a spherical CMB. Therefore, the CMB undulation with a wavelength below 50 km can also be one of the possible reasons for the relatively small PcP/P amplitude ratio.

### PcP/P amplitude ratios



### ScS/S amplitude ratios

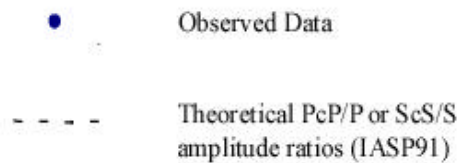
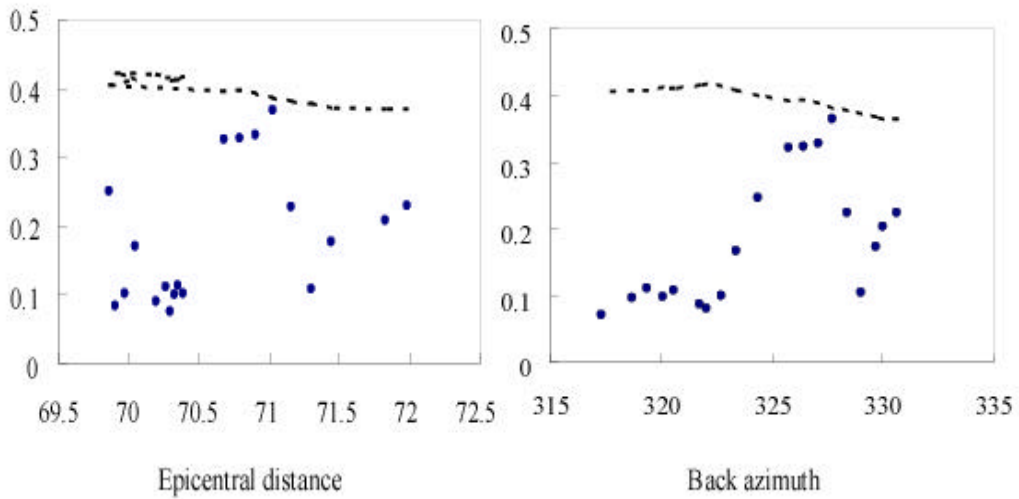


**Figure 10.3** PcP/P and ScS/S amplitude ratios shown as function of the epicentral distance and the azimuth. The upper graphs show the PcP/P amplitude ratios and the lower graphs show the ScS/S amplitude ratio for each subarray using all events. Since all the events are used to calculate the PcP/P or ScS/S amplitude ratios, the effect of the radiation pattern has been taken into consideration, so it is possible to compare the observed PcP/P (or ScS/S) amplitude ratios to synthetic ones, directly. In comparison with the PcP/P amplitude ratios, ScS/S amplitude ratios are quite unstable.

## 10.5 Mislocation of Events and other Problems

Mislocation of the sources can influence the depth of the detected discontinuities. One of the tests concerning event mislocation shows that the influence on the travel time is not crucial as long as the relative travel time differences are used. There is a systematical depth error between the Harvard CMT solution and Engdahl solution, which are used in this study. The average depth difference is 14.25 km. If the depth, for instance, is shifted 20 km upwards—which can be the maximum error—the travel time of PcP itself has a 1.89 s time delay and the travel time difference of PcP-P is +0.19 s (for Event1 at station KTJ). This travel time error of 0.19 s corresponds to approximately 10 km depth shift of the CMB or discontinuities in the D' layer. This issue concerns the source parameters for the Hi-net data set taken from the Harvard CMT catalogue. In Table 1 in Appendix 6, the source parameters from Harvard CMT are compared with those of PDE (Preliminary Determination of Epicenters). The source parameters determined by Engdahl (1998) are also shown. The most influential parameter for the RWB method or the migration method is the depth. If the PDE depth values are compared with those of the Harvard CMT catalogue, it is recognized that the determined depth in the PDE is systematically shallower by about 10 km than those of the Harvard CMT solution. The reason is that short-period seismic data (about 1s) are used for the PDE localization, while longer-period seismic data ( $T > 40s$ ) are used for the Harvard CMT solution. If the depth parameters change systematically, it would not influence the accuracy of the travel time which is needed to extract the weak signals from the lowermost mantle. As mentioned above, the resulting depth shift of the CMB or discontinuities in the D' layer is approximately half of the mislocation of the source depth, so 10 km depth difference between the Harvard CMT and the PDE solution can shift the CMB depth by 5km. This is the same distance as that used for discontinuity's vertical interval spacing. As regards the effect of the source parameter differences among different catalogs is relatively small in this study. As to the horizontal mislocation, there is approximately 0.04 degrees error in the direction of longitude and approximately 0.15 degrees error in the direction of the latitude on average (using Event1 - Event7) between the Harvard CMT solution and Engdahl solution, though some events show a maximum difference of 0.3 degrees. The average longitude error of 0.04 degrees makes the travel time difference between P and PcP longer and the latitude error of 0.15 degrees makes the travel time difference between P and PcP shorter with respect to the Engdahl solution. These opposite effects cancel each other partially. If there is 0.1 degrees error in the direction of great circle path, the travel time shift of the P-wave itself is 0.59 s and that of PcP wave is 0.42 s (for 500 km source depth and 70 degrees epicentral distance). Therefore, the travel time difference between P and PcP which was used in this study is changed by 0.17 s which is corresponding to 20 km depth error.

In connection with the difference of the source parameters between the J-Array and the Hi-net, the

systematical shift of the location between the Harvard CMT solution (used for Hi-net data) and the Engdahl solution (used for J-Array) may affect the beamforming. An expected travel time error caused by the systematical difference between the Harvard CMT solution and Engdahl solution is approximately 0.2 s, which may reduce the amplitude of the stacked waveform, but can not shift the detected discontinuities more than 10 km.

## 11. Conclusion

The D' layer beneath the southwestern Pacific was investigated by stacking 2017 traces (P-wave) and 863 traces (S-wave) using data from Tonga-Fiji deep events. A DAM (Double Array Method) and a PWSEM (Phase Weighted Semblance) method were applied to the data in order to get a better resolution. The combination of these methods has improved the vertical and lateral resolution in the lowermost mantle, which enabled us to detect small-scale heterogeneities (a few hundreds of kilometer). In the results of the RWB method, three distinguished discontinuities can be detected at about 2530 km depth, at about 2650 km depth, and at about 2800 km depth in the P-wave data. The reflected waves from the two discontinuities at the depth of 2530 km and 2650 km show negative polarity (see also Kito and Krüger 2001). Additionally, a relative large energy peak is recognized at about 2800 km depth. The reflected waves from this anomalous region show positive polarity, which is not consistent with the polarity of a reflected wave from the top of an ULVZ. The analysis using subarrays indicates that the discontinuities at the depth of 2530km, 2650km and 2800km appear intermittently. The lateral extension of the discontinuities is a few hundred km.

Among the three different frequency band (1-2s, 2-5s and 5-10s) for P-waves which could be analyzed, the heterogeneous structure could be imaged in the middle frequency band (2-5s) more clearly than in the other frequency bands. The short-period frequency band (1-2s) is relatively noisy and the long-period frequency band (5-10s) has too low resolution to image the small-scale heterogeneities in the lowermost mantle.

In the case of S-waves, the two discontinuities at a depth of around 2600 km and 2850 km were detected. The two discontinuities at the depth of 2530 km and 2650 km in the P-waves seem to be one discontinuity in the S-waves due to a lower resolution of S-waves. The S-wave velocity discontinuity at the depth of 2850 km corresponds to the P-wave velocity discontinuity at the depth of 2800 km. The 50 km difference between the P-wave velocity discontinuity and the S-wave velocity discontinuity in depth indicates that the S-wave velocity reduction in the D' layer is stronger than P-wave velocity reduction beneath the southwestern Pacific.

In the migration, there might be some candidates for scattering objects in the depth range of about 2550 km and about 2650 km within the PcP aliasing ring. As synthetic data show that there is little energy within the PcP aliasing ring, it would be likely that the weak energy patches within the PcP aliasing ring are scattering objects or reflectors. In the case of S-wave migration, resolution is not

high enough to detect the scattering objects. Of course, the detected heterogeneities in the RWB and in the migration belong to the same objects.

PcP and ScS beams both for each subarray and for each event show about 1.2s (maximum) delay for P-waves and about 6.8 s delay (maximum) for S-waves with respect to IASP91. This is a strong evidence for the low velocity zone in the lowermost mantle beneath the southwestern Pacific region. These travel time delays of PcP and ScS also vary along the subarray, indicating lateral heterogeneities do exist in the lowermost mantle beneath the southwestern Pacific.

Geodynamical considerations lead to the conclusion that these heterogeneities are connected to hot plume generation. The detected P- and S-wave velocity anomalies may be heterogeneities generated in process of hot plume formation. Since upwelling streams are prominent in the lowermost mantle beneath the southwestern Pacific, the source of these heterogeneities could be a mixed structure of thermal and chemical anomalies, which may originate from reaction between mantle materials and outer core's iron.

## **Acknowledgments**

I would like to acknowledge all people who somehow contributed to this thesis. First, I am deeply grateful to Dr. Frank Krüger for his numerous helpful and fruitful advices throughout this thesis. Without his help, I could not have achieved this work. I would like to thank the J-Array group for allowing me to use valuable data and T. Shibutani for providing me with the Tonga-Fiji events data. Dr. Negishi of the National Research Institute for Earth Science and Disaster Prevention provided me with valuable data from the Hi-net. I also wish to thank F. Scherbaum for allowing me to use his ray-tracing program and for his constructive comments. I am grateful to Mathias Ohrenberger for his helpful comments and suggestions, especially regarding technical problems. Amy Langenhorst, Mark Preier and Dr. Anke Friedrich corrected the grammatical errors in the text. I used the processing software 'Seismic-Handler' by K.Stammler (SZGRF) for the analysis of the data, and the Figures were created with GMT (P. Wessel and W.H.F. Smith, EOS Trans. AGU 76, 329, 1995).

## References

- Aki, K., A. Christoffersson, and E. S. Husebye, Determination of the three-dimensional seismic structure of the lithosphere, *J. Geophys. Res.*, 80, 3322-3342, 1976.
- Bataille, K., and S. M. Flatte, Inhomogeneities near the core-mantle boundary inferred from short-period scattered PKP waves recorded at the Global Digital Seismograph Network, *J. Geophys. Res.*, 93, 15057-15064, 1988.
- Bataille, K., and F. Lund, Strong scattering of short-period seismic waves by the core-mantle boundary and the P-diffracted wave, *Geophys. Res. Lett.*, 23, 2413-2416, 1996.
- Bataille, K., R. S. Wu, and S. M. Flatte, Inhomogeneities near the core-mantle boundary evidenced from scattered waves: a review, *Pure Appl. Geophys.*, 132, 151-173, 1990.
- Bilek, S. L., and T. Lay, Lower mantle heterogeneity beneath Eurasia imaged by parametric migration of shear waves, *Phys. Earth Planet. Inter.*, 108, 201-218, 1998
- Boschi, L., and A. M. Dziewonski, High- and low-resolution images of the Earth's mantle: Implications of different approaches to tomographic modeling, *J. Geophys. Res.*, 104, 25567-25594, 1999.
- Bracewell, R. N., The Fourier transform and its applications, *Mcgraw-Hill, New York, NY.*, 1965.
- Bullen, K. E., Compressibility-pressure hypothesis and the Earth's interior, *Mon. Not. R. Astron. Soc., Geophys. Suppl.*, 5, 355-368, 1949.
- Castle, J. C., K. C. Creager, A steeply dipping discontinuity in the lower mantle beneath Izu-Bonin, *J. Geophys. Res.*, 104, 7279-7292, 1999.
- Castle, J. C., K. C. Creager, J. P. Winchester, and R. D. van der Hilst, Shear wave speeds at the base of the mantle, *J. Geophys. Res.*, 105, 21543-21557, 2000.
- Castle, J. C., and R. D. van der Hilst, The core-mantle boundary under the Gulf of Alaska: No ULVZ for shear waves, *Earth Planet. Sci. Lett.*, 176, 311-321, 2000.
- Clayton, R. W., and R. A. Wiggins, Source shape estimation and deconvolution of teleseismic body waves, *Geophys. J. R. Astron. Soc.*, 41, 151-177, 1976.
- Cleary, J. R., and R. A. W. Haddon, Seismic Wave Scattering near the CMB: A New Interpretation of Precursors to PKP, *Nature*, 240, 549-551, 1972.
- Cormier, V. F., Some problems with S, SKS and ScS observations and implications for the structure of the base of the mantle and the outer core, *J. Geophys.*, 57, 14-22, 1985.
- Cormier, V., Synthesis of body waves in transversely isotropic Earth models, *Bull. Seis. Soc. Amer.*, 76, 231-240, 1986.
- Creager, K. C., and T. H. Jordan, Slab penetration into the lower mantle beneath the Mariana and other island arcs of the northwest Pacific, *J. Geophys. Res.*, 91, 3573-3580, 1986.
- Dalziel, I. W. D., Antarctica; A tale of two supercontinents ? *Ann. Rev. Earth Planet. Sci.*, 20,

- 501-526, 1992.
- Davies, G. F., Thermal histories of convective earth models and constraints on radiogenic heat production in the earth, *J. Geophys. Res.*, 85, 2517-2530, 1980.
- Davies, G. F., Geophysical and isotopic constraints on mantle convection: an interim synthesis *J. Geophys. Res.*, 89, 6017-6040, 1984.
- Davies, G. F., Mantle plumes, mantle stirring and hotspot chemistry, *Earth Planet. Sci. Lett.*, 99, 94-109, 1990.
- Davis, J. P., and I. H. Henson, Xgbm-an X-windows system to compute Gaussian beam synthetic seismograms. *Teledyne Geotech, Alexandria Lab*, 1993.
- Doornbos, D. J., The anelasticity of the inner core. *Geophys. J. Roy. Astron. Soc.*, 38, 397-415
- Doornbos, D. J., On seismic-wave scattering by a rough core-mantle boundary, *Geophys. J. Roy. Astron. Soc.*, 53, 643-662, 1978.
- Doornbos, D. J., and N. J. Vlaar, Regions of seismic wave scattering in the Earth's mantle and precursors to PKP, *Nature*, 243, 58-61, 1973.
- Douze, E. J., and S. J. Laster, Statistics of semblance, *Geophysics*, vol. 44, No. 12 December, 1999-2003, 1979.
- Dziewonski, A. M., Mapping the lower mantle: Determination of lateral heterogeneity in P velocity up to degree and order 6, *J. Geophys. Res.*, 89, 5929-5952, 1984.
- Dziewonski, A. M., and D. L. Anderson, Preliminary Reference Earth Model. *Phys. Earth Planet. Int.*, 25, 297-356, 1981.
- Efron, B., and R. Tibshirani, Bootstrap Methods for Standard Errors, Confidence Intervals, and Other Measures of Statistical Accuracy, *Statistical Science*, No.1, 54-77, 1986.
- Emmerich, H., Theoretical study on the influence of CMB topography on the core reflection ScS, *Phys. Earth Planet. Inter.*, 80, 125-134, 1993.
- Engdahl, E. R., and R. Kind, Interpretation of broadband seismograms from central Aleutian earthquakes, *Ann. Geophys.*, 4, B, 3, 233-240, 1986.
- Engdahl, E. R., R. van der Hilst, and R. Buland, Global teleseismic earthquake relocation with improved travel times and procedures for depth determination, *Bull. Seismol. Soc. Am.*, 88, 722-743, 1998.
- Freybourger, M., F. Krüger, and U. Achauer, A 22° long seismic profile for the study of the top of D", *Geophys. Res. Lett.*, 26, 3409-3412, 1999.
- Freybourger, M., S. Chevrot, F. Krüger, and U. Achauer, A waveform migration for the investigation of P wave structure at the top of D" beneath northern Siberia, *J. Geophys. Res.*, 106, 4129-4140, 2001.
- Fukao, Y., M. Obayashi, H. Inoue, and M. Nenbai, Subducting slabs stagnant in the mantle transition zone, *J. Geophys. Res.*, 97, 4809-4822, 1992.



- Fukao, Y., Seismic tomogram of the earth's mantle: Geodynamic implications. *Science*, 258, 625-630, 1993.
- Fukao, Y., S. Maruyama, M. Obayashi, and H. Inoue, Geologic implication of the whole mantle P-wave tomography, *Jour. Geol. Soc. Japan*, 100, 1,4-23, 1994.
- Fukao, Y., S. Widiyantoro, and M. Obayashi, Stagnant slabs in the upper and lower mantle transition region, *Rev. Geophys.*, 39, 291-323, 2001.
- Furumoto, M., Fine Topography of the Core-Mantle Boundary Inferred from Scattered S waves, *Central Core of the Earth*, 2, 345-348, 1992.
- Gaherty, J. B., and T. Lay, Investigation of laterally heterogeneous shear velocity structure in D'' beneath Eurasia, *J. Geophys. Res.*, 97, 417-435, 1992.
- Garnero, E., S. P. Grand, and D. V. Helmberger, Low P wave velocity at the base of the mantle, *Geophys. Res. Lett.*, 20, -612, 1843-1846, 1993.
- Garnero, E., D. V. Helmberger, and G. Engen, Lateral variations near the core-mantle boundary, *Geophys. Res. Lett.*, 15, 609-612, 1988.
- Garnero, E., D. V. Helmberger, Travel times of S and SKS: Implications for three-dimensional lower mantle structure beneath the central Pacific, *J. Geophys. Res.*, 98, 8225-8241, 1993.
- Garnero, E., D. V. Helmberger, and S. Grand, Preliminary evidence for a lower mantle shear wave velocity discontinuity beneath the central Pacific, *Phys. Earth Planet. Inter.*, 79, 335-347, 1993.
- Garnero, E., and D. V. Helmberger, A very slow basal layer underlying large-scale low-velocity anomalies in the lower mantle beneath the Pacific: evidence from core phases, *Phys. Earth Planet. Inter.*, 91, 161-176, 1995.
- Garnero, E., and D. V. Helmberger, Seismic detection of a thin laterally varying boundary layer at the base of the mantle beneath the central-Pacific, *Geophys. Res. Lett.*, 23, 977-980, 1996.
- Garnero, E., and T. Lay, Lateral variation in lowermost mantle shear velocity anisotropy beneath the north Pacific and Alaska, *J. Geophys. Res.*, 102, 8121-8135, 1997.
- Garnero, E. J., J. Revenaugh, Q. Williams, T. Lay, and L. H. Kellog, Ultralow velocity zone at the core-mantle boundary, in *The Core-Mantle Boundary Region, Geodynam. Ser.*, 28, edited by M. Gurnis et al., pp. 319-334, AGU, Washington, D. C., 1998.
- Garnero, E. J., Heterogeneity of the lowermost mantle, *Annu. Rev. Earth Planet. Sci.* 28, 509-537, 2000.
- Grand SP, van der Hilst RD, Widiyantoro S., Global seismic tomography: a snapshot of convection in the Earth. *GSA Today* 7:1-7, 1997.
- Gurnis, M., and G. F. Davies, Mixing in numerical models of mantle convection incorporating plate tectonics, *J. Geophys. Res.*, 91, 6375-6395, 1986.
- Gutenberg, B., Über Erdbebenwellen A. Beobachtungen an Registrierungen von Fernbeben in Göttingen und Folderungen über die Konstitution des Erdkörpers, *Nachr. K. Ges. D. Wiss.*

- Göttingen Math. Phys. Kl.*, 125-177, 1914.
- Haddon, R. A., and J. R. Cleary, Evidence for scattering of seismic PKP waves near the core-mantle boundary, *Phys. Earth Planet. Inter.*, 8, 211-234, 1974.
- Hager, B. H., R. W. Clayton, M. A. Richards, R. P. Comer, and A. M. Dziewonski, Lower mantle heterogeneity, dynamic topography and the geoid, *Nature*, 313, 541-545, 1985.
- Harvard CMT Catalog, <http://www.seismology.harvard.edu/CMTsearch.html>
- Hedlin, Michael A. H., P. M. Shearer, and P. S. Earle, Seismic evidence for small-scale heterogeneity throughout the Earth's mantle, *Nature*, 387, 145-150, 1997.
- Helmberger, D., S. Ni, L. Wen, and J. Ritsema, Seismic evidence for ultralow-velocity zones beneath Africa and eastern Atlantic, *J. Geophys. Res.*, 105, 23865-23878, 2000.
- Hilterman, F. J., Interpretive lessons from three-dimensional modeling: *Geophysics*, 47, 784-808, 1982.
- Hoffman, P., Did the breakout of Laurentia turn Gondwanaland inside-out ? *Science*, 252, 141109-14112, 1991.
- Holmes, A., Radioactivity and Earth movements, *Trans. Geol. Soc. Glasgow*, Part 3, 1928-1931, 18, 550-606, 1931.
- Holmes, A., The thermal history of the Earth, *J. Wash. Acad. Sci.* 23, 169-195, 1933.
- Holmes, A., Principles of Physical Geology, *Ronald Press*, New York, 532pp, 1945.
- Inoue, H., Y. Fukao, K. Tanabe, and Y. Ogata, Whole mantle P-wave travel time tomography, *Phys. Earth Planet. Inter.*, 59, 294-328, 1990.
- J-Array Group, The J-Array program: System and present status, *J. Geomag. Geoelectr.*, 45, 1265-1274, 1993.
- Jarvis, G. T., and W. R. Peltier, Mantle convection as a boundary layer phenomenon, *Geophys. J. R. astro. Soc.*, 68, 389-427, 1984.
- Jeanloz, R., and S. Morris, Temperature distribution in the crust and mantle, *Ann. Rev. Earth Planet. Sci.*, 14, 377, 1986.
- Jeanloz, R., and F. M. Richter, Convection, composition, and thermal state of the lower mantle, *J. Geophys. Res.*, 84, 5497-5504, 1979.
- Jeffreys, H., The times of P, S and SKS and the velocities of P and S. *Mon. Not. R. Astr. Soc. Geophys. Suppl.*, 4, 498-533, 1939.
- Jones, G. M., Thermal Interaction of the core and the mantle and long term behavior of the geomagnetic field, *J. Geophys. Res.*, 82, 1703-1709, 1977.
- Kampfmann, W., and G. Müller, PcP amplitude calculations for a core-mantle boundary with topography, *Geophys. Res. Lett.*, 16, 653-656, 1989.
- Kanamori, H., and D. L. Anderson, Importance of physical dispersion in surface wave and free oscillation problems: review. *Rev. Geophys. Space phys.*, 15, 105-112, 1977.

- Kanasewich, E. R., C. D. Hemmings, and T. Alpaslan, N-th root stack nonlinear multichannel filter, *Geophys.*, 38, 327-338, 1973.
- Kaneshima, S., and G. Helffrich, Detection of the lower mantle scatterers northeast of the Mariana subduction zone using short-period array data, *J. Geophys. Res.*, 103, 4825-4838, 1998.
- Kaneshima, S., and G. Helffrich, Dipping low-velocity layer in the mid-lower mantle: Evidence for geochemical heterogeneity, *Science*, 283, 1888-1891, 1999.
- Karason, H., and R. D. van der Hilst, Tomographic imaging of the lowermost mantle with differential times of refracted and diffracted core phases (PKP, Pdiff), *J. Geophys. Res.*, 106, 6569-6587, 2001.
- Kawakatsu, H., and F. Niu, Seismic evidence for a 920-km discontinuity in the mantle, *Nature*, 371, 301-305, 1994.
- Kennett, B. L. N., and E. R. Engdahl, Traveltimes for global earthquake location and phase identification, *Geophys. J. Int.*, 105, 429-465, 1991.
- Kendall, J. M., and P. M. Shearer, Lateral variations in D' thickness from long-period shear wave data, *J. Geophys. Res.*, 99, 11575-11590, 1994.
- Kendall, J. M., and P. G. Silver, Constraints from seismic anisotropy on the nature of the lowermost mantle, *Nature*, 381, 409-412, 1996.
- Kendall, J. M., and P. G. Silver, Investigating causes of D' anisotropy, in Core-mantle boundary region, 97-118, eds. M. Gurnis, M. Wyssession, E. Knittle and B. Buffet, *Geodynamic Series*, 28, American Geophysical Union, Washington D.C., U.S.A., 1998.
- Kingma, K. J., R. E. Cohen, R. J. Hemley, and H. K. Mao, Transformation of stishovite to a denser phase at lower-mantle pressures, *Nature*, 374, 243-245, 1995.
- Kito, T., Heterogeneities near the Core-Mantle Boundary inferred from short-period scattered P wave, *Master thesis, Kyoto University, Kyoto*, p.1-59, 1997.
- Kito, T., T. Shibutani, and K. Hirahara, Scattering objects in the lower mantle beneath northeastern China observed with a short-period seismic array, accepted in *Phys. Earth Planet. Inter*, 2003.
- Kito, T., and F. Krüger, Heterogeneities in D' beneath the southwestern Pacific inferred from scattered and reflected P-waves, *Geophys. Res. Lett.*, 28, 2545-2548, 2001.
- Krüger, F., M. Weber, F. Scherbaum, and J. Schlittenhardt, Double beam analysis of anomalies in the core-mantle boundary region, *Geophys. Res. Lett.*, 20, 1475-1478, 1993.
- Krüger, F., M. Weber, F. Scherbaum, and J. Schlittenhardt, Evidence for normal and inhomogeneous lowermost mantle and core-mantle boundary structure under the Arctic and northern Canada, *Geophys. J. Int.*, 122, 637-657, 1995.
- Krüger, F., F. Scherbaum, M. Weber, and J. Schlittenhardt, Analysis of Asymmetric Multipathing with a Generalization of the Double-Beam Method, *Bull. Seismol. Soc. Am.*, 86, 737-749, 1996.
- Lay, T., Structure of the core-mantle transition zone: A chemical and thermal boundary layer, *Eos*

- Trans. AGU*, 70, 49, 1989.
- Lay, T., and D. V. Helmberger, A lower mantle S wave triplication and the shear velocity structure of D", *J. Geophys. Res.*, 75, 799-838, 1983.
- Lay, T., and C. J. Young, Waveform complexity in teleseismic broadband SH displacements: Slab diffractions or deep mantle reflections ?, *Geophys. Res. Lett.*, 16, 605-608, 1989.
- Lay, T., and C. J. Young, Analysis of seismic SV waves in the core's penumbra, *Geophys. Res. Lett.*, 18, 1373-1376, 1991.
- Lay, T., and C. J. Young, Imaging scattering structures in the lower mantle by migration of long-period S waves, *J. Geophys. Res.*, 101, 20023-20040, 1996.
- Lay, T., Q. Williams, and E. J. Garnero, The core-mantle boundary layer and deep Earth dynamics, *Nature*, 392, 461-468, 1998.
- Lehmann, I., "P". *Publ. Bur. Cent. Seism. Int. Ser. A* 14, 3, 1936.
- Li, X.-D., and B. Romanowicz, Global mantle shear-velocity model using nonlinear asymptotic coupling theory, *J. Geophys. Res.*, 101, 22245-22272, 1996.
- Liu, H. P., D. L. Anderson, and H. Kanamori, Velocity dispersion due to anelasticity; implications for seismology and mantle composition, *Geophys. J. R. Astr. Soc.*, 47, 41-58, 1976.
- Liu X-F, Dziewonski A. M., Lowermost mantle shear wave velocity structure. *EOS Trans. AGU Fall Supplement*. 75:663, 1994.
- Loper, D.E., and T. Lay, The core-mantle boundary region, *J. Geophys. Res.*, 100, 6397-6420, 1995.
- Matzel, E., Sen, and S. Grand, Evidence for anisotropy in the deep mantle beneath Alaska, *Geophys. Res. Lett.*, 23, 2417-2420, 1996.
- Mitchell, B. J., and D. V. Helmberger, Shear velocities at the base of the mantle from observations of S and ScS, *J. Geophys. Res.*, 78, 6009-6019, 1973.
- Mohorovicic, A., Das Beben vom 8.x., jb, met, Obs, Zagreb, 9, 1-63, 1909.
- Montagner, J. P., Can seismology tell us anything about convection in the mantle ?, *Rev. Geophys.*, 32, 115-137, 1994.
- Morelli, A., and A. M. Dziewonski, The harmonic expansion approach to the retrieval of deep Earth structure, in *Seismic Tomography* (edited by Nolet, G.) D. Reidel publishing Company, 1987.
- Mori, J., and D. V. Helmberger, Localized boundary layer below the mid-pacific velocity anomaly identified from a PcP precursor, *J. Geophys. Res.*, 100, 20359-20365, 1995.
- Muirhead, K. J., Eliminating false alarms when detecting seismic events automatically, *Nature*, 217, 533-534, 1968.
- Müller, G., The reflectivity method: a tutorial, *J. Geophys.* 58, 153-174, 1985.
- Nakajima, J., T. Matsuzawa, and A. Hasegawa, Three-dimensional structure of Vp, Vs, and Vp/Vs beneath northeastern Japan: Implications for arc magmatism and fluids, *J. Geophys. Res.*, 106, 21,843-21,857, 2001.

- Nakajima, J., T Matsuzawa, and A. Hasegawa, Moho depth variation in the central part of northeastern Japan estimated from reflected and converted waves, *Phys. Earth Planet. Inter.*, 130, 31-47, 2002.
- Nataf, H. C., I. Nakanishi, and D. L. Anderson, Measurements of mantle wave velocities and inversion for lateral heterogeneity and anisotropy, 3 Inversion, *J. Geophys. Res.*, 91, 7261-7307, 1986.
- Neidell, N. S., and M. T. Taner, Semblance and other coherency measures for multichannel data, *Geophysics*, 36, 482-497, 1971.
- Niazi, M., and D. L. Anderson, Upper mantle structure of western North America from apparent velocities of P waves, *J. Geophys. Res.*, 70, 4633-4640, 1965.
- Niu, F., and H. Kawakatsu, Direct evidence for the undulation of the 660-km discontinuity beneath Tonga: Comparison of Japan and California array data, *Geophys. Res. Lett.*, 22, 531-534, 1995.
- Niu, F., and L. Wen, Strong seismic scatterers near the core-mantle boundary west of Mexico, *Geophys. Res. Lett.*, 28, 3557-3560, 2001.
- Pulliam, J., and M. K. Sen, Seismic anisotropy in the core-mantle transition zone, *Geophys. J. Int.*, 135, 113-128, 1998.
- Reasiner, C., and J. Revenaugh, ScP constraints on ultralow-velocity zone density and gradient thickness beneath the Pacific, *J. Geophys. Res.*, 105, 28173-28182, 1997.
- Revenaugh, J., A scattered-wave image of subduction beneath the transverse ranges, *Science*, 268, 1888-1892, 1995.
- Revenaugh, J., and R. Meyer, Seismic evidence of partial melt within a possibly ubiquitous low velocity layer at the base of the mantle, *Science*, 277, 670-673, 1997.
- Richards, P. G., Seismic waves reflected from velocity gradient anomalies within the Earth's upper mantle, *Z. Geophys.*, 38, 517-527, 1972.
- Richards, M. A., and C. W. Wicks, Jr, S-P conversions from the transition zone beneath Tonga and the nature of the 670 km discontinuity, *Geophys. J. Int.*, 101, 1-35, 1990.
- Ritsema, J., E. Garnero, and T. Lay, A strongly negative shear velocity gradient and lateral variability in the lowermost mantle beneath the Pacific, *J. Geophys. Res.*, 102, 20395-20411, 1997.
- Ritsema, J., E. Garnero, T. Lay, and H. Benz, Seismic anisotropy in the lowermost mantle beneath the Pacific, *Geophys. Res. Lett.*, 25, 1229-1232, 1998.
- Ritsema, J., H. Jan van Heijst, and J. H. Woodhouse, Complex shear wave velocity structure imaged beneath Africa and Iceland, *Science*, 286, 1925-1928, 1999.
- Romanowicz, B., 3D models of elastic and inelastic structure in the mantle, *EOS Trans AGU*, 78, F466, 1997.
- Romanowicz, B., Attenuation tomography of the earth's mantle: a review of current status, *Pageoph.*,

- 153, 257-272, 1998.
- Russell, S. A., T. Lay, and E. J. Garnero, Seismic evidence for small-scale dynamics in the lowermost mantle at the root of the Hawaiian hotspot, *Nature*, 396, 255-258, 1998.
- Russell, S. A., T. Lay, and E. J. Garnero, Small-scale lateral shear velocity and anisotropy heterogeneity near the core-mantle boundary beneath the central Pacific imaged using broadband ScS waves, *J. Geophys. Res.*, 104, 13183-13199, 1999.
- Russell, S. A., C. Reasoner, T. Lay, and J. Revenaugh, Coexisting shear- and compressional-wave seismic velocity discontinuities beneath the central Pacific, *Geophys. Res. Lett.*, 28, 2281-2284, 2001.
- Rybach, L., Radioactive heat production in rocks and its relation to other petrophysical parameters, *Pure Appl. Geophys.*, 114, 309-318, 1976.
- Scherbaum, F., F. Krüger, and M. Weber, Double beam imaging: Mapping lower mantle heterogeneities using combinations of source and receiver arrays, *J. Geophys. Res.*, 102, 507-522, 1997.
- Sheriff, R. E., Encyclopedia dictionary of exploration geophysics: *Soc. Explor. Geophys.*, Tulsa., 1984.
- Schimmel, M., and H. Paulssen, Noise reduction and detection of weak, coherent signals through phase-weighted stacks, *Geophys. J. Int*, 130, 497-505, 1997.
- Schlittenhardt, J., Investigation of the velocity and Q-structure of the lowermost mantle using PcP/P amplitude ratios from arrays at distances of 70° – 84°, *J. Geophys.*, 60, 1-18, 1986.
- Shibutani, T., K. Hirahara, and M. Kato, P-wave Velocity Discontinuity in D'' layer beneath Western Pacific with J-Array Records, *The Earth's Central Part: Its Structure and Dynamics*, edited by T. Yukutake, pp.1-11, 1995.
- Sidorin, I., M. Gurnis, and D. V. Helmberger, Dynamics of a phase change at the base of the mantle consistent with seismological observations, *J. Geophys. Res.*, 104, 15005-15023, 1999.
- Spudich, P., and T. Bostwick, Studies of the seismic coda using an earthquake cluster as a deeply buried seismograph array, *J. Geophys. Res.*, 92, 10526-10546, 1987.
- Stammler, K., Seismic Handler – Programmable multichannel data handler for interactive and automatic processing of seismological analysis. *Computer and Geosciences*, 19, 135-140, 1993.
- Su, W., R. L. Woodward, and A. M. Dziewonski, Degree 12 model of shear velocity heterogeneity in the mantle, *J. Geophys. Res.*, 99, 6945-6980, 1994.
- Taner, M. T., and F. Koehler, Velocity spectra-digital derivation and applications of velocity functions, *Geophys.*, 84, 859-881, 1969.
- Tanimoto, T., The three dimensional shear wave structure in the mantle by overtone waveform inversion 1. Radial seismogram inversion, *Geophys. J. R. Astron. Soc.*, 89, 713-740, 1987.
- Tanimoto, T., The 3-D shear wave structure in the mantle by overtone waveform inversion 2.

- Inversion of X-waves, R-waves and G-waves, *Geophysical Journal*, 93, 321-334, 1988.
- Thomas, C., and M. Weber, P velocity heterogeneities in the lower mantle determined with the German Regional Seismic Network: improvement of previous models and results of 2D modeling, *Phys. Earth Planet. Inter.*, 101, 105-117, 1997.
- Thomas, C., M. Weber, A. Agnon, and A. Hofstetter, A low-velocity lamella in D', *Geophys. Res. Lett.* 25, 2885-2888, 1998.
- Thomas, C., M. Weber, C. W. Wicks, and F. Scherbaum, Small scatterers in the lower mantle observed at German broadband arrays, *J. Geophys. Res.*, 104, 15073-15088, 1999.
- Tkalèœ, H., B. Romanowicz, and N. Houy, Constraints on D'' structure using PKP(AB-DF), PKP(BC-DF) and PcP-P travelttime data from broad-band records, *Geophys. J. Int.*, 148, 599-616, 2002.
- Tozer, D. C., The present thermal state of the terrestrial planets, *Phys. Earth Planet. Inter.*, 6, 182-197, 1972.
- Ungerer, J., diploma thesis at the University of Stuttgart, 1990.
- Valenzuela, R. W., and M. E. Wysession, Illuminating the base of the mantle with core-diffracted waves, in *Observational and Theoretical Constraints on the Core-Mantle Boundary Region*, *Geodynam. Ser.*, vol. 28, edited by M. Gurnis et al., pp. 57-71, AGU, Washington, D. C., 1998.
- Valenzuela, R. W., M. E. Wysession, M. O. Neustadt, and J. Butler, Lateral variations at the base of the mantle from profiles of digital S<sub>diff</sub> data, *J. Geophys. Res.*, 105, 6201-6220, 2000.
- Van der Hilst, R. D., E. R. Engdahl, W. Spakman, and G. Nolet, Tomographic imaging of subducted lithosphere below northwest Pacific island arcs, *Nature*, 353, 37-43, 1991.
- Van der Hilst, R. D., E. R. Engdahl, and W. Spakman, Tomographic inversion of P and pP data for aspherical mantle structure below the northwest Pacific region, *Geophys. J. Int.*, 115, 264-302, 1993.
- Van der Hilst, R. D., Complex morphology of subducted lithosphere in the mantle beneath the Tonga trench, *Nature*, 374, 154-157, 1995.
- Van der Hilst, R. D., S. Widiyantoro, and E. R. Engdahl, Evidence for deep mantle circulation from global tomography, *Nature*, 386, 578-584, 1997.
- Vidale, J. E., and H. M. Benz, Seismological mapping of fine structure near the base of the Earth's mantle, *Nature*, 361, 529-532, 1993.
- Vidale, J. E., and M. A. H. Hedlin, Evidence for partial melt at the core-mantle boundary north of tonga from the strong scattering of seismic waves, *Nature*, 391, 682-685, 1998.
- Vinnik, L. P., V. Farra, and B. Romanowicz, Observational evidence for diffracted SV in the shadow of the Earth's core, *Geophys. Res. Lett.*, 16, 519-522, 1989.
- Vinnik, L., B. Romanowicz, Y. LeStunff, L. Makeyeva, Seismic anisotropy in the D'' layer, *Geophys. Res. Lett.*, 22, 1657-1660, 1995.

- Vinnik, L., L. Breger, and B. Romanowicz, Anisotropic structures at the base of the Earth's mantle, *Nature*, 393, 564-567, 1998.
- Weber, M., and J. P. Davis, Evidence of a laterally variable lower mantle structure from P- and S waves, *Geophys. J. Int.*, 102, 231-255, 1990.
- Weber, M., and M. Koenig, A search for anomalies in the lowermost mantle using seismic bulletins, *Phys. Earth Planet. Int.*, 73, 1-28, 1992.
- Weber, M., P and S wave reflections from anomalies in the lowermost mantle, *Geophys. J. Int.*, 115, 183-210, 1993.
- Weber, M., Lamella in D' ? , An alternative model for lowermantle anomalies, *Geophys. Res. Lett.*, 21, 2531-2534, 1994.
- Wiens, D. A., Effects of near source bathymetry on teleseismic P waveforms, *Geophys. Res. Lett.*, 14, 761-764, 1987.
- Williams, Q., and E. J. Garnero, Seismic evidence of partial melt at the base of Earth's mantle, *Science*, 273,1528-1530, 1996.
- Woodhouse, J. H., and A. M. Dziewonski, Mapping the upper mantle: Three-dimensional modeling of earth structure by inversion of seismic waveforms, *J. Geophys. Res.*, 89, 5953-5986, 1984.
- Wright, C., and JA. Lyons, Further evidence for radial velocity anomalies in the lower mantle, *Pageoph*, 119, 137-162, 1980.
- Wright, C., K. J. Muirhead, and A. E. Dixon, The P wave velocity structure near the base of the mantle, *J. Geophys. Res.*, 90, 623-634, 1985.
- Wyssession, M. E., Continents of the core, *Nature*, 381, 373-374, 1996.
- Wyssession, M. E., Large-scale structure at the core-mantle boundary from diffracted waves, *Nature*, 382, 244-248, 1996.
- Wyssession, M. E., L. Bartko, and J. Wilson, Mapping the lowermost mantle using core-reflected shear waves, *J. Geophys. Res.*, 99, 13,667-13,684, 1994.
- Wyssession, M. E., T. Lay, J. Revenaugh, Q. Williams, E. J. Garnero, R. Jeanloz, and L. H. Kellog, The D' discontinuity and its implications, in *The Core-Mantle Boundary Region, Geodynam. Ser.*, 28, edited by M. Gurnis et al., pp. 273-297, AGU, Washington, D. C., 1998.
- Yamada, A., and I. Nakanishi, Detection of P-wave reflection in D" beneath the south-western Pacific using double-array stacking, *Geophys. Res. Lett.* 23, 1553-1556, 1996.
- Yamada, A., and I. Nakanishi, Short-wavelength lateral variation of a D" P-wave reflector beneath the southwestern Pacific, *Geophys. Res. Lett.*, 25, 4545-4548, 1998.
- Young, C. J., and T. Lay, Evidence for a shear wave velocity discontinuity in the lower mantle beneath India and the Indian Ocean, *Phys. Earth Planet. Inter.*, 49, 37-53, 1987.
- Young, C. J., and T. Lay, Multiple phase analysis of the shear velocity structure in the D' region beneath Alaska, *J. Geophys. Res.*, 95, B11, 17385-17402, 1990.



- Zhao, D., Y. Xu, D. A. Wiens, L. Dorman, J. Hiderbrand, and S. Webb, Depth extent of the Lau back-arc spreading center and its relation to subduction processes, *Science*, 278, 254-257, 1997
- Zhou, H.-W., Mapping of P-wave slab anomalies beneath the Tonga, Kermadec and New Hebrides arcs, *Phys. Earth Planet. Inter.*, 61, 199-229, 1990.

**Appendix. 1 Results in the RWB using synthetic data**

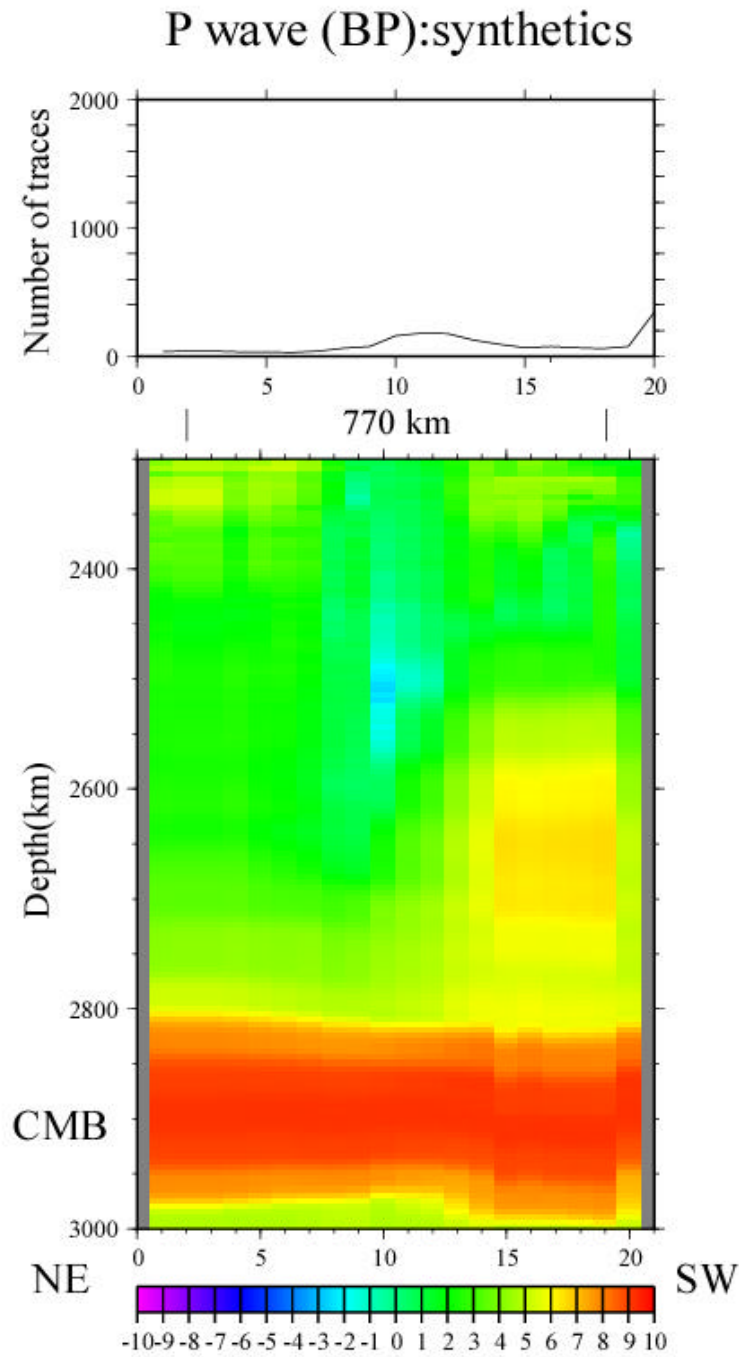


**Figure 1A** BP for P wave synthetic data with a  $-1\%$  velocity discontinuity at the depth of 2650 km. The introduced discontinuity is only in the subarray from 15-19.

**Appendix. 2 Diagrams of results by the RWB method**

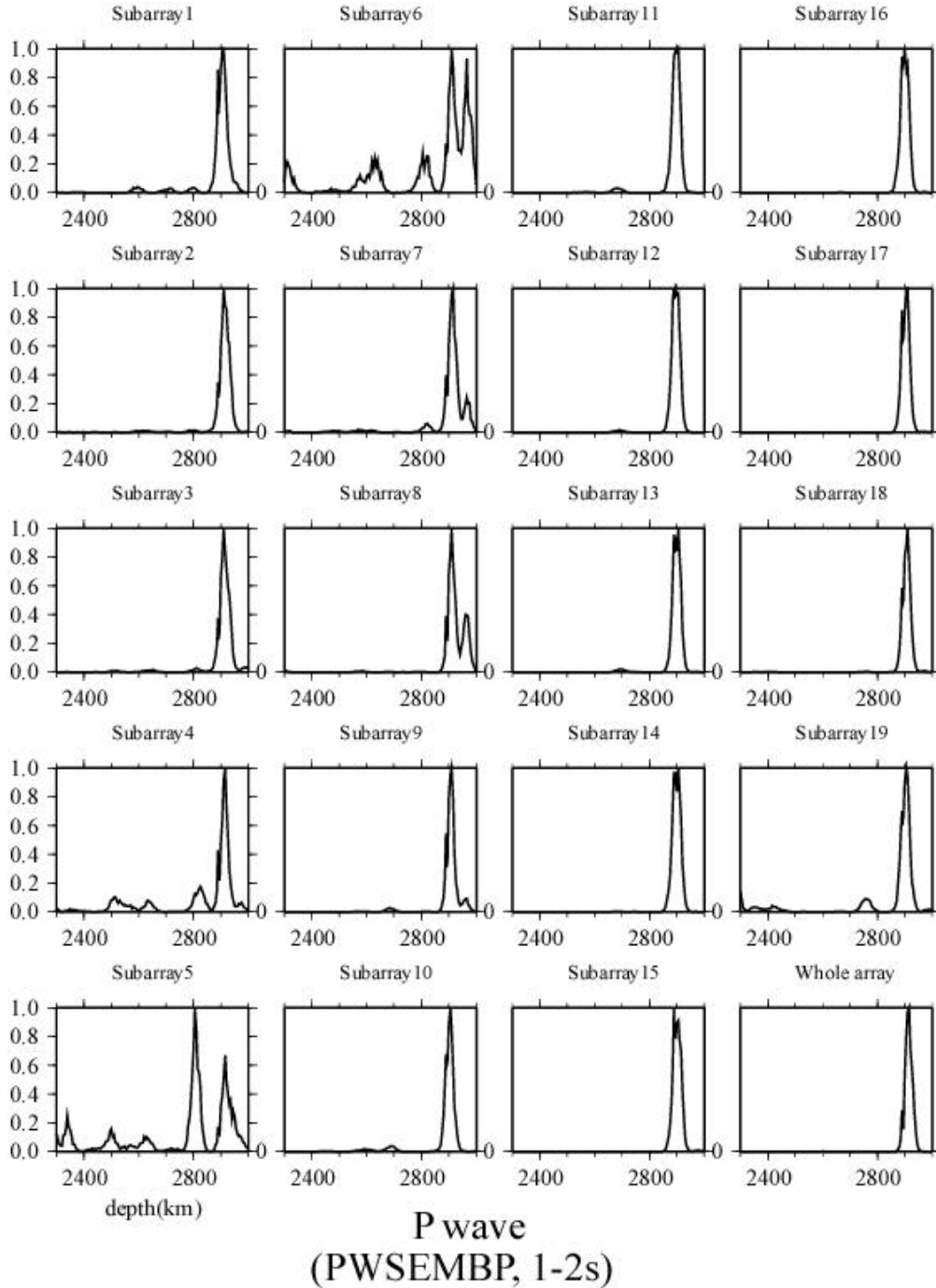


**Figure 1A.a** PWSEMBP from each synthetic discontinuity with P wave data in the frequency range of 1-2s. The values are normalized by the maximum energy of PcP. In each panel clear PcP phase can be seen. The last one labeled whole array was calculated using all traces, which could indicate the horizontally average, smoothed structure of the study area.

The width of 'PcP pulse' can be regarded as a reference resolution in the (vertical) depth direction.

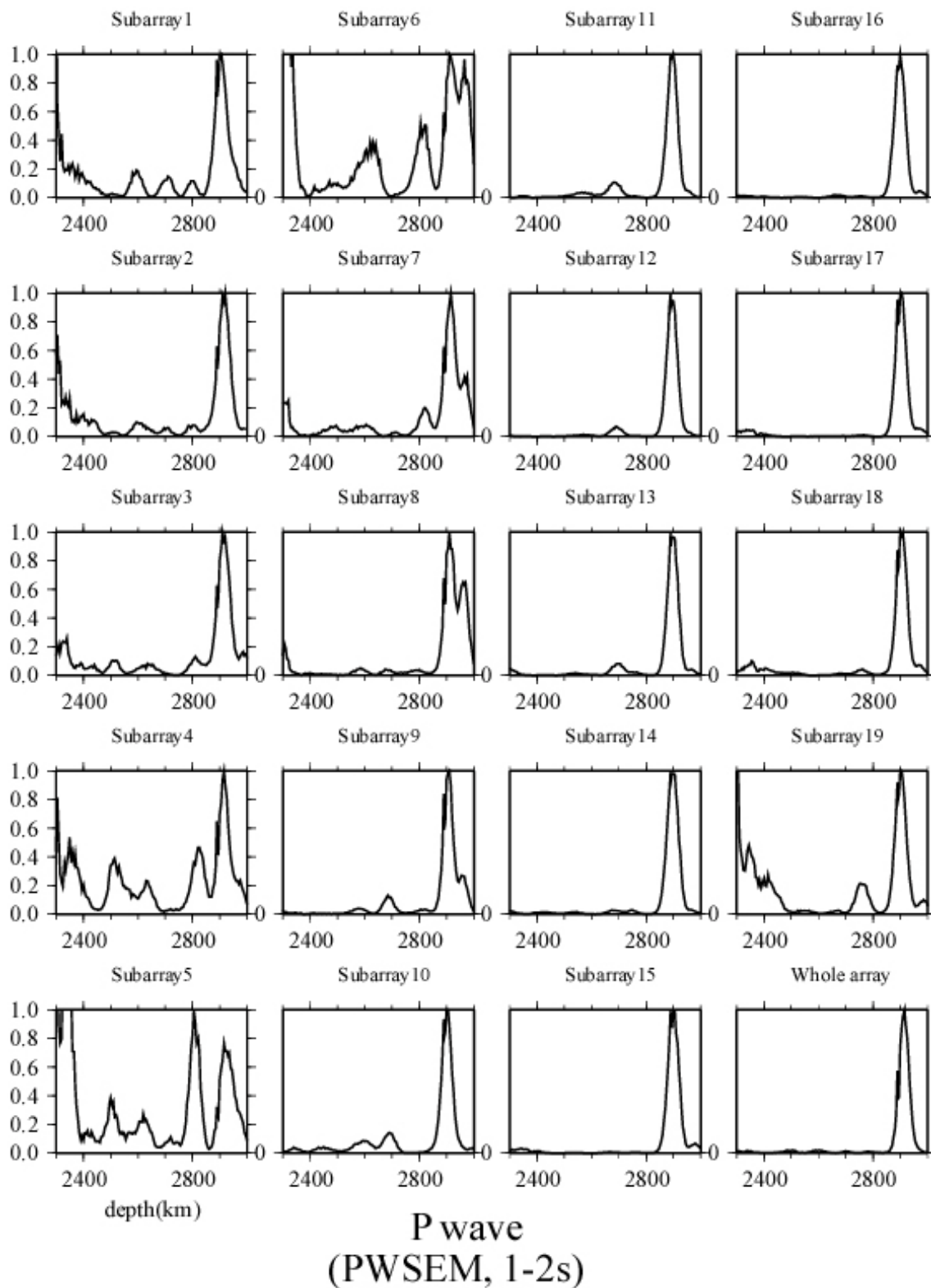
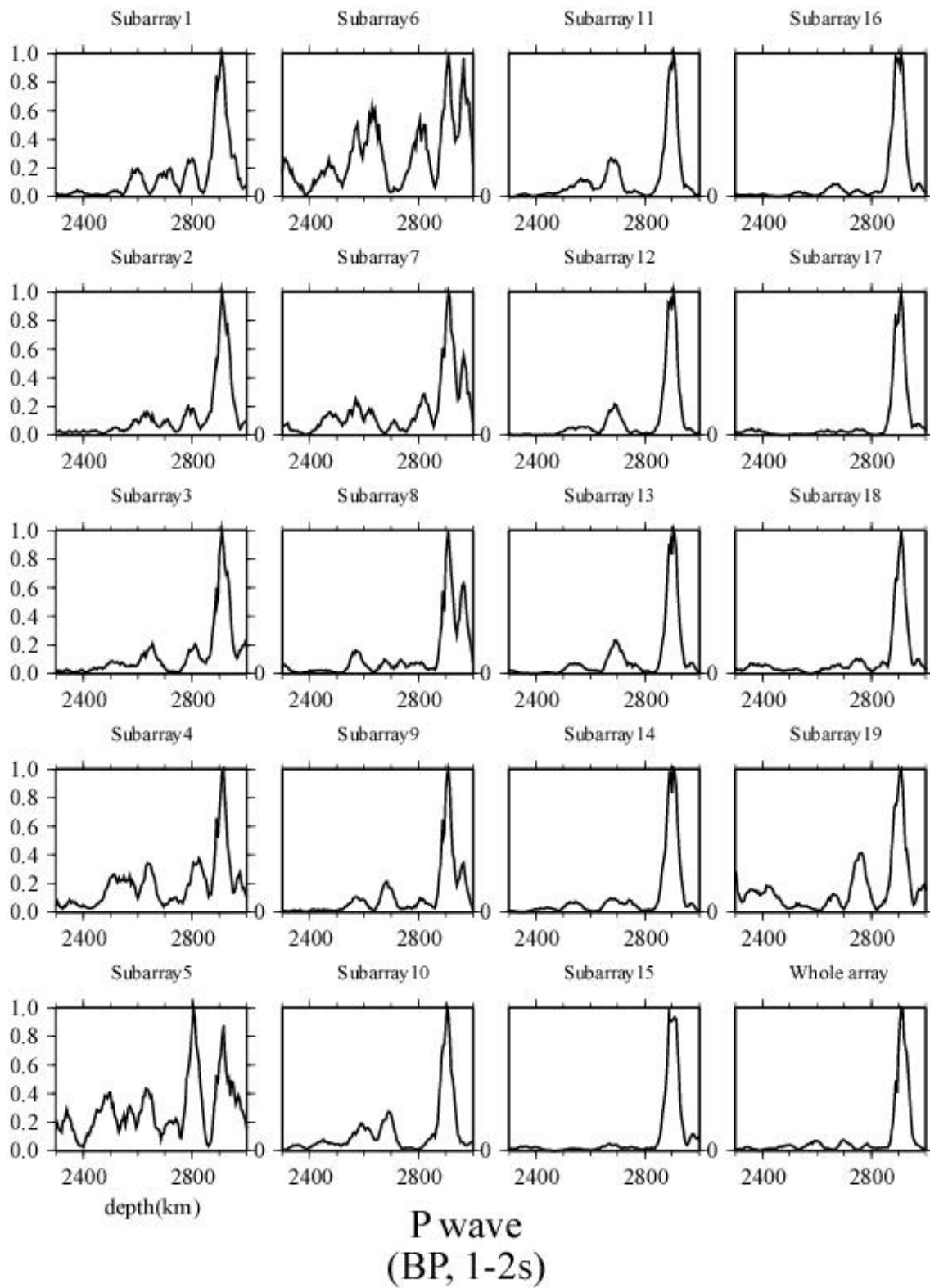
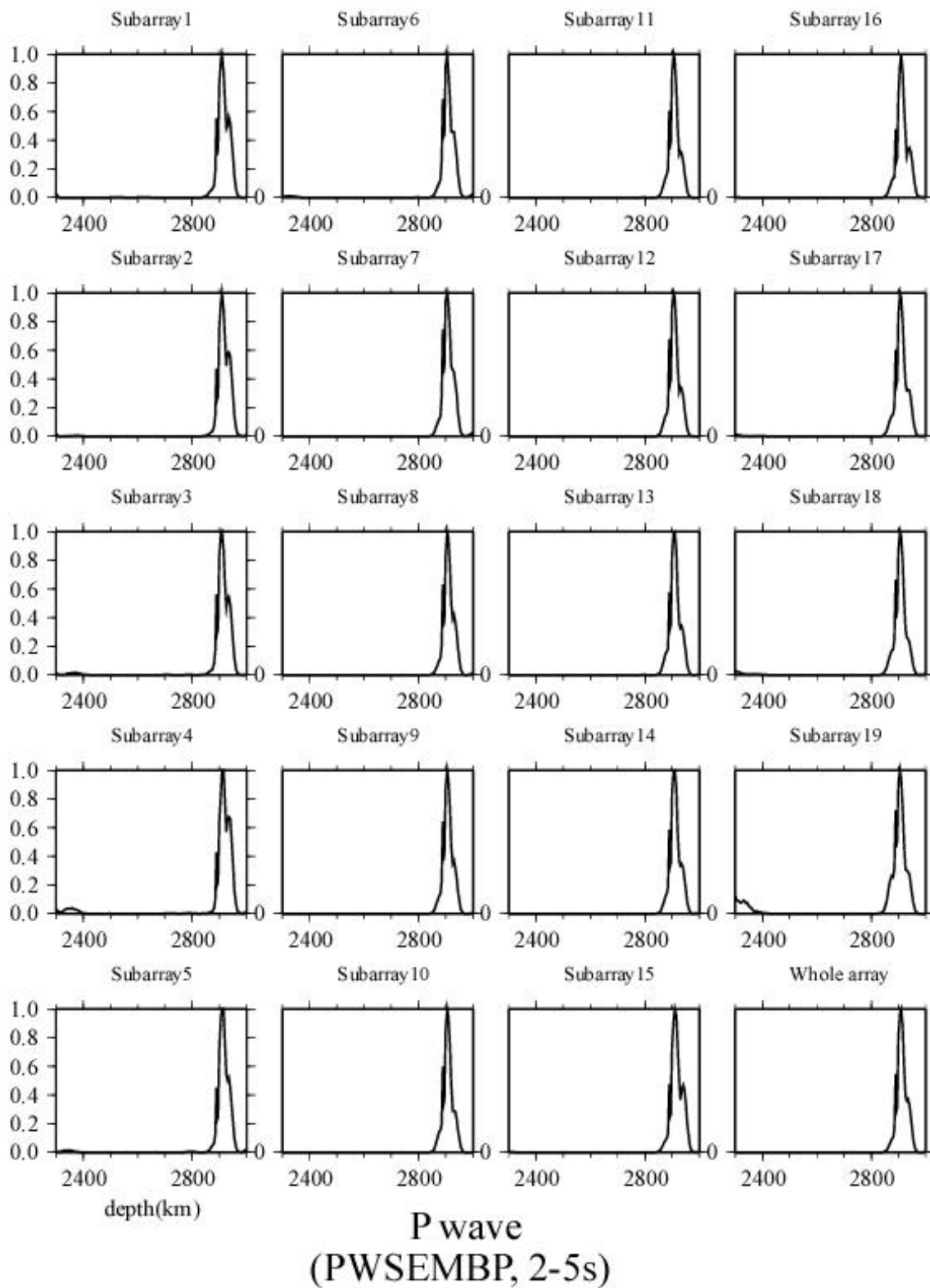


Figure 1A.b same as Figure 9.1A.a, but for PWSEM.



**Figure 1A.c** same as Figure 9.1A.a, but for BP.



**Figure 2A.a** same as Figure 1A.a, but with frequency band of 2-5s.

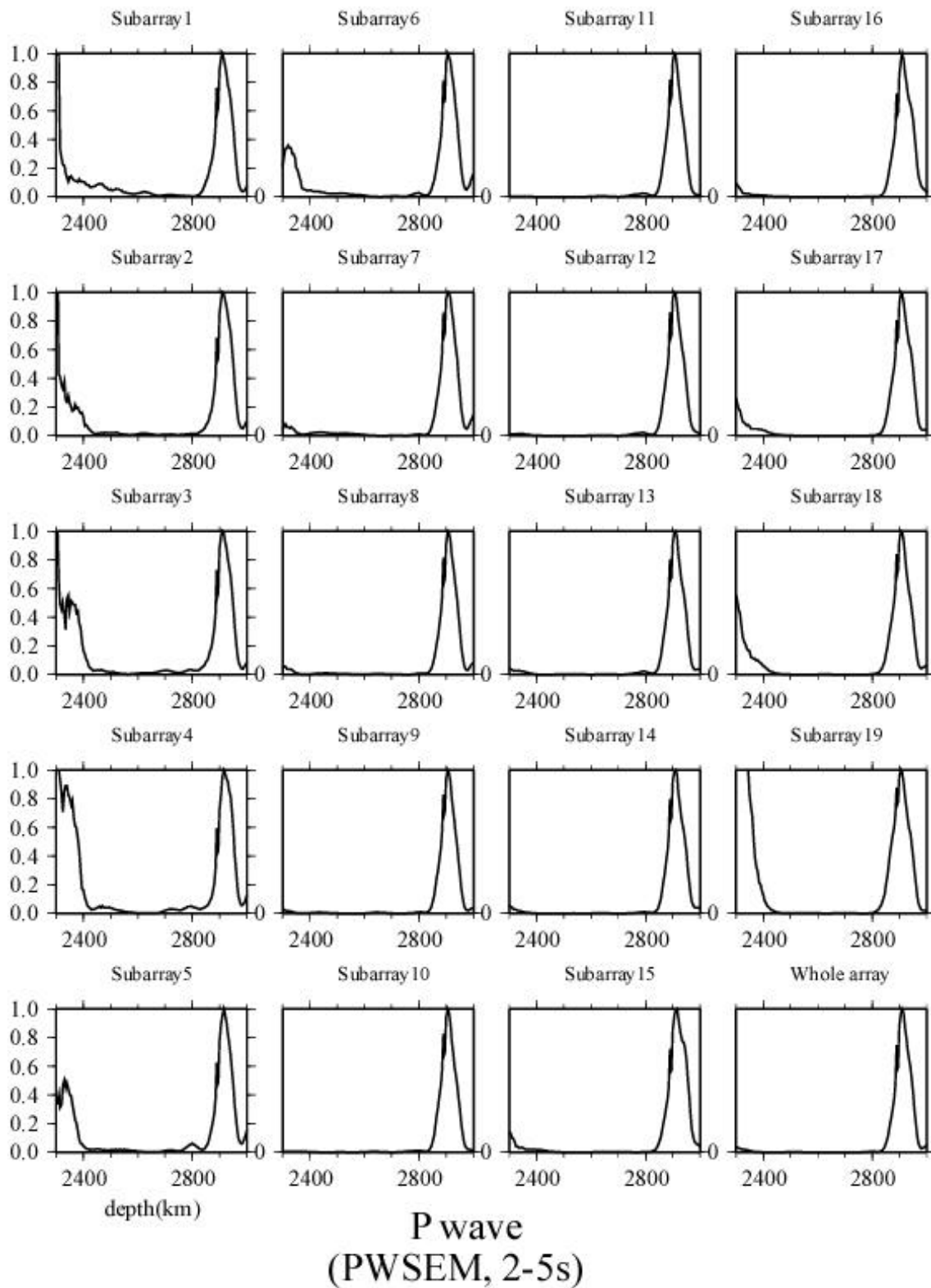


**Figure 2A.b** same as Figure 1A.b, but with frequency band of 2-5s.

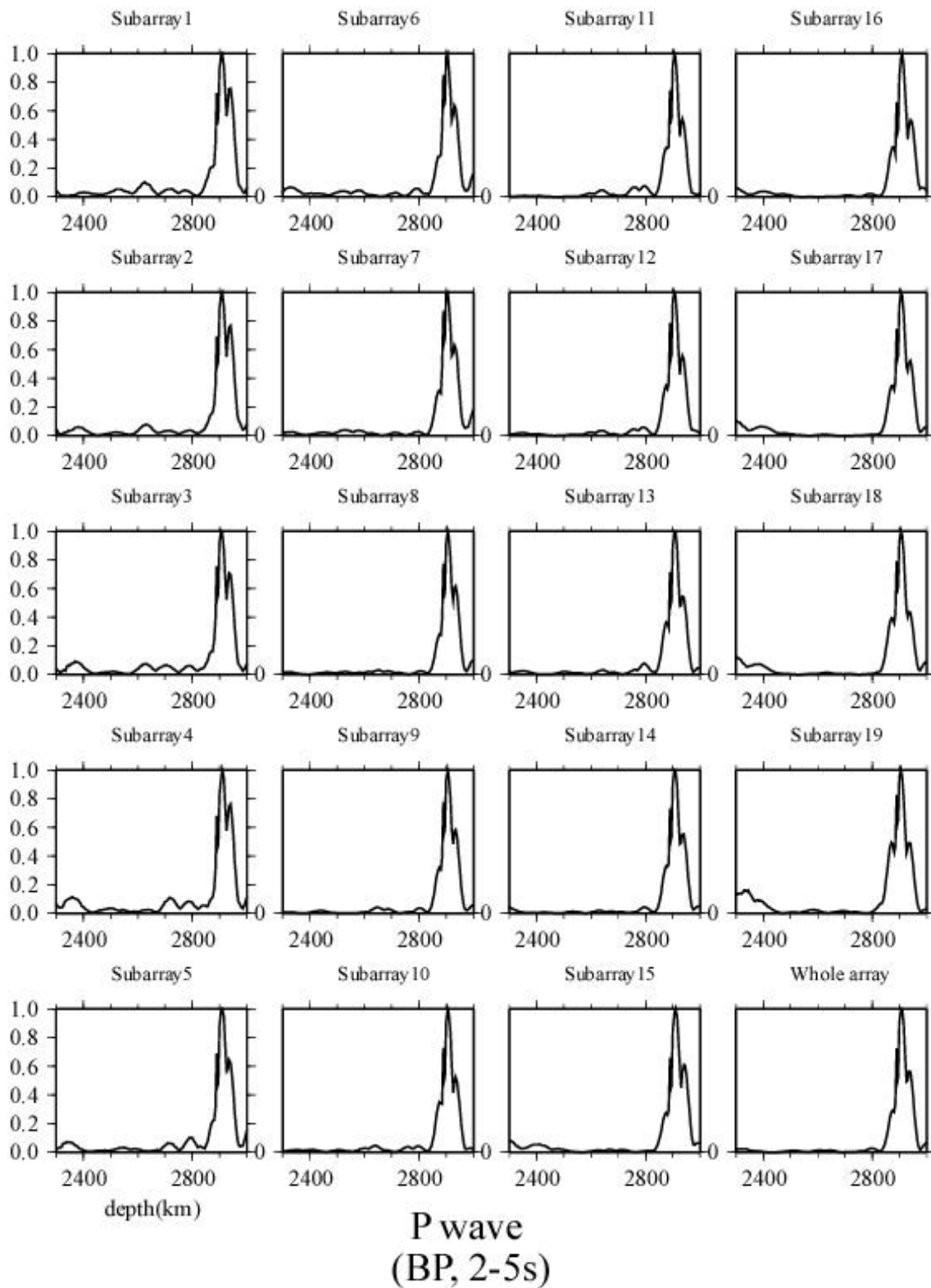


**Figure 2A.c** same as Figure 1A.c, but with frequency band of 2-5s.



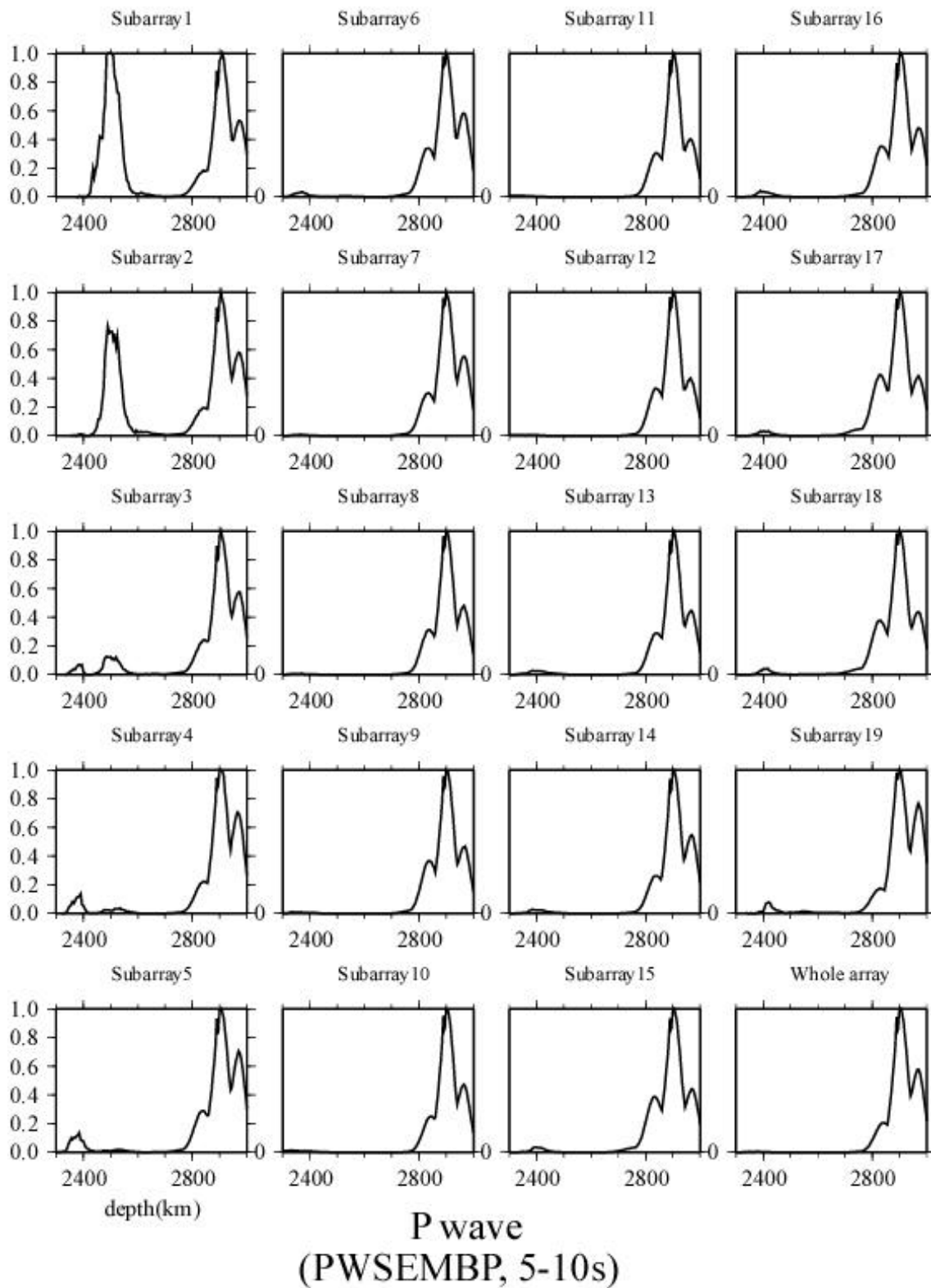


**Figure 3A.a** same as Figure 1A.a, but with frequency band of 5-10s.

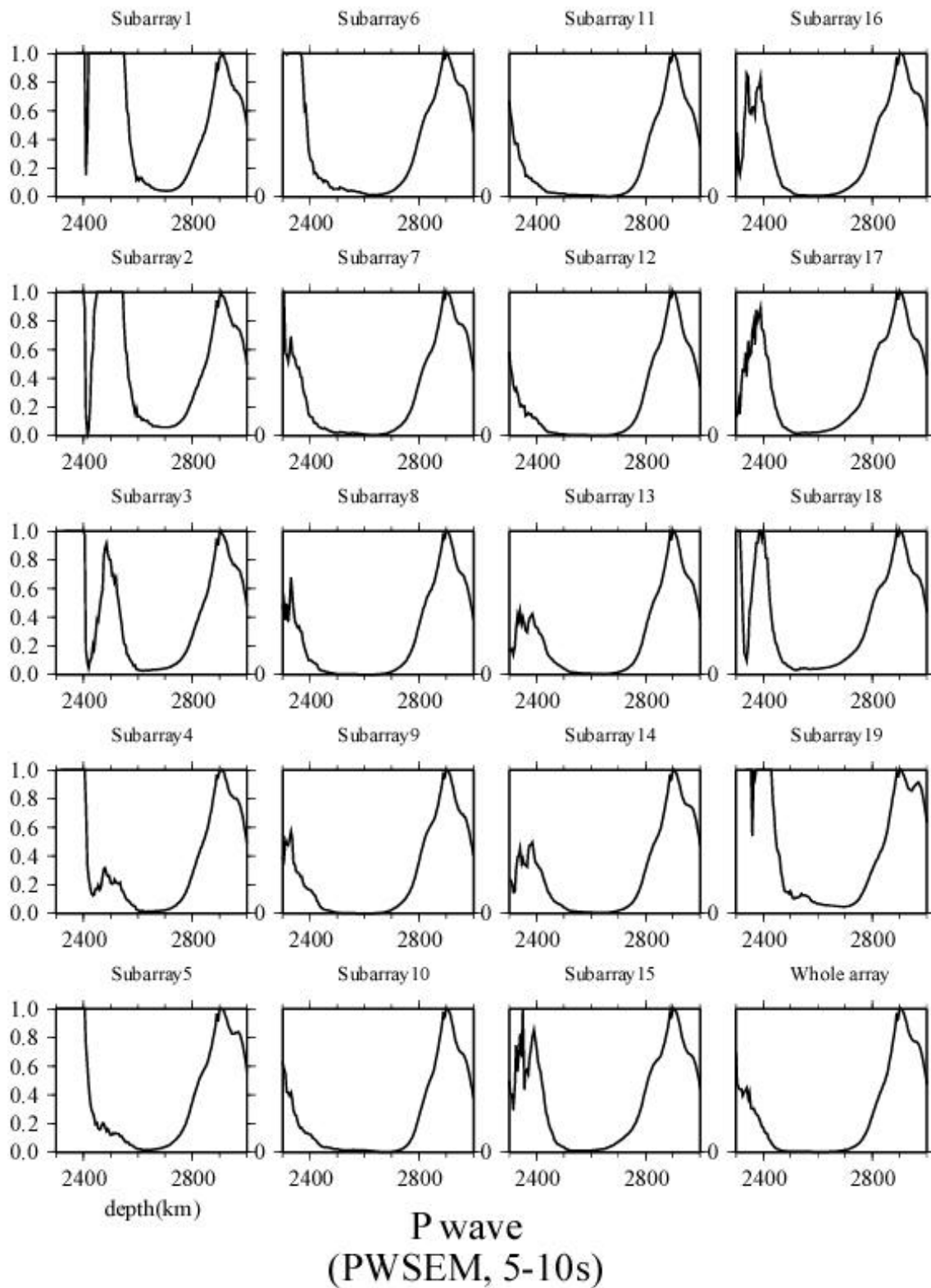


**Figure 3A.b** same as Figure 1A.b, but with frequency band of 5-10s.

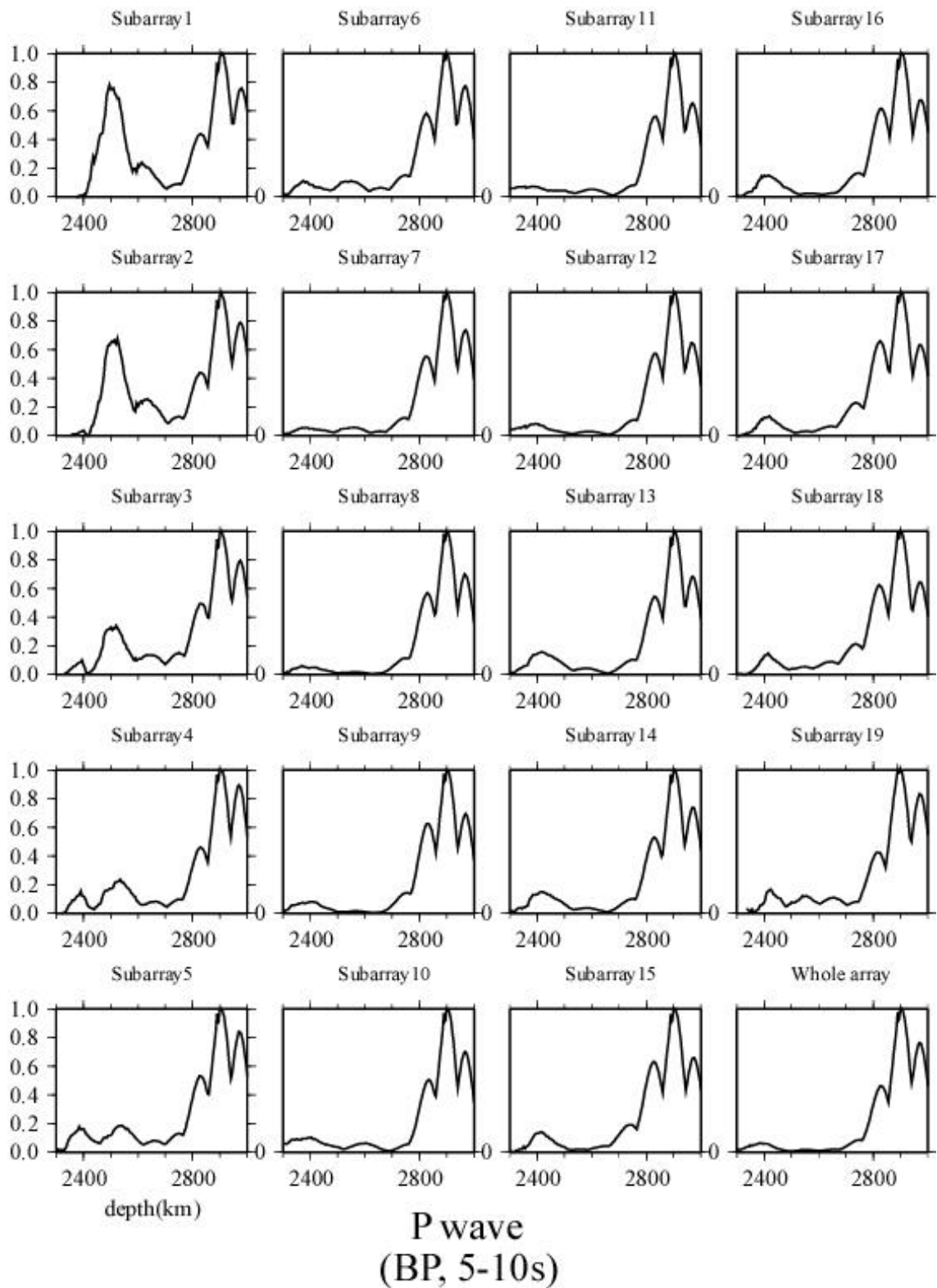


**Figure 3A.c** same as Figure 1A.c, but with frequency band of 5-10s.

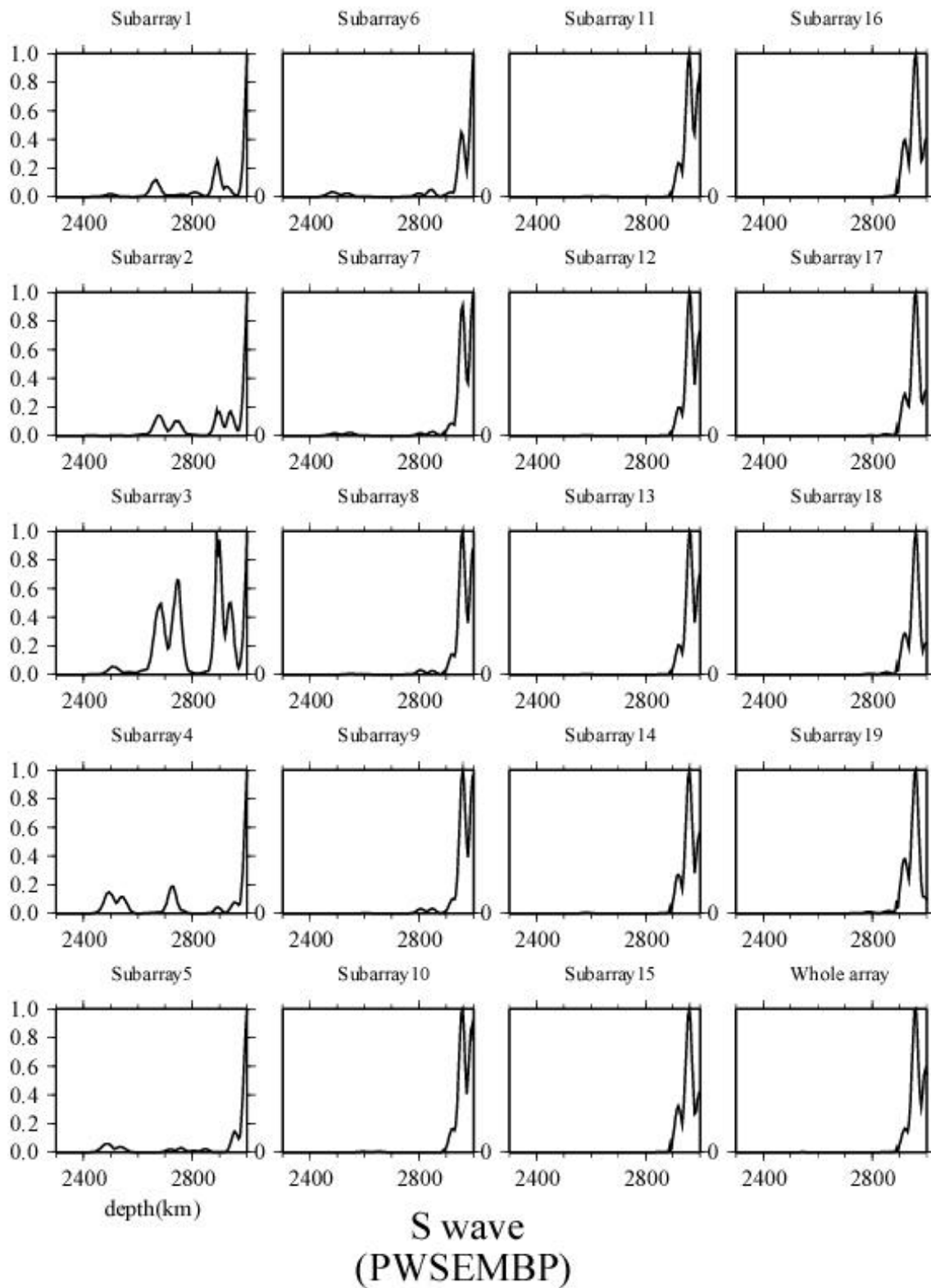


**Figure 4A.a** same as Figure 1A.a, but for S-wave.

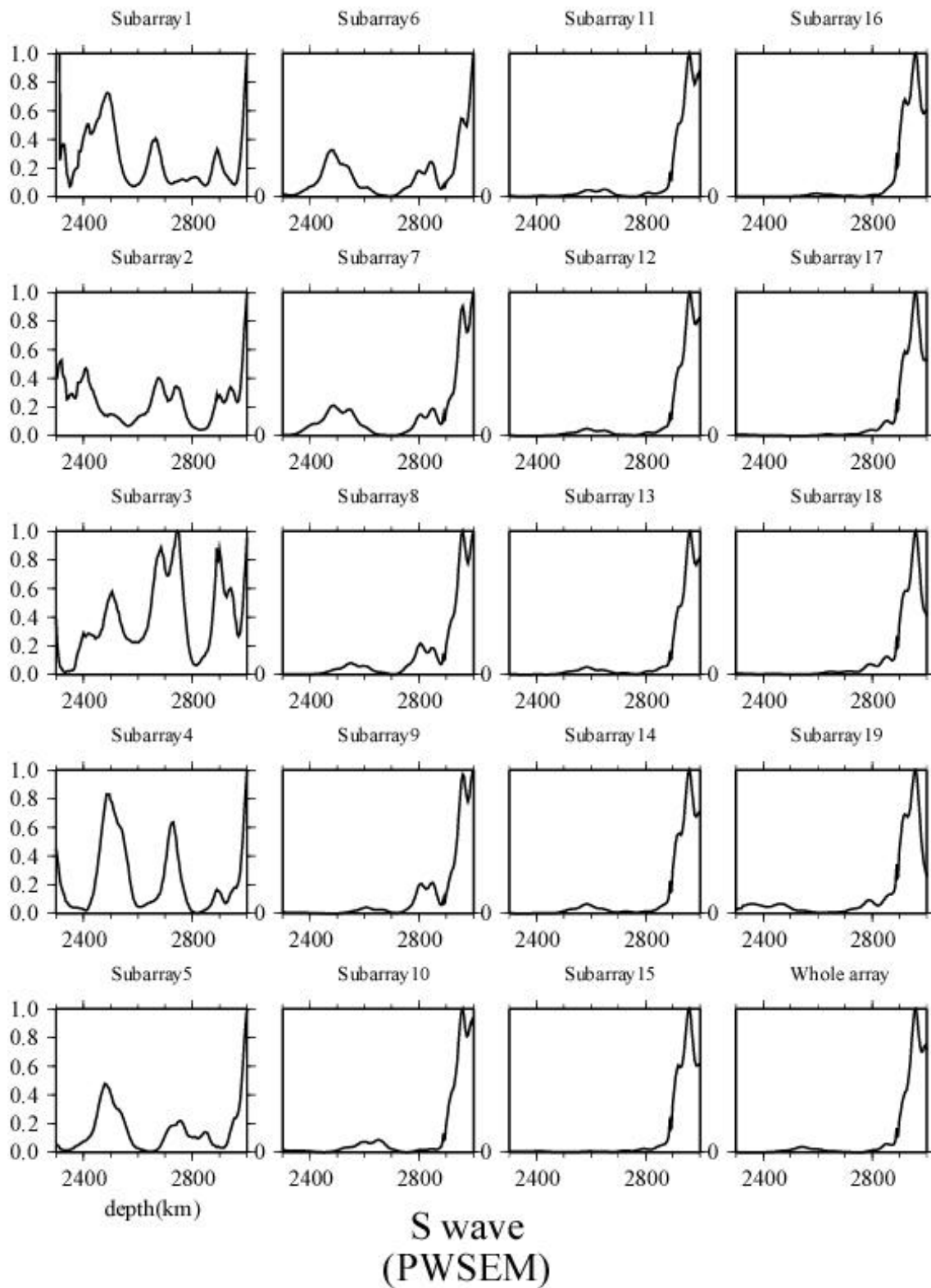


**Figure 4A.b** same as Figure 1A.b, but for S-wave.

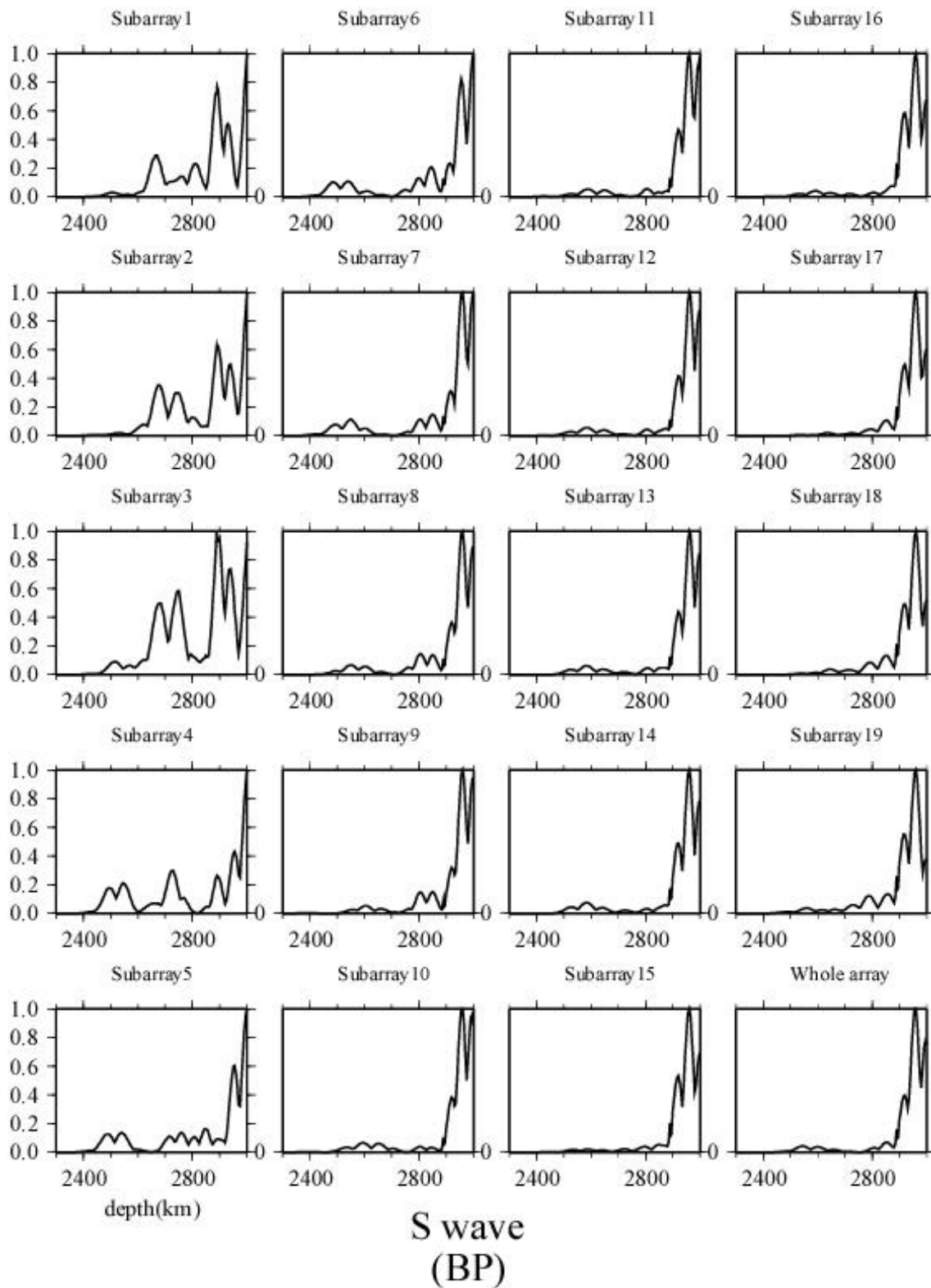


**Figure 4A.c** same as Figure 1A.c, but for S-wave.

**Appendix. 3 Diagrams with synthetic data for P wave (2-5s).**

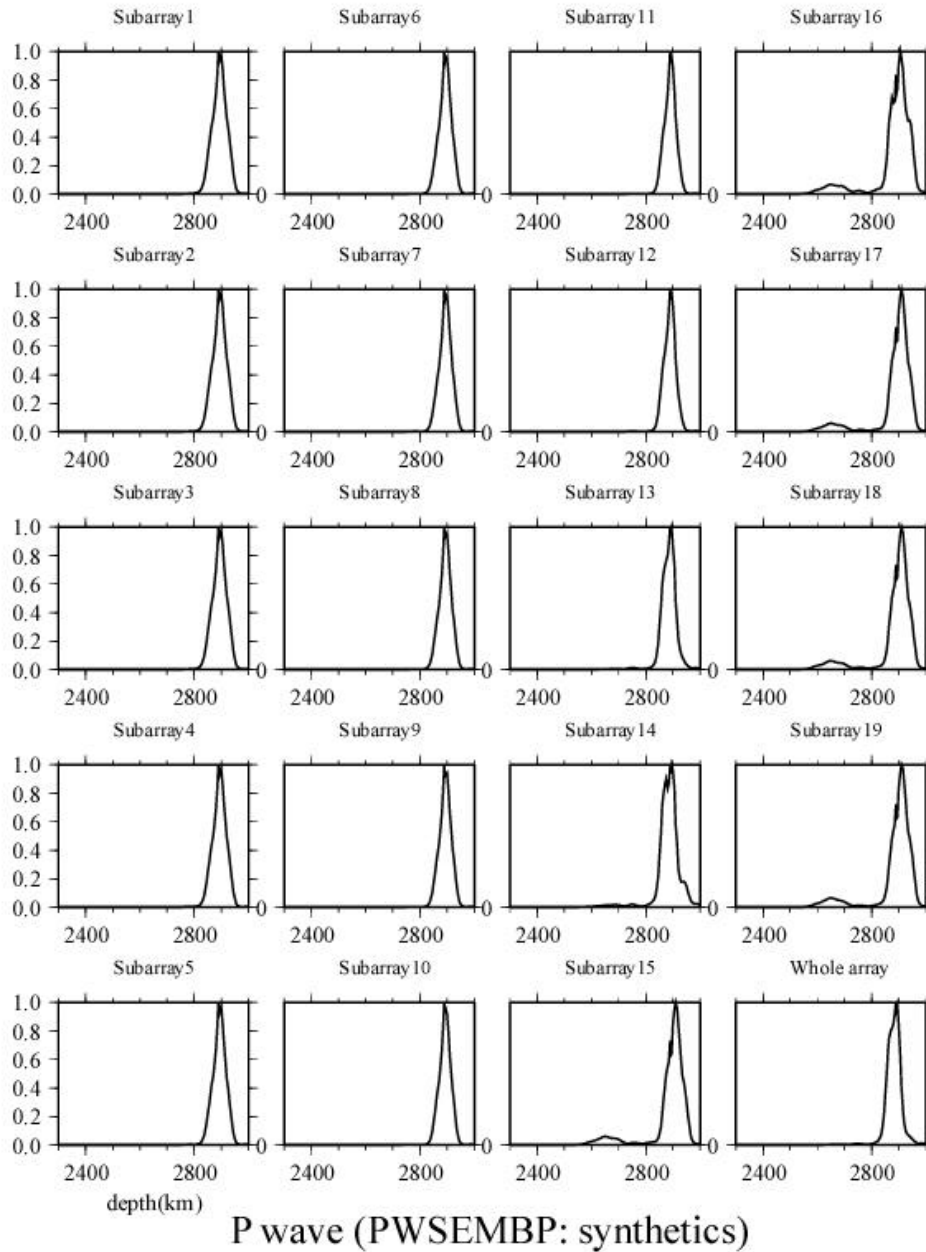


**Figure 1A.a** PWSEMBP from each synthetic discontinuity with synthetic data in the frequency band of 2-5s. The values are normalized by the maximum energy of PcP. The synthetic seismograms were calculated based on a model with a  $-1\%$  discontinuity at the depth of 2650 km, which were set in the subarray from 15-19 in order to examine the lateral resolution.

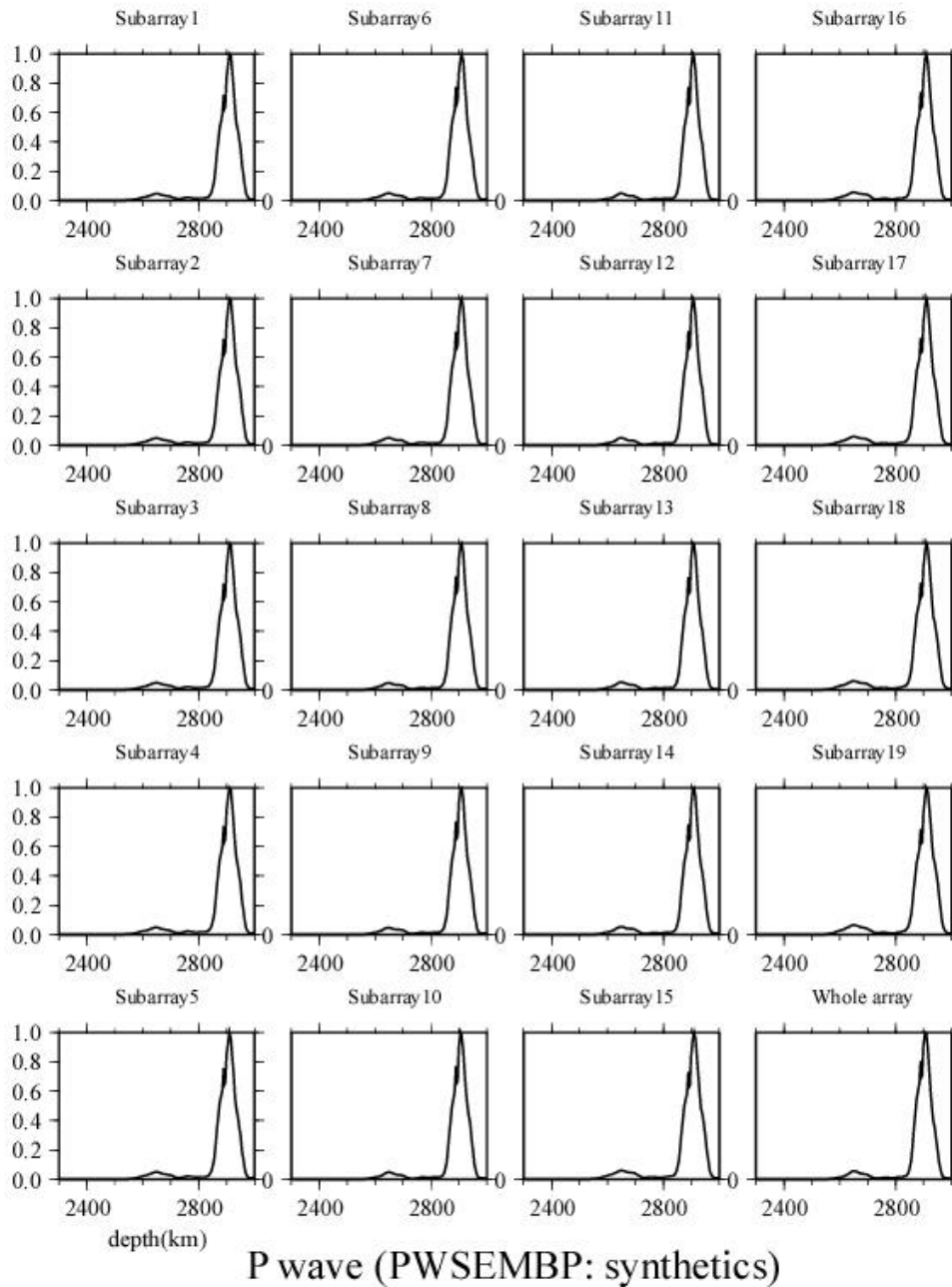


**Figure 1A.b** PWSEMBP from each synthetic discontinuity with synthetic data. The values are normalized by the maximum energy of PcP. The synthetic seismograms were calculated based on a model with a  $-1\%$  discontinuity at the depth of 2650 km. For S-wave synthetic data.



Appendix. 4. Results of the RWB for P wave (1-2s and 5-10s)

## P wave (PWSEMBP, 1-2s)

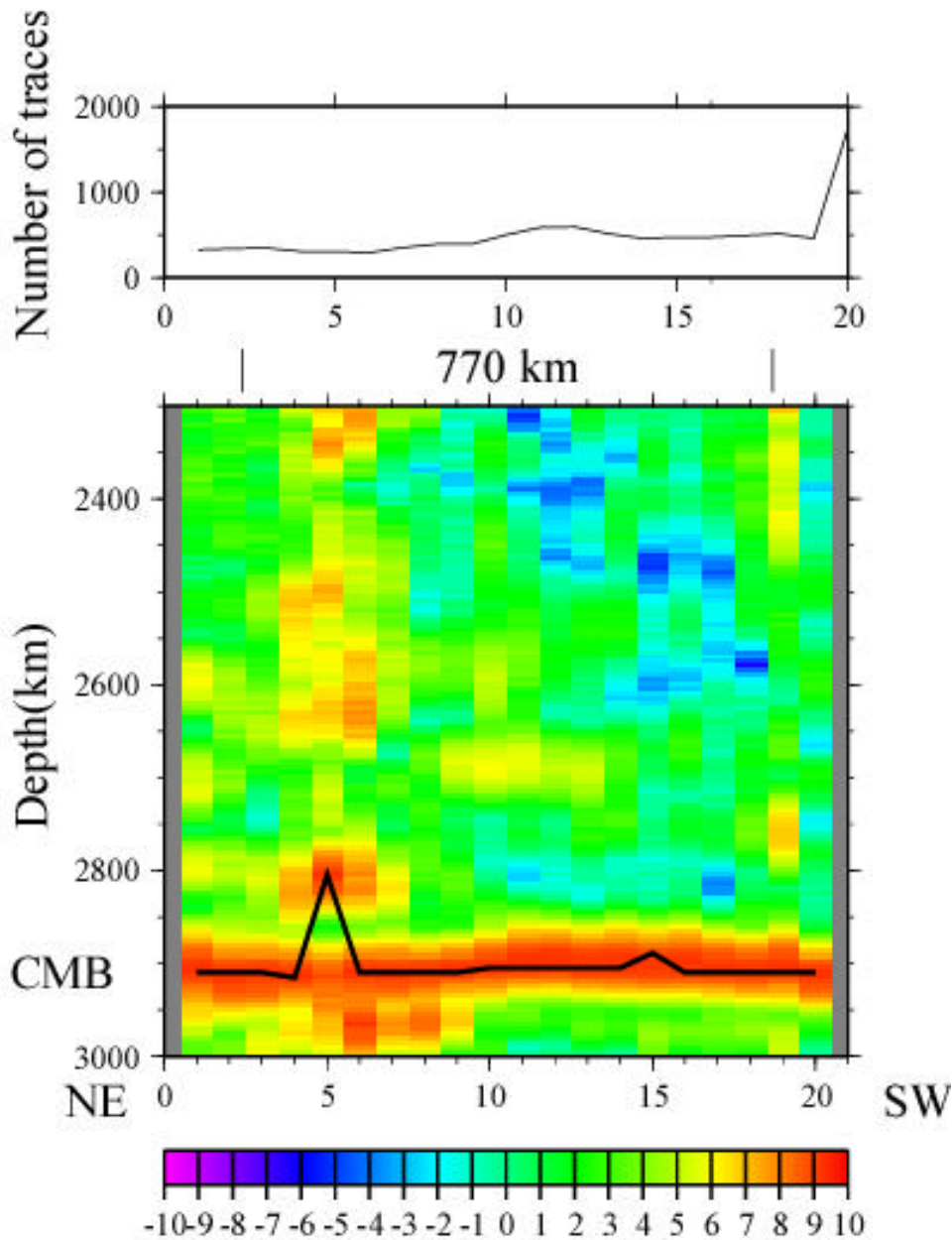


**Figure 1A.a** PWSEMBP, PWSEM and BP from each synthetic discontinuity with P wave data in the frequency range of 1-2s, respectively. The values are normalized by the maximum energy of PcP. In each panel clear PcP phase can be seen. From upper left to lower right the PWSEMBP, PWSEM and BP values in each subarray are plotted. The last one labeled whole array was calculated using all traces, which could indicate the horizontally average, smoothed structure of the study area. The PWSEMBP shows the lowest background noise in comparison with the other two coherency measures. The width of 'PcP pulse' can be regarded as a reference resolution in the (vertical) depth direction.

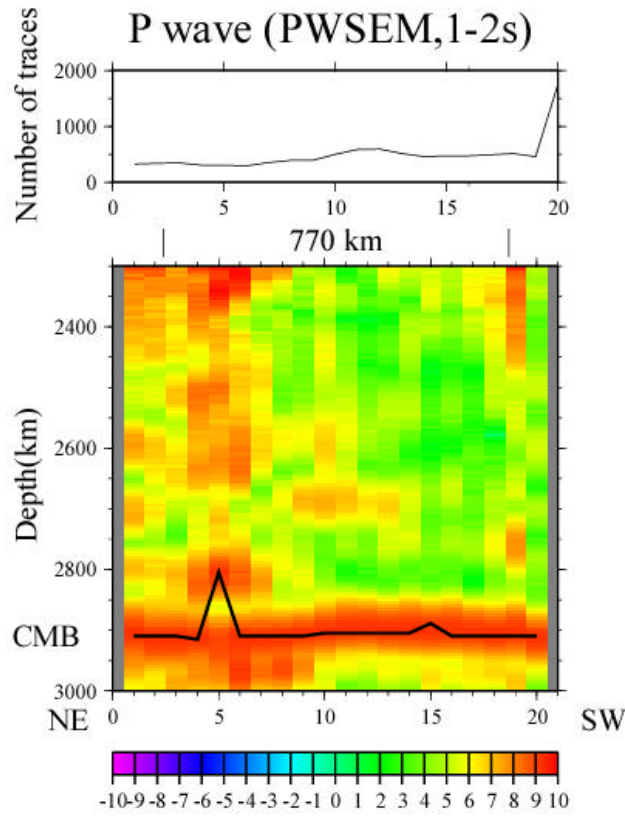


Figure 1A.b same as Figure 1A.a, but for PWSEM.

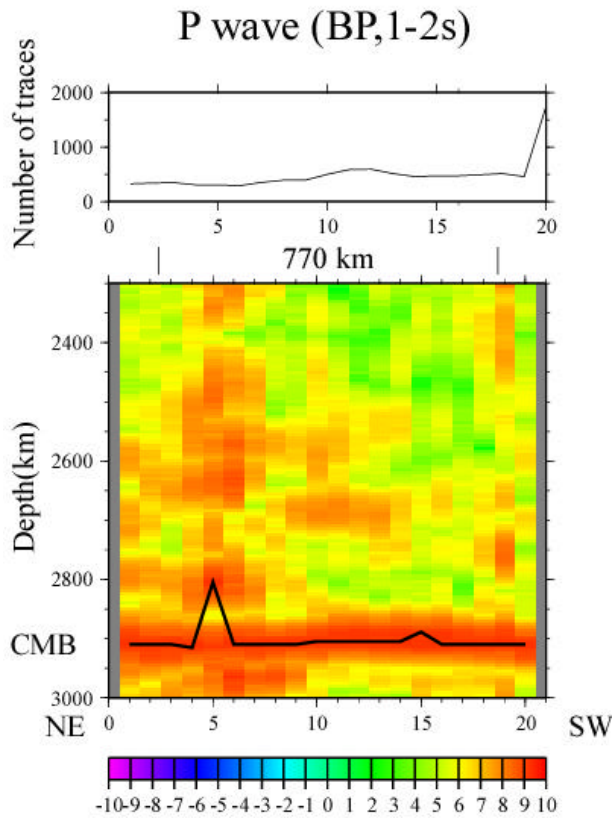
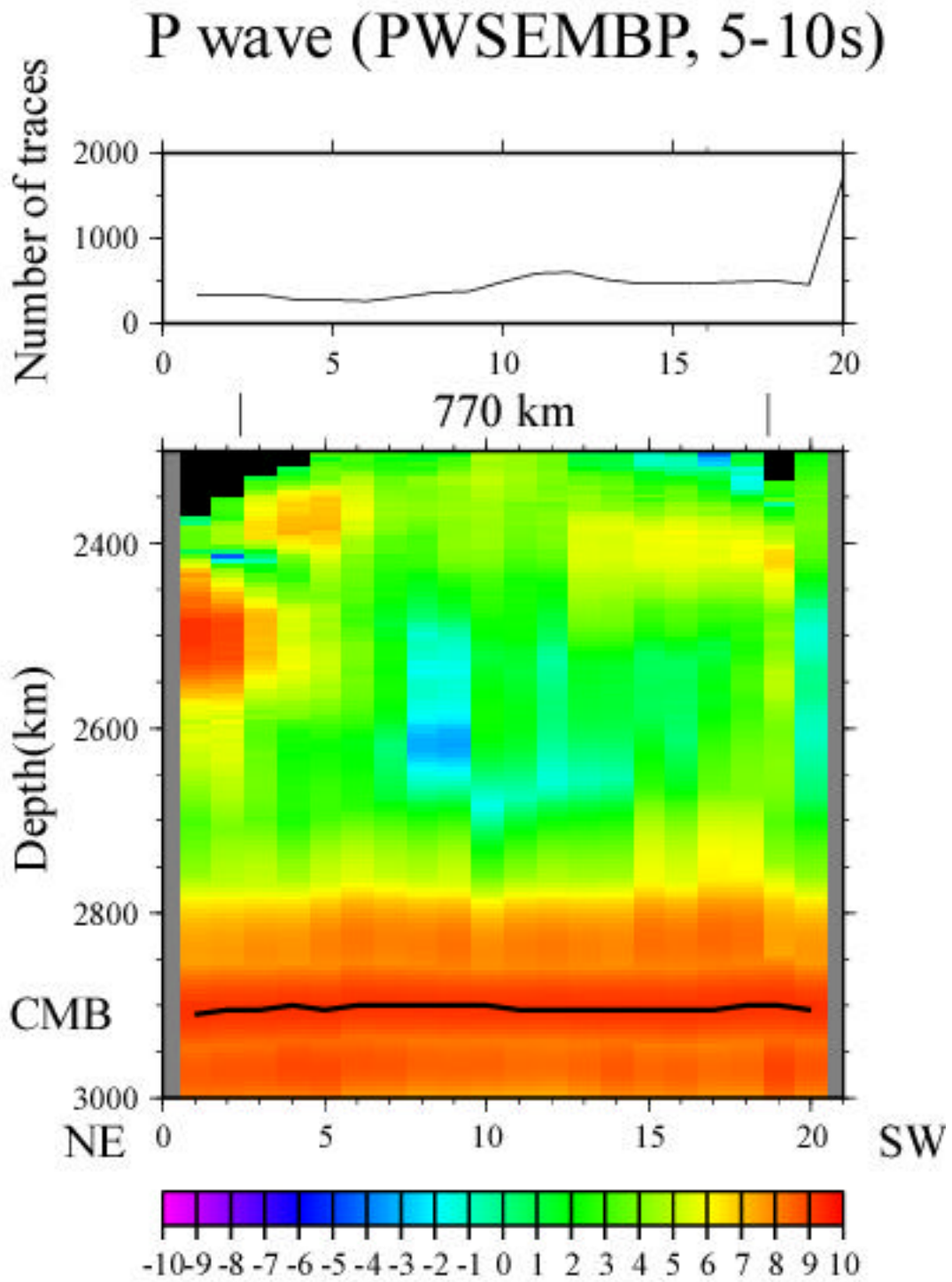
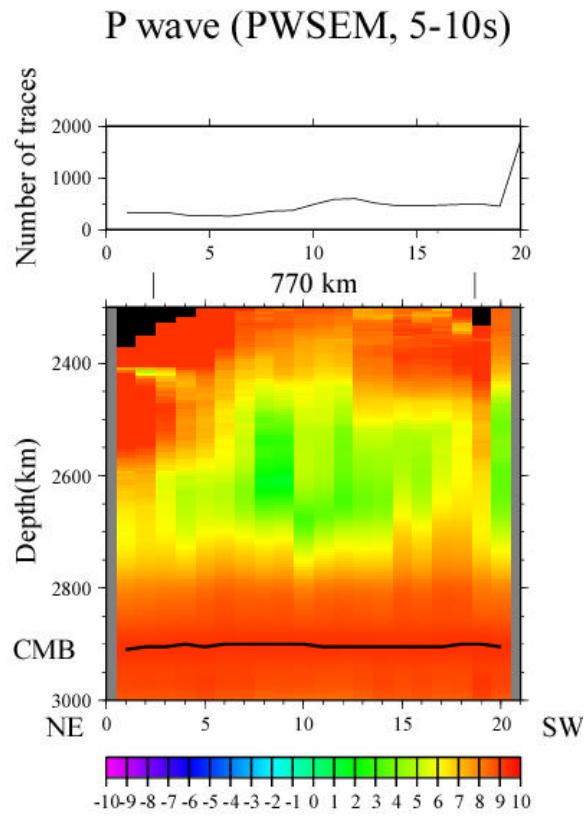


Figure 1A.c same as Figure 1A.a, but for BP.



**Figure 2A.a** same as Figure 1A.a, but in the frequency band of 5-10s.



**Figure 2A.b** same as Figure 1A.b, but in the frequency band of 5-10s.

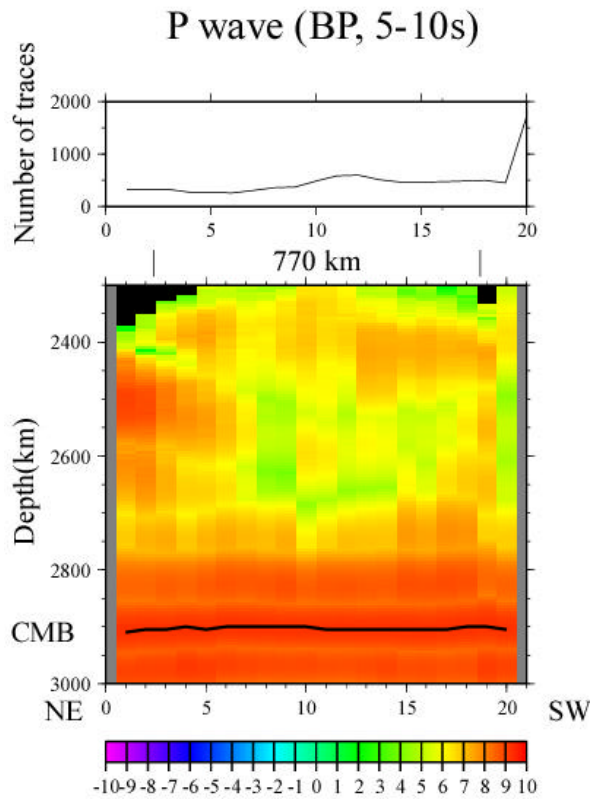


**Figure 2A.c** same as Figure.1A.c, but in the frequency band of 5-10s.

Appendix. 5. Results of the RWB for P (2-5s) without upper mantle correction

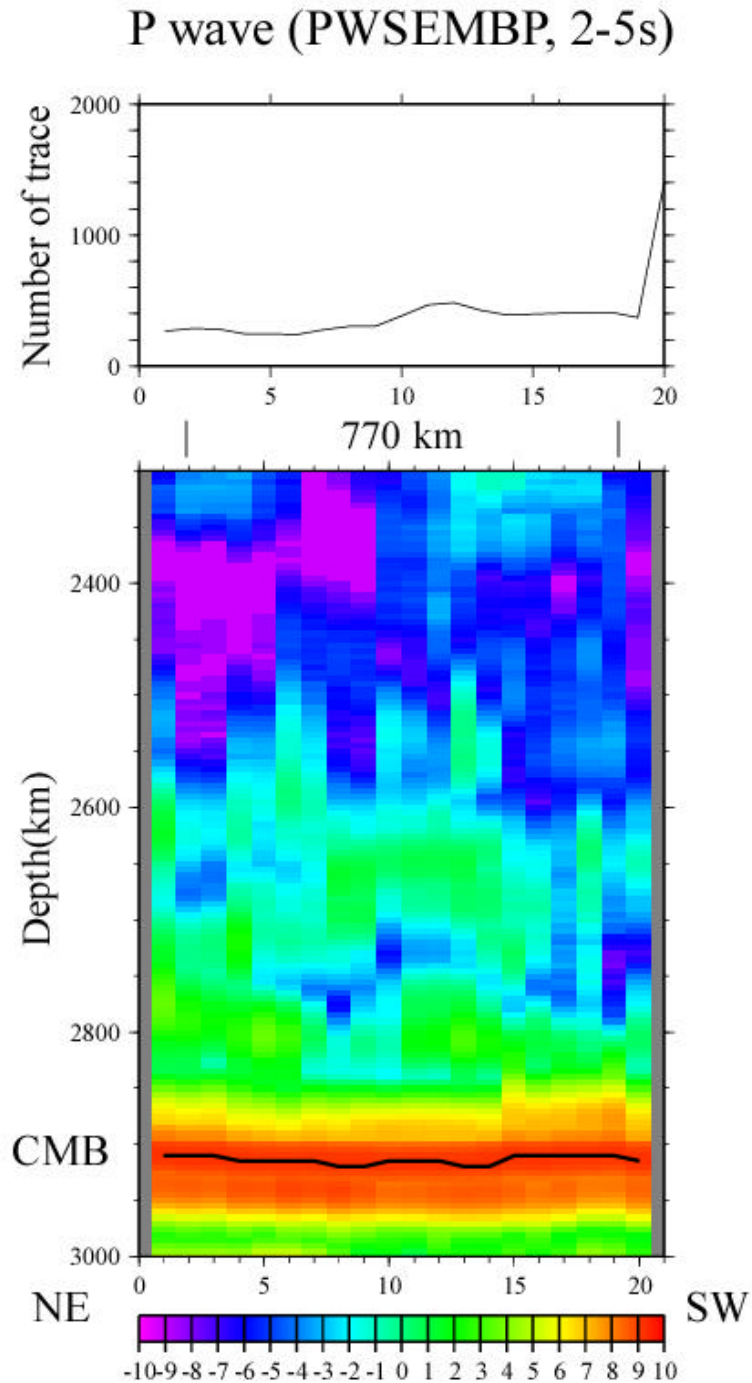


**Figure 1A.a** Without upper mantle correction and with 15s taper. In this condition the CMB depth is also quite stable.

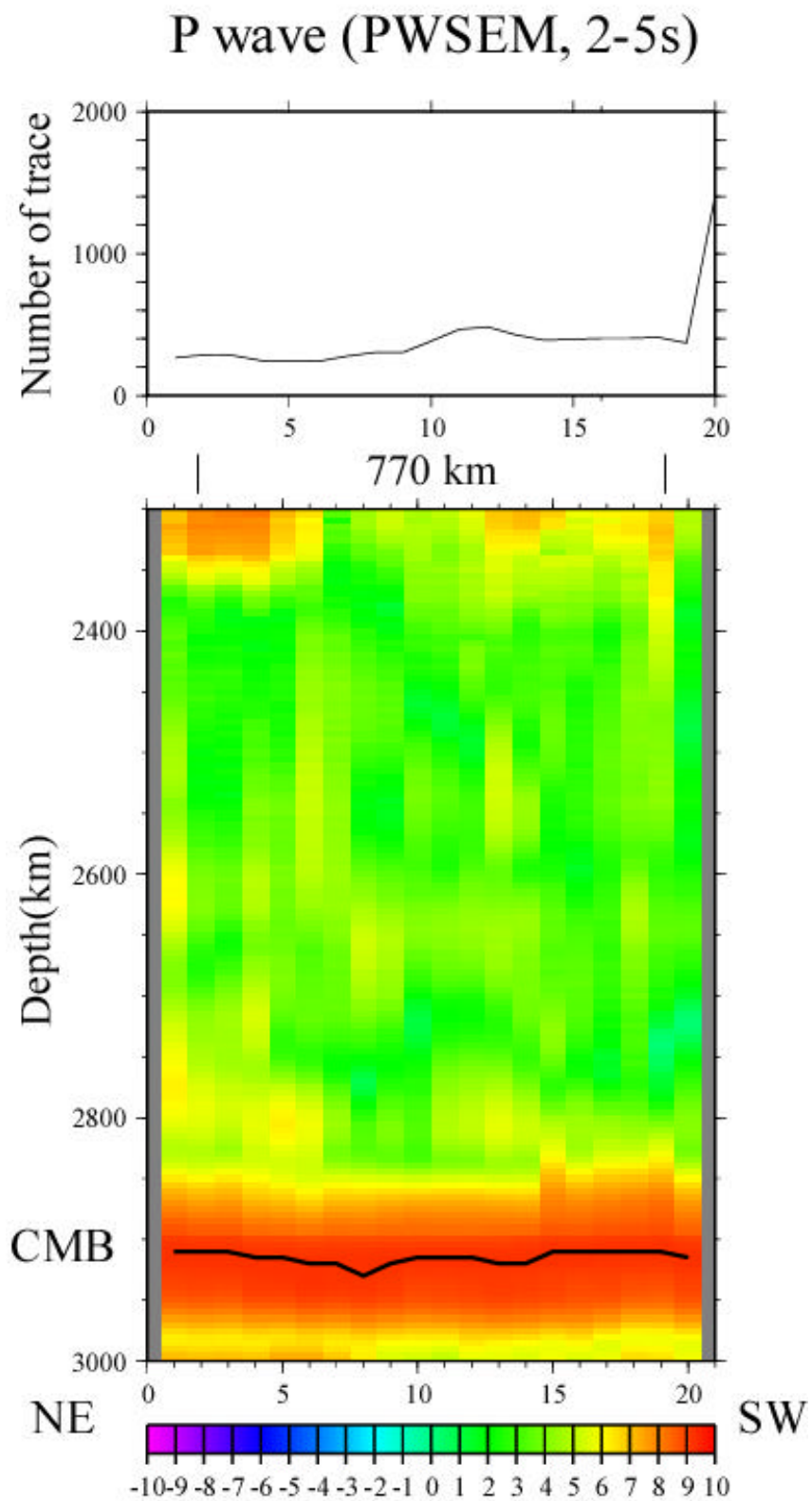


**Figure 1A.b** same as Figure 1A.a, but for PWSEM.

# P wave (BP, 2-5s)

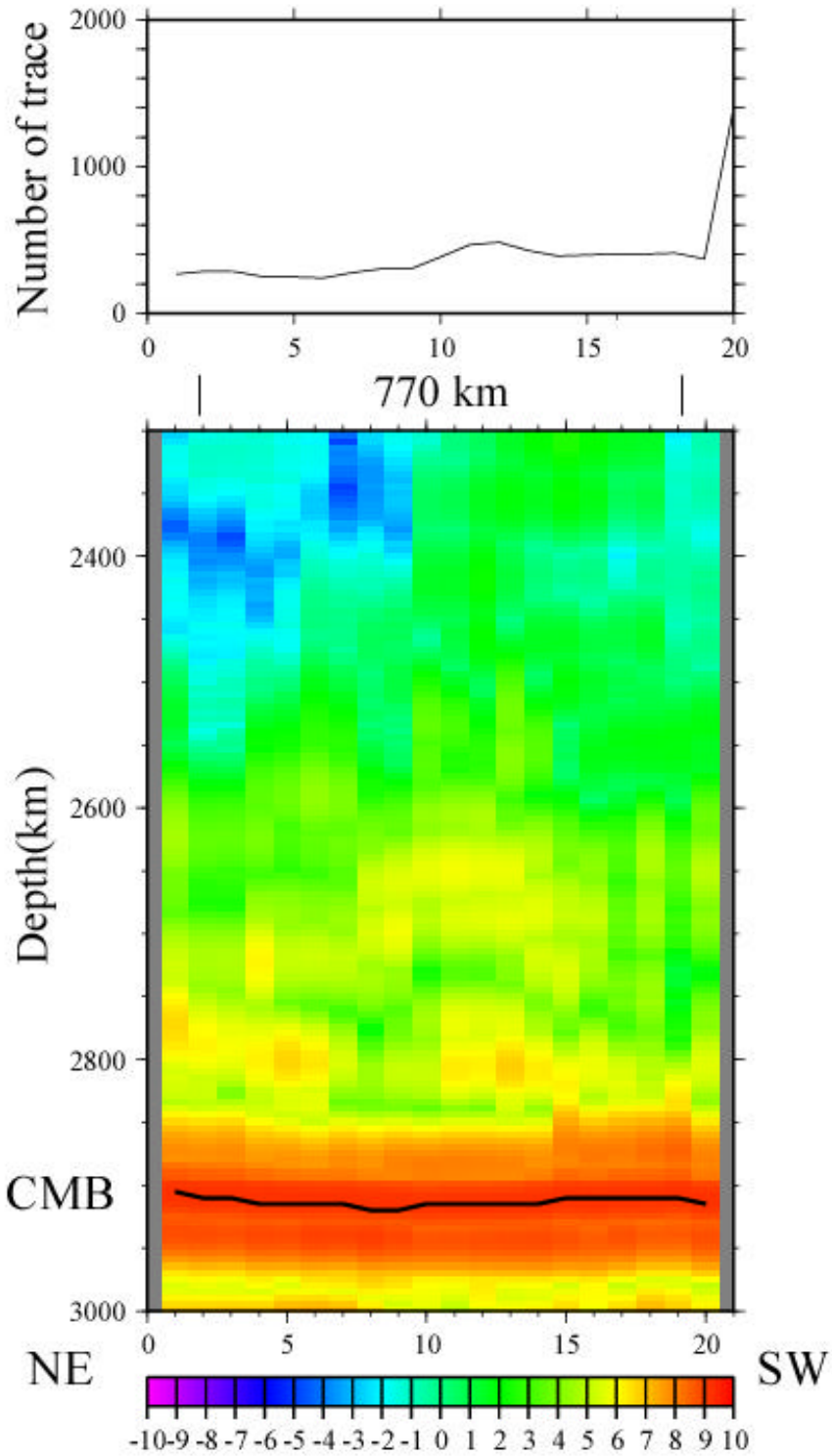


Figure 1A.c same as Figure 1A.a, but for BP.

## Appendix. 6

**Table 1. Events used in this study (Fiji-Tonga region)**

Event	Date Y/M/D	Origin Time (GMT)	Latitude (deg.)	Longitude (deg.)	Depth (km)	M <sub>b</sub>	Traces (*S-wave)	Remarks
1	92/08/30	20:09:07.1	17.87S	178.65W	569.3	5.8	109 (J-Array)	Engdahl
		20:09:10.9	17.75S	178.59W	574.2	5.8		Harvard
		20:09:05.7	17.92S	178.71W	565.0			PDE
2	93/03/21	05:05:00.2	18.01S	178.44W	589.1	6.0	90 (J-Array)	Engdahl
		05:05:07.5	17.71S	178.42W	607.6	6.2		Harvard
		05:04:59.2	18.04S	178.53W	588.9			PDE
3	93/04/16	14:08:39.8	17.76S	178.79W	567.2	6.0	107 (J-Array)	Engdahl
		14:08:46.7	17.54S	178.76W	591.7	6.0		Harvard
		14:08:38.9	17.78S	178.86W	565.1			PDE
4	93/07/09	15:37:55.3	19.78S	177.43W	404.3	5.9	145 (J-Array)	Engdahl
		15:38:00.8	19.74S	177.31W	418.2	5.9		Harvard
		15:37:53.6	19.78S	177.49W	398.2			PDE
5	93/08/07	17:53:27.0	24.01S	179.91E	549.5	6.0	143 (J-Array)	Engdahl
		17:53:34.1	23.91S	179.99E	546.8	6.0		Harvard
		17:53:24.2	23.87S	179.85E	523.1			PDE
6	93/08/21	09:42:36.3	21.35S	177.85W	424.7	5.6	102 (J-Array)	Engdahl
		09:42:44.1	21.23S	177.65W	453.4	5.8		Harvard
		09:42:35.9	21.28S	178.02W	426.9			PDE
7	91/09/30	00:21:48.5	20.84S	178.50W	580.8	6.3	95 (J-Array)	Engdahl
		00:21:54.0	20.67S	178.52W	589.8	6.0		Harvard
		00:21:46.4	20.88S	178.59W	591.0			PDE
8	00/12/18	01:19:28	21.11S	178.98W	655.7	6.4	402(164*) (Hi-net)	Harvard
		01:19:21	21.18S	179.12W	644.0			PDE
9	00/12/18	21:15:35	21.08S	178.98W	654.9	5.2	66 (Hi-net)	Harvard
		21:15:30	21.18S	179.09W	648.7			PDE
10	01/04/28	04:50:02	18.07S	176.68W	367.4	6.2	462(330*) (Hi-net)	Harvard
		04:49:53	18.06S	176.93W	359.0			PDE
11	01/05/26	10:57:31	20.25S	177.65W	413.9	5.3	258(369*) (Hi-net)	Harvard
		10:57:26	20.29S	177.84W	402.0			PDE
12	01/06/14	12:27:09	21.99S	179.34W	603.3	5.3	38 (Hi-net)	Harvard
		12:27:04	22.05S	179.46W	592.0			PDE



